

Partitioned Solution of Geometrical Multiscale Problems for the Cardiovascular System: Models, Algorithms, and Applications

THÈSE N° 5453 (2012)

PRÉSENTÉE LE 6 SEPTEMBRE 2012
À LA FACULTÉ DES SCIENCES DE BASE
CHAIRE DE MODÉLISATION ET CALCUL SCIENTIFIQUE
PROGRAMME DOCTORAL EN MATHÉMATIQUES

ÉCOLE POLYTECHNIQUE FÉDÉRALE DE LAUSANNE

POUR L'OBTENTION DU GRADE DE DOCTEUR ÈS SCIENCES

PAR

Adelmo Cristiano Innocenza MALOSSÌ

acceptée sur proposition du jury:

Prof. Ph. Michel, président du jury
Prof. A. Quarteroni, Dr S. Deparis, directeurs de thèse
Prof. A. Abdulle, rapporteur
Prof. C. A. Figueroa, rapporteur
Prof. J. Peiró, rapporteur



ÉCOLE POLYTECHNIQUE
FÉDÉRALE DE LAUSANNE

Suisse
2012

Alle persone a me più care

Elisa e Anita

Acknowledgements

First of all, I would like to express my gratitude to Prof. Alfio Quarteroni for giving me the opportunity to join his group at EPFL and work under his supervision. He has provided me with a stimulating research subject and he has strongly supported my work with deep enthusiasm and worthy ideas. His aptitude to go straight to the point together with his talent in studying and solving problems have made a crucial contribution to the outcome of this work.

I am very grateful to Dr. Simone DeParis who has represented a solid and reliable reference point throughout these years at CMCS. I wish to thank him especially for his careful supervision, his continuous and valuable support in any circumstances, and also for his priceless help on mathematical and software development topics.

A special thanks goes to Prof. Pablo J. Blanco for always being available to help and support me despite the huge distance. I am particularly grateful for giving me the opportunity to visit his research laboratory in Petropolis and for his kindness and patience during the several video conferences between EPFL and LNCC.

Several people have contributed to the achievement of this thesis. In particular, I would like to acknowledge Dr. Paolo Crosetto, for his support in the integration of the three-dimensional fluid-structure interaction model in the geometrical multiscale framework, as well as Dr. Matteo Astorino and Dr. Toni Lasilta, for the stimulating interactions and discussions during the development of a patient-specific left ventricular model. Moreover, I particularly thank Jean Bonnemain and Matteo Lesinigo for their profitable collaboration in the study of left ventricular assist device clinical problems. A special thanks goes to Prof. Luca Formaggia for his precious feedbacks on the development of reduced order models for cardiovascular flows. In addition, I would like to thank Prof. Joaquim Peiró and co-authors for giving us access to the data of their *in vitro* and *in silico* results published in the Journal of Biomechanics, as well as Dr. Philippe Reymond, for sharing with us the three-dimensional geometry of the aorta and other data from his one-dimensional arterial network simulations. I also wish to thank all the members of the jury for their precious remarks which have contributed to improve the clarity and completeness of the thesis. This work has also benefited from the collaboration with Mahmoud Jafarholi and Stanislas Hubeaux, who have carried out their semester projects under my supervision.

Desidero ringraziare Elisa per essermi sempre stata vicina, soprattutto nei momenti di difficoltà, e per rendere ogni giornata della mia vita incredibilmente meravigliosa. Ringrazio inoltre mia madre Anita per la stima, il supporto morale e l'incoraggiamento verso i miei studi.

A huge thanks goes to my friends Andrea, Anna, and Matteo, with whom I shared a wonderful office experience at MOX the year before my departure for Lausanne. I also thank Pierfrancesco and Simone who animated my doctoral adventure with amazing stories and never-ending laughter.

Last but not least, I would like to thank my CMCS colleagues, particularly Samuel, Laura, Peng, Ricardo, Gwenol, Matteo, and Luca, for their understanding, support, and for the many dinners and trips we had together. Thank you!

Lausanne, 1st June 2012

A. Cristiano I. Malossi

Projects and funds



Funding project: ERC-2008-AdG 227058

Mathematical modelling and simulation of the cardiovascular system.

- Task A (Mathematical Models for the Integrated Cardiovascular System)
 - Task G (Software Development)
 - Task H (Further Relevant Clinical Applications)
-

The **Mathcard** European project aims to describe and simulate the anatomic structure and the physiological response of the human cardiovascular system in healthy or diseased states. The emphasis of the project is on mathematical modeling, numerical analysis, algorithm implementation, computational efficiency, validation and verification. The final purpose is to set up a mathematical simulation platform eventually leading to the improvement of vascular diseases diagnosis, setting up of surgical planning, and cure of inflammatory processes in the circulatory system. This platform might also help physicians to construct and evaluate combined anatomic/physiological models to predict the outcome of alternative treatment plans for individual patients.



Funding project: HP2C 581947

HPC for Cardiovascular System Simulations.

The **High-Performance and High-Productivity Computing** (HP2C) Swiss platform aims at developing applications to run at scale and make efficient use of the next generation of supercomputers. The platform consists of domain science projects that are lead by research groups at Swiss universities and Institutes of the ETH Domain, and supported by a core group of scientific computing experts in the Lugano area. HP2C is jointly operated by the Swiss National Supercomputer Center (CSCS) and the Institute for Computational Sciences of the University of Lugano (USI). Project teams engage in high-risk and high-impact application development for HPC systems at scale.

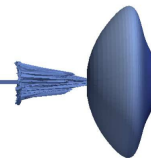


Funding project: BJRП 011010

Modeling and simulation of the human cardiovascular system with application to the diagnosis, treatment, and surgical planning of cardiovascular diseases.

The **Brazilian Swiss Joint Research Programme (BSJRP)** aims at carrying out research and development activities and human resources formation (master, doctoral and postdoctoral levels) in computational modeling and scientific computing and their applications in health-related areas. Specifically, it focuses on the development of simulation tools for complex physiological systems and, particularly, for the modeling of the human cardiovascular system. The final goal is to provide physicians with complementary/auxiliary elements based on physical-mathematical models to support them in the diagnosis and/or treatment of diseases as well as in surgical planning.

LIFE V



LifeV is a finite element library providing implementations of state of the art mathematical and numerical methods. It serves both as a research and production library. It has been used already in medical and industrial context to simulate fluid-structure interaction and mass transport. LifeV is the joint collaboration between four institutions: École Polytechnique Fédérale de Lausanne (CMCS) in Switzerland, Politecnico di Milano (MOX) in Italy, INRIA (REO, ESTIME) in France, and Emory University (Math&CS) in the United States of America.

Preface

This thesis represents the culmination of a research work that has taken place over a period of three years and half (from January, 2009 to June, 2012) at the Chair of Modeling and Scientific Computing, at the École Polytechnique Fédérale de Lausanne, in Switzerland. The models, the algorithms, and the main results presented in this work have been previously organized in several scientific papers. Most of these articles have already been published or submitted to international mathematical and biomedical engineering journals. Others are still in preparation and will be submitted by the end of the current year. This thesis has been structured in order to summarize, in a single text and with a coherent notation, all the results achieved in these works. To properly acknowledge the coauthors of such articles, the most relevant references are mentioned at the end of each chapter. Last but not least, an important part of this work has been achieved during two visits (from August 30th to September 10th, in 2010, and from May 30th to June 17th, in 2011) at the Laboratório Nacional de Computação Científica, in Brazil, where we have established a strong and fruitful scientific collaboration with the group of Prof. Raúl Feijóo and, in particular, with Prof. Pablo J. Blanco.

Lausanne, 1st June 2012

A. Cristiano I. Malossi

Abstract

The aim of this work is the development of a geometrical multiscale framework for the simulation of the human cardiovascular system under either physiological or pathological conditions. More precisely, we devise numerical algorithms for the partitioned solution of geometrical multiscale problems made of different heterogeneous compartments that are implicitly coupled with each others. The driving motivation is the awareness that cardiovascular dynamics are governed by the global interplay between the compartments in the network. Thus, numerical simulations of stand-alone local components of the circulatory system cannot always predict effectively the physiological or pathological states of the patients, since they do not account for the interaction with the missing elements in the network. As a matter of fact, the geometrical multiscale method provides an automatic way to determine the boundary (more precisely, the interface) data for the specific problem of interest in absence of clinical measures and it also offers a platform where to study the interaction between local changes (due, for instance, to pathologies or surgical interventions) and the global systemic dynamics.

To set up the framework an abstract setting is devised; the local specific mathematical equations (partial differential equations, differential algebraic equations, etc.) and the numerical approximation (finite elements, finite differences, etc.) of the heterogeneous compartments are hidden behind generic operators. Consequently, the resulting global interface problem is formulated and solved in a completely transparent way. The coupling between models of different dimensional scale (three-dimensional, one-dimensional, etc.) and type (Navier–Stokes, fluid-structure interaction, etc.) is addressed writing the interface equations in terms of scalar quantities, i.e., area, flow rate, and mean (total) normal stress. In the resulting flexible framework the heterogeneous models are treated as black boxes, each one equipped with a specific number of compatible interfaces such that (i) the arrangement of the compartments in the network can be easily manipulated, thus allowing a high level of customization in the design and optimization of the global geometrical multiscale model, (ii) the parallelization of the solution of the different compartments is straightforward, leading to the opportunity to make use of the latest high-performance computing facilities, and (iii) new models can be easily added and connected to the existing ones.

The methodology and the algorithms devised throughout the work are tested over several applications, ranging from simple benchmark examples to more complex cardiovascular networks. In addition, two real clinical problems are addressed: the simulation of a patient-specific left ventricle affected by myocardial infarction and the study of the optimal position for the anastomosis of a left ventricle assist device cannula.

Keywords: geometrical multiscale modeling, fluid-structure interaction, iterative methods, parallel algorithms, blood flow models, wave propagation, patient-specific geometries, clinical applications.

Résumé

Cette thèse de doctorat a pour but de développer un modèle géométrique multi-échelles pour la simulation du système cardio-vasculaire humain, aussi bien au niveau physiologique que pathologique. Plus précisément, l'objectif est de concevoir des algorithmes numériques qui permettent de coupler implicitement des géométries à différentes échelles et donc hétérogènes. L'intérêt pour cette méthode résulte du fait que l'étude des dynamiques du système cardio-vasculaire ne peut pas être séparée de l'analyse de l'interaction entre les différentes composantes qui le constituent. En d'autres termes, des simulations numériques ayant pour objet l'étude d'une composante isolée ne sont pas en mesure de prédire efficacement l'état physiologique ou pathologique du patient, parce qu'elles ne tiennent pas compte de l'influence que les autres parties du système ont sur la composante en cours d'examen. Dans cette perspective, le modèle géométrique multi-échelles se révèle particulièrement utile pour déterminer, d'une façon automatique et efficace, les conditions au bord du problème, même en l'absence de données cliniques. De plus, il permet d'étudier l'interaction entre les changements locaux (dus, par exemple, à une maladie ou une intervention chirurgicale) et les dynamiques du système.

Les algorithmes et les méthodes numériques pour la résolution de modèles multi-échelle de type géométrique ont été développés à partir d'une configuration générique abstraite, dans laquelle les équations de chaque sous-problème (équations différentielles aux dérivées partielles, équations algébriques, etc.) et la relative approximation numérique (éléments finis, différences finies, etc.) sont cachés derrière des opérateurs génériques. Les modèles d'échelles (tridimensionnel, unidimensionnel, etc) et types différents (équations de Navier–Stokes, interaction fluide-structure, etc.) sont couplés en écrivant les équations à l'interface en termes de quantités scalaires, comme par exemple, aire, débit et effort normal moyen. Le résultat est un système flexible dans lequel les différents modèles sont traités et couplés indépendamment de leurs caractéristiques géométriques ou mathématiques, de telle façon que (i) la disposition des compartiments dans le réseau puisse être facilement manipulée, offrant ainsi un haut niveau de personnalisation dans la conception et l'optimisation du modèle global, (ii) la parallélisation de la solution des différents compartiments soit simple, conduisant à la possibilité d'utiliser des systèmes de calcul de dernière génération à haute performance, et (iii) de nouveaux modèles puissent être facilement ajoutés et reliés à ceux déjà existants.

La méthodologie et les algorithmes conçus tout au long de cette thèse ont été testés sur plusieurs applications, qui vont de tests simples à réseaux cardio-vasculaires complexes. En outre, deux cas d'intérêt clinique ont été abordés : la simulation du ventricule gauche d'un patient atteint d'infarctus du myocarde et l'étude de la position optimale de l'anastomose de la canule d'un dispositif d'assistance ventriculaire.

Mots clés : modélisation géométrique multi-échelles, interaction fluide-structure, méthodes itératives, algorithmes parallèles, modèle du flux sanguin, propagation des ondes, géométrie spécifique du patient, applications cliniques.

Riassunto

Questa tesi di dottorato ha come obiettivo lo sviluppo di modelli multiscala in senso geometrico in grado di simulare il sistema cardiovascolare umano sia in condizioni fisiologiche che patologiche. Più precisamente, lo scopo è quello di elaborare algoritmi numerici che permettano di accoppiare implicitamente geometrie definite su scale differenti e quindi eterogenee. L'interesse nei confronti di questa metodologia deriva dalla consapevolezza che lo studio delle dinamiche insite nell'apparato cardiovascolare non può prescindere dall'analisi dell'interazione tra le varie componenti che lo costituiscono. In altre parole, simulazioni numeriche basate sullo studio di componenti isolate non sono in grado di predire lo stato fisiologico o patologico del paziente, poiché non tengono in considerazione l'influenza che le altre parti del sistema hanno sulla componente in esame. Da questo punto di vista, i modelli multiscala si rivelano particolarmente utili per determinare in maniera automatica ed efficiente le condizioni al bordo del problema anche in assenza di dati clinici, oltre a permettere di studiare l'interazione tra i mutamenti locali (dovuti, ad esempio, a patologie o interventi chirurgici) e le dinamiche dell'intero sistema.

Gli algoritmi e i metodi numerici per la risoluzione di modelli multiscala di tipo geometrico sono stati sviluppati a partire da una generica configurazione astratta, nella quale le equazioni dei singoli sottoproblemi matematici (equazioni differenziali parziali, equazioni algebriche differenziali, ecc.) e la relativa approssimazione numerica (elementi finiti, differenze finite, ecc.) sono nascoste tramite operatori generici. I modelli di diversa scala (tridimensionali, monodimensionali, ecc.) e tipo (Navier-Stokes, interazione fluido-struttura, ecc.) sono quindi accoppiati scrivendo le equazioni all'interfaccia in funzione di grandezze scalari come, ad esempio, area, flusso e sforzo normale mediato. Il risultato è un sistema flessibile nel quale i diversi modelli sono gestiti e accoppiati indipendentemente dalle loro caratteristiche geometriche o matematiche, in modo tale che sia possibile (i) manipolare facilmente la disposizione delle diverse componenti nel sistema, fornendo così un elevato livello di personalizzazione nella progettazione e ottimizzazione del modello globale, (ii) parallelizzare la soluzione dei diversi compartimenti, offrendo l'opportunità di utilizzare sistemi di calcolo di ultima generazione maggiormente performanti, e (iii) aggiungere nuovi modelli ed accoppiarli facilmente a quelli esistenti.

La metodologia e gli algoritmi sviluppati nel corso di questa tesi sono stati testati su diverse applicazioni, a partire da semplici casi test fino a più complessi sistemi cardiovascolari. Sono inoltre stati studiati due casi di interesse clinico: la simulazione del ventricolo sinistro in un paziente affetto da infarto del miocardio e lo studio della posizione ottimale dell'anastomosi della cannula di un dispositivo di assistenza ventricolare.

Parole chiave: modellazione multiscala in senso geometrico, interazione fluido-struttura, metodi iterativi, algoritmi paralleli, modelli di flusso sanguigno, propagazione delle onde, geometrie specifiche del paziente, applicazioni cliniche.

Contents

Acknowledgements	v
Projects and funds	vii
Preface	xi
Abstract (English/Français/Italiano)	xiii
List of figures	xxv
List of tables	xxvii
List of algorithms	xxix
Introduction	1
Cardiovascular physiology	1
Cardiovascular pathologies	3
Numerical simulation of cardiovascular problems: state of the art	4
Thesis objectives and outline	5
I Geometrical multiscale modeling	9
1 Fluid-structure interaction models for the cardiovascular system	11
1.1 3-D FSI model	11
1.1.1 Equations	12
1.1.2 Robin condition for the solid external wall	14
1.1.3 Interface conditions for the solid rings	15
1.1.3.1 Fixed solid ring boundary condition	15
1.1.3.2 Free solid ring boundary condition	16
1.1.3.3 Scaled area solid ring boundary condition	17
1.1.3.4 Qualitative comparison of the solid ring boundary conditions	18
1.1.4 Solution strategy for the FSI problem	19
1.1.5 Numerical approximation	19
1.1.5.1 Fully implicit time discretization	21
1.1.5.2 Geometric convective explicit time discretization	22
1.2 1-D FSI model	23
1.2.1 Mass and momentum conservation laws	23
1.2.2 Constitutive law of the arterial wall	24
1.2.3 Numerical approximation	25
	xix

1.2.3.1	First step: elastic response	26
1.2.3.2	Second step: viscoelastic correction	27
1.2.4	Compatibility conditions	28
2	Algorithms for the coupling of heterogeneous networks	31
2.1	Interface problem	31
2.2	Averaged/integrated interface quantities	33
2.3	Interface equations	35
2.3.1	Continuity of mean normal stress	37
2.3.2	Continuity of mean total normal stress	39
2.3.3	Continuity of the vessel area	40
2.4	Numerical methods	42
2.4.1	Aitken method	43
2.4.2	Newton method	44
2.4.3	Broyden method	45
2.4.4	Simplified algorithms for continuity of the vessel area	46
2.4.4.1	Explicit time discretization	47
2.4.4.2	Implicit with hierarchy time discretization	48
2.5	Framework implementation	48
3	Jacobian matrix for the interface problem	51
3.1	Matrix assembling	51
3.1.1	Matrix blocks: continuity of the mean normal stress	53
3.1.2	Matrix blocks: continuity of the mean total normal stress	54
3.1.3	Matrix blocks: continuity of the vessel area	56
3.2	Matrix entries computation/approximation	56
3.2.1	3-D models	58
3.2.1.1	Rigid wall model	58
3.2.1.2	FSI model	60
3.2.2	1-D FSI model	62
3.2.2.1	Exact tangent problem formulation	62
3.2.2.2	Two-level time step technique	66
II	Examples and cardiovascular simulations	69
4	Benchmark examples	71
4.1	Seven 3-D rigid wall pipes in a steady Stokes regime	71
4.1.1	Interface problem: continuity of mean normal stress	74
4.1.2	Interface problem: continuity of mean total normal stress	76
4.2	Five 3-D rigid wall pipes in a Womersley regime	79
4.3	Two 1-D FSI pipes	81
4.3.1	Iterations analysis	81
4.3.2	Reflections analysis	82
4.4	Wave reflection analysis in a series of heterogeneous FSI pipes	83
4.4.1	From 1-D to 3-D wave flow propagation	83
4.4.2	From 3-D to 1-D wave flow propagation	86

5	Cardiovascular networks	89
5.1	Numerical comparison of 3-D rigid wall carotid bifurcation geometries	90
5.2	Assessment of 1-D FSI numerical simulations against published data	92
5.2.1	Reference experimental and numerical setting	93
5.2.2	Three-element windkessel terminal lumped parameters model	94
5.2.3	Elastic wall simulations	96
5.2.4	Viscoelastic wall simulations	99
5.3	1-D modeling of the human arterial tree	101
5.3.1	Model predictions	101
5.3.2	Error analysis	102
5.3.3	Modeling analysis	103
5.3.4	Iterations and CPU time analyses	106
5.3.5	Interface equations comparison	108
5.4	Numerical comparison and calibration of geometrical multiscale models	110
5.4.1	Geometry reconstruction and mesh generation	110
5.4.2	Geometrical multiscale modeling	112
5.4.2.1	External tissues parameters comparisons: 3-D aorta	112
5.4.2.2	External tissues parameters comparisons: 3-D iliac	115
5.4.2.3	Solid ring boundary condition comparisons	118
5.4.2.4	Geometrical multiscale models comparisons	118
5.4.2.5	Interface equations comparison	120
5.4.2.6	Wall inertia comparison	123
5.4.3	Stand-alone 3-D FSI modeling	124
5.5	Computational cost analysis in a heterogeneous FSI abdominal aorta simulation	128
III	Clinical problems	133
6	Data acquisition and simulation of pathological left ventricle dynamics	135
6.1	State of the art	135
6.2	Data acquisition	137
6.2.1	Subject enrollment	137
6.2.2	MRI acquisition	138
6.2.3	Image processing and endocardium reconstruction	138
6.3	Left ventricle model	139
6.3.1	Definition of the ideal reference domain	139
6.3.2	Alignment and sizing	140
6.3.3	Ideal reference domain deformation	141
6.3.4	Epicardial displacement extrapolation	142
6.3.5	Set up of the problem: boundary conditions	143
6.3.6	Ideal lumped model for heart valves	144
6.4	Results	145
6.4.1	Regularization of the assimilated data	146
6.4.2	Sensitivity analysis with respect to the main parameters of the fictitious structure	147
6.4.3	Influence of boundary conditions at the heart valves	148
6.4.4	Patient-specific calibration of the systemic arterial circulation	150
6.5	Discussions	152

Contents

7 Numerical simulation of left ventricular assist device implantation	155
7.1 Clinical problem and state of the art	155
7.2 Lumped parameters model of the global circulation	158
7.2.1 Validation and results	160
7.2.2 Inflow boundary data for the 1-D network	162
7.3 Numerical comparisons of LVAD implantations	163
7.4 Discussions	164
Conclusions	169
Perspectives and future works	170
Bibliography	173
Curriculum vitæ	187

List of figures

1	Human circulatory system.	2
1.1	Scheme of the 3-D FSI model.	12
1.2	Scheme of the 1-D FSI model.	24
2.1	Decomposition of a trifurcation into five subdomains.	32
2.2	Examples of 3-D and 1-D FSI models with connections.	33
2.3	Generic coupling node configuration.	36
2.4	General scheme of a serial network of cylinders and related coupling nodes.	44
2.5	Continuity of the vessel area: algorithm flow diagram.	47
2.6	Continuity of the vessel area: simplified algorithm flow diagram (explicit).	47
2.7	Continuity of the vessel area: simplified algorithm flow diagram (implicit with hierarchy).	48
2.8	Framework implementation in LifeV.	49
3.1	Jacobian entries computation: 3-D rigid wall trifurcation example.	59
3.2	Jacobian entries computation: 1-D FSI.	63
3.3	Two-level time step technique interpolation example.	67
4.1	Seven 3-D rigid wall pipes in a steady Stokes regime: velocity magnitude.	72
4.2	Seven 3-D rigid wall pipes in a steady Stokes regime: pressure field.	72
4.3	Seven 3-D rigid wall pipes in a steady Stokes regime: pressure convergence.	72
4.4	Seven 3-D rigid wall pipes in a steady Stokes regime: benchmark configurations.	73
4.5	Five 3-D rigid wall pipes in a Womersley regime: configuration scheme.	80
4.6	Five 3-D rigid wall pipes in a Womersley regime: velocity profiles.	80
4.7	Two 1-D FSI pipes: configuration scheme.	81
4.8	Two 1-D FSI pipes: iteration analysis.	82
4.9	Two 1-D FSI pipes: reflection analysis.	82
4.10	From 1-D to 3-D wave flow propagation: configuration scheme.	84
4.11	From 1-D to 3-D wave flow propagation: wall parameters comparison.	84
4.12	From 1-D to 3-D wave flow propagation: interface equations comparison.	85
4.13	From 1-D to 3-D wave flow propagation: mesh size comparison.	86
4.14	From 3-D to 1-D wave flow propagation: configuration scheme.	87
4.15	From 3-D to 1-D wave flow propagation: flow rate.	87
4.16	From 3-D to 1-D wave flow propagation: radial scale factor.	87
5.1	3-D rigid wall carotid bifurcations comparison: scheme.	90
5.2	3-D rigid wall carotid bifurcations comparison: flow rate splitting.	91
5.3	3-D rigid wall carotid bifurcations comparison: coupling stress.	91

List of figures

5.4	3-D rigid wall carotid bifurcations comparison: velocity profiles.	92
5.5	Three-element windkessel model scheme.	94
5.6	1-D FSI simulations assessment: flow rate comparison (elastic wall, resistive terminals). . .	97
5.7	1-D FSI simulations assessment: pressure comparison (elastic wall, resistive terminals). . .	97
5.8	1-D FSI simulations assessment: terminals comparison (elastic wall).	99
5.9	1-D FSI simulations assessment: elastic versus viscoelastic wall comparison.	100
5.10	1-D FSI human arterial tree: model predictions (global view).	103
5.11	1-D FSI human arterial tree: model predictions (cerebral view).	104
5.12	1-D FSI human arterial tree: modeling analysis (flow rate).	105
5.13	1-D FSI human arterial tree: modeling analysis (pressure).	106
5.14	1-D FSI human arterial tree: iterations analysis.	107
5.15	1-D FSI human arterial tree: interface equations comparison.	109
5.16	Geometrical multiscale comparisons: aorta and iliac geometries and wall regions.	111
5.17	Geometrical multiscale comparisons: aorta flow rate (elastic).	114
5.18	Geometrical multiscale comparisons: aorta wall displacement (elastic tissues).	114
5.19	Geometrical multiscale comparisons: aorta flow rate (viscoelastic tissues).	115
5.20	Geometrical multiscale comparisons: iliac flow rate (viscoelastic tissues).	116
5.21	Geometrical multiscale comparisons: iliac wall displacement (bifurcations tissues).	117
5.22	Geometrical multiscale comparisons: iliac wall displacement (enlarged view).	118
5.23	Geometrical multiscale comparisons: fixed versus coupled area (aorta wall displacement).	119
5.24	Geometrical multiscale comparisons: fixed versus coupled area (iliac wall displacement).	119
5.25	Geometrical multiscale comparisons: fixed versus coupled area (flow rate and pressure).	120
5.26	Geometrical multiscale comparisons: aorta and iliac networks flow rate (aorta interfaces).	121
5.27	Geometrical multiscale comparisons: aorta and iliac networks flow rate (iliac interfaces).	122
5.28	Geometrical multiscale comparisons: aorta and iliac networks pressure and area.	123
5.29	Geometrical multiscale comparisons: aorta and iliac networks displacement (wall inertia).	124
5.30	Geometrical multiscale comparisons: aorta stand-alone flow rate and pressure.	125
5.31	Geometrical multiscale comparisons: aorta stand-alone wall displacement.	126
5.32	Geometrical multiscale comparisons: iliac stand-alone flow rate and pressure.	127
5.33	Geometrical multiscale comparisons: iliac stand-alone wall displacement.	127
5.34	Heterogeneous FSI abdominal aorta simulation: scheme and boundary data.	128
6.1	Heart modeling: hierarchical model tree for the simulation of the human heart.	136
6.2	Heart modeling: ideal reference fluid and solid domains.	140
6.3	Heart modeling: lumped valves configuration.	144
6.4	Heart modeling: regularization level analysis.	147
6.5	Heart modeling: Young's modulus analysis.	148
6.6	Heart modeling: ventricle valves boundary condition analysis.	149
6.7	Heart modeling: calibration of the systemic arterial circulation (pressure).	151
6.8	Heart modeling: calibration of the systemic arterial circulation (flow rate).	152
6.9	Heart modeling: calibration of the systemic arterial circulation (ventricular pressure).	153
7.1	LVAD: scheme of the two devices.	157
7.2	LVAD: 0-D model diagram.	158
7.3	LVAD: 0-D model results (pressure-volume diagrams).	161
7.4	LVAD: 0-D model results (flow rate at cannula and aortic root).	162
7.5	LVAD: 1-D model results (flow rate and pressure, AA versus DA; MHF + LVAD at 8k RPM).	165
7.6	LVAD: 1-D model results (flow rate and pressure, AA versus DA; SHF + LVAD at 10k RPM).	166

7.7 LVAD: 1-D model results (flow rate at different RPM; MHF + LVAD connected to AA). . . . 166
7.8 LVAD: 1-D model results (flow rate at different RPM; SHF + LVAD connected to AA). . . . 167

List of tables

1.1	Pros and cons qualitative comparison of the 3-D solid ring interface conditions.	18
2.1	Continuity of the vessel area: residuals vectors.	41
2.2	Continuity of the vessel area: unknowns vectors.	42
2.3	Aitken method: qualitative convergence.	44
2.4	Aitken method: iterations versus number of coupling nodes.	44
3.1	Continuity of the vessel area: diagonal block elements of the Jacobian matrix.	57
3.2	Continuity of the vessel area: additional off-diagonal block entries.	57
4.1	Seven 3-D rigid wall pipes in a steady Stokes regime: stress boundary quantities.	73
5.1	1-D FSI simulations assessment: parameters.	96
5.2	1-D FSI simulations assessment: errors (elastic wall, resistive terminals).	98
5.3	1-D FSI simulations assessment: errors (viscoelastic wall, resistive-compliant terminals).	100
5.4	1-D FSI human arterial tree: parameters.	102
5.5	1-D FSI human arterial tree: two-level time step technique error analysis.	105
5.6	1-D FSI human arterial tree: two-level time step technique iterations analysis.	107
5.7	1-D FSI human arterial tree: two-level time step technique CPU time.	108
5.8	1-D FSI human arterial tree: interface equations error analysis.	109
5.9	Geometrical multiscale comparisons: 3-D aorta and iliac wall parameters.	111
5.10	Geometrical multiscale comparisons: aorta tissues coefficients (elastic).	114
5.11	Geometrical multiscale comparisons: aorta tissues coefficients (viscoelastic).	115
5.12	Geometrical multiscale comparisons: iliac tissues coefficients.	116
5.13	Geometrical multiscale comparisons: iliac tissues coefficients (bifurcations).	117
5.14	Geometrical multiscale comparisons: interface equations error analysis.	122
5.15	Heterogeneous FSI abdominal aorta simulation: 3-D abdominal aorta wall parameters.	129
5.16	Heterogeneous FSI abdominal aorta simulation: iterations.	130
5.17	Heterogeneous FSI abdominal aorta simulation: CPU time.	130
6.1	Heart modeling: clinical data.	138
6.2	Heart modeling: left ventricular wall and mitral valve parameters.	146
6.3	Heart modeling: regularization level analysis.	147
7.1	LVAD: 0-D model heart failure parameters.	160
7.2	LVAD: 0-D model results compared to reference clinical data.	161
7.3	LVAD: 1-D model results (AA and DA mean flow rate comparison).	164



List of algorithms

2.1	Parallel time advancing with Newton.	45
2.2	Parallel time advancing with Newton and Broyden.	46
3.1	Jacobian matrix block assembling procedure.	52

Introduction

Nowadays cardiovascular diseases are the first cause of morbidity and mortality in the world, thus motivating huge attention and economical investments in the research. Thanks to the increasing computational power and the progress in imaging and geometry reconstruction techniques, blood flow numerical simulations have become an effective tool to study and understand the physiology of the cardiovascular system as well as to predict the development of very common and dangerous cardiovascular pathologies.

The aim of this thesis is to develop new numerical algorithms for the simulation of complex cardiovascular problems, taking into account all the main heterogeneous components responsible for the global circulation (heart, arteries, etc.). In the following, for the reader's convenience, we first briefly recall the main elements of cardiovascular anatomy and the most common associated pathologies, to situate the context of the thesis. Then, we provide an overview of the most recent achievements in the field of computational hemodynamics. More precisely, we recall the main models used to account for the different compartments of the cardiovascular system, with a focus on the dimensional-heterogeneity of the constituent components. Finally, we close the introduction presenting a brief overview of the thesis objectives and outline.

Cardiovascular physiology

The human cardiovascular system mainly consists of two parallel networks, the systemic and the pulmonary circulations. In the systemic circulation the oxygenated blood flows from the left atrium into the left ventricle through the mitral valve, which prevents backflow. The contraction of the ventricle forces the blood into the aortic arch and the aorta. The coronary arteries stem from the aortic root and nourish the heart muscle itself. Three major arteries originate from the aortic arch, supplying blood to the head and the upper limbs (the arms). The other major arteries originating from the aorta are (i) the renal arteries, which supply kidneys, (ii) the celiac and the superior and inferior mesenteric arteries, which supply intestines, spleen, and liver, and (iii) the iliac arteries, which branch out to the lower trunk and become the femoral and popliteal arteries of the thighs and legs, respectively. At the far end of the arterial circulation the blood flows through the capillary bed where it delivers nutrients and oxygen to organs and muscles and removes carbon dioxide. Then, the capillaries converge to form venules, which in turn form veins. The inferior vena cava returns blood to the heart from the legs and trunk; it is supplied by the iliac veins from the legs, the hepatic veins from the liver, and the renal veins from the kidneys. The subclavian veins, draining the arms, and the jugular veins, draining the head, join to form the superior vena cava. The two vena cavae, together with the coronary veins, return deoxygenated blood to the right atrium of the heart. There, the pulmonary circulation starts: the blood flows from the right atrium into the right ventricle through the tricuspid valve. The right ventricle contracts to

Introduction

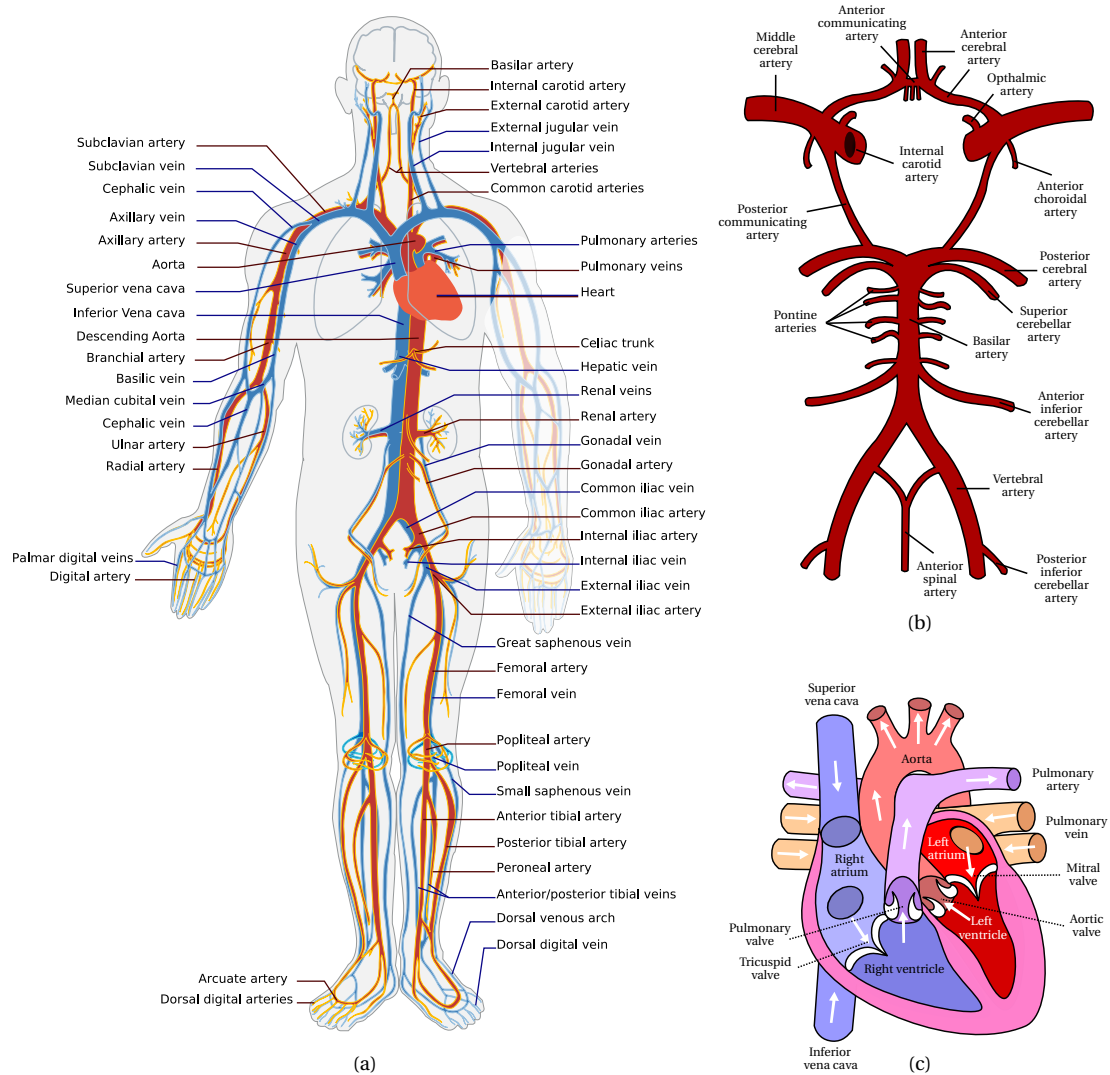


Figure 1: Schemes of the human circulatory system¹: red and blue colors indicate oxygenated and deoxygenated blood. (a) Main arteries and veins. (b) Circle of Willis (main cerebral arteries). (c) Heart circulation.

force blood into the lungs through the pulmonary arteries. In the lungs oxygen is picked up and carbon dioxide eliminated, and the oxygenated blood returns to the left atrium of the heart via the pulmonary veins, thus completing the circuit. Indeed, in pulmonary circulation the arteries carry deoxygenated blood, and the veins bear oxygenated blood. Few schematic pictures describing the main elements of the circulatory system are shown in Figure 1.

The structure and the mechanical properties of the arterial wall are rather complex. Large arteries ranges approximately from 2.5 cm to 0.1 cm of diameter and are made of three layers: the tunica intima (the inner coat), the tunica media (the middle coat), and the tunica adventitia (the outer coat). The tunica intima contains the endothelial cells, which sense and react to the normal and shear stress coming from the fluid. The tunica media is the thickest layer and is composed mainly of elastin and

¹Images from Wikipedia: <http://en.wikipedia.org>.

collagen fibers. The tunica adventitia is basically an outer covering and does not contribute significantly to the compliance of the vessel. Therefore, the mechanical properties of the wall are mainly determined by the tunica media, which has a nearly elastic behavior in physiological conditions. Regarding the small arteries, their wall is almost rigid and contains smooth muscle cells, which allow to change the intraluminal pressure and radius, in order to satisfy the needs of the surrounding tissues and to regulate the global arterial pressure.

The blood is composed mainly of erythrocytes, or red blood cells, numbering from 4.5 millions to 6 millions per cubic millimeter. They are responsible for the exchange of oxygen and carbon dioxide between the lungs and the body tissues. The leukocytes, or white blood cells, range approximately from 5000 to 10000 per cubic millimeter and defend the body against infecting organisms and foreign agents, both in the tissues and in the bloodstream itself. The blood also contains thrombocytes, or platelets, and several other factors active in blood clotting. Serum, a straw-colored liquid essentially composed of plasma (made 98% of water) without fibrinogen, makes up the liquid component of blood that separates from the clot. The behavior of blood is found to be non-Newtonian and its viscosity depends on the shear. The reason is that when the shear is low the red blood cells tend to interact, thus increasing the macroscopic viscosity of blood (the shear thinning effect). For high shear there is no interaction and the viscosity of blood in large arteries is approximately constant (approximately between 0.03 g/cm/s and 0.04 g/cm/s).

For more details about the cardiovascular system and its components see Netter (1997), Nichols et al. (2011), and references therein.

Cardiovascular pathologies

Cardiovascular pathologies are a class of diseases that involve heart, arteries, or veins. In the following we briefly describe some of the main cardiovascular problems together with a possible treatment, with the aim to show how numerical simulations of such pathological situations can potentially help clinicians and medical doctors in the decision making process.

Atherosclerosis is a condition in which the arterial wall thickens due to the accumulation of fatty materials, such as cholesterol. It is caused by the formation of multiple atherosclerotic plaques that might grow and, in an advanced stage, generate a severe stenosis or the total occlusion of the vessel. Moreover, possible ruptures of the fibrous cap can expose thrombogenic material (such as collagen) to the circulation and eventually induce thrombus formation in the lumen. Upon formation, intraluminal thrombi can occlude arteries outright (e.g., coronary occlusion), but more often they detach, move into the circulation and eventually occlude smaller downstream branches causing thromboembolism. The main clinical procedures to treat stenotic arteries are the creation of arterial bypass or the insertion of a stent, a device which supports the vessel wall preserving the original lumen area. Experimental evidences suggest that the wall shear stress is involved in the formation of atherosclerotic plaques. By computing this and other quantities numerical simulations can help clinicians to identify the higher risk locations and choose optimal strategies for the surgical interventions.

Aneurysms are localized gradual dilations in the arterial vessels. They mainly appear in arteries at the base of the brain (e.g., in the circle of Willis) or in the aorta. When the size of an aneurysm increases, there is a significant risk of rupture (see, e.g., Rahman et al. (2010)), resulting in severe hemorrhage, other complications, or death. An aneurysm can be either fusiform or saccular. The

former case is generally treated by grafting or by using stents. In contrast, a saccular aneurysm is either clipped or filled with thin metallic coils. In both cases, numerical predictions can help clinicians to decrease the post-operative risks, such as recanalisation.

Congenital defects are conditions that exist at birth or that develop during the first few months of life. A congenital defect may be the result of genetic or chromosomal abnormalities, intrauterine (uterus) environments, errors of morphogenesis, and infections. Examples of these pathologies are bileaflet aortic valves, heart septal defects, and pulmonary or tricuspid atresia. These defects usually require a surgical intervention, such as the Fontan procedure for tricuspid atresia (see Fontan and Baudet (1971)). In this regard, numerical simulations can give a prediction of the main hemodynamics features (e.g., pressure and flow rate) before and after the intervention.

Heart failure is the inability of the heart to supply sufficient blood flow to the body. It can cause a number of symptoms including shortness of breath, leg swelling, and exercise intolerance. Depending on the level of failure, treatment procedures range from non-invasive lifestyle measures (e.g., light exercise including breathing protocols and dietary changes) to the implantation of a ventricular assist device (VAD). The latter is used as a bridge to transplantation, bridge to recovery, or destination therapy (for patients who are not eligible for heart transplantation). It consists of an extracorporeal or intracorporeal circulation device used to bypass the left ventricle and to pump the oxygenated blood directly into the aorta. Frequently the hemodynamics modifications due to this treatment lead to complications that can be investigated using numerical simulations.

Numerical simulation of cardiovascular problems: state of the art

Blood flow dynamics is governed by the classical laws of mass, momentum, and energy conservation. The constitutive equations of the vessel wall provide an additional constraint that strongly influences the dynamics of the blood; indeed, the deformation of the vessel has to be taken into account to correctly predict the pulse wave propagation along the systemic network of arteries. In addition, the macroscopic modeling of the blood flow as a Newtonian fluid and of the arterial wall as an elastic structure is justified only for large arteries, while the circulation in arterioles and capillaries should be simulated using more complex models accounting for the effects mentioned in the previous sections. Furthermore the mechanical propulsion is provided by the muscle of the heart, governed by its own constitutive equations including active components.

The selection of the appropriate model and geometrical dimension representation depends on the aims and on the required accuracy of the research study. Being the time constraint important in a medical environment, a compromise between model complexity and computational cost is mandatory. For this reason usually only few specific components of the problem are represented by complex three-dimensional models, while the remaining parts are in general accounted for through reduced models. Indeed, the dimensional-heterogeneity of the constituent components becomes unavoidable to correctly model the global and local circulation.

Three-dimensional (3-D) fluid-structure interaction (FSI) models provide a detailed pointwise description of the flow dynamics in complex geometrical situations, such as those occurring at bifurcations, aneurysms, and stenoses among others. Moreover, thanks to the advancements in 3-D imaging techniques, they can now be employed to simulate patient-specific geometries starting from medical imaging data (see, e.g. Čanić et al. (2005), Gerbeau et al. (2005), Torii et al. (2008), Taylor and Figueroa (2009), and Faggiano et al. (2012)). Several techniques can be used

to model the interaction between the blood and the vessel wall. Here we mention the arbitrary Lagrangian–Eulerian (ALE) formulation (see, e.g., Nobile (2001), DeParis et al. (2006a), Küttler et al. (2010), Crosetto et al. (2011a) and references therein), the coupled momentum method (see Figueroa et al. (2006, 2009)), the Eulerian space-time formulation (see Tezduyar et al. (2006), Tezduyar and Sathe (2006)), and the isogeometric analysis (see Bazilevs et al. (2006, 2008)).

One-dimensional (1-D) FSI models are generally used to simulate the pulse wave propagation along large networks of arteries (see Wemple and Mockros (1972), Avolio (1980), Stettler et al. (1981), Stergiopoulos et al. (1992), Karamanoglu et al. (1994), Olufsen et al. (2000), Sherwin et al. (2003), Wang and Parker (2004), Formaggia et al. (2006), Alastruey et al. (2007), Huo and Kassab (2007), Mynard and Nithiarasu (2008), Reymond et al. (2009), and references therein). Originally introduced by Euler (1844), they provide a cheap and accurate description of the main physiological quantities of interest (flow rate, pressure, and average wall deformation) along the global systemic network of arteries, thus accounting for the global interplay among the physical phenomena taking place in the different compartments.

Zero-dimensional (0-D) or lumped parameters models provide averaged spatial information about the fundamental variables (pressure, flow rate, and volume) of the compartment of interest (organ, vessel, or part of vessel) at any instant in time, differentiating themselves from higher dimensional models that are also able to capture the spatial variation of these parameters. They are particularly appreciated in the description of complex multi-compartmental systems as they are easy to develop and prototype, fast to solve, and may be refined by adding equations for second-order effects and nonlinearities. Usually, lumped parameter models consist of sets of differential algebraic equations describing the conservation of mass and momentum which are complemented by a pressure-volume relation (see, e.g., Stergiopoulos et al. (1999), Segers et al. (2003), Milišić and Quarteroni (2004), Ottesen et al. (2004), and references therein). System models assembled from 0-D components generally feature the major components of the cardiovascular network (see, e.g., Ursino (1998), Liang and Liu (2005), and Lanzarone et al. (2007)). For a recent review on lumped parameters models for cardiovascular problems see Shi et al. (2011) and references therein.

The use of these dimensionally-heterogeneous models together with their correct mathematical coupling is called *geometrical multiscale* and has been firstly studied by Formaggia et al. (1999). Its efficient solution is a challenging task which has been addressed by several research groups with the final goal of accounting for the whole circulation and autoregulation of the systemic network of arteries (see Migliavacca et al. (2006), Vignon-Clementel et al. (2006), Grinberg and Karniadakis (2008), Blanco et al. (2009), Kim et al. (2009b), Papadakis (2009), Reichold et al. (2009), and references therein).

Thesis objectives and outline

The aim of this work is the development of a geometrical multiscale framework for the simulation of the human cardiovascular system under either physiological or pathological conditions. More precisely, we devise numerical algorithms for the partitioned solution of geometrical multiscale problems made of different heterogeneous compartments that are implicitly coupled with each others. To achieve this goal the algorithms have to be designed in an abstract setting. In particular, the local specific mathematical description and numerical approximation of the heterogeneous compartments must be hidden behind abstract operators, such that the resulting global interface problem can be formulated and solved in a completely transparent way. This leads to a flexible framework where the heterogeneous models are

treated as black boxes, each one equipped with a specific number of compatible interfaces, such that (i) the arrangement of the compartments in the network can be easily manipulated, thus allowing a high level of customization in the design and optimization of the global geometrical multiscale model, (ii) the parallelization of the solution of the different compartments is straightforward, leading to the opportunity to make use of the latest high-performance computing facilities, and (iii) new models can be easily added and connected to the existing ones, thus guaranteeing the future extensibility of the framework.

The driving motivation for the development of such a complex and flexible framework is the awareness that cardiovascular dynamics are governed by the global interplay between the components in the network. Indeed, numerical simulations of stand-alone local compartments of the circulatory system cannot always predict effectively the physiological or pathological states of the patient, since they do not account for the interaction with the missing elements in the network. As a matter of fact, the geometrical multiscale method provides an automatic way to determine the boundary data for the specific problem of interest in absence of clinical measures and it also offers a platform where to study the interaction between local changes (due, for instance, to pathologies or surgical interventions) and global systemic dynamics.

This work is structured in three parts and seven chapters. In Part I we set up an abstract setting where we develop the numerical algorithms for the assembling and the solution of a general geometrical multiscale problem.

Chapter 1 introduces the 3-D and the 1-D FSI models for the simulation of arterial flows. For the two models we provide the full set of equations and the used numerical approximation. An important part of the development is focused on the boundary conditions for the 3-D solid problem; in particular, we propose three different sets of equations for the inlet/outlet solid rings, while for the external wall we recall a suitable model to account for the dynamic response of the tissues. Regarding the 1-D model, a particular emphasis is devoted to the compatibility equations for the numerical scheme, which are here extended to account for the non-uniformities of both the material and the geometrical properties of the vessels.

Chapter 2 describes the methodology for the weak coupling of cardiovascular networks. After analyzing the main features of a generic interface problem, we devise different sets of interface equations for the coupling of dimensionally-heterogeneous networks. In particular, we compare an approach that preserves the total energy of the problem with another that takes advantage of the nature of the variational form of the 3-D FSI model. For both of them we also address the problem of the continuity of the area between two heterogeneous models. Our main contribution is in the writing of the interface equation in an abstract setting, such that the type of boundary data is not forced by the chosen set of interface equations. The last part of the chapter is focused on the numerical algorithms for the partitioned solution of the global network, which is solved through a nonlinear Richardson strategy, where the update is computed with either the Aitken, the Newton, or the Broyden methods. In this regard, we propose new algorithms for a two-level parallelization of the code.

Chapter 3 is focused on the computation of the exact Jacobian matrix required by the Newton method when this is used to solve the interface problem. For all the sets of interface equations developed in the previous chapter, we propose a new block assembling procedure of the Jacobian matrix. The Jacobian entries are computed by solving the exact tangent problem for both the 3-D and 1-D FSI models described in Chapter 1. For the latter, we also devise a new two-level time step technique to overcome the limitations introduced at the numerical level by the chosen explicit time discretization scheme.

In Part II we use benchmark examples and cardiovascular networks to set up several analyses focused on both numerical and modeling aspects.

Chapter 4 presents several simple examples to test and, somehow, validate the methodology devised in Part I. The examples range from small networks of 3-D rigid wall pipes in a steady Stokes regime, to simple configurations of dimensionally-homogeneous and dimensionally-heterogeneous FSI pipes connected in series. The aim is to analyze some critical aspects as a function of the available methods and algorithms. In particular, we study the entity of the numerical spurious reflections at the coupling interfaces between the models and the number of nonlinear Richardson iterations required to achieve the convergence of the global problem.

Chapter 5 is focused on the simulation of cardiovascular networks in a physiological regime. One of the main goals is to assess the benefits of complex geometrical multiscale problems made of several heterogeneous elements (3-D FSI vessels, networks of 1-D arteries, and terminal lumped parameters models) compared to the results of simpler models, such as full networks of 1-D arteries or stand-alone 3-D FSI models with boundary data taken from precomputed 1-D network simulations. In this aim, we first validate the 1-D networks through comparisons with published data (*in vitro* and *in silico*) and then we set up an analysis to calibrate the main parameters of the 3-D FSI models. In addition, we further extend the iteration analysis of the previous chapter in a cardiovascular context.

In Part III we select a couple of real clinical problems as an example of possible applications that could have not been addressed outside the geometrical multiscale setting.

Chapter 6 proposes a new approach for the data acquisition and simulation of a patient-specific left ventricle based on cardiac magnetic resonance images. The dynamics of the ventricle are captured by a set of tracking points on the endocardium identified from a time series of magnetic resonance images. From these tracking points the displacement of the endocardium is interpolated using radial basis functions to produce a smooth global deformation field in both space and time. These data are then used to impose the displacement on a 3-D fictitious elastic structure surrounding the 3-D fluid domain. The geometrical multiscale method is used for the coupling of the 3-D ventricle with a network of 1-D arteries, thus accounting for the interaction between the global circulation and the ventricle pressure and cardiac output: in particular, in case of myocardial infarction, the main parameters of the multiscale model are calibrated to account for the systolic dysfunction of the left ventricle.

Chapter 7 presents numerical simulations of left ventricle assist device implantation with the aim of comparing the ascending and descending aorta cannulations. Despite the fact that the second approach is less invasive, since it does not require a sternotomy and a cardiopulmonary bypass, clinicians still tend to prefer the first technique whose benefits are less controversial. With the aim of assessing the differences between these two approaches in terms of flow rate and pressure waveforms, we extend the 1-D network of arteries introduced in Chapter 5 to account for the presence of an outflow cannula that can be anastomosed to different locations of the aorta. Then, we use the resulting network to compare the results of the two different cannulations for several stages of heart failure and different rotational speed of the machine. The inflow boundary data for the heart and the cannulas are obtained from a lumped parameters model of the entire circulatory system.

We close this thesis with a summary of the main conclusions drawn throughout the text and the full list of bibliographic references.

Geometrical multiscale modeling **Part I**

1 Fluid-structure interaction models for the cardiovascular system

Some of the main indicators for vascular pathologies are consequence of the vessel wall compliance (e.g., the pulse wave velocity), the deformation of the vessel has therefore to be taken into account to have reliable simulations and to draw meaningful conclusions. The interaction between the blood and the arterial wall can be modeled in several ways, e.g., using a 1-D model that integrates the blood and the arterial wall (see, e.g., Sherwin et al. (2003), Formaggia et al. (2003), and Blanco et al. (2011)), performing a 3-D simulation for the fluid inside the deformable lumen, where the deformation of the wall is accounted at the variational level by a proper boundary condition on the endothelial wall (see, e.g. Vignon-Clementel et al. (2006), Figueroa et al. (2006), Nobile and Vergara (2008), Figueroa et al. (2009), and Kim et al. (2009b)), or considering the full interaction between the 3-D blood flow and a 3-D vessel wall by coupling the equations for the fluid flow with those for a solid structure (see Matthies and Steindorf (2003), Deparis et al. (2006a), Tezduyar et al. (2006), Bazilevs et al. (2008), Küttler et al. (2010), Crosetto (2011), and references therein).

In this chapter we describe two dimensionally-heterogeneous FSI models for the simulation of arterial flows. More precisely, in Section 1.1 we briefly recall from Quarteroni and Formaggia (2003) the main equations and the solution algorithm of the 3-D FSI model, where both the blood and the vessel wall are described in 3-D. An important part of the development is focused on the boundary conditions for the solid problem; in particular, we propose three different sets of equations for the inlet/outlet solid rings, while for the external wall we recall a suitable model to account for the dynamic response of the tissues, which has been developed in Moireau et al. (2012). Then in Section 1.2 we introduce the 1-D FSI model. The solution of the resulting hyperbolic equations is addressed with the explicit numerical scheme described in Formaggia et al. (2003), here extended to account for the non-uniformities of both the material and the geometrical properties of the vessel. We remark that all the numerical algorithms described throughout the chapter do not depend on the chosen FSI model.

1.1 3-D FSI model

In a geometrical multiscale setting, 3-D FSI models are used to simulate the hemodynamics in complex geometrical situations such as those occurring at bifurcations, aneurysms, and stenoses among others. In addition, when aiming at patient-specific analyses, the correct characterization of the local arterial flow has to be carried out by using patient-specific data obtained from 3-D medical images (see, e.g., Bonnemain et al. (2012a) and Faggiano et al. (2012)).

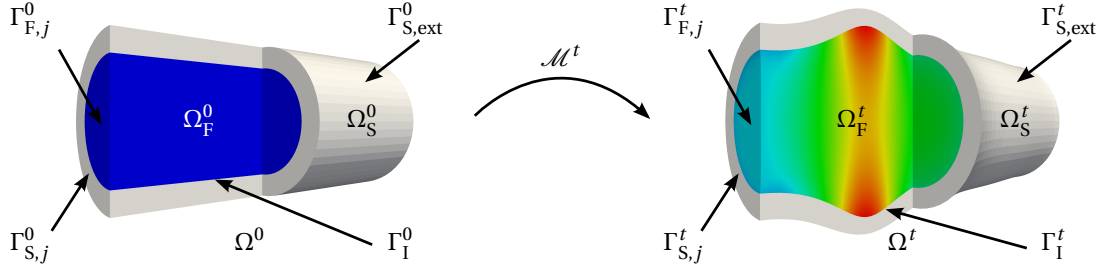


Figure 1.1: Reference and current configurations with ALE mapping. The colors in the scheme refer to the computed pressure field.

1.1.1 Equations

Despite the complexity of the blood rheology, a Newtonian incompressible fluid is a suitable model for blood at the scale of large arteries (see, e.g., Formaggia et al. (2009)). Following Formaggia and Nobile (1999) the arterial blood flow is modeled with the incompressible Navier–Stokes equations in the case of a moving fluid domain, resulting in the so-called Arbitrary Lagrangian Eulerian (ALE) formulation. This approach is motivated by the need of imposing the boundary conditions for the fluid equations on a moving domain.

Let $\Omega^0 \subset \mathbb{R}^3$ be a 3-D bounded domain with Lipschitz continuous boundary $\partial\Omega^0$, where $\bar{\Omega}^0 = \bar{\Omega}_F^0 \cup \bar{\Omega}_S^0$ denotes the reference configuration of the fluid-solid problem, being Ω_F^0 and Ω_S^0 the fluid and solid reference domains, respectively (see Figure 1.1). In addition, we denote by Γ_I^0 the reference fluid-solid interface $\partial\Omega_F^0 \cap \partial\Omega_S^0$. The ALE formulation leads to an arbitrary choice of the *geometrical problem*. In this work we describe the fluid domain displacement \mathbf{d}_F as harmonic extension of the solid displacement \mathbf{d}_S at the fluid-solid interface Γ_I^0 to the interior of the fluid reference domain Ω_F^0 , i.e.,

$$\begin{cases} -\Delta \mathbf{d}_F = \mathbf{0} & \text{in } \Omega_F^0, \\ \mathbf{d}_F - \mathbf{d}_S = \mathbf{0} & \text{on } \Gamma_I^0, \\ \nabla \mathbf{d}_F \cdot \mathbf{n}_F = \mathbf{0} & \text{on } \partial\Omega_F^0 \setminus \Gamma_I^0, \end{cases} \quad (1.1)$$

being \mathbf{n}_F the outgoing normal direction on the fluid domain boundary. The solid displacement \mathbf{d}_S changes with time, therefore the harmonic extension (1.1) defines the current configuration of the fluid domain Ω_F^t , which is parametrized by the ALE map

$$\begin{aligned} \mathcal{M}^t : \Omega_F^0 &\rightarrow \Omega_F^t \subset \mathbb{R}^3 \\ \mathbf{x}^0 &\mapsto \mathcal{M}^t(\mathbf{x}^0) = \mathbf{x}^0 + \mathbf{d}_F(\mathbf{x}^0), \end{aligned}$$

such that $\Omega_F^t = \mathcal{M}^t(\Omega_F^0)$, with $\mathbf{x}^0 \in \Omega_F^0$ a fluid point in the reference configuration. This approach is very convenient in the description of deforming arteries since it allows to preserve the mesh topology during the simulations and just move its vertices. Nevertheless, it is important to check that the finite elements remain geometrically valid after the mapping, but this is usually the case in the hemodynamics context where the wall deformations are relatively small.

The *fluid problem* is modeled by the incompressible Navier–Stokes equations written in the ALE formulation

$$\left\{ \begin{array}{ll} \rho_F \left(\frac{\partial \mathbf{u}_F}{\partial t} \Big|_{x^0} + ((\mathbf{u}_F - \mathbf{w}_F) \cdot \nabla) \mathbf{u}_F \right) - \nabla \cdot \boldsymbol{\sigma}_F = \mathbf{0} & \text{in } \Omega_F^t \times (0, T], \\ \nabla \cdot \mathbf{u}_F = 0 & \text{in } \Omega_F^t \times (0, T], \\ \mathbf{u}_F - \bar{\mathbf{u}}_F = \mathbf{0} & \text{in } \Omega_F^t \times \{0\}, \end{array} \right. \quad (1.2)$$

where $(0, T]$ is the time interval, ρ_F the fluid density, $\boldsymbol{\sigma}_F = -p_F \mathbf{I} + 2\mu_F \boldsymbol{\epsilon}_F(\mathbf{u}_F)$ the Cauchy stress tensor (with \mathbf{I} the identity matrix), $\boldsymbol{\epsilon}_F(\mathbf{u}_F) = (\nabla \mathbf{u}_F + (\nabla \mathbf{u}_F)^\top)/2$ the strain rate tensor, \mathbf{u}_F the fluid velocity vector field, $\bar{\mathbf{u}}_F$ the initial fluid velocity vector field, p_F the fluid hydrostatic pressure, μ_F the given fluid dynamic viscosity, and \mathbf{w}_F the fluid domain velocity, which is defined as

$$\mathbf{w}_F = \frac{\partial \mathcal{M}^t}{\partial t} \Big|_{x^0} = \frac{\partial \mathbf{d}_F}{\partial t} \Big|_{x^0}.$$

Problem (1.2) is closed by imposing an interface condition with the solid problem on Γ_I^0 and inflow and outflow boundary conditions on $\Gamma_{F,j}^t \subset \partial\Omega_F^t \setminus \Gamma_I^t$, $j = 1, \dots, n_F^t$. In a geometrical multiscale setting, some of these inflow/outflow boundaries are coupling interfaces with the nearby reduced dimensional model, where interface equations are imposed, as we discuss in Chapter 2. On the remaining boundaries we can impose given data, such as inlet/outlet time flow/velocity profiles.

Remark 1.1. The rigid wall form of problem (1.2) is

$$\left\{ \begin{array}{ll} \rho_F \left(\frac{\partial \mathbf{u}_F}{\partial t} + (\mathbf{u}_F \cdot \nabla) \mathbf{u}_F \right) - \nabla \cdot \boldsymbol{\sigma}_F = \mathbf{0} & \text{in } \Omega_F^0 \times (0, T], \\ \nabla \cdot \mathbf{u}_F = 0 & \text{in } \Omega_F^0 \times (0, T], \\ \mathbf{u}_F = \mathbf{0} & \text{on } \Gamma_I^0 \times (0, T], \\ \mathbf{u}_F - \bar{\mathbf{u}}_F = \mathbf{0} & \text{in } \Omega_F^0 \times \{0\}, \end{array} \right. \quad (1.3)$$

with a proper set of inflow and outflow boundary conditions on $\Gamma_{F,j}^0 \subset \partial\Omega_F^0 \setminus \Gamma_I^0$, $j = 1, \dots, n_F^0$. As discussed before, rigid wall simulations fail to predict some essential characteristics of the blood flow, such as the pressure wave propagation. Thus they cannot be considered reliable for arterial flow problems. However, they can be used in other contexts, such as the study of industrial flows in networks of rigid pipes. In Chapter 4 we make use of them to set up some preliminary benchmark cases and examples of networks.

The *solid problem* is formulated in a purely Lagrangian frame of reference. Several models of the arterial wall are described in literature, with different levels of complexity (see, e.g., Fung (1993), Holzapfel et al. (2000), Holzapfel and Ogden (2006), Li and Robertson (2009), and Robertson et al. (2011)). An accurate model for the arterial wall should take into account the three layers (intima, media, and adventitia), the incompressibility constraint, and the mechanical response of the wall to a given strain, which is mainly due to the *elastin* and *collagen* components. The former is responsible for the isotropic hyperelastic response, while the latter incorporates anisotropy and constitutive nonlinearity to the strain-stress relation; it is activated only when the strains reach a certain critical value and in certain directions (according to fiber orientation).

The full description of the solid mechanics of the arterial wall is not the focus of this work. Moreover, a linear elastic isotropic structure, which assumes small displacements of the wall compared to the radius of the vessels, is still considered a reasonable approximation for the large healthy arteries, as demonstrated numerically in, e.g., Crosetto et al. (2011b, 2012) and validated experimentally in, e.g., Kanyanta et al. (2009). Therefore, we consider a linear elastic model for the elastin and neglect the nonlinearities due to fiber orientation and activation. In addition, we assume a quasi-incompressible behavior for the arterial tissue and neglect its viscoelastic response. In fact, an equivalent viscoelastic effect is accounted for through proper boundary conditions acting over the external wall surface coming from a model of the surrounding tissues, as we discuss in Chapter 5. As a result of these considerations, in this work we consider a linear elastic isotropic St. Venant–Kirchhoff model to describe the solid displacement

$$\begin{cases} \rho_S \frac{\partial^2 \mathbf{d}_S}{\partial t^2} - \nabla \cdot \boldsymbol{\sigma}_S = \mathbf{0} & \text{in } \Omega_S^0 \times (0, T], \\ \mathbf{d}_S - \bar{\mathbf{d}}_S = \mathbf{0} & \text{in } \Omega_S^0 \times \{0\}, \\ \frac{\partial \mathbf{d}_S}{\partial t} - \bar{\mathbf{v}}_S = \mathbf{0} & \text{in } \Omega_S^0 \times \{0\}, \end{cases} \quad (1.4)$$

where ρ_S is the solid density, $\boldsymbol{\sigma}_S = \lambda_S \text{tr}(\boldsymbol{\epsilon}_S(\mathbf{d}_S))\mathbf{I} + 2\mu_S \boldsymbol{\epsilon}_S(\mathbf{d}_S)$ the first Piola–Kirchhoff stress tensor, being $\boldsymbol{\epsilon}_S(\mathbf{d}_S) = (\nabla \mathbf{d}_S + (\nabla \mathbf{d}_S)^\top)/2$, λ_S and μ_S are the first and second Lamé parameters, respectively, $\bar{\mathbf{d}}_S$ is the initial solid displacement, and $\bar{\mathbf{v}}_S$ the initial solid velocity. The St. Venant–Kirchhoff materials are usually characterized by the Young’s modulus E_S and the Poisson’s ratio ν_S . The following relations hold between the two sets of coefficients

$$\lambda_S = \frac{E_S \nu_S}{(1 - 2\nu_S)(1 + \nu_S)}, \quad \mu_S = \frac{E_S}{2(1 + \nu_S)}.$$

Problem (1.4) is closed by imposing an interface condition with the fluid problem on Γ_1^0 and a proper set of boundary conditions on $\partial\Omega_S^0 \setminus \Gamma_1^0$. In a geometrical multiscale setting, the area of the n_S^Γ inlet/outlet solid rings $\Gamma_{S,j}^0$, $j = 1, \dots, n_S^\Gamma$, can be related to the one of the surrounding models, as we show in Chapter 2; on the contrary, if there exists any uncoupled boundary interface, a different approach must be followed, as we discuss in Section 1.1.3. In turn, on the solid external wall $\Gamma_{S,\text{ext}}^0$ we can apply either a Neumann boundary condition, to account for a distributed pressure field, or a viscoelastic Robin boundary condition, to model the presence of the external tissues on the arteries, as we detail in the next section.

1.1.2 Robin condition for the solid external wall

From the modeling viewpoint, one critical aspect to get physiological results in 3-D FSI simulations is the tuning of the boundary condition to be prescribed on the solid external wall. The influence of external tissues and organs tethering and constraining the movement of blood vessels is of critical importance when simulating 3-D FSI problems in the arterial system (see, e.g., Liu et al. (2007)). At the present time, the modeling of the detailed multi-contact relations between the arteries and the other tissues is unfeasible. However, Crosetto et al. (2011b) show that for 3-D FSI problems the elastic behavior of external tissues support on the outer arterial wall can be handled by enforcing a Robin boundary condition on $\Gamma_{S,\text{ext}}^0$. This approach has been further extended in Moireau et al. (2012) to include also the viscoelastic response of the tissues, such that the resulting Robin boundary condition

for the 3-D FSI problem reads

$$\sigma_S \cdot \mathbf{n}_S + k_S \mathbf{d}_S + c_S \mathbf{v}_S + P_{\text{ext}} \mathbf{n}_S = \mathbf{0} \quad \text{on } \Gamma_{S,\text{ext}}^0 \times (0, T], \quad (1.5)$$

where \mathbf{v}_S is the velocity of the solid domain and P_{ext} the reference external pressure, i.e., the pressure level at which the vessel is considered undeformed and the area is equal to the reference value. The parameters k_S and c_S account for the elastic and viscoelastic response of the external tissues, respectively. More generally, they are empirical coefficients that depend on space and, possibly, on time (e.g., to represent the change of mechanical properties over time due to growth and remodeling of arterial structures).

Tuning the value of the parameters k_S and c_S is rather difficult. In Crosetto et al. (2011b) a range of orders of magnitude for the aorta is identified on the basis of qualitative considerations about the pulse wave velocity and the maximum admissible displacement of the vessel wall. In Moireau et al. (2012) similar values for the coefficients are identified on the basis of matching observations given by time-resolved image data. Indeed, these data are in general not available, thus representing a possible limitation of the model. Moreover, a sensitivity analysis showing the effect of the variation of the parameters on the main quantities of interest is missing in the literature. Therefore, in Chapter 5 we perform several comparisons in terms of flow rate, pressure, and displacement magnitude on two selected 3-D arterial geometries (an aorta and an iliac), as a function of different sets of values for the parameters k_S and c_S , with the aim of studying the effect of a variation these parameters on the main quantities of interest, and possibly to find a simple empiric way to calibrate these parameters in absence of measures and clinical data.

1.1.3 Interface conditions for the solid rings

As discussed before, problem (1.4) requires n_S^Γ boundary conditions on the inlet and outlet solid rings $\Gamma_{S,j}^0$, $j = 1, \dots, n_S^\Gamma$. These boundary conditions can either be provided from data, or computed by using information related to the surrounding models. In this section, we propose three different approaches to close the solid problem. For each approach we highlight the main pros and cons. The analysis of the numerically-induced wave reflections in a geometrical multiscale setting is deferred until Chapter 4.

1.1.3.1 Fixed solid ring boundary condition

A first approach, widely used in the literature, consists in fixing the solid rings of the 3-D FSI model by imposing a homogeneous Dirichlet boundary condition on the solid displacement, i.e.,

$$\mathbf{d}_S = \mathbf{0} \quad \text{on } \Gamma_{S,j}^0 \times (0, T], \quad (1.6)$$

with $j = 1, \dots, n_S^\Gamma$. This approach is very easy to implement, since no additional equations are required. However, this type of boundary condition is far from representing the behavior of the arterial wall at those locations. First of all, the value of the solid displacement near the fixed rings cannot be considered reliable, neither are the values of other physical quantities such as the wall stress state. In addition, spurious backward reflections may be generated at the outlets of the 3-D domain; in a geometrical multiscale setting, this problem can also affect the surrounding 1-D FSI models.

1.1.3.2 Free solid ring boundary condition

A more realistic behavior of the arterial wall at the inlet/outlet rings is in principle obtained by imposing homogeneous Neumann boundary conditions on the normal component of the first Piola–Kirchhoff stress tensor, i.e.,

$$\sigma_S \cdot \mathbf{n}_S = \mathbf{0} \quad \text{on } \Gamma_{S,j}^0 \times (0, T), \quad (1.7)$$

with $j = 1, \dots, n_S^\Gamma$. However, this approach may lead to an ill-posed problem, since the six rigid-body modes of the vessel are not all constrained. In addition, from the physical viewpoint, the continuation of the vessel beyond the boundaries is not represented; in particular, the solid rings are free to move along the longitudinal direction. The remedy that we propose is based on the following set of conditions:

$$\left\{ \begin{array}{l} \mathbf{d}_S \cdot \mathbf{n}_S = 0 \quad \text{on } \Gamma_{S,j}^0 \times (0, T), \\ \int_{\Gamma_{S,j}^0} \mathbf{d}_S \cdot \boldsymbol{\tau}_{1S} \, d\Gamma = 0, \quad \int_{\Gamma_{S,j}^0} \mathbf{d}_S \cdot \boldsymbol{\tau}_{2S} \, d\Gamma = 0 \quad \text{on } \Gamma_{S,j}^0 \times (0, T), \\ \int_{\Gamma_{S,j}^0} \left(\nabla_\Gamma \wedge [0, \mathbf{d}_S \cdot \boldsymbol{\tau}_{1S}, \mathbf{d}_S \cdot \boldsymbol{\tau}_{2S}]^\top \right) \cdot \mathbf{n}_S \, d\Gamma = 0 \quad \text{on } \Gamma_{S,j}^0 \times (0, T), \end{array} \right. \quad (1.8)$$

where $\boldsymbol{\tau}_{1S}$ and $\boldsymbol{\tau}_{2S}$ are the two tangential directions lying on $\Gamma_{S,j}^0$, $j = 1, \dots, n_S^\Gamma$. The first restriction prevents the normal displacement of the solid ring (in the longitudinal direction), representing the continuation of the vessel beyond the domain boundaries. In addition, it removes three rigid-body modes: the normal translation and the two non-planar rotations. The second restriction removes the two planar translation rigid-body modes, without imposing any constraint on the area of the vessel. More precisely, the boundary rings can enlarge or reduce their size around a fixed geometric center. This restriction can be rewritten in the following form:

$$\int_{\Gamma_{S,j}^0} P \mathbf{d}_S \, d\Gamma = \mathbf{0} \quad \text{on } \Gamma_{S,j}^0 \times (0, T),$$

being $P = I - \mathbf{n}_S \cdot \mathbf{n}_S^\top$ the local projection operator over the tangential plane where each solid ring lies. Finally, the third restriction removes the planar rotation rigid-body mode. Indeed, it can also be rewritten as

$$\int_{\Gamma_{S,j}^0} (\nabla_\Gamma \wedge P \mathbf{d}_S) \cdot \mathbf{n}_S \, d\Gamma = 0 \quad \text{on } \Gamma_{S,j}^0 \times (0, T).$$

Note that $P \mathbf{d}_S$ is a vector lying on the two-dimensional plane defined by its normal \mathbf{n}_S , while $\nabla_\Gamma \wedge$ denotes the curl operator defined in terms of the tangential coordinates and applied to such a tangent vector, whose action yields a vector aligned with \mathbf{n}_S . Furthermore, we can use a variant of the Green theorem to change the last restriction into the following one

$$\int_{C_{S,j}^0} P \mathbf{d}_S \cdot \boldsymbol{\tau}_C \, dC = 0 \quad \text{on } C_{S,j}^0 \times (0, T),$$

where $C_{S,j}^0$ denotes the internal and external curves that define the ring $\Gamma_{S,j}^0$, $j = 1, \dots, n_S^\Gamma$, and $\boldsymbol{\tau}_C$ is the tangent vector to these curves.

Remark 1.2. Cinthio et al. (2006) provide evidences of a significant longitudinal component of the motion of the arterial wall in some vessels (e.g., the carotid artery). In contrast to the current conjecture, they observed a distinct longitudinal movement of the arterial wall which is of the same magnitude as the local diameter change for an healthy patient. In view of this result, the first restriction in (1.8) can be either modified to prescribe a given longitudinal displacement field obtained from, e.g., a lumped parameters model, or relaxed through a Robin boundary condition (similar to Section 1.1.2).

Remark 1.3. In the most general case, where there exists at least one solid ring whose normal is not aligned with one of the Cartesian axes, it is convenient to impose the three restrictions by introducing different Lagrange multipliers in the weak form of the solid problem.

Remark 1.4. If there exists at least three boundary solid rings equipped with a different normal (as, e.g., in the case of a bifurcating artery), all the six rigid-body modes can be removed by imposing just the first restriction. However, from the physical point of view, the other two restrictions are still relevant.

The main advantage of this approach compared to (1.6), is the very general way of addressing the boundary conditions for the 3-D solid problem, without over-constraining the structure displacement at the coupling interfaces. In particular, it suits both stand-alone 3-D FSI problems and geometrical multiscale approaches, where the 3-D domain is coupled with 1-D problems although the continuity of the area is not guaranteed.

1.1.3.3 Scaled area solid ring boundary condition

A third different strategy is to prescribe the value of the boundary area of each fluid coupling interface. Following the approach devised in Formaggia et al. (2007), this can be done by prescribing a radial displacement of the internal contour of the j -th 3-D solid ring, $j = 1, \dots, n_S^F$, i.e.,

$$\left\{ \begin{array}{ll} \mathbf{d}_S \cdot \mathbf{n}_S = 0 & \text{on } \Gamma_I^0 \cap \Gamma_{S,j}^0 \times (0, T], \\ \left[\mathbf{d}_S - \Psi_j^t(\mathbf{x}^0 - \mathbf{x}_{G,j}^0) \right] \cdot \boldsymbol{\tau}_{1S} = 0 & \text{on } \Gamma_I^0 \cap \Gamma_{S,j}^0 \times (0, T], \\ \left[\mathbf{d}_S - \Psi_j^t(\mathbf{x}^0 - \mathbf{x}_{G,j}^0) \right] \cdot \boldsymbol{\tau}_{2S} = 0 & \text{on } \Gamma_I^0 \cap \Gamma_{S,j}^0 \times (0, T], \end{array} \right. \quad (1.9)$$

which corresponds to a geometric rescaling of the surface, where the radial scale factor is defined as

$$\Psi_j^t = \sqrt{\frac{A_j^t}{A_j^0}} - 1, \quad (1.10)$$

being A_j^0 and $\mathbf{x}_{G,j}^0$ the reference area of the j -th coupling interface of the 3-D fluid problem and its geometric center, respectively. This approach preserves the original shape of each 3-D solid ring, whose size is scaled by the value of the given boundary area A_j^t . Note that in (1.9) the normal and tangent vectors are defined on the j -th solid ring $\Gamma_{S,j}^0$.

Table 1.1: Qualitative comparison of the main pros and cons of each proposed interface ring boundary condition for the 3-D solid problem. Note that in the third column some comments depend on the chosen approach (local model versus continuity of the vessel area).

	Fixed	Free	Scaled area
Code implementation	Very easy	Very complex	Complex
Physics at the boundaries	Unrealistic	Realistic	Realistic
Continuity of the vessel area	No	No	No/Yes
Usable in stand-alone 3-D FSI problems	Yes	Yes	Yes/No
Usable in geometrical multiscale problems	Yes	Yes	Yes

Remark 1.5. As (1.8), also (1.9) constrains all the rigid-body modes of the 3-D FSI problem. However, this condition is applied only to the inner contour of the boundary rings, i.e., $\Gamma_I^0 \cap \Gamma_{S,j}^0$, $j = 1, \dots, n_S^\Gamma$. To close the 3-D FSI solid problem, we need to impose an additional boundary condition on $\Gamma_{S,j}^0 \setminus \Gamma_I^0 \cap \Gamma_{S,j}^0 \times (0, T]$, $j = 1, \dots, n_S^\Gamma$, which can be either (1.7) or (1.8). The former leaves some degrees of freedom to the displacement of the boundary solid rings, e.g., the external contour of the rings can move in the longitudinal direction or rotate on itself. However if the thickness of the solid wall is small compared to the vessel area, these movements are negligible.

Since, in general, boundary data of the vessels area are not available for cardiovascular simulations, the value of the area can be obtained either by modeling its dynamic through a local simple model, or, in a geometrical multiscale setting, by imposing the continuity of the boundary area with the surrounding models. The latter case is explored in Chapter 2. Regarding the former one, the dynamic of the local boundary area can be expressed as a function of the time and of some local boundary quantities, e.g., volumetric flow rate and average pressure. Among the several possibilities, a straightforward choice is to use the same differential-algebraic pressure-area relation employed in the 1-D FSI models (see the forthcoming Section 1.2), eventually adding some further contributions, such as the inertia of the wall, in order to match the physics of the 3-D solid problem given in (1.4).

1.1.3.4 Qualitative comparison of the solid ring boundary conditions

Finally, it is worthwhile to summarize the main pros and cons of the three methodologies described above. This comparison is shown in Table 1.1.

In Part II we set up several numerical comparisons between the three proposed approaches. In particular, in Chapter 4 a quantitative analysis of the wave reflections generated at the coupling interfaces is addressed for all the three cases through simple benchmark examples. Then, in Chapter 5 we make use of complex cardiovascular networks to compare the results of geometrical multiscale models in which the boundary solid rings of the 3-D geometries are fixed, with respect to those obtained where the boundary interfaces are scaled to enforce the continuity of the vessels size with the surrounding 1-D arteries. Indeed, problem (1.8) has been implemented only for the case of simple pipes, where all the boundary interfaces are aligned with one of the Cartesian axes.

1.1.4 Solution strategy for the FSI problem

The solution of the FSI problem can be obtained by using either a *modular* (segregated) or *non-modular* (monolithic) strategy. Depending on the choice of the boundary conditions applied to the fluid and solid domains, the former approach may lead to Dirichlet–Neumann (see, e.g., Deparis et al. (2006a,b)), Neumann–Dirichlet (see, e.g., Causin et al. (2005)), Robin–Neumann (see, e.g., Badia et al. (2008)), or Robin–Robin (see, e.g., Gerardo-Giorda et al. (2010)) approaches. In all the cases, the main drawback is that an additional subiteration algorithm is required to achieve strong coupling between the fluid and the solid problems. To avoid fluid–solid subiterations we choose the non-modular strategy, where the fluid and the solid are treated as a single problem. The solution algorithm relies on the parallel block preconditioner developed in Crosetto et al. (2011a), which is based on an inexact block factorization, where each factor is indeed an algebraic additive Schwarz preconditioner. The resulting preconditioner has proven to be effective and scalable, since each different factor addresses a single subproblem in a specific way.

Problems (1.2) and (1.4) are coupled through interface conditions on Γ_I^0 , which comprise the continuity of the velocity field and that of the traction; for the latter we use Lagrange multipliers. The resulting *interface problem* reads

$$\left\{ \begin{array}{ll} \mathbf{u}_F \circ \mathcal{M}^t - \frac{\partial \mathbf{d}_S}{\partial t} = \mathbf{0} & \text{on } \Gamma_I^0 \times (0, T), \\ \boldsymbol{\sigma}_S \cdot \mathbf{n}_S - \boldsymbol{\lambda}_{\Gamma_I} = \mathbf{0} & \text{on } \Gamma_I^0 \times (0, T), \\ \boldsymbol{\lambda}_{\Gamma_I} - J_S \mathbf{G}_S^{-T} (\boldsymbol{\sigma}_F \circ \mathcal{M}^t) \cdot \mathbf{n}_S = \mathbf{0} & \text{on } \Gamma_I^0 \times (0, T), \end{array} \right. \quad (1.11)$$

where $\boldsymbol{\lambda}_{\Gamma_I}$ is the Lagrange multiplier, \mathbf{n}_S the outgoing normal direction on the solid domain, $\mathbf{G}_S = \mathbf{I} + \nabla \mathbf{d}_S$ the solid deformation gradient, and $J_S = \det(\mathbf{G}_S)$. For the ease of writing, let us formally denote problems (1.1), (1.2), (1.4), and (1.11) in their weak form as \mathbf{G} , \mathbf{F} , \mathbf{S} , and \mathbf{I} , respectively. This allows us to write the global variational formulation of the FSI problem in a compact form as follows: find $(\mathbf{u}_F, p_F) \in \mathcal{V}_F$, $\mathbf{d}_S \in \mathcal{V}_S$, $\boldsymbol{\lambda}_{\Gamma_I} \in \mathcal{V}_I$ and $\mathbf{d}_F \in \mathcal{V}_G$ such that

$$\left\{ \begin{array}{ll} \mathbf{F}((\mathbf{u}_F, p_F), \boldsymbol{\lambda}_{\Gamma_I}, \mathbf{d}_F), (\mathbf{u}_F^*, p_F^*) = \mathbf{0} & \forall (\mathbf{u}_F^*, p_F^*) \in \mathcal{V}_F^*, \\ \mathbf{S}((\mathbf{d}_S, \boldsymbol{\lambda}_{\Gamma_I}), \mathbf{d}_S^*) = \mathbf{0} & \forall \mathbf{d}_S^* \in \mathcal{V}_S^*, \\ \mathbf{I}((\mathbf{u}_F, \mathbf{d}_S), \boldsymbol{\lambda}_{\Gamma_I}^*) = \mathbf{0} & \forall \boldsymbol{\lambda}_{\Gamma_I}^* \in \mathcal{V}_I^*, \\ \mathbf{G}((\mathbf{d}_S, \mathbf{d}_F), \mathbf{d}_F^*) = \mathbf{0} & \forall \mathbf{d}_F^* \in \mathcal{V}_G^*, \end{array} \right. \quad (1.12)$$

where \mathcal{V}_F , \mathcal{V}_S , \mathcal{V}_I , and \mathcal{V}_G are appropriate Hilbert spaces including the corresponding essential conditions according to the boundary data, while the superscript * identifies test functions and spaces.

1.1.5 Numerical approximation

The fluid problem is discretized in space by a $\mathbb{P}1$ – $\mathbb{P}1$ finite element method, stabilized by an interior penalty technique (see Burman et al. (2006)). The solid and the geometric problems are discretized in space by $\mathbb{P}1$ finite elements. These discretizations show a first order convergence in space.

A large variety of time discretizations for the incompressible Navier–Stokes equations on moving domains can be found in the literature, depending on the target application. In this work we use a first order Euler scheme. Regarding the structural problem, we use an explicit second order mid-point

scheme, which can be interpreted as a Newmark scheme with a particular choice of the coefficients. The extension of the proposed methodology to other space and time discretizations is straightforward and it is not a matter of concern here. The global time interval $[0, T]$ is split into several uniform subintervals $[t^n, t^{n+1}]$, $n = 0, 1, 2, \dots$, such that $t^n = n\Delta t$, Δt being the time step.

Regarding the notation in the following we use the superscripts n and $n + 1$ to refer to quantities at time t^n and t^{n+1} , respectively, and the h subscript for quantities discretized in space.

Remark 1.6. From the numerical viewpoint, the Robin boundary condition on the external wall must be implemented according to the time discretization scheme used in the solid problem. In particular, since in this work we use an explicit second order mid-point scheme, the following relation holds

$$\frac{\mathbf{v}_{S,h}^{n+1} + \mathbf{v}_{S,h}^n}{2} = \frac{\mathbf{d}_{S,h}^{n+1} - \mathbf{d}_{S,h}^n}{\Delta t},$$

such that, for $n = 0, 1, 2, \dots$, the discrete form of (1.5) reads

$$\sigma_{S,h} \cdot \mathbf{n}_S + \left(k_S + c_S \frac{2}{\Delta t} \right) \mathbf{d}_{S,h}^{n+1} = \left(c_S \frac{2}{\Delta t} \mathbf{d}_{S,h}^n + c_S \mathbf{v}_{S,h}^n \right) - P_{\text{ext}} \mathbf{n}_S \quad \text{on } \Gamma_{S,\text{ext}}^0,$$

where $\mathbf{v}_{S,h}^n$ is computed a posteriori as a post-processing variable.

Problem (1.12) is nonlinear due to the Navier–Stokes convective term and to the displacement of the fluid domain. Following Crosetto et al. (2011a), we use two different time discretization strategies to address such nonlinearities, as detailed in the next two sections. Regarding the solution of the coupled FSI problem it is possible to use fixed point algorithms (see, e.g., Mok and Wall (2001) and Deparis et al. (2006b)) or the Newton method (see, e.g., Crosetto et al. (2011a)). The driving motivation for choosing the latter is the appealing feature of a quadratic convergence to the solution of the coupled problem, even if it requires the computation of the exact Jacobian matrix. Several approximations of the corresponding Jacobian matrix by finite difference methods are proposed in the literature (see, e.g., Matthies and Steindorf (2003), Tezduyar et al. (2006), and Küttler et al. (2010) for a review). However, these schemes may lead to a substantial increase of the number of iterations required for the convergence to the solution of the FSI problem. For this reason, in this work we choose to compute the Jacobian blocks by an analytic formulation, which takes into account the shape derivatives, i.e., the cross derivatives of the fluid problem with respect to the domain motion. For a detailed description, including the derivation of the Jacobian blocks, see Fernández and Moubachir (2005) and Crosetto (2011, Section 3.4).

Let $\mathbf{u}_{\text{FSI},h}$ be the vector of unknowns of the FSI problem. The p -th iteration of the Newton method reads

$$\mathbf{u}_{\text{FSI},h}^{p+1} = \mathbf{u}_{\text{FSI},h}^p + \delta \mathbf{u}_{\text{FSI},h}^p, \quad (1.13)$$

where the update $\delta \mathbf{u}_{\text{FSI},h}^p$ is computed by solving

$$\mathcal{J}_{\text{FSI}} \left(\mathbf{u}_{\text{FSI},h}^p \right) \delta \mathbf{u}_{\text{FSI},h}^p = -\mathcal{R}_{\text{FSI}} \left(\mathbf{u}_{\text{FSI},h}^p \right). \quad (1.14)$$

This requires the computation of the Jacobian matrix $\mathcal{J}_{\text{FSI}} \left(\mathbf{u}_{\text{FSI},h}^p \right)$ and the evaluation of the residuals vector $\mathcal{R}_{\text{FSI}} \left(\mathbf{u}_{\text{FSI},h}^p \right)$ at each p -th iteration. The specific expression of these two elements depends on the chosen time discretization strategy.

1.1.5.1 Fully implicit time discretization

In the fully implicit (FI) time discretization scheme, the geometric and convective terms in the equations are considered implicitly, such that the unknowns vector is $\mathbf{u}_{\text{FSI},h} = (\mathbf{y}_{\text{F},h}^\top, \mathbf{d}_{\text{S},h}^\top, \boldsymbol{\lambda}_{\Gamma_1,h}^\top, \mathbf{d}_{\text{F},h}^\top)^\top$, being $\mathbf{y}_{\text{F},h} = (\mathbf{u}_{\text{F},h}^\top, p_{\text{F},h}^\top)^\top$. The FI formulation reads: given $\mathbf{u}_{\text{FSI},h}^n$, find $\mathbf{u}_{\text{FSI},h}^{n+1}$ such that

$$\mathbf{A}_{\text{FSI}}(\mathbf{u}_{\text{FSI},h}^{n+1}) \mathbf{u}_{\text{FSI},h}^{n+1} = \mathbf{b}_{\text{FSI}}(\mathbf{u}_{\text{FSI},h}^{n+1}),$$

where the finite element matrix \mathbf{A}_{FSI} depends on the solution vector $\mathbf{u}_{\text{FSI},h}^{n+1}$ and can be written in a block form as

$$\mathbf{A}_{\text{FSI}}(\mathbf{u}_{\text{FSI},h}^{n+1}) = \begin{bmatrix} \mathbf{F}_{\text{FF}}(\mathbf{y}_{\text{F},h}^{n+1}, \mathbf{d}_{\text{F},h}^{n+1}) & \mathbf{F}_{\text{FF}\Gamma_1}(\mathbf{y}_{\text{F},h}^{n+1}, \mathbf{d}_{\text{F},h}^{n+1}) & 0 & 0 & 0 & 0 & 0 \\ \mathbf{F}_{\Gamma_1\text{F}}(\mathbf{y}_{\text{F},h}^{n+1}, \mathbf{d}_{\text{F},h}^{n+1}) & \mathbf{F}_{\Gamma_1\Gamma_1}(\mathbf{y}_{\text{F},h}^{n+1}, \mathbf{d}_{\text{F},h}^{n+1}) & 0 & 0 & \Lambda_{\text{F}} & 0 & 0 \\ 0 & 0 & \mathbf{S}_{\text{SS}} & \mathbf{S}_{\text{S}\Gamma_1} & 0 & 0 & 0 \\ 0 & 0 & \mathbf{S}_{\Gamma_1\text{S}} & \mathbf{S}_{\Gamma_1\Gamma_1} & -\mathbf{I} & 0 & 0 \\ 0 & \Lambda_{\text{F}}^\top & 0 & -\mathbf{I}/\Delta t & 0 & 0 & 0 \\ 0 & 0 & 0 & 0 & 0 & \mathbf{G}_{\text{FF}} & \mathbf{G}_{\text{FF}\Gamma_1} \\ 0 & 0 & 0 & -\mathbf{I} & 0 & 0 & \mathbf{I} \end{bmatrix},$$

while

$$\mathbf{u}_{\text{FSI},h}^{n+1} = \begin{pmatrix} \mathbf{y}_{\text{FF},h}^{n+1} \\ \mathbf{y}_{\text{FF}\Gamma_1,h}^{n+1} \\ \mathbf{d}_{\text{SS},h}^{n+1} \\ \mathbf{d}_{\text{S}\Gamma_1,h}^{n+1} \\ \boldsymbol{\lambda}_{\Gamma_1,h}^{n+1} \\ \mathbf{d}_{\text{FF},h}^{n+1} \\ \mathbf{d}_{\text{FF}\Gamma_1,h}^{n+1} \end{pmatrix}, \quad \mathbf{b}_{\text{FSI}}(\mathbf{u}_{\text{FSI},h}^{n+1}) = \begin{pmatrix} \mathbf{b}_{\text{FF}}(\mathbf{d}_{\text{F},h}^{n+1}) \\ \mathbf{b}_{\text{FF}\Gamma_1}(\mathbf{d}_{\text{F},h}^{n+1}) \\ \mathbf{b}_{\text{SS}} \\ \mathbf{b}_{\text{S}\Gamma_1} \\ -\mathbf{d}_{\text{S}\Gamma_1,h}^n / \Delta t \\ \mathbf{0} \\ \mathbf{0} \end{pmatrix}.$$

In the algebraic form, for the sake of clarity, we distinguish between the degrees of freedom lying

on the fluid-solid interface (adding the subscript Γ_1 to the blocks) and those that are internal to the domains Ω_{F}^t and Ω_{S}^0 (for which we keep the same subscripts as for the continuous case). In particular, $\mathbf{y}_{\text{F},h} = (\mathbf{y}_{\text{FF},h}^\top, \mathbf{y}_{\text{FF}\Gamma_1,h}^\top)^\top$, $\mathbf{d}_{\text{S}} = (\mathbf{d}_{\text{SS},h}^\top, \mathbf{d}_{\text{S}\Gamma_1,h}^\top)^\top$, and $\mathbf{d}_{\text{F},h} = (\mathbf{d}_{\text{FF},h}^\top, \mathbf{d}_{\text{FF}\Gamma_1,h}^\top)^\top$. Blocks (1,1), (2,2), and (4,4) represent the discrete fluid, solid, and geometric problems, respectively. The off-diagonal entries enforce the coupling conditions between the three fields. The rectangular block matrix Λ_{F} coincides with $[\mathbf{I}, 0]^\top$, such that it selects the fluid velocity degrees of freedom of $\mathbf{y}_{\text{FF}\Gamma_1,h}$ to apply the fluid-solid interface conditions. Note that in this discrete formulation we suppose a first order time discretization of the velocity continuity condition. The nonlinearities, i.e., the dependence of the fluid blocks from the fluid displacement and from the fluid velocity and pressure fields, are explicitly indicated in the matrix entries. The fluid and solid right-hand sides including the terms generated by the time discretization of the momentum conservation equations are denoted by $\mathbf{b}_{\text{F}} = (\mathbf{b}_{\text{FF}}^\top, \mathbf{b}_{\text{FF}\Gamma_1}^\top)^\top$ and $\mathbf{b}_{\text{S}} = (\mathbf{b}_{\text{SS}}^\top, \mathbf{b}_{\text{S}\Gamma_1}^\top)^\top$, respectively. We remark that, due to the implicit formulation adopted for the fluid domain, also the fluid right-hand side depends on the fluid domain displacement.

The residual of the Newton method is defined as

$$\mathcal{R}_{\text{FSI}}(\mathbf{u}_{\text{FSI},h}^{n+1}) = \mathbf{A}_{\text{FSI}}(\mathbf{u}_{\text{FSI},h}^{n+1}) \mathbf{u}_{\text{FSI},h}^{n+1} - \mathbf{b}_{\text{FSI}}(\mathbf{u}_{\text{FSI},h}^{n+1}),$$

while the Jacobian matrix assumes the form

$$\mathcal{J}_{\text{FSI}}(\mathbf{u}_{\text{FSI},h}^{n+1}) = \begin{bmatrix} D_{\mathbf{y}_{\text{FF}}} \mathbf{F}_{\text{F}} & D_{\mathbf{y}_{\text{F}\Gamma_1}} \mathbf{F}_{\text{F}} & 0 & 0 & 0 & D_{\mathbf{d}_{\text{FF}}}(\mathbf{F}_{\text{F}} - \mathbf{b}_{\text{F}}) & D_{\mathbf{d}_{\text{F}\Gamma_1}}(\mathbf{F}_{\text{F}} - \mathbf{b}_{\text{F}}) \\ D_{\mathbf{y}_{\text{FF}}} \mathbf{F}_{\Gamma_1} & D_{\mathbf{y}_{\text{F}\Gamma_1}} \mathbf{F}_{\Gamma_1} & 0 & 0 & \Lambda_{\text{F}} & D_{\mathbf{d}_{\text{FF}}}(\mathbf{F}_{\Gamma_1} - \mathbf{b}_{\Gamma_1}) & D_{\mathbf{d}_{\text{F}\Gamma_1}}(\mathbf{F}_{\Gamma_1} - \mathbf{b}_{\Gamma_1}) \\ 0 & 0 & S_{\text{SS}} & S_{\text{S}\Gamma_1} & 0 & 0 & 0 \\ 0 & 0 & S_{\Gamma_1\text{S}} & S_{\Gamma_1\Gamma_1} & -\text{I} & 0 & 0 \\ 0 & \Lambda_{\text{F}}^{\text{T}} & 0 & -\text{I}/\Delta t & 0 & 0 & 0 \\ 0 & 0 & 0 & 0 & 0 & G_{\text{FF}} & G_{\text{F}\Gamma_1} \\ 0 & 0 & 0 & -\text{I} & 0 & 0 & \text{I} \end{bmatrix}.$$

Note that in the Jacobian matrix we have used the abridged notations

$$\begin{aligned} D_{\mathbf{x}} \mathbf{F}_{\text{F}} &= D_{\mathbf{x}} \mathbf{F}_{\text{FF}}(\mathbf{y}_{\text{F},h}^{n+1}, \mathbf{d}_{\text{F},h}^{n+1}) + D_{\mathbf{x}} \mathbf{F}_{\text{F}\Gamma_1}(\mathbf{y}_{\text{F},h}^{n+1}, \mathbf{d}_{\text{F},h}^{n+1}), & D_{\mathbf{x}} \mathbf{b}_{\text{F}} &= D_{\mathbf{x}} \mathbf{b}_{\text{FF}}(\mathbf{d}_{\text{F},h}^{n+1}) + D_{\mathbf{x}} \mathbf{b}_{\text{F}\Gamma_1}(\mathbf{d}_{\text{F},h}^{n+1}), \\ D_{\mathbf{x}} \mathbf{F}_{\Gamma_1} &= D_{\mathbf{x}} \mathbf{F}_{\Gamma_1\text{F}}(\mathbf{y}_{\text{F},h}^{n+1}, \mathbf{d}_{\text{F},h}^{n+1}) + D_{\mathbf{x}} \mathbf{F}_{\Gamma_1\Gamma_1}(\mathbf{y}_{\text{F},h}^{n+1}, \mathbf{d}_{\text{F},h}^{n+1}), & D_{\mathbf{x}} \mathbf{b}_{\Gamma_1} &= D_{\mathbf{x}} \mathbf{b}_{\Gamma_1\text{F}}(\mathbf{d}_{\text{F},h}^{n+1}) + D_{\mathbf{x}} \mathbf{b}_{\Gamma_1\Gamma_1}(\mathbf{d}_{\text{F},h}^{n+1}), \end{aligned}$$

being $D_{\mathbf{x}}$ the total derivative of a given functional with respect to a variable \mathbf{x} .

1.1.5.2 Geometric convective explicit time discretization

In the geometric convective explicit (GCE) time discretization scheme, at each new time iteration we define appropriate extrapolations $\mathbf{d}_{\text{S}\Gamma_1,h}^{\diamond}$ and $\mathbf{u}_{\text{F},h}^{\diamond}$ of the geometric and convective terms, respectively. In particular, we choose the simple approximation $\mathbf{d}_{\text{S}\Gamma_1,h}^{\diamond} = \mathbf{d}_{\text{S}\Gamma_1,h}^n$ and $\mathbf{u}_{\text{F},h}^{\diamond} = \mathbf{u}_{\text{F},h}^n$, such that the geometric and the fluid-solid parts of the problem can then be split. Hence, at each time step, first we compute the fluid displacement $\mathbf{d}_{\text{F},h}^{n+1}$ by solving the linear system associated to the geometric problem, i.e.,

$$\begin{bmatrix} G_{\text{FF}} & G_{\text{F}\Gamma_1} \\ 0 & \text{I} \end{bmatrix} \begin{pmatrix} \mathbf{d}_{\text{FF},h}^{n+1} \\ \mathbf{d}_{\text{F}\Gamma_1,h}^{n+1} \end{pmatrix} - \begin{pmatrix} \mathbf{0} \\ \mathbf{d}_{\text{S}\Gamma_1}^{\diamond} \end{pmatrix} = \mathbf{0}, \quad (1.15)$$

and we move the fluid mesh accordingly. Then, by computing the resulting fluid domain velocity as

$$\mathbf{w}_{\text{F},h}^{n+1} = \frac{\mathbf{d}_{\text{F},h}^{n+1} - \mathbf{d}_{\text{F},h}^n}{\Delta t},$$

we replace the convective term in the fluid momentum equation by $\left((\mathbf{u}_{\text{F},h}^{\diamond} - \mathbf{w}_{\text{F},h}^{n+1}) \cdot \nabla \right) \mathbf{u}_{\text{F},h}^{n+1}$. The unknowns vector is reduced to $\mathbf{u}_{\text{FSI},h} = (\mathbf{y}_{\text{F},h}^{\text{T}}, \mathbf{d}_{\text{S},h}^{\text{T}}, \boldsymbol{\lambda}_{\Gamma_1,h}^{\text{T}})^{\text{T}}$, and the second step reads: given $\mathbf{u}_{\text{FSI},h}^n$, find $\mathbf{u}_{\text{FSI},h}^{n+1}$ such that

$$\mathbf{A}_{\text{FSI}} \mathbf{u}_{\text{FSI},h}^{n+1} = \mathbf{b}_{\text{FSI}},$$

where now the the finite element matrix A_{FSI} does not depend on $\mathbf{u}_{\text{FSI},h}^{n+1}$, such that its block form reads

$$A_{\text{FSI}} = \begin{bmatrix} F_{\text{FF}} & F_{\text{FF}\Gamma_1} & 0 & 0 & 0 \\ F_{\Gamma_1\text{F}} & F_{\Gamma_1\Gamma_1} & 0 & 0 & \Lambda_{\text{F}} \\ \hline 0 & 0 & S_{\text{SS}} & S_{\text{S}\Gamma_1} & 0 \\ 0 & 0 & S_{\Gamma_1\text{S}} & S_{\Gamma_1\Gamma_1} & -\text{I} \\ \hline 0 & \Lambda_{\text{F}}^{\text{T}} & 0 & -\text{I}/\Delta t & 0 \end{bmatrix},$$

while

$$\mathbf{u}_{\text{FSI},h}^{n+1} = \begin{pmatrix} \mathbf{y}_{\text{FF},h}^{n+1} \\ \mathbf{y}_{\text{FF}\Gamma_1,h}^{n+1} \\ \mathbf{d}_{\text{SS},h}^{n+1} \\ \mathbf{d}_{\text{S}\Gamma_1,h}^{n+1} \\ \lambda_{\Gamma_1,h}^{n+1} \end{pmatrix}, \quad \mathbf{b}_{\text{FSI}} = \begin{pmatrix} \mathbf{b}_{\text{FF}} \\ \mathbf{b}_{\text{FF}\Gamma_1} \\ \mathbf{b}_{\text{SS}} \\ \mathbf{b}_{\text{S}\Gamma_1} \\ -\mathbf{d}_{\text{S}\Gamma_1}^n/\Delta t \end{pmatrix}.$$

The residual of the Newton method is defined as

$$\mathcal{R}_{\text{FSI}}(\mathbf{u}_{\text{FSI},h}^{n+1}) = A_{\text{FSI}}\mathbf{u}_{\text{FSI},h}^{n+1} - \mathbf{b}_{\text{FSI}},$$

and, since the problem is linear, the Jacobian matrix is equal to the system matrix and the Newton method converges in one iteration.

1.2 1-D FSI model

The 1-D FSI model provides a simplified representation of the blood flow in deformable vessels. Although inadequate to give a detailed description of the full 3-D structure of the flow field (such as recirculation or wall shear stress), it can effectively describe the wave propagation phenomena due to the compliance of the wall. In this section we first describe the governing equations for the 1-D FSI model. Then we introduce a numerical discretization of the problem. Finally, we close the resulting discrete formulation with an appropriate set of compatibility conditions.

1.2.1 Mass and momentum conservation laws

The 1-D FSI model is derived from the incompressible Navier–Stokes equations, by making some simplifying assumptions and integrating over the cross-section of the artery $\Sigma(t, z)$, being $z \in [0, L]$ the axial coordinate, with L the length of the vessel (see Euler (1844), Stettler et al. (1981), Olufsen (1998), Formaggia et al. (2009), and references therein). The pressure on each transversal section is assumed to be constant, and the axial velocity profile $s(r)$ is chosen a priori through the power-law relation $s(r) = \theta^{-1}(\theta + 2)(1 - r^\theta)$, where r is the relative radial coordinate and θ is a proper coefficient. This is a commonly accepted approximation (see, e.g., Pullan et al. (2002) and Quarteroni and Veneziani (2003)), where $\theta = 2$ identifies a parabolic velocity profile, while $\theta = 9$ leads to a more physiological profile, following the Womersley theory (see Womersley (1957)).

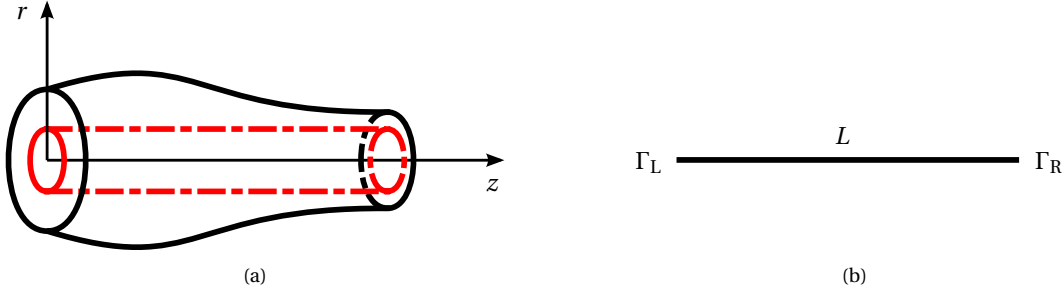


Figure 1.2: Scheme of the 1-D FSI model. (a) The vessel is assumed to be a straight cylinder with a circular cross-section: the red (dashed) and black (solid) lines indicate the reference and current configurations, respectively. (b) The resulting 1-D model is a straight line with two boundary interfaces.

A 1-D model scheme is depicted in Figure 1.2. The resulting state variables are

$$A(t, z) = \int_{\Sigma(t, z)} d\Sigma, \quad Q(t, z) = \int_{\Sigma(t, z)} [\mathbf{u}_F]_z(t, z) d\Sigma, \quad P(t, z) = \frac{1}{A(t, z)} \int_{\Sigma(t, z)} p_F(t, z) d\Sigma,$$

where A is the cross-sectional area, Q the volumetric flow rate, $[\mathbf{u}_F]_z$ the axial component of the fluid velocity field, and P the average pressure. A straightforward derivation of the 1-D FSI model can be found in Quarteroni and Formaggia (2003). The resulting governing equations for continuity of mass and momentum are

$$\begin{cases} \frac{\partial A}{\partial t} + \frac{\partial Q}{\partial z} = 0 & \text{in } (0, L) \times (0, T), \\ \frac{\partial Q}{\partial t} + \frac{\partial}{\partial z} \left(\alpha_F \frac{Q^2}{A} \right) + \frac{A}{\rho_F} \frac{\partial P}{\partial z} + \kappa_F \frac{Q}{A} = 0 & \text{in } (0, L) \times (0, T), \\ A = \bar{A}, \quad Q = \bar{Q} & \text{in } (0, L) \times \{0\}, \end{cases} \quad (1.16)$$

where α_F and κ_F are the Coriolis and friction coefficients, respectively defined as

$$\alpha_F = \frac{1}{\pi} \int_0^{2\pi} \int_0^1 r s^2(r) dr d\varrho, \quad \kappa_F = -2\pi \frac{\mu_F}{\rho_F} \frac{ds}{dr} \Big|_{r=1},$$

being $(r, \varrho) \in [0, 1] \times [0, 2\pi]$ the two-dimensional polar coordinates. In (1.16) we also provide two initial values for the area \bar{A} and for the volumetric flow rate \bar{Q} . The initial condition for the average pressure can be retrieved from the pressure-area relation introduced in the next section.

Remark 1.7. In Hughes and Lubliner (1973) the authors derive a more general set of 1-D FSI governing equations without assuming neither a circular cross-section nor an axisymmetric flow. Compared to (1.16), the main difference is the presence of an outflow term in the momentum equation, together with minor modifications to the fluid viscous term. In particular, the relaxing of axisymmetry requires the computation of the directional derivative with respect to the unit outward normal vector to the closed curve bounding the cross-section $\Sigma(t, z)$.

1.2.2 Constitutive law of the arterial wall

The reduced Navier–Stokes equations (1.16) are coupled with a simple 1-D structural model for the vessel wall, which is assumed to be axisymmetric and only radial displacements are considered. This

results in a pressure-area relation which may account for several phenomena, as described in Formaggia et al. (2003). In this work we consider the elastic and viscoelastic responses of the vessel wall, since the other terms (e.g., wall inertia and longitudinal prestress) provide negligible contributions in the cardiovascular 1-D modeling context (see, e.g., Blanco et al. (2007), Reymond et al. (2009), and Alastruey et al. (2011)). The resulting pressure-area relation is

$$P = \psi(A, z) = P_{\text{ext}} + \hat{\psi}(A, z) + \tilde{\psi}(A, z) \quad \text{in } (0, L) \times (0, T], \quad (1.17)$$

with

$$\hat{\psi}(A, z) = \beta_S(z) \left(\sqrt{\frac{A}{A^0(z)}} - 1 \right), \quad \tilde{\psi}(A, z) = \gamma_S(z) \left(\frac{1}{A\sqrt{A}} \frac{\partial A}{\partial t} \right),$$

being A^0 the reference area of the vessel and

$$\beta_S(z) = \sqrt{\frac{\pi}{A^0(z)} \frac{h_S(z) E_S(z)}{1 - \nu_S^2}}, \quad \gamma_S(z) = \frac{T_S \tan(\phi_S(z)) h_S(z) E_S(z)}{4\sqrt{\pi} (1 - \nu_S^2)},$$

where T_S is the wave characteristic time and ϕ_S the viscoelastic angle. In cardiovascular applications T_S is usually taken equal to the systolic period, while the viscoelastic angle is a parameter which provides a measure of the relative magnitude of the parietal viscosity force to the elastic one (see Kivity and Collins (1974)). We remark that both the elastic and viscoelastic coefficients, as well as the reference area, are function of the axial coordinate z . The 1-D FSI problem is finally closed by providing a proper set of boundary conditions on the inflow and outflow boundaries Γ_L and Γ_R . Recall that in a cardiovascular physiological range the flow regime is typically sub-critical (see, e.g., Formaggia et al. (2003)); the eigenvalues of the hyperbolic problem have opposite sign leading to the imposition of one boundary condition on each side of the model. These conditions can be either given data, such as time-dependent flow rate or terminal absorbing condition (see, e.g., Sherwin et al. (2003)), or coupling conditions relating a certain arterial segment with the surrounding vessels. We postpone the discussion of the latter case to Chapter 2.

1.2.3 Numerical approximation

By plugging (1.17) into (1.16), we get a closed system of differential equations. On the one hand, the elastic component of the pressure-area relation is an algebraic expression and can be easily manipulated. On the other hand, the viscoelastic term depends on the temporal derivative of the area and requires a special treatment.

In the literature, several approaches have been proposed for the numerical approximation of the 1-D FSI problem, ranging from explicit discontinuous Galerkin (see Sherwin et al. (2003)), implicit finite element (see Blanco et al. (2007)), or implicit finite difference (see Reymond et al. (2009)) methods. Following Formaggia et al. (2003) and Passerini et al. (2009), in this work we use an operator splitting technique based on an explicit second order Taylor–Galerkin discretization, where the volumetric flow rate is split into two components such that $Q = \hat{Q} + \tilde{Q}$, being \hat{Q} the solution of the pure elastic problem and \tilde{Q} the viscoelastic correction. The main advantage of this approach resides in its very low computational cost, due to the explicit treatment of the main terms. As for the 3-D FSI problem, the global time interval $[0, T]$ is divided into several uniform subintervals $[t^n, t^{n+1}]$, with $n = 0, 1, 2, \dots$, such that $t^n = n\Delta t$, Δt being the time step. On each time subinterval, we solve the 1-D FSI problem by performing two steps.

1.2.3.1 First step: elastic response

By removing the viscoelastic component from the formulation we can write the closed system of equations in the classical conservative form as

$$\frac{\partial \hat{\mathbf{U}}}{\partial t} + \frac{\partial \mathbf{F}(\mathbf{U})}{\partial z} + \mathbf{S}(\mathbf{U}) = \mathbf{0} \quad \text{in } (0, L) \times (0, T], \quad (1.18)$$

where $\mathbf{U} = [A, Q]^\top$ and $\hat{\mathbf{U}} = [A, \hat{Q}]^\top$ are the total and elastic conservative variables, respectively, $\mathbf{F} = [Q, F_2]^\top$ are the corresponding fluxes, and $\mathbf{S} = [0, S_2]^\top$ accounts for the friction and the non-uniformity of the geometry and the material, with

$$F_2 = \int_{A^0}^A \frac{A}{\rho_F} \frac{\partial \hat{\psi}}{\partial A} dA + \alpha_F \frac{Q^2}{A},$$

$$S_2 = B_2 - \frac{\partial}{\partial A^0} \int_{A^0}^A \frac{A}{\rho_F} \frac{\partial \hat{\psi}}{\partial A} dA \frac{\partial A^0}{\partial z} - \frac{\partial}{\partial \beta_S} \int_{A^0}^A \frac{A}{\rho_F} \frac{\partial \hat{\psi}}{\partial A} dA \frac{\partial \beta_S}{\partial z},$$

being

$$B_2 = \kappa_F \frac{Q}{A} + \frac{A}{\rho_F} \left(\frac{\partial \hat{\psi}}{\partial A^0} \frac{\partial A^0}{\partial z} + \frac{\partial \hat{\psi}}{\partial \beta_S} \frac{\partial \beta_S}{\partial z} \right).$$

Remark 1.8. Since in general the only non-uniformities present in a cardiovascular setting are related to the reference area $A^0 = A^0(z)$ and to the elastic and viscoelastic coefficients $\beta_S = \beta_S(z)$ and $\gamma_S = \gamma_S(z)$ (see, e.g., Segers and Verdonck (2000)), for the sake of simplicity, we assume that all the other parameters are constant along the z -axis. The extension of the present formulation to other non-uniformities (e.g., in α_F and κ_F) is straightforward.

The expression of the flux \mathbf{F} is algebraic, since it includes only the elastic part of (1.17). In particular,

$$F_2 = \frac{(A^0)^3 \beta_S}{3\rho_F} \left(\left(\frac{A}{A^0} \right)^{3/2} - 1 \right) + \alpha_F \frac{Q^2}{A},$$

while \mathbf{S} is

$$S_2 = \kappa_F \frac{Q}{A} - \frac{1}{\rho_F} (A - A^0) \frac{\partial \beta_S}{\partial z} + \frac{3}{2\rho_F} \left(\left(\frac{A}{A^0} \right)^{3/2} - 1 \right) \left(A^0 \frac{\partial \beta_S}{\partial z} - \frac{\beta_S}{2} \frac{\partial \beta_S}{\partial z} \right).$$

The derivatives of these quantities with respect to the conservative variables are

$$\frac{\partial \mathbf{F}}{\partial \mathbf{U}} = \begin{bmatrix} 0 & 1 \\ \frac{\partial F_2}{\partial A} & \frac{\partial F_2}{\partial Q} \end{bmatrix}, \quad \frac{\partial \mathbf{S}}{\partial \mathbf{U}} = \begin{bmatrix} 0 & 0 \\ \frac{\partial S_2}{\partial A} & \frac{\partial S_2}{\partial Q} \end{bmatrix},$$

with

$$\frac{\partial F_2}{\partial A} = \frac{\beta_S}{2\rho_F} \sqrt{\frac{A}{A^0}} - \alpha_F \frac{Q^2}{A^2}, \quad \frac{\partial F_2}{\partial Q} = 2\alpha_F \frac{Q}{A},$$

$$\frac{\partial S_2}{\partial A} = -\kappa_F \frac{Q}{A^2} + \frac{1}{\rho_F} \left(\frac{\beta_S}{2A^0} \sqrt{\frac{A}{A^0}} \right) \frac{\partial A^0}{\partial z} + \frac{1}{\rho_F} \left(\sqrt{\frac{A}{A^0}} - 1 \right) \frac{\partial \beta_S}{\partial z}, \quad \frac{\partial S_2}{\partial Q} = \frac{\kappa_F}{A}.$$

Let \mathbf{U}_h be the discrete counterpart of \mathbf{U} , where h refers to the spatial discretization. In addition, let \mathcal{V}_A and $\mathcal{V}_{\hat{Q}}$ be two sets of piecewise linear finite element functions with adequate boundary conditions and \mathcal{V}_A^* and $\mathcal{V}_{\hat{Q}}^*$ the associated linear spaces of admissible variations. From (1.18) the Taylor–Galerkin

formulation for the elastic problem reads: given $\mathbf{U}_h^n = [A_h^n, Q_h^n]^\top$, find $\hat{\mathbf{U}}_h^{n+1} = [A_h^{n+1}, \hat{Q}_h^{n+1}]^\top \in \mathcal{V}_A \otimes \mathcal{V}_{\hat{Q}}$ such that

$$\begin{aligned} (\hat{\mathbf{U}}_h^{n+1}, \varphi_h) &= (\hat{\mathbf{U}}_h^n, \varphi_h) + \Delta t \left[\mathbf{F}(\mathbf{U}_h^n) - \frac{\Delta t}{2} \frac{\partial \mathbf{F}(\mathbf{U}_h^n)}{\partial \mathbf{U}} \left(\mathbf{S}(\mathbf{U}_h^n) + \frac{\partial \mathbf{F}(\mathbf{U}_h^n)}{\partial z} \right), \frac{\partial \varphi_h}{\partial z} \right] \\ &\quad - \Delta t \left[\mathbf{S}(\mathbf{U}_h^n) - \frac{\Delta t}{2} \frac{\partial \mathbf{S}(\mathbf{U}_h^n)}{\partial \mathbf{U}} \left(\mathbf{S}(\mathbf{U}_h^n) + \frac{\partial \mathbf{F}(\mathbf{U}_h^n)}{\partial z} \right), \varphi_h \right] \quad \forall \varphi_h \in \mathcal{V}_A^* \otimes \mathcal{V}_{\hat{Q}}^*. \end{aligned} \quad (1.19)$$

At the discrete level, the numerical problem is closed by introducing two compatibility conditions, as we discuss in Section 1.2.4. The main advantage of this approach resides in its very low computational cost in view of the explicit nature of the numerical method (1.19). Moreover, the solution of the problem for the area (mass conservation equation) is decoupled from the one for the volumetric flow rate (momentum conservation equation). However, the explicit time discretization entails a limitation on the time step related to the Courant–Friedrichs–Lewy (CFL) number. In particular, the result of the von Neumann stability analysis, in presence of a consistent mass matrix, is (see, e.g., Quartapelle (1993))

$$\frac{\Delta t}{h} < \frac{\sqrt{3}}{3}. \quad (1.20)$$

This is, as a matter of fact, a central issue when coupling 1-D and 3-D FSI problems, as we discuss in Chapter 3.

1.2.3.2 Second step: viscoelastic correction

By using the mass conservation equation, we remove the time dependence from the viscoelastic wall term. The resulting problem is

$$\frac{1}{A} \frac{\partial \tilde{Q}}{\partial t} - \frac{\partial}{\partial z} \left(\frac{\gamma_S}{\rho_F A^{3/2}} \frac{\partial Q}{\partial z} \right) = 0 \quad \text{in } (0, L) \times (0, T],$$

which is closed by an appropriate set of homogeneous boundary conditions for \tilde{Q} , as we will discuss in more detail later. The corresponding finite element formulation reads: given $(A_h^{n+1}, \hat{Q}_h^{n+1}) \in \mathcal{V}_A \otimes \mathcal{V}_{\hat{Q}}$, find $\tilde{Q}_h^{n+1} \in \mathcal{V}_{\tilde{Q}}$ such that

$$\begin{aligned} \left(\frac{\tilde{Q}_h^{n+1}}{A_h^{n+1}}, \varphi_h \right) + \Delta t \left(\frac{\gamma_S}{\rho_F (A_h^{n+1})^{3/2}} \frac{\partial \tilde{Q}_h^{n+1}}{\partial z}, \frac{\partial \varphi_h}{\partial z} \right) &= \left(\frac{\tilde{Q}_h^n}{A_h^n}, \varphi_h \right) \\ - \Delta t \left(\frac{\gamma_S}{\rho_F (A_h^{n+1})^{3/2}} \frac{\partial \hat{Q}_h^{n+1}}{\partial z}, \frac{\partial \varphi_h}{\partial z} \right) + \Delta t \left[\frac{\gamma_S}{\rho_F (A_h^{n+1})^{3/2}} \frac{\partial \hat{Q}_h^{n+1}}{\partial z} \varphi_h \right]_0^L &\quad \forall \varphi_h \in \mathcal{V}_{\tilde{Q}}^*, \end{aligned} \quad (1.21)$$

where $\mathcal{V}_{\tilde{Q}}$ is a set of piecewise linear finite element functions with adequate boundary conditions and $\mathcal{V}_{\tilde{Q}}^*$ is the associated linear space of admissible variations. From equation (1.21) it is clear that we have considered homogeneous Neumann boundary conditions for \tilde{Q}_h^{n+1} . Another possibility is to consider homogeneous Dirichlet boundary conditions as proposed in Formaggia et al. (2003). The former choice suits situations in which the boundary information is the area or the pressure, while the latter one suits when the volumetric flow rate is imposed as boundary data. We remark that possible non-uniformities related to the viscoelastic coefficient γ_S are already included in (1.21).

1.2.4 Compatibility conditions

As discussed at the end of Section 1.2.2 in a cardiovascular physiological range the differential problem requires only one physical boundary condition at each interface of the 1-D FSI model. Nevertheless, the solution of the Taylor–Galerkin problem involves the computation of a full set of values for A and Q at the first and the last finite element node. We thus need two extra relations, namely compatibility conditions, which can be recovered by extrapolating the outgoing characteristic variables. In Formaggia et al. (2003) the authors illustrate the main ingredients of this technique for the fully uniform case, where the reference area and the elastic and viscoelastic coefficients of the vessel wall are constant in space. Here we extend their result to the case of non-uniformity of the geometry and of the material properties.

Let us write the non-conservative form of problem (1.18):

$$\frac{\partial \hat{\mathbf{U}}}{\partial t} + \mathbf{H}(\mathbf{U}) \frac{\partial \mathbf{U}}{\partial z} + \mathbf{B}(\mathbf{U}) = \mathbf{0}, \quad (1.22)$$

where $\mathbf{H} = \partial \mathbf{F} / \partial \mathbf{U}$ and $\mathbf{B} = [0, B_2]^\top$ is the counterpart of \mathbf{S} . Let \mathbf{W} and \mathbf{L} be the eigenvalue and left eigenvectors matrices of \mathbf{H} , respectively, such that $\mathbf{LHL}^{-1} = \mathbf{W}$. In particular they read

$$\mathbf{W} = \begin{bmatrix} w_1 & 0 \\ 0 & w_2 \end{bmatrix}, \quad \mathbf{L} = \zeta \begin{bmatrix} -w_2 & 1 \\ -w_1 & 1 \end{bmatrix},$$

where ζ can be chosen equal to $1/A$, as detailed in Formaggia et al. (2003), and

$$w_{1,2} = \alpha_F \frac{Q}{A} \pm \sqrt{(\alpha_F^2 - \alpha_F) \left(\frac{Q}{A} \right)^2 + \frac{A}{\rho_F} \frac{\partial \hat{\psi}}{\partial A}}.$$

We define the pseudo-characteristic variable \mathbf{Z} as

$$\frac{\partial \mathbf{Z}}{\partial \mathbf{U}} = \mathbf{L},$$

such that, after right multiplying by \mathbf{L} , equation (1.22) becomes

$$\mathbf{L} \frac{\partial \hat{\mathbf{U}}}{\partial t} + \mathbf{W} \left[\frac{\partial \mathbf{Z}}{\partial z} - \frac{\partial \mathbf{L}}{\partial z} \mathbf{U} \right] + \mathbf{LB}(\mathbf{U}) = \mathbf{0}, \quad (1.23)$$

where $\partial \mathbf{Z} / \partial z = 0$ along each pseudo-characteristic and

$$\frac{\partial \mathbf{L}}{\partial z} = \zeta \begin{bmatrix} -\frac{\partial w_2}{\partial z} & 0 \\ -\frac{\partial w_1}{\partial z} & 0 \end{bmatrix},$$

with

$$\frac{\partial w_{1,2}}{\partial z} = \frac{\partial w_{1,2}}{\partial A^0} \frac{\partial A^0}{\partial z} + \frac{\partial w_{1,2}}{\partial \beta_S} \frac{\partial \beta_S}{\partial z} = \pm \frac{A}{2\rho_F} \left(\frac{\partial^2 \hat{\psi}}{\partial A \partial A^0} \frac{\partial A^0}{\partial z} + \frac{\partial^2 \hat{\psi}}{\partial A \partial \beta_S} \frac{\partial \beta_S}{\partial z} \right),$$

$$\sqrt{(\alpha_F^2 - \alpha_F) \left(\frac{Q}{A} \right)^2 + \frac{A}{\rho_F} \frac{\partial \hat{\psi}}{\partial A}},$$

where

$$\frac{\partial \hat{\psi}}{\partial A} = \frac{\beta_S}{2A^0} \left(\frac{A}{A^0} \right)^{-1/2}, \quad \frac{\partial^2 \hat{\psi}}{\partial A \partial A^0} = \frac{\beta_S}{(2A^0)^2} \left(\frac{A}{A^0} \right)^{-1/2}, \quad \frac{\partial^2 \hat{\psi}}{\partial A \partial \beta_S} = \frac{1}{2A^0} \left(\frac{A}{A^0} \right)^{-1/2}.$$

By introducing the same time discretization used in the Taylor–Galerkin problem, we write (1.23) on the pseudo-characteristic departing from \mathbf{U}_\star^n towards one of the two boundary sides of the 1-D segment (more generally we use the subscript \star for all the quantities evaluated at the foot of the pseudo-characteristic),

$$\mathbf{L}^n \hat{\mathbf{U}}^{n+1} = \mathbf{L}^n \hat{\mathbf{U}}_\star^n + \Delta t \left(\mathbf{W}^n \frac{\partial \mathbf{L}^n}{\partial z} (\mathbf{U}_\star^n) - \mathbf{L}^n \mathbf{B} (\mathbf{U}_\star^n) \right). \quad (1.24)$$

Finally, at the numerical level, we need to balance the equations to avoid the presence of fictitious boundary flows in the reference case $\mathbf{U}^0 = [A^0, 0]^T$. From (1.24), the balanced version of the compatibility condition reads

$$\mathbf{L}^n (\hat{\mathbf{U}}^{n+1} - \mathbf{U}^0) = \mathbf{L}^n (\hat{\mathbf{U}}_\star^n - \mathbf{U}_\star^0) + \Delta t \mathbf{W}^n \frac{\partial \mathbf{L}^n}{\partial z} (\mathbf{U}_\star^n - \mathbf{U}_\star^0) - \Delta t \mathbf{L}^n (\mathbf{B} (\mathbf{U}_\star^n) - \mathbf{B} (\mathbf{U}_\star^0)).$$

The full set of boundary conditions for the finite element problem is computed solving a 2×2 linear system on each side of the 1-D segment. There are four possible cases depending on the side and type of physical boundary condition applied to the model:

$$\begin{aligned} \text{given } Q_L: \begin{bmatrix} L_{21}^n & L_{22}^n \\ 0 & 1 \end{bmatrix} \begin{pmatrix} A_h^{n+1} \\ \hat{Q}_h^{n+1} \end{pmatrix} &= \begin{pmatrix} f_L^n \\ Q_L \end{pmatrix} & \text{on } \Gamma_L, & \text{given } Q_R: \begin{bmatrix} L_{11}^n & L_{12}^n \\ 0 & 1 \end{bmatrix} \begin{pmatrix} A_h^{n+1} \\ \hat{Q}_h^{n+1} \end{pmatrix} &= \begin{pmatrix} f_R^n \\ Q_R \end{pmatrix} & \text{on } \Gamma_R, \\ \text{given } A_L: \begin{bmatrix} L_{21}^n & L_{22}^n \\ 1 & 0 \end{bmatrix} \begin{pmatrix} A_h^{n+1} \\ \hat{Q}_h^{n+1} \end{pmatrix} &= \begin{pmatrix} f_L^n \\ A_L \end{pmatrix} & \text{on } \Gamma_L, & \text{given } A_R: \begin{bmatrix} L_{11}^n & L_{12}^n \\ 1 & 0 \end{bmatrix} \begin{pmatrix} A_h^{n+1} \\ \hat{Q}_h^{n+1} \end{pmatrix} &= \begin{pmatrix} f_R^n \\ A_R \end{pmatrix} & \text{on } \Gamma_R, \end{aligned} \quad (1.25)$$

where the subscripts L and R stand for left and right sides of the segment, respectively, A_L , A_R , Q_L , and Q_R are the prescribed physical boundary conditions on the two sides of the segment, and

$$\begin{aligned} f_L^n &= f_L(A_h^n, Q_h^n, \hat{Q}_h^n) = L_{21}^n (A^0 + A_\star^n - A_\star^0) + L_{22}^n \hat{Q}_\star^n + w_2 \left(\frac{\partial L_{21}^n}{\partial z} (A_\star^n - A_\star^0) + \frac{\partial L_{22}^n}{\partial z} Q_\star^n \right) \Delta t \\ &\quad - L_{21}^n (B_1(\mathbf{U}_\star^n) - B_1(\mathbf{U}^0_\star)) \Delta t - L_{22}^n (B_2(\mathbf{U}_\star^n) - B_2(\mathbf{U}^0_\star)) \Delta t, \\ f_R^n &= f_R(A_h^n, Q_h^n, \hat{Q}_h^n) = L_{11}^n (A^0 + A_\star^n - A_\star^0) + L_{12}^n \hat{Q}_\star^n + w_1 \left(\frac{\partial L_{11}^n}{\partial z} (A_\star^n - A_\star^0) + \frac{\partial L_{12}^n}{\partial z} Q_\star^n \right) \Delta t \\ &\quad - L_{11}^n (B_1(\mathbf{U}_\star^n) - B_1(\mathbf{U}^0_\star)) \Delta t - L_{12}^n (B_2(\mathbf{U}_\star^n) - B_2(\mathbf{U}^0_\star)) \Delta t. \end{aligned}$$

At the discrete level, the position of the foot of the pseudo-characteristic is computed by evaluating the CFL number of the corresponding wave

$$N_L^{\text{CFL}} = |w_{2,L}| \frac{\Delta t}{h}, \quad N_R^{\text{CFL}} = 0 |w_{1,R}| \frac{\Delta t}{h}.$$

Chapter 1. Fluid-structure interaction models for the cardiovascular system

More precisely, since we use an explicit method, the CFL number is supposed to be less than one, i.e., the foot of the pseudo-characteristic is placed in the first, last respectively, finite element of the segment. Therefore, depending on the boundary side, we approximate the quantities in the foot of the pseudo-characteristic by using one of the following first order Lagrange polynomial interpolation:

$$\text{left: } \mathbf{U}_*^n = (1 - N_L^{\text{CFL}}) \mathbf{U}_h^n|_{z=0} + N_L^{\text{CFL}} \mathbf{U}_h^n|_{z=h}, \quad \text{right: } \mathbf{U}_*^n = (1 - N_R^{\text{CFL}}) \mathbf{U}_h^n|_{z=L} + N_R^{\text{CFL}} \mathbf{U}_h^n|_{z=L-h}.$$

Main references of the chapter:

- ☆ A. C. I. Malossi, P. J. Blanco, and S. Deparis. A two-level time step technique for the partitioned solution of one-dimensional arterial networks. *Comp. Meth. Appl. Mech. Engrg.*, 237–240:212–226, 2012.
- ☆ A. C. I. Malossi, P. J. Blanco, P. Crosetto, S. Deparis, and A. Quarteroni. Implicit coupling of one-dimensional and three-dimensional blood flow models with compliant vessels. Submitted, 2012.

2 Algorithms for the coupling of heterogeneous networks

In this chapter we propose several algorithms for the weak coupling of different blood flow models. The main field of application of the methodology devised here is the modeling of complex cardiovascular networks (see, e.g., Stergiopoulos et al. (1992), Formaggia et al. (1999), Alastruey et al. (2008), Papadakis (2009), Blanco et al. (2010), and references therein), but it can also be employed to deal with other problems, such as the study of fluid/gas flows in pipe networks (see, e.g., Kiuchi (1994) and Ivanova and Bournaski (1996)) and structural frames in solid mechanics (see Yang et al. (2002), Marin-Artieda and Dargush (2007), Blanco et al. (2008), and references therein), among others. As aforesaid in the introduction, the driving motivation is to investigate the set up and computational implementation of a decomposition methodology aimed at a geometrical multiscale framework, in such a way that it will be possible to assemble a network through the contribution of components of different geometrical dimension (e.g., 3-D, and 1-D) and governed by partial differential equations of various nature.

The layout of the chapter is the following: in Section 2.1 we set up the local interface problem for a generic global network of dimensionally-heterogeneous models. The definition of the interface quantities is detailed in Section 2.2, while in Section 2.3 we devise different sets of interface equations to couple the elements at each node of the network. In Section 2.4 we focus on the numerical algorithms for the partitioned solution of the global geometrical multiscale problem. Finally, in Section 2.5 we provide a brief description of the framework implementation in the `LifeV` library.

2.1 Interface problem

In the field of computational hemodynamics, dimensional heterogeneity of the constituent models, or components, is a convenient approach to model at the same time both the global and the local circulation. In particular, the coupling of 3-D detailed models based on the Navier–Stokes equations with 1-D and 0-D lumped parameters models to account for the proximal and distal compartments of the network has become common practice (see, e.g., Formaggia et al. (2001), Migliavacca et al. (2006), Urquiza et al. (2006), and Kim et al. (2009b)). One of the main issues of this approach is the coupling of the different models without losing abstraction and generality; indeed, the models are in general equipped with dimensionally-heterogeneous boundary interfaces.

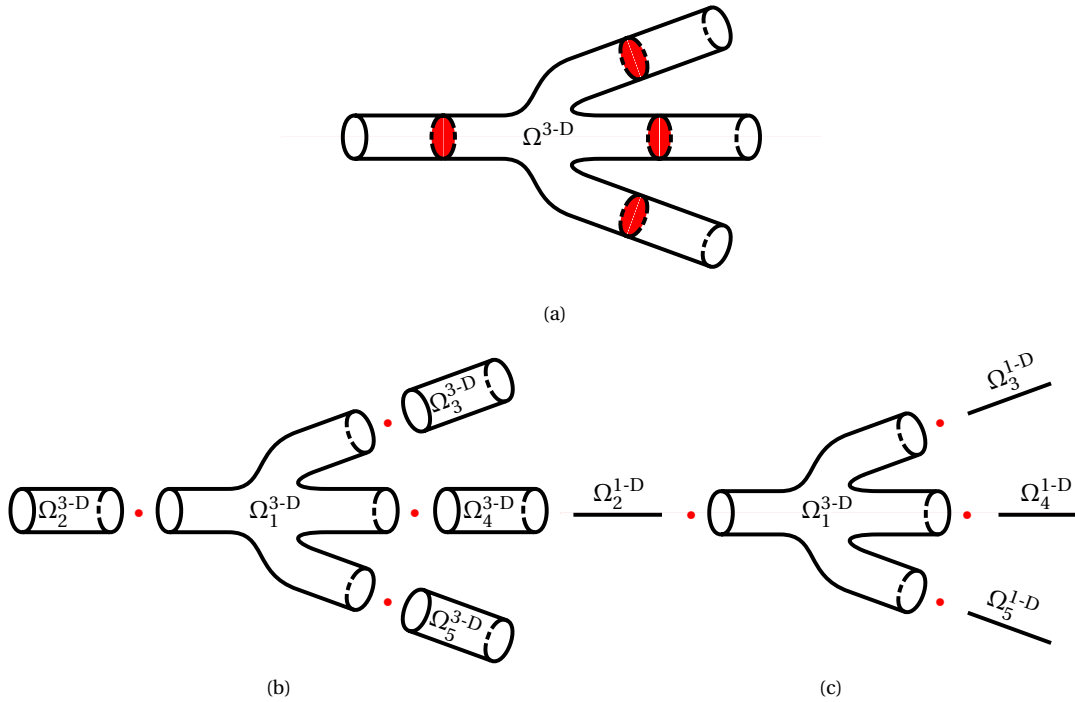


Figure 2.1: Decomposition of a trifurcation into five subdomains. (a) Four cutting sections (in red) are identified. (b) The trifurcation is partitioned in five dimensionally-homogeneous subdomains. (c) The trifurcation is partitioned in five dimensionally-heterogeneous subdomains: the main part is modeled with a 3-D model, while the four branches are accounted through 1-D models.

Let us consider a generic 3-D domain Ω^{3-D} , which may represent a set of branching arteries (see Figure 2.1a). The original domain Ω^{3-D} can be partitioned into \mathcal{M} subdomains Ω_m^{3-D} , $m = 1, \dots, \mathcal{M}$, each one representing a specific part of the original problem (see Figure 2.1b). From the geometrical viewpoint, the resulting partitioned configuration is equivalent to the original one and can be solved by using a segregated approach. In addition, in order to further simplify the problem, in a geometrical multiscale setting we can replace some of the original 3-D subdomains with reduced order models, e.g., 1-D models, as shown in Figure 2.1c.

In both cases, the partitioning of the original domain requires the imposition of an additional set of continuity conditions on the fictitious boundaries, hereafter referred to as *coupling conditions*. From the geometrical point of view, we have two different scenarios.

1. **The models are defined in the same geometrical space:** coupling conditions consist in imposing directly the continuity of the unknowns seen as elements of a functional space (e.g., pointwise velocity and stresses for the 3-D Navier–Stokes equations), which is the classical approach in domain decomposition.
2. **The models are defined in different geometrical spaces:** coupling conditions consist in the continuity/conservation of averaged/integrated quantities (e.g., mean stresses and flow rate), which do not depend on the geometrical dimension of the models since they are scalar quantities.

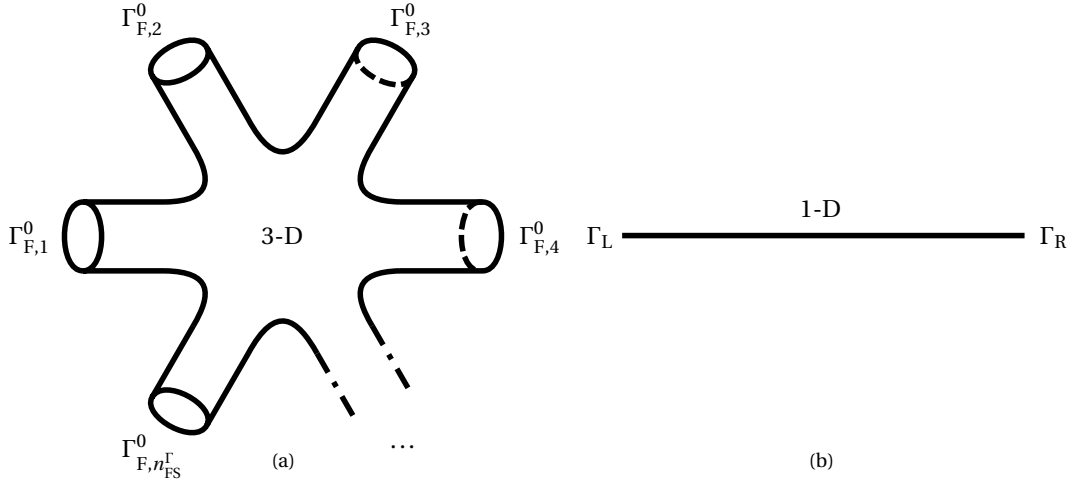


Figure 2.2: Examples of 3-D (fluid domain Ω_F^0) and 1-D models with connections (coupling interfaces). (a) The 3-D model has $n_{FS}^\Gamma \geq 1$ coupling interfaces. (b) The 1-D model has two coupling interfaces.

Remark 2.1. By using the second approach for the coupling of dimensionally-homogeneous 3-D subdomains, the resulting partitioned problem is not equivalent to the original global one. In particular, compared to classic domain decomposition methods, the coupling conditions are relaxed by averaging/integrating the quantities over the interfaces.

Despite the fact that the methodology devised here is general and can be applied to any fluid flow model, in the following we mainly focus on the coupling of the 3-D and 1-D FSI models introduced in Chapter 1. Regarding the notation, we remark that each 1-D FSI model has only two coupling interfaces, while a 3-D FSI model may have an arbitrary number of coupling interfaces, as schematically shown in Figure 2.2. In particular, since generally the number of fluid and solid coupling interfaces of a 3-D FSI models is the same (i.e., $n_F^\Gamma = n_S^\Gamma$), in the following we refrain from distinguishing between the two and we denote the number of coupling interfaces of the 3-D FSI models as n_{FS}^Γ . In Chapter 6 we address a problem in which this assumption does not hold; however, all the methodology devised throughout the work remains valid.

2.2 Averaged/integrated interface quantities

We consider a general network of heterogeneous models connected by \mathcal{C} coupling nodes. In view of the geometrical considerations discussed in the previous section, we set up the coupling of the heterogeneous problems by imposing the continuity/conservation of averaged/integrated quantities over the interfaces, such that the interface problem does not have any dependency on the geometrical nature nor on the mathematical formulation of each model. In a cardiovascular setting, these averaged/integrated boundary quantities are:

- the *coupling flow* \mathcal{Q} , i.e., the volumetric flow rate;
- the *coupling area* \mathcal{A} , i.e., the area of the fluid section.
- the *coupling stress* \mathcal{S} , i.e., the averaged normal component of the traction vector (also referred to as the mean normal stress);
- the *coupling total stress* \mathcal{T} , i.e., the averaged normal component of the total stress (also referred to as the mean total normal stress).

The quantities \mathcal{Q} , \mathcal{A} , and \mathcal{S} , represent a natural choice of boundary data for the FSI models described in Chapter 1. On the contrary \mathcal{T} , which is given by the sum of the coupling stress and the dynamic contribution associated to the kinetic energy of the flow, cannot be imposed as boundary condition on the 3-D FSI problem without changing the Navier–Stokes formulation (integrating by parts the convective term). Nevertheless, all of them can be evaluated on the interface boundaries of the two FSI models. More precisely, on the j -th boundary interface of the 3-D FSI model they are computed as

$$\begin{aligned} \mathcal{Q}_j^{3-D} &= \int_{\Gamma_{F,j}^t} \mathbf{u}_F \cdot \mathbf{n}_F \, d\Gamma, & \mathcal{A}_j^{3-D} &= |\Gamma_{F,j}^t|, \\ \mathcal{S}_j^{3-D} &= \frac{1}{|\Gamma_{F,j}^t|} \int_{\Gamma_{F,j}^t} (\sigma_F \cdot \mathbf{n}_F) \cdot \mathbf{n}_F \, d\Gamma, & \mathcal{T}_j^{3-D} &= \mathcal{S}_j^{3-D} - \frac{1}{2} \rho_F \frac{1}{|\Gamma_{F,j}^t|} \int_{\Gamma_{F,j}^t} (\mathbf{u}_F \cdot \mathbf{n}_F)^2 \, d\Gamma, \end{aligned}$$

where we assume that each boundary surface $\Gamma_{F,j}^t$, $j = 1, \dots, n_{FS}^\Gamma$, is planar.

Remark 2.2. In the present work we consider the quantity $(\sigma_F \cdot \mathbf{n}_F) \cdot \mathbf{n}_F$ constant over $\Gamma_{F,j}^t$, $j = 1, \dots, n_{FS}^\Gamma$, such that we can rewrite the coupling stress as: $\mathcal{S}_j^{3-D} = (\sigma_F \cdot \mathbf{n}_F) \cdot \mathbf{n}_F$. Indeed, as we clarify in the next remark, \mathcal{S}_j^{3-D} has the meaning of the Lagrange multiplier responsible for enforcing the imposition of the flow rate \mathcal{Q}_j^{3-D} through $\Gamma_{F,j}^t$, $j = 1, \dots, n_{FS}^\Gamma$.

Remark 2.3. Following the approach in Formaggia et al. (2002), the imposition of the coupling flow on a coupling interface of the 3-D FSI fluid problem is addressed in a weak sense through a Lagrange multiplier. This choice leads to a uniform value of the normal component of the traction vector on the same boundary interface (see Heywood et al. (1996)). Moreover it is coherent with the other chosen fluid coupling condition, i.e., the coupling stress. Note, however, that the same methodology holds when imposing the coupling flow through a given normal velocity profile.

Remark 2.4. The 3-D FSI fluid problem (as well as the 3-D rigid wall problem) needs an additional set of boundary conditions on the two tangential directions lying on $\Gamma_{F,j}^t$, $j = 1, \dots, n_{FS}^\Gamma$. Since, for modeling reasons, we assume that at these coupling interfaces the flow is fully developed and orthogonal to the plane, we impose $(\sigma_F \cdot \mathbf{n}_F) \cdot \boldsymbol{\tau}_{2F} = 0$ and $(\sigma_F \cdot \mathbf{n}_F) \cdot \boldsymbol{\tau}_{1F} = 0$, where $\boldsymbol{\tau}_{1F}$ and $\boldsymbol{\tau}_{2F}$ are the two tangential directions. Another possibility would be to impose $\mathbf{u}_F \cdot \boldsymbol{\tau}_{1F} = 0$ and $\mathbf{u}_F \cdot \boldsymbol{\tau}_{2F} = 0$.

Regarding the 1-D FSI model we have

$$\begin{aligned} \mathcal{Q}_L^{1-D} &= -Q_L, & \mathcal{A}_L^{1-D} &= A_L, & \mathcal{S}_L^{1-D} &= -P_L, & \mathcal{T}_L^{1-D} &= \mathcal{S}_L^{1-D} - \frac{1}{2} \rho_F \alpha_F \left(\frac{Q_L^{1-D}}{\mathcal{A}_L^{1-D}} \right)^2 & \text{on } \Gamma_L, \\ \mathcal{Q}_R^{1-D} &= Q_R, & \mathcal{A}_R^{1-D} &= A_R, & \mathcal{S}_R^{1-D} &= -P_R, & \mathcal{T}_R^{1-D} &= \mathcal{S}_R^{1-D} - \frac{1}{2} \rho_F \alpha_F \left(\frac{Q_R^{1-D}}{\mathcal{A}_R^{1-D}} \right)^2 & \text{on } \Gamma_R. \end{aligned}$$

In particular, to follow the global convention of positive outflows at the boundaries (the coupling interfaces), we have defined $\mathcal{Q}_L^{1-D} = -Q_L$. In fact, in (1.16), and more generally in all the equations of the 1-D model, the volumetric flow rate is assumed to be positive in the direction of the axial coordinate z (say from the left to the right of each 1-D segment).

2.3 Interface equations

In the literature, several approaches are proposed for the coupling of heterogeneous networks. In particular, one of the most popular is obtained by imposing the conservation of mass and the continuity of mean normal stress at each coupling node. This approach is supported by arguments based on both the strong formulation (see Formaggia et al. (2001)) and the variational formulation (see Blanco et al. (2007)) of the interface problem.

More recently Formaggia et al. (2012) introduced the concept of energetic consistency between 1-D and 3-D FSI models. More precisely, the authors show that the imposition of the conservation of mass and the continuity of mean normal stress at the coupling interfaces does not guarantee that the energy of the problem is preserved, i.e., it is not possible to write an energy estimate. In view of this undesired feature, the same authors state that instabilities could occur at the interface between the models, although neither in their work, nor in the aforementioned works numerical instabilities have been reported. More generally, instabilities might arise in particular situations such as (i) in presence of substantial in-plane velocity fields near the boundary interfaces, which can be addressed by adding a weak constraint on the inlet/outlet velocity profiles, as proposed by Kim et al. (2009a), or (ii) by an uncontrolled reversal flow at the outlet boundaries, which might be avoided by adding an arbitrary traction to the outflow face whenever the reversal of the flow is detected, as proposed by Moghadam et al. (2011).

With the aim to preserve the total energy of the problem, in Formaggia et al. (2007) and Nobile (2009) as well as in Formaggia et al. (2012), an energetic preserving set of interface equations has been proposed, which is based on the conservation of mass and on the continuity of mean total normal stress. The main drawback of this set of interface equations is that it does not lead to classical type of boundary data for the connected models. More precisely, in the classical Navier–Stokes formulation the total normal stress cannot be imposed as a boundary condition. A possible workaround is to impose the flow rate on the 3-D coupling interfaces, as done in Formaggia et al. (2012). There, the authors use a Gauss–Seidel iterative procedure where the 3-D and the 1-D FSI models are fed with flow rate and total pressure boundary data, respectively. Nevertheless, the convergence properties are rather limited to the chosen numerical algorithm. In addition, the flexibility of choosing the boundary data to be applied on each model of the network is lost due to the need of prescribing a flow rate boundary condition on all the 3-D FSI coupling interfaces.

Another possible solution to meet the continuity of mean total normal stress, in presence of 3-D FSI models, is to change the Navier–Stokes formulation integrating by parts the convective term, as done in Formaggia et al. (2007) and Nobile (2009). The resulting formulation is compatible with total stress boundary data, however, in a FSI context, the stress coupling condition at the interface between the fluid and the solid problem is also affected by the modifications in the 3-D Navier–Stokes formulation. Therefore, some additional changes in the FSI approach are required to match the new formulation. The solution to this issue is not discussed in the aforementioned works, as also pointed out in Gravemeier et al. (2012). Moreover, from the coding viewpoint, any modification in the Navier–Stokes formulation might be an issue when dealing with black box codes (e.g., commercial codes).

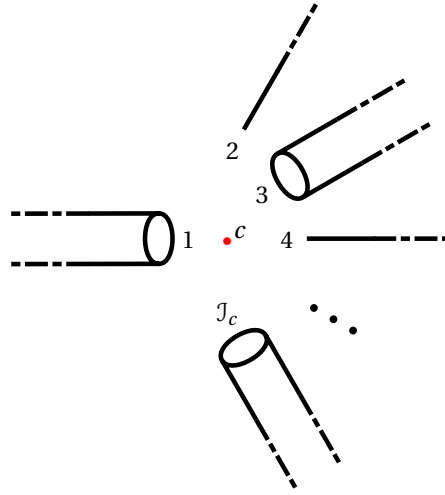


Figure 2.3: Generic configuration for the c -th coupling between J_c dimensionally-heterogeneous models.

With the aim of preserving the appealing flexibility to impose the desired boundary data at each coupling interface of the network, being able, at the same time, to choose the set of coupling equations without any constraint, we resort to an abstract residual form of the interface problem. More precisely, let us consider a generic c -th node of the network, where J_c is the local number of connected interfaces (see Figure 2.3). The local abstract residual form reads

$$\mathcal{R}_c(\boldsymbol{\chi}_c, \cdot) = \mathbf{0}, \quad (2.1)$$

where \mathcal{R}_c and $\boldsymbol{\chi}_c$ are the local vectors of residuals and unknowns, respectively, $c = 1, \dots, \mathcal{C}$, while the dot in the round parentheses expresses a possible dependence of the local residual on non-local unknowns, i.e., coupling quantities introduced in other nodes of the network. The dependence of the local residuals vector on the connected models is expressed through abstract boundary operators that given a proper set of (local and non-local) coupling quantities return the corresponding boundary value at a specific interface of the network. More precisely:

- the operator $\mathcal{Q}_{c,i}(\cdot, \cdot)$ returns the coupling flow at the i -th coupling interface of the c -th coupling node;
- the operator $\mathcal{A}_{c,i}(\cdot, \cdot)$ returns the coupling area at the i -th coupling interface of the c -th coupling node;
- the operator $\mathcal{S}_{c,i}(\cdot, \cdot)$ returns the coupling stress at the i -th coupling interface of the c -th coupling node;
- the operator $\mathcal{T}_{c,i}(\cdot, \cdot)$ returns the coupling total stress at the i -th coupling interface of the c -th coupling node;

All the equations and the numerical methods of the specific models are hidden behind the evaluation of the corresponding boundary operator. For example, if the i -th interface of the c -th coupling node belongs to a 3-D FSI model, the evaluation of operator $\mathcal{Q}_{c,i}(\cdot, \cdot)$, for the computation of the boundary flow rate, requires the solution of the 3-D FSI problem described in Section 1.1.5, while in the case of

a 1-D FSI model it involves the solution of the two steps described in Section 1.2.3. We remark that the first and the second dot in the round parentheses express the dependence on local and non-local coupling quantities, respectively.

The form of the local residual vector depends both on the chosen set of interface equations and on the boundary data applied on each interface. In particular, in the following sections we detail the expressions behind (2.1) for the two aforementioned cases, the continuity of mean normal stress and the continuity of mean total normal stress. The novelty of the proposed approach is that, in both cases, the type of the boundary condition is not forced by the set of interface equations, nor by the numerical coupling algorithm. In addition, even when imposing the continuity of mean total normal stress, the interfaces of the models are fed with either classical Neumann boundary data (coupling stress), which are consistent with the 3-D FSI context and do not require modifications to the Navier–Stokes formulation, or flow rate quantities (coupling flow), by introducing Lagrange multipliers in the 3-D FSI system matrix. Indeed, we remark that despite the possible benefits of preserving the continuity of the mean total normal stress when coupling 1-D and 3-D models, there exist situations where this technique cannot be used since it is not possible to define the kinetic term; for instance, in windkessel terminals or other lumped parameters models the area does not have an interpretation, such that the interface equations have to be anyway written in terms of continuity of mean normal stress. Finally, for the specific case of the coupling of 3-D and 1-D FSI models, we extend the two proposed approaches to account for the continuity of the vessel area.

2.3.1 Continuity of mean normal stress

The first set of interface equations we consider ensures the conservation of the mass and the continuity of the mean normal stress at the coupling interfaces. We denote by \mathcal{L}^S the set of coupling nodes where the continuity of mean normal stress is imposed; for $c \in \mathcal{L}^S$ the coupling conditions reads

$$\begin{cases} \sum_{i=1}^{J_c} Q_{c,i} = 0, \\ S_{c,1} - S_{c,i} = 0, \quad i = 2, \dots, J_c. \end{cases} \quad (2.2)$$

Note that, for a network of 1-D models, the last equations can be satisfied by imposing directly the continuity of the pressure at the interfaces, as done in Formaggia et al. (2003). Indeed, $S^{1-D} = -P$.

Remark 2.5. Equation (2.2) does not take into account any energy loss at bifurcations. In the literature there are several proposed models (see, e.g., Gardel (1957) and Formaggia et al. (2003)) to include this effect, however, as shown in, e.g., Matthys et al. (2007, Section 3.2), their impact on the main physical quantities is negligible in a cardiovascular setting.

The form of the local residuals vector associated to the set of equations (2.2) changes accordingly to the boundary data applied on each connected interface. In other words, we can set up each subproblem with different combinations of boundary data over the coupling interfaces. Among the several possible combinations, in Malossi et al. (2011b, Section 2.5) three significant cases are addressed. Here we

generalize that approach writing a single residual form that holds in all the possible cases, i.e.,

$$\mathcal{R}_c(\boldsymbol{\chi}_c, \cdot) = \begin{pmatrix} \sum_{i=1}^{n_c^Q} Q_{c,i} + \sum_{i=n_c^Q+1}^{J_c} \mathcal{Q}_{c,i}(\mathcal{S}_c, \cdot) \\ \mathcal{S}_{c,1}(Q_{c,1}, \cdot) - \mathcal{S}_c \\ \mathcal{S}_{c,2}(Q_{c,2}, \cdot) - \mathcal{S}_c \\ \vdots \\ \mathcal{S}_{c,n_c^Q}(Q_{c,n_c^Q}, \cdot) - \mathcal{S}_c \end{pmatrix}, \quad \text{for } c \in \mathcal{L}^S, \quad (2.3)$$

being n_c^Q the number of interfaces where flow rate boundary data is applied, $0 \leq n_c^Q \leq J_c$; more precisely, we use the convention that among the J_c local coupling interfaces, the first n_c^Q take coupling flow boundary data, while the last $J_c - n_c^Q$ get coupling stress boundary data. In view of this, the size \mathcal{L}_c of the unknowns vector $\boldsymbol{\chi}_c$ is equal to $n_c^Q + 1$, such that

$$\boldsymbol{\chi}_c = (Q_{c,1}, Q_{c,2}, \dots, Q_{c,n_c^Q}, \mathcal{S}_c)^\top, \quad \text{for } c \in \mathcal{L}^S. \quad (2.4)$$

In particular, if coupling stress boundary data are imposed on all the interfaces (i.e., $n_c^Q = 0$), the local interface problem has just one unknown (the local coupling stress \mathcal{S}_c), while, in the dual case (coupling flow boundary data imposed on all the interfaces, i.e., $n_c^Q = J_c$), the local number of unknowns is $J_c + 1$. Regarding the other terms in (2.3), we remark that the boundary operators $\mathcal{Q}_{c,i}(\mathcal{S}_c, \cdot)$ and $\mathcal{S}_{c,i}(Q_{c,i}, \cdot)$ are global, as they may depend also on non-local coupling quantities, i.e., unknowns introduced at other coupling nodes; again, this dependence is indicated by the dot in the round parentheses.

The first equation in (2.3) ensures the conservation of mass. In case $n_c^Q = 0$, the continuity of the mean normal stress is satisfied implicitly by the fact that the same coupling stress \mathcal{S}_c (which is the only local unknown, i.e., $\boldsymbol{\chi}_c = \mathcal{S}_c$) is imposed on all the interfaces of the c -th node. In case $n_c^Q > 0$, on the interfaces where flow rate boundary data are applied, the continuity of the mean normal stress is enforced explicitly through a relation in the form: $\mathcal{S}_{c,i}(Q_{c,i}, \cdot) - \mathcal{S}_c = 0$, $i = 1, \dots, n_c^Q$.

Remark 2.6. In case $n_c^Q = J_c$, i.e., coupling flow imposed on all the interfaces, the residual form can be reduced to have just J_c unknowns:

$$\mathcal{R}_c(\boldsymbol{\chi}_c, \cdot) = \begin{pmatrix} \sum_{i=1}^{J_c} Q_{c,i} \\ \mathcal{S}_{c,2}(Q_{c,2}, \cdot) - \mathcal{S}_{c,1}(Q_{c,1}, \cdot) \\ \vdots \\ \mathcal{S}_{c,J_c}(Q_{c,J_c}, \cdot) - \mathcal{S}_{c,1}(Q_{c,1}, \cdot) \end{pmatrix}, \quad \text{for } c \in \mathcal{L}^S,$$

being

$$\boldsymbol{\chi}_c = (Q_{c,1}, Q_{c,2}, \dots, Q_{c,J_c})^\top, \quad \text{for } c \in \mathcal{L}^S,$$

where the unknown \mathcal{S}_c has been dropped since the continuity of mean normal stress is now enforced explicitly on all the interface through a relation in the form: $\mathcal{S}_{c,i}(Q_{c,i}, \cdot) - \mathcal{S}_{c,1}(Q_{c,1}, \cdot) = 0$, $i = 1, \dots, J_c$.

Remark 2.7. Note that, independently of the value of n_c^Q and, consequently, from the chosen repartition of boundaries where coupling flow and coupling stress boundary data are applied, the solution of the problem is the same. In fact, the general form of the local residuals vector is derived from the set of coupling equations without any approximation. Nevertheless, in case of rigid wall models (and incompressible fluids), e.g., 3-D Navier–Stokes equations, the imposition of flow rate boundary data cannot be used systematically, since the incompressibility constraint may not be fulfilled. In this case, to guarantee the well-posedness of the subproblems, the imposition of the flow rate on all boundaries of the same model must be avoided.

2.3.2 Continuity of mean total normal stress

The second set of interface equations we consider ensures the conservation of the mass and the continuity of the mean total normal stress at the coupling interfaces. We denote by \mathcal{L}^J the set of coupling nodes where the continuity of mean total normal stress is imposed; for $c \in \mathcal{L}^J$ the coupling conditions reads

$$\begin{cases} \sum_{i=1}^{\mathcal{J}_c} Q_{c,i} = 0, \\ \mathcal{T}_{c,1} - \mathcal{T}_{c,i} = 0, \quad i = 2, \dots, \mathcal{J}_c. \end{cases} \quad (2.5)$$

Similarly to the previous case, for a network of 1-D models the last equations can be satisfied by directly imposing the continuity of the total pressure at the coupling interfaces.

In view of the aforementioned drawbacks associated to the imposition of the coupling total stress on the coupling interfaces, we consider only coupling flow and coupling stress as possible boundary data to set up the interface problem. The resulting generalized residual form reads

$$\mathcal{R}_c(\boldsymbol{\chi}_c, \cdot) = \begin{pmatrix} \sum_{i=1}^{n_c^Q} Q_{c,i} + \sum_{i=n_c^Q+1}^{\mathcal{J}_c} \mathcal{Q}_{c,i}(\mathcal{S}_{c,i}, \cdot) \\ \mathcal{T}_{c,1}(Q_{c,1}, \cdot) - \mathcal{T}_c \\ \mathcal{T}_{c,2}(Q_{c,2}, \cdot) - \mathcal{T}_c \\ \vdots \\ \mathcal{T}_{c,n_c^Q}(Q_{c,n_c^Q}, \cdot) - \mathcal{T}_c \\ \mathcal{T}_{c,n_c^Q+1}(\mathcal{S}_{c,n_c^Q+1}, \cdot) - \mathcal{T}_c \\ \mathcal{T}_{c,n_c^Q+2}(\mathcal{S}_{c,n_c^Q+2}, \cdot) - \mathcal{T}_c \\ \vdots \\ \mathcal{T}_{c,\mathcal{J}_c}(\mathcal{S}_{c,\mathcal{J}_c}, \cdot) - \mathcal{T}_c \end{pmatrix}, \quad \text{for } c \in \mathcal{L}^J, \quad (2.6)$$

where in this case the size \mathcal{L}_c of the unknowns vector $\boldsymbol{\chi}_c$ does not depends on the chosen set of interface quantities and is always equal to $\mathcal{J}_c + 1$, such that

$$\boldsymbol{\chi}_c = \left(Q_{c,1}, Q_{c,2}, \dots, Q_{c,n_c^Q}, \mathcal{S}_{c,n_c^Q+1}, \mathcal{S}_{c,n_c^Q+2}, \dots, \mathcal{S}_{c,\mathcal{J}_c}, \mathcal{T}_c \right)^\top, \quad \text{for } c \in \mathcal{L}^J. \quad (2.7)$$

Therefore, compared to the previous case, if coupling stress boundary data are imposed on all the interfaces (i.e., $n_c^Q = 0$), the local interface problem has \mathcal{J}_c additional unknowns, while, in the dual case (coupling flow boundary data imposed on all the interfaces, i.e., $n_c^Q = \mathcal{J}_c$), the local number of unknowns is the same as before.

As in the set of coupling conditions introduced in Section 2.3.1, the first equation in (2.6) ensures the conservation of mass. The other J_c equations enforce the continuity of the mean total normal stress through an explicit relation in the form: $\mathcal{T}_{c,i}(\cdot, \cdot) - \mathcal{T}_c = 0$, $i = 1, \dots, J_c$, where we remark that the first (local) argument in the round parenthesis can be either a coupling flow or a coupling stress, depending on the type of boundary condition imposed on the i -th interface.

Remark 2.8. Similarly to what has been done in *Remark 2.6* for the continuity of the mean normal stress, also in this case it is possible to reduce the size of the residual form when $n_c^Q = J_c$, such that

$$\mathcal{R}_c(\chi_c, \cdot) = \begin{pmatrix} \sum_{i=1}^{J_c} Q_{c,i} \\ \mathcal{T}_{c,2}(Q_{c,2}, \cdot) - \mathcal{T}_{c,1}(Q_{c,1}, \cdot) \\ \vdots \\ \mathcal{T}_{c,J_c}(Q_{c,J_c}, \cdot) - \mathcal{T}_{c,1}(Q_{c,1}, \cdot) \end{pmatrix}, \quad \text{for } c \in \mathcal{L}^{\mathcal{T}},$$

being

$$\chi_c = (Q_{c,1}, Q_{c,2}, \dots, Q_{c,J_c})^{\top}, \quad \text{for } c \in \mathcal{L}^{\mathcal{T}}.$$

Remark 2.9. In case the coupling total stress is considered an admissible boundary data for the models, the residual form can be rewritten as

$$\mathcal{R}_c(\chi_c, \cdot) = \begin{pmatrix} \sum_{i=1}^{n_c^Q} Q_{c,i} + \sum_{i=n_c^Q+1}^{J_c} \mathcal{Q}_{c,i}(\mathcal{T}_c, \cdot) \\ \mathcal{T}_{c,1}(Q_{c,1}, \cdot) - \mathcal{T}_c \\ \mathcal{T}_{c,2}(Q_{c,2}, \cdot) - \mathcal{T}_c \\ \vdots \\ \mathcal{T}_{c,n_c^Q}(Q_{c,n_c^Q}, \cdot) - \mathcal{T}_c \end{pmatrix}, \quad \text{for } c \in \mathcal{L}^{\mathcal{T}},$$

being

$$\chi_c = (Q_{c,1}, Q_{c,2}, \dots, Q_{c,n_c^Q}, \mathcal{T}_c)^{\top}, \quad \text{for } c \in \mathcal{L}^{\mathcal{T}}.$$

The resulting residuals and unknowns vectors are similar to those described in Section 2.3.1; indeed, the only difference between the two cases is that the coupling stress boundary data and operators are replaced with the corresponding coupling total stress ones.

2.3.3 Continuity of the vessel area

In a geometrical multiscale setting, the interfaces of 3-D FSI models are generally connected with those of reduced models, such as 1-D FSI models. In this case, it is possible to write an additional relation at the coupling interfaces of the two heterogeneous models to impose the continuity of the vessel area.

Table 2.1: Detailed form of the local residuals vector $\mathcal{R}_c(\chi_c, \cdot)$ when the continuity of the vessel area is imposed between a 1-D and a 3-D FSI model. For each residuals vector the corresponding unknowns vector is given in Table 2.2.

n_c^Q	$c \in \mathcal{L}^S \cap \mathcal{L}^A$	$c \in \mathcal{L}^T \cap \mathcal{L}^A$
0	$\begin{pmatrix} \mathcal{Q}_{c,1}^{1-D}(\mathcal{S}_c, \cdot) + \mathcal{Q}_{c,2}^{3-D}(\mathcal{S}_c, \mathcal{A}_c, \cdot) \\ \mathcal{A}_{c,1}^{1-D}(\mathcal{S}_c, \cdot) - \mathcal{A}_c \end{pmatrix}$	$\begin{pmatrix} \mathcal{Q}_{c,1}^{1-D}(\mathcal{S}_{c,1}, \cdot) + \mathcal{Q}_{c,2}^{3-D}(\mathcal{S}_{c,2}, \mathcal{A}_c, \cdot) \\ \mathcal{T}_{c,1}^{1-D}(\mathcal{S}_{c,1}, \cdot) - \mathcal{T}_c \\ \mathcal{T}_{c,2}^{3-D}(\mathcal{S}_{c,2}, \mathcal{A}_c, \cdot) - \mathcal{T}_c \\ \mathcal{A}_{c,1}^{1-D}(\mathcal{S}_{c,1}, \cdot) - \mathcal{A}_c \end{pmatrix}$
1	$\begin{pmatrix} \mathcal{Q}_{c,1} + \mathcal{Q}_{c,2}^{3-D}(\mathcal{S}_c, \mathcal{A}_c, \cdot) \\ \mathcal{S}_{c,1}^{1-D}(\mathcal{Q}_{c,1}, \cdot) - \mathcal{S}_c \\ \mathcal{A}_{c,1}^{1-D}(\mathcal{Q}_{c,1}, \cdot) - \mathcal{A}_c \end{pmatrix}$	$\begin{pmatrix} \mathcal{Q}_{c,1} + \mathcal{Q}_{c,2}^{3-D}(\mathcal{S}_{c,2}, \mathcal{A}_c, \cdot) \\ \mathcal{T}_{c,1}^{1-D}(\mathcal{Q}_{c,1}, \cdot) - \mathcal{T}_c \\ \mathcal{T}_{c,2}^{3-D}(\mathcal{S}_{c,2}, \mathcal{A}_c, \cdot) - \mathcal{T}_c \\ \mathcal{A}_{c,1}^{1-D}(\mathcal{Q}_{c,1}, \cdot) - \mathcal{A}_c \end{pmatrix}$
2	$\begin{pmatrix} \mathcal{Q}_{c,1} + \mathcal{Q}_{c,2} \\ \mathcal{S}_{c,1}^{1-D}(\mathcal{Q}_{c,1}, \cdot) - \mathcal{S}_c \\ \mathcal{S}_{c,2}^{3-D}(\mathcal{Q}_{c,2}, \mathcal{A}_c, \cdot) - \mathcal{S}_c \\ \mathcal{A}_{c,1}^{1-D}(\mathcal{Q}_{c,1}, \cdot) - \mathcal{A}_c \end{pmatrix}$	$\begin{pmatrix} \mathcal{Q}_{c,1} + \mathcal{Q}_{c,2} \\ \mathcal{T}_{c,1}^{1-D}(\mathcal{Q}_{c,1}, \cdot) - \mathcal{T}_c \\ \mathcal{T}_{c,2}^{3-D}(\mathcal{Q}_{c,2}, \mathcal{A}_c, \cdot) - \mathcal{T}_c \\ \mathcal{A}_{c,1}^{1-D}(\mathcal{Q}_{c,1}, \cdot) - \mathcal{A}_c \end{pmatrix}$

Let \mathcal{L}^A be the set of coupling nodes where the continuity of the area between the two heterogeneous FSI models is imposed. For $c \in \mathcal{L}^S \cap \mathcal{L}^A$ the set of equations (2.2) becomes

$$\begin{cases} \mathcal{Q}_{c,1}^{1-D} + \mathcal{Q}_{c,2}^{3-D} = 0, \\ \mathcal{S}_{c,1}^{1-D} - \mathcal{S}_{c,2}^{3-D} = 0, \\ \mathcal{A}_{c,1}^{1-D} - \mathcal{A}_{c,2}^{3-D} = 0, \end{cases} \quad (2.8)$$

while, for $c \in \mathcal{L}^T \cap \mathcal{L}^A$, the set of equations (2.5) reads

$$\begin{cases} \mathcal{Q}_{c,1}^{1-D} + \mathcal{Q}_{c,2}^{3-D} = 0, \\ \mathcal{T}_{c,1}^{1-D} - \mathcal{T}_{c,2}^{3-D} = 0, \\ \mathcal{A}_{c,1}^{1-D} - \mathcal{A}_{c,2}^{3-D} = 0. \end{cases} \quad (2.9)$$

For the sake of clarity, in both cases the model to which each quantity belongs is indicated in the superscript. Indeed, we remark that (2.8) and (2.9) are written for the specific case of a 3-D FSI interface coupled with a single 1-D FSI model. In the case of a generalization to two or more 1-D models connected to the same 3-D FSI interface, the continuity of the area does not make sense, and for this reason we do not address this case. In addition, as described in Section 1.2, the 1-D FSI problem needs just one physical boundary condition on each side of the segment; by imposing either the coupling flow or the coupling stress, the value of the coupling area of the 1-D segment is already determined by the solution of the 1-D problem. In view of these considerations, for each coupling approach there are only three possible residual forms, depending on the value of n_c^Q , as summarized in Table 2.1; the corresponding local vectors of unknowns are detailed in Table 2.2.

Table 2.2: Detailed form of the local unknowns vector χ_c when the continuity of the vessel area is imposed between a 1-D and a 3-D FSI model. For each unknowns vector the corresponding residuals vector is given in Table 2.1.

n_c^Q	$c \in \mathcal{L}^S \cap \mathcal{L}^A$	$c \in \mathcal{L}^T \cap \mathcal{L}^A$
0	$(\mathcal{S}_c, \mathcal{A}_c)^\top$	$(\mathcal{S}_{c,1}, \mathcal{S}_{c,2}, \mathcal{T}_c, \mathcal{A}_c)^\top$
1	$(\mathcal{Q}_{c,1}, \mathcal{S}_c, \mathcal{A}_c)^\top$	$(\mathcal{Q}_{c,1}, \mathcal{S}_{c,2}, \mathcal{T}_c, \mathcal{A}_c)^\top$
2	$(\mathcal{Q}_{c,1}, \mathcal{Q}_{c,2}, \mathcal{S}_c, \mathcal{A}_c)^\top$	$(\mathcal{Q}_{c,1}, \mathcal{Q}_{c,2}, \mathcal{T}_c, \mathcal{A}_c)^\top$

Remark 2.10. In the development discussed in Sections 2.3.1 and 2.3.2 the interface equations do not imply any specific choice of the interface quantities, leaving the flexibility to impose either the coupling flow or the coupling stress on each coupling interface. In contrast, the sets of equations (2.8) and (2.9) require a particular care due to the presence of the coupling area. More precisely, the coupling area can be imposed only on the 3-D FSI problem, since the 1-D FSI model needs just one physical boundary condition on each side of the segment. Therefore, the last equation in the residual forms detailed in Table 2.1 cannot be replaced by an equivalent version written by replacing the 1-D boundary area operator with the 3-D one. For instance, in terms of components, for $n_c^Q = 0$ and $c \in \mathcal{L}^S \cap \mathcal{L}^A$ notice that the 3-D model receives as input \mathcal{S}_c and \mathcal{A}_c and yields as output $\mathcal{Q}_{c,2}^{3-D}$, while the 1-D model receives only \mathcal{S}_c and gives back $\mathcal{Q}_{c,1}^{1-D}$ and $\mathcal{A}_{c,1}^{1-D}$.

2.4 Numerical methods

The interface problem introduced in the previous section is characterized by having a very small number of degrees of freedom, since the unknowns are averaged/integrated quantities. Despite the small size of the problem, the solution of a dimensionally-heterogeneous network is challenging due to the global dynamic interplay between the different elements. Explicit algorithms cannot be used in general, since they do not account for the correct splitting of the flow at branching points. Moreover, even in serial configurations, they require a specific repartition of the boundary quantities over the interfaces, for the correct propagation of the flow. Therefore, we solve the interface problem implicitly, by using iterative techniques.

Let $\chi_{\mathcal{G}} = (\chi_1^\top, \chi_2^\top, \dots, \chi_c^\top)^\top$ be the global vector of unknowns, which includes all the coupling quantities defined in the network. In addition, let

$$\mathcal{R}_{\mathcal{G}}(\chi_{\mathcal{G}}) = \left(\mathcal{R}_1(\chi_1, \cdot)^\top, \mathcal{R}_2(\chi_2, \cdot)^\top, \dots, \mathcal{R}_c(\chi_c, \cdot)^\top \right)^\top,$$

be the global residuals vector. More generally, in the following we use the subscript \mathcal{G} to refer to quantities of the global interface problem, which reads

$$\mathcal{R}_{\mathcal{G}}(\chi_{\mathcal{G}}) = \mathbf{0}.$$

Given the solution of the interface problem at time t^n and assuming that all the models in the network are advanced in time by using the same time step Δt , we compute the solution at time t^{n+1} by a nonlinear Richardson method. Being $\chi_{\mathcal{G}}^k$ the current state and $\delta \chi_{\mathcal{G}}^k$ the computed update, the k -th

iteration of the nonlinear Richardson method reads

$$\boldsymbol{\chi}_{\mathcal{G}}^{k+1} = \boldsymbol{\chi}_{\mathcal{G}}^k + \delta \boldsymbol{\chi}_{\mathcal{G}}^k.$$

The initial guess $\boldsymbol{\chi}_{\mathcal{G}}^0$ is assigned by an extrapolation of the solution of the previous time steps and the method is applied recursively until the following stopping criteria is satisfied

$$\left\| \mathcal{R}_{\mathcal{G}}(\boldsymbol{\chi}_{\mathcal{G}}^{k+1}) \right\| < \varepsilon, \quad (2.10)$$

where ε is the tolerance of the interface problem.

Remark 2.11. The global vector of unknowns $\boldsymbol{\chi}_{\mathcal{G}}$ may consist in a combination of different types of local vectors $\boldsymbol{\chi}_c$, $c = 1, \dots, \mathcal{C}$, leading to a quite arbitrary assignment of the boundary conditions on the subproblems. Such flexibility, which is another appealing feature of the present approach, holds as long as the local problems are well-posed.

Remark 2.12. As mentioned before, to set up the iterative procedure for the solution of the globally coupled problem we need to define a global time step for all the elements in the network. In some circumstances this can be considered a strong limitation. Nevertheless, it is always possible to define a specific local smaller time step according to the needs of the different subproblems, as we show at the end of Chapter 3. Indeed, the global time step should be chosen according to the physics of the problem, rather than to the local limitations of the models in the network.

The update $\delta \boldsymbol{\chi}_{\mathcal{G}}^k$ can be computed with several approaches as we detail in the next sections.

2.4.1 Aitken method

The size of the interface problem suggests to start with a cheap iterative method to compute the update $\delta \boldsymbol{\chi}_{\mathcal{G}}^k$. Fixed point iterations convergence might benefit from an adaptive relaxation parameter; hence, the first method we propose is generalized Aitken's (see, e.g., Quarteroni et al. (2000) and Deparis (2004)), based on the following update procedure

$$\delta \boldsymbol{\chi}_{\mathcal{G}}^k = \omega^k \mathcal{R}_{\mathcal{G}}(\boldsymbol{\chi}_{\mathcal{G}}^k), \quad (2.11)$$

where the value of the relaxation parameter ω^k is computed using either the direct relaxation

$$\omega^k = \frac{(\mathcal{R}_{\mathcal{G}}(\boldsymbol{\chi}_{\mathcal{G}}^k) - \mathcal{R}_{\mathcal{G}}(\boldsymbol{\chi}_{\mathcal{G}}^{k-1})) \cdot (\boldsymbol{\chi}_{\mathcal{G}}^k - \boldsymbol{\chi}_{\mathcal{G}}^{k-1})}{\left\| \mathcal{R}_{\mathcal{G}}(\boldsymbol{\chi}_{\mathcal{G}}^k) - \mathcal{R}_{\mathcal{G}}(\boldsymbol{\chi}_{\mathcal{G}}^{k-1}) \right\|^2},$$

or the inverse relaxation

$$\omega^k = \frac{\left\| \boldsymbol{\chi}_{\mathcal{G}}^k - \boldsymbol{\chi}_{\mathcal{G}}^{k-1} \right\|^2}{(\mathcal{R}_{\mathcal{G}}(\boldsymbol{\chi}_{\mathcal{G}}^k) - \mathcal{R}_{\mathcal{G}}(\boldsymbol{\chi}_{\mathcal{G}}^{k-1})) \cdot (\boldsymbol{\chi}_{\mathcal{G}}^k - \boldsymbol{\chi}_{\mathcal{G}}^{k-1})}.$$

Note that if $\omega^k = 1$, then (2.11) coincides with a fixed point method.

Unfortunately, the results provided by the Aitken method are not satisfactory and convergence is guaranteed only in few simple cases, with strong restrictions on the values of \mathbb{J}_c , as shown in Table 2.3.

Table 2.3: Qualitative convergence results of the Aitken method.

n_c^Q	$\omega^k = 1$	Direct relaxation	Inverse relaxation
0	slow convergence only for $\max_{c=1,\dots,\mathcal{C}} (\mathcal{J}_c) = 2$	not converging	not converging
> 0	slow convergence only for $\max_{c=1,\dots,\mathcal{C}} (\mathcal{J}_c) = 2$	not converging	convergence only for $\max_{c=1,\dots,\mathcal{C}} (\mathcal{J}_c) = 2$

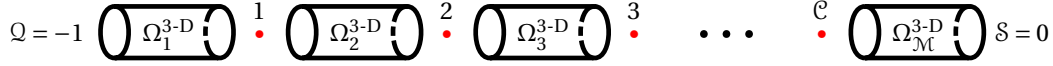


Figure 2.4: General scheme of a serial network made of \mathcal{M} cylinders connected by $\mathcal{C} = \mathcal{M} - 1$ coupling nodes. On the leftmost inflow we impose a unitary flow rate, while on the rightmost outflow a homogeneous Neumann boundary condition is applied.

As an example, let us consider the systematic coupling of 3-D rigid wall fluid flow models connected in series as shown in Figure 2.4.

We set up a stationary simulation of a Poiseuille flow using (2.11). Even in the best case (inverse relaxation with $n_c^Q = 1$, $c = 1, \dots, \mathcal{C}$) the number of iterations grows quickly with the number of elements inside the serial network, as shown in Table 2.4.

Table 2.4: Convergence results of the Aitken method for a series of elements connected one by one, such that $\max_{c=1,\dots,\mathcal{C}} (\mathcal{J}_c) = 2$, as shown in Figure 2.4.

\mathcal{C}	2	3	4	5	6
Iterations	4	17	21	24	26

Such unsatisfactory results motivate the use of more sophisticated algorithms, like those presented in the next sections.

2.4.2 Newton method

A possible alternative to Aitken method is Newton method. In this case the update $\delta \chi_{cg}^k$ is computed by solving the linear system

$$\mathcal{J}_{cg}(\chi_{cg}^k) \delta \chi_{cg}^k = -\mathcal{R}_{cg}(\chi_{cg}^k),$$

where the Jacobian matrix $\mathcal{J}_{cg}(\chi_{cg}^k)$ can be either exact or approximated (in the latter case it leads to an inexact-Newton method). In both cases, the Jacobian matrix can be assembled in two steps. First, the Jacobian graph is built and the required type of entries (partial derivatives with respect to coupling quantities) are identified. Then, during the second step, the matrix entries are either computed by solving the tangent problems associated to the coupled models, or approximated by using a simpler finite difference approach; the latter is known to provide a good approximation at a reasonable cost (see Blanco et al. (2011)). We postpone the details about the computation/approximation of the Jacobian matrix to Chapter 3.

In our experience this approach is more robust than the Aitken method. The flow regime and the network size may slightly affect the number of iterations. Nevertheless, as we show in Part II, the Newton and the inexact-Newton methods converge for all the simulated networks.

One of the most appealing features of the Newton method is the straightforward two-level parallelization of the algorithm. Indeed, thanks to the partitioning of the domain discussed in Section 2.1, each subproblem exchanges information with its neighbours only through the coupling conditions imposed on its artificial boundaries. Unlike a Gauss–Seidel method which implies a sequential exchange of information at the boundaries, the Newton method is perfectly suited for a parallelization of the algorithm at the higher-level (i.e., the level of the management of the different subproblems). Let us consider Algorithm 2.1, which synthetically illustrates the main steps required for the parallel solution of a general problem at each time step.

Algorithm 2.1 – Parallel time advancing with Newton.

```

1: for  $n = 1, 2, \dots, T/\Delta t$ 
2:   if  $n = 1$  (first time step)
3:     initialize  $\chi_{cg}^0 = \mathbf{0}$ 
4:   else
5:     extrapolate  $\chi_{cg}^0$  from previous time steps
6:   end
7:   solve  $\Omega_m$ ,  $m = 1, \dots, \mathcal{M}$ , and compute  $\mathcal{R}_{cg}(\chi_{cg}^0)$  [parallel step]
8:   while  $\mathcal{R}_{cg}(\chi_{cg}^k) \geq \text{tolerance}$ 
9:     compute/approximate  $\mathcal{J}_{cg}(\chi_{cg}^k)$  [parallel step]
10:    solve  $\mathcal{J}_{cg}(\chi_{cg}^k) \delta \chi_{cg}^k = -\mathcal{R}_{cg}(\chi_{cg}^k)$  and compute  $\chi_{cg}^{k+1} = \chi_{cg}^k + \delta \chi_{cg}^k$  [cheap!]
11:    solve  $\Omega_m$ ,  $m = 1, \dots, \mathcal{M}$ , and compute  $\mathcal{R}_{cg}(\chi_{cg}^{k+1})$  [parallel step]
12:   end
13: end

```

From the computational point of view, the most expensive steps are the solution of the subproblems and the computation of the coefficients of the Jacobian matrix. Nevertheless, both phases can be easily parallelized. In particular, the solution of the subproblems, performed in steps 7 and 11, is function of vector χ_{cg}^k , which is fixed at each Newton iteration. Hence, each subproblem can be solved on a different cluster node (where also a lower-level parallelization can be performed), without exchanging any information with the others. The same happens for the computation/approximation of the Jacobian matrix entries performed in step 9. Indeed, for each subproblem we can solve the tangent problem or compute the finite difference approximation in a completely independent manner.

2.4.3 Broyden method

The computation of the Jacobian matrix at each iteration of the Newton method may be expensive. This is even more critical when dealing with many 3-D FSI boundary interfaces, where for each interface the computation of a Jacobian entry requires the solution of a 3-D FSI problem. In view of this, some further approximations can be introduced. For example, it is possible to reuse the same Jacobian matrix for more than one iteration and, possibly, more than one time step. However, a better solution in the same direction is to use a Broyden method (see, e.g., Kelley (1995)) for the update of the Jacobian matrix at each nonlinear Richardson iteration. Indeed, this approach has been successfully applied for cardiovascular applications made of networks of 1-D models (see Blanco et al. (2011)) and for heterogeneous networks of rigid fluid problems (see Leiva et al. (2011)), requiring just a cheap evaluation of the global residuals vector of the interface problem.

Following the idea in Blanco et al. (2011), we combine our algorithm with the Broyden method for the update of the Jacobian matrix. More precisely, we initialize the Jacobian matrix at the first iteration of the first time step as described in the previous section. Then, for the rest of the simulation, we update the Jacobian matrix by using the Broyden method:

$$\mathcal{J}_{ig}(\boldsymbol{\chi}_{ig}^k) = \mathcal{J}_{ig}(\boldsymbol{\chi}_{ig}^{k-1}) + \frac{(\mathcal{R}_{ig}(\boldsymbol{\chi}_{ig}^k) - \mathcal{R}_{ig}(\boldsymbol{\chi}_{ig}^{k-1}))(\delta\boldsymbol{\chi}_{ig}^{k-1})^\top}{(\delta\boldsymbol{\chi}_{ig}^{k-1})^\top \delta\boldsymbol{\chi}_{ig}^{k-1}} - \frac{(\mathcal{J}_{ig}(\boldsymbol{\chi}_{ig}^{k-1})\delta\boldsymbol{\chi}_{ig}^{k-1})(\delta\boldsymbol{\chi}_{ig}^{k-1})^\top}{(\delta\boldsymbol{\chi}_{ig}^{k-1})^\top \delta\boldsymbol{\chi}_{ig}^{k-1}}. \quad (2.12)$$

Equation (2.12) does not require the solution of any tangent problem and it is based just on the evaluation of the residuals vector of the interface problem, which is needed in any case by the Newton method. On the basis of these considerations, Algorithm 2.1 can be upgraded to the version described in Algorithm 2.2.

Algorithm 2.2 – Parallel time advancing with Newton and Broyden.

```

1: for  $n = 1, 2, \dots, T/\Delta t$ 
2:   if  $n = 1$  (first time step)
3:     initialize  $\boldsymbol{\chi}_{ig}^0 = \mathbf{0}$ 
4:   else
5:     extrapolate  $\boldsymbol{\chi}_{ig}^0$  from previous time steps
6:   end
7:   solve  $\Omega_m$ ,  $m = 1, \dots, \mathcal{M}$ , and compute  $\mathcal{R}_{ig}(\boldsymbol{\chi}_{ig}^0)$  [parallel step]
8:   while  $\mathcal{R}_{ig}(\boldsymbol{\chi}_{ig}^k) \geq \text{tolerance}$ 
9:     if  $n = 1$  and  $k = 0$  (very first nonlinear iteration)
10:      compute/approximate  $\mathcal{J}_{ig}(\boldsymbol{\chi}_{ig}^k)$  [parallel step]
11:     else
12:       update  $\mathcal{J}_{ig}(\boldsymbol{\chi}_{ig}^k)$  with Broyden [cheap!]
13:     end
14:     solve  $\mathcal{J}_{ig}(\boldsymbol{\chi}_{ig}^k)\delta\boldsymbol{\chi}_{ig}^k = -\mathcal{R}_{ig}(\boldsymbol{\chi}_{ig}^k)$  and compute  $\boldsymbol{\chi}_{ig}^{k+1} = \boldsymbol{\chi}_{ig}^k + \delta\boldsymbol{\chi}_{ig}^k$  [cheap!]
15:     solve  $\Omega_m$ ,  $m = 1, \dots, \mathcal{M}$ , and compute  $\mathcal{R}_{ig}(\boldsymbol{\chi}_{ig}^{k+1})$  [parallel step]
16:   end
17: end

```

Remark 2.13. As suggested in Blanco et al. (2011), we also considered the orthogonalized version of the Broyden method. Nevertheless, in all our tested cases, this approach does not improve the performances compared to the classical version.

Remark 2.14. A simpler approach would be to initialize the Jacobian matrix with the identity matrix, in order to avoid, at all, the need of the techniques devised in the previous sections. However, this strategy leads to non-convergent schemes in all the tested cases. Moreover, the initialization of the Jacobian matrix is needed only at the very first iteration of the nonlinear Richardson algorithm, such that its impact on the global computational cost is negligible.

2.4.4 Simplified algorithms for continuity of the vessel area

In Section 2.3.3 we extended the interface equations to enforce the continuity of the vessel area between two dimensionally-heterogeneous FSI models. The residual forms provided there are general, such that the algorithms discussed in the previous sections hold without any change. The resulting flow diagram at a given time step is shown in Figure 2.5.

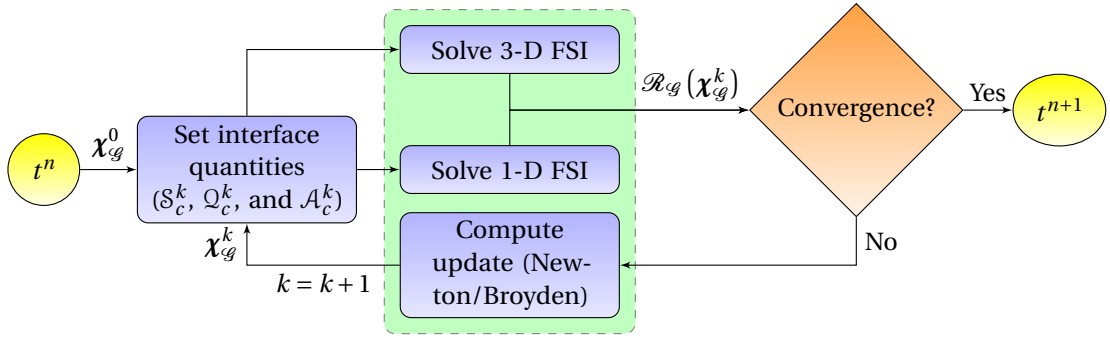


Figure 2.5: Algorithm flow diagram for the coupling of two dimensionally-heterogeneous FSI models, by using the approach devised in Section 2.3.3. In the diagram, χ_{cg} includes the coupling area, as detailed in Table 2.2.

Nevertheless, as we will discuss in more detail in Chapter 3, the presence of the coupling area in the residual forms requires an additional effort for the computation of the exact Jacobian matrix needed by the Newton method. For this reason, we devise two strategies to simplify the algorithm and the computational cost of the problem, as described in the following sections.

2.4.4.1 Explicit time discretization

In cardiovascular simulations the area of the vessel at the boundaries changes very smoothly in time. We can therefore treat it explicitly, in which case the area of each interface of the 3-D FSI model at time t^{n+1} is imposed equal to the one of the nearby 1-D interface at the previous time step. Then the radial scale factors Ψ_j^t , $j = 1, \dots, n_{FS}^\Gamma$, are computed explicitly at the beginning of each time step. Therefore, the residual form at the coupling interfaces is written just in terms of the coupling flow and the coupling stress or the coupling total stress as in (2.3) and (2.6), respectively. The corresponding flow diagram is shown in Figure 2.6.

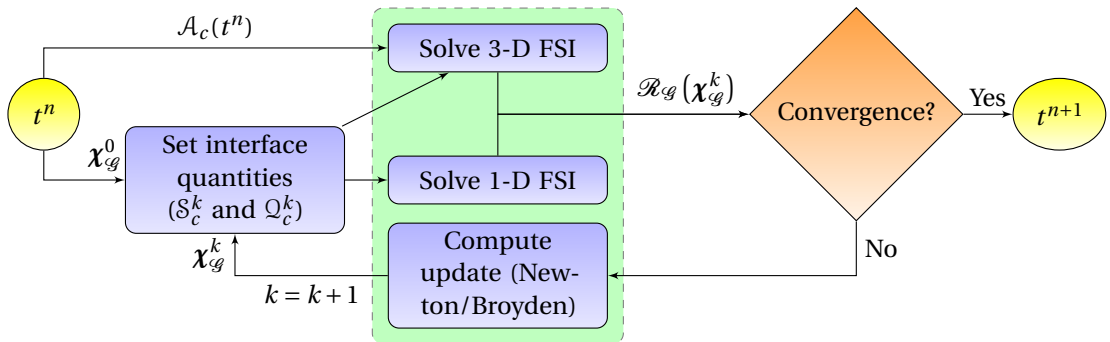


Figure 2.6: Algorithm flow diagram, for the coupling of two dimensionally-heterogeneous FSI models, by using an explicit time discretization scheme for the continuity of the vessel area. In the diagram χ_{cg} does not include the coupling area.

2.4.4.2 Implicit with hierarchy time discretization

A different strategy to preserve the implicit coupling of the area of the vessel without adding an equation in the residual form is to introduce a hierarchy among the models, such that at each nonlinear Richardson iteration first we solve the 1-D FSI models by computing the boundary area of each 1-D segment, and then we use these values to close and solve the nearby 3-D FSI models. As in the explicit case, the residual form at the coupling interfaces is written in terms of the coupling flow and the coupling stress or the coupling total stress. However, the radial scale factor $\Psi_j^t, j = 1, \dots, n_{FS}^T$, is updated with the new value of the area of the 1-D problem at each iteration of the interface problem. Since the dependence on the varying area is not taken into account in the 3-D boundary operators, the resulting Jacobian matrix is inexact and might lead to an increase of the number of iterations. Another drawback is that, due to the introduced hierarchy, the models cannot be solved at the same time on different machines. Nevertheless, if convergence is achieved, both this and the original non-simplified approaches yield the same solution. The flow diagram of this scheme is shown in Figure 2.7.

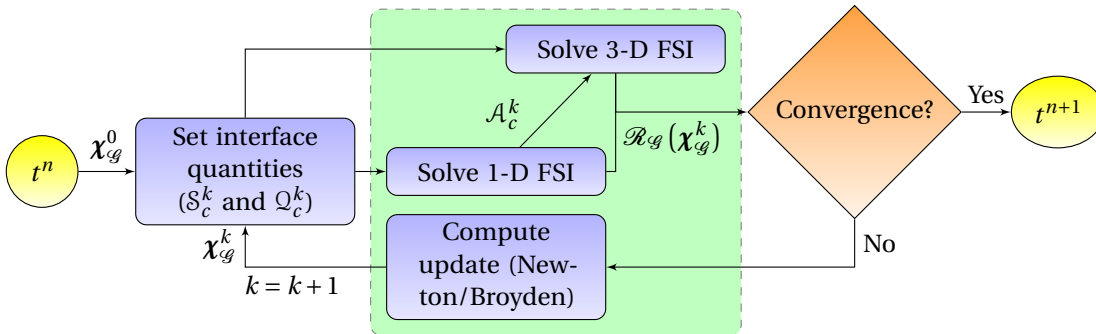


Figure 2.7: Algorithm flow diagram for the coupling of two dimensionally-heterogeneous FSI models, by using an implicit with hierarchy time discretization scheme for the continuity of the vessel area. In the diagram χ_{cg} does not include the coupling area.

2.5 Framework implementation

The geometrical multiscale framework has been implemented in `LifeV`¹, a C++ finite element library, following the same idea of abstraction used throughout the chapter. In particular, all the specific models, coupling conditions, and algorithms have been derived from three common abstract base classes, which provide transparent interfaces between the objects in the framework.

A detailed description of the structure of the geometrical multiscale framework is included in the `doxygen` documentation of the library and is not reported here. In the following, we briefly mention the main classes that set up and solve the problem.

MultiscaleSolver is the main class of the framework. It manages the global time loop applied to a single model, which can be either a specific model, to solve, e.g., a stand-alone 3-D FSI problem, or a geometrical multiscale model, to solve a network of heterogeneous problems.

MultiscaleData is a data container for the main global parameters of the problem (e.g., time data, fluid density, fluid viscosity, etc.).

¹<http://www.lifev.org>.

MultiscaleModel is a base abstract class from which all the specific model classes are derived. It provides a set of transparent interfaces to set up, update, and solve the specific problems (3-D FSI, 1-D FSI, etc.).

MultiscaleCoupling is a base abstract class from which all the specific coupling condition classes are derived. It provides a set of transparent interfaces to apply the chosen set of interface equations to the connected models and to compute the residuals vector and the exact or approximated Jacobian matrix of the interface problem.

MultiscaleAlgorithm is a base abstract class from which all the specific iterative method classes are derived. It provides a set of transparent interfaces to solve the global interface problem.

MultiscaleCommunicatorsManager is a class designed to assign each specific model to a different subset of processors or cluster nodes, leading to the aforementioned two-level parallelization of the algorithms (see Section 2.4.2).

Figure 2.8 provides a schematic overview of the main structure of a geometrical multiscale simulation; the solver class creates an instance of a geometrical multiscale model, which in turn makes use of a factory design pattern to create the instances of the given set of specific models, coupling conditions, as well as of the specific algorithm for the solution of the interface problem. At the level of the geometrical

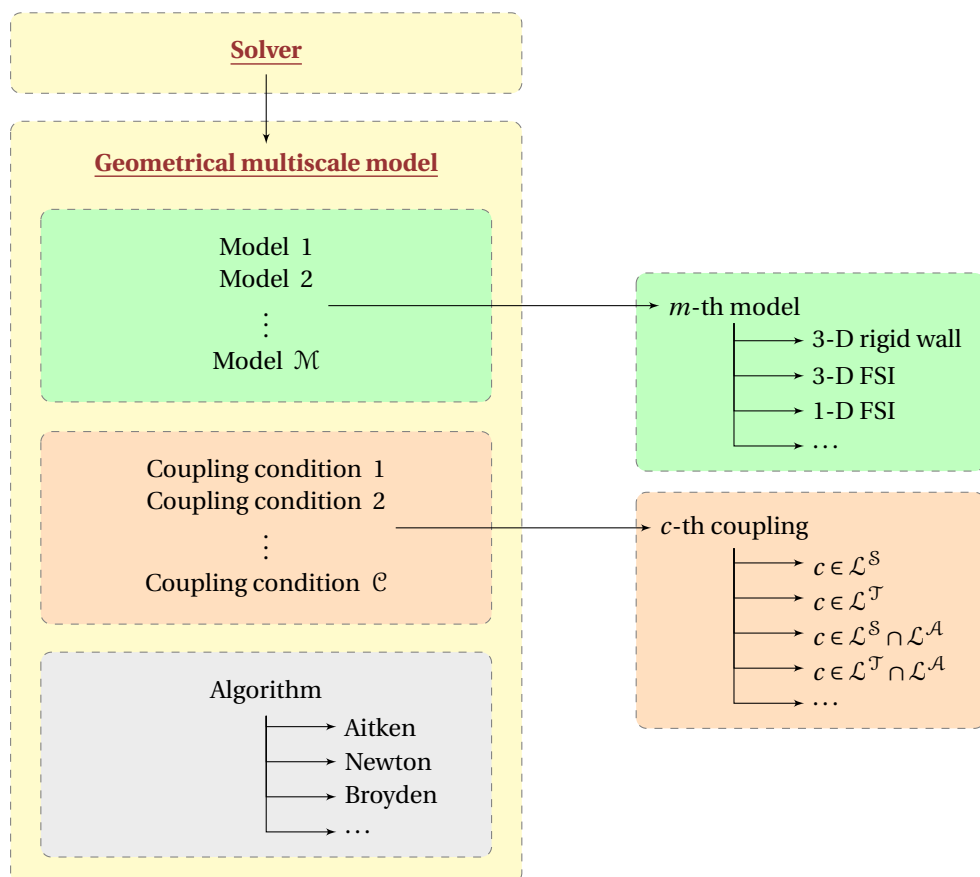


Figure 2.8: Geometrical multiscale framework implementation in the LiFeV library.

multiscale model class, all these elements are seen as black boxes, managed through common abstract interfaces, without any preliminary assumption regarding the equations, the geometries, and the numerical approximations behind each object. In other words, the geometrical multiscale model class acts as a global container of the elements in the network. The description of the network topology as well as the data of the models, the algorithms, and of the set of interface equations are provided through a set of data files.

The parallelism is handled by the multiscale communicators manager, which distributes the models across the available processors and cluster nodes. Each model can be either assigned to a single processor or partitioned across several nodes. In our implementation, we distribute the models as a function of their type and computational cost. More precisely, the reduced order models (e.g., 1-D FSI models and the lumped parameters terminals) are distributed one per each available processor. If the number of models exceeds the number of processors, the communicators manager assigns more models to each processor. For examples, on a small cluster composed by 48 processors, a network of 150 reduced order models is split such that each processor holds at least 3 models, while there are 6 processors that have one more model each. The more expensive 3-D (FSI or rigid wall) models are then partitioned across all the available processors (including the processors already holding one or more reduced order models). If more 3-D models are present in the network, each of them is split on a subset of nodes such that they globally use all the available resources. Thanks to the parallelism intrinsic in our algorithms, this choice leads in general to a balanced load.

Main references of the chapter:

- ☆ A. C. I. Malossi, P. J. Blanco, S. Deparis, and A. Quarteroni. Algorithms for the partitioned solution of weakly coupled fluid models for cardiovascular flows. *Int. J. Num. Meth. Biomed. Engng.*, 27(12):2035–2057, 2011.
- ☆ A. C. I. Malossi, P. J. Blanco, P. Crosetto, S. Deparis, and A. Quarteroni. Implicit coupling of one-dimensional and three-dimensional blood flow models with compliant vessels. Submitted, 2012.
- ☆ P. J. Blanco, S. Deparis, and A. C. I. Malossi. On the continuity of mean total normal stress in geometrical multiscale cardiovascular problems. In preparation, 2012.

3 Jacobian matrix for the interface problem

In this chapter we provide the details for the assembling and the computation/approximation of the Jacobian matrix of the interface problem. Since the graph of the matrix depends on both the global connectivity of the elements in the network and the chosen set of interface equations and boundary data at each node, the computation of the exact Jacobian is a challenging task. Leiva et al. (2011) propose a matrix-free Newton–GMRES algorithm for the solution of the interface problem. The main drawback of this method is that the Jacobian matrix cannot be reused at the subsequent iterations. Indeed, being the interface equations written in terms of averaged/integrated quantities, the size of the Jacobian matrix is very small, and its storage is not an issue. For this reason, in this work we devise an approach for the assembling of the full Jacobian matrix. In particular, we take advantage of the block structure of the Jacobian, which allows the global problem to be split in smaller blocks. For each of them we can identify a precise structure depending the local connectivity and the chosen set of interface equations at the corresponding coupling node. Regarding the computation of the Jacobian entries, Leiva et al. (2010) propose a finite difference method, which may lead to a good approximation at a reasonable cost. However, this might affect the convergence of the Newton method, leading to a sensible increase in the number of iterations. To overcome this limitation, we propose to compute the exact Jacobian entries through the definition of the tangent problem for both the 3-D and 1-D FSI models. The former makes use of the same Jacobian matrix used for the solution of the FSI problem, while for the latter we compute analytically the expressions of the Jacobian entries.

The layout of the chapter is the following: in Section 3.1 we describe the assembling procedure for the three sets of interface equations devised in Chapter 2. For all of them we provide the general form of the diagonal and off-diagonal block elements. In addition, we provide a simple algorithm to build the Jacobian by blocks. Then in Section 3.2 we describe the tangent problem for the exact computation of the Jacobian entries for the two FSI models described in Chapter 1.

3.1 Matrix assembling

The Jacobian matrix of the interface problem is given by the derivative of the global residuals vector with respect to the global unknowns vector:

$$\mathcal{J}_{\mathcal{G}}(\boldsymbol{\chi}_{\mathcal{G}}) = \frac{\partial \mathcal{R}_{\mathcal{G}}(\boldsymbol{\chi}_{\mathcal{G}})}{\partial \boldsymbol{\chi}_{\mathcal{G}}}.$$

Chapter 3. Jacobian matrix for the interface problem

Both depend on the set of interface equations imposed at each node of the network. Therefore, the block structure of the Jacobian and the type of matrix entries are problem dependent.

Let $\mathcal{J}_{c_1 c_2}(\chi_{c_1}, \cdot)$ be a block of the Jacobian matrix, with c_1 and c_2 two coupling nodes inside the network, $c_1, c_2 = 1, \dots, \mathcal{C}$; $\mathcal{J}_{c_1 c_2}(\chi_{c_1}, \cdot)$ expresses the connectivity between coupling nodes c_1 and c_2 , such that

$$\mathcal{J}_{c_1 c_2}(\chi_{c_1}, \cdot) = \frac{\partial \mathcal{R}_{c_1}(\chi_{c_1}, \cdot)}{\partial \chi_{c_2}}.$$

In particular, there are three possible cases:

1. $c_1 \equiv c_2$: a perturbation $\delta \chi_{c_2}$ produces a variation of the interface quantities χ_{c_2} through a diagonal block element of the Jacobian matrix (c_2 is connected with itself);
2. $c_1 \neq c_2$ and these nodes are connected through a certain model (i.e., they are at the boundaries of a common model): a perturbation $\delta \chi_{c_2}$ produces a variation of the interface quantities χ_{c_1} through an off-diagonal block element of the Jacobian matrix;
3. $c_1 \neq c_2$ and they are not connected through any model (i.e., there are two or more models between them): a perturbation $\delta \chi_{c_2}$ does not affect the interface quantities χ_{c_1} and $\mathcal{J}_{c_1 c_2}(\chi_{c_1}, \cdot) = 0$.

The block structure of the Jacobian matrix is

$$\mathcal{J}_{\mathcal{G}}(\chi_{\mathcal{G}}) = \begin{bmatrix} \mathcal{J}_{11}(\chi_1, \cdot) & \mathcal{J}_{12}(\chi_1, \cdot) & \dots & \mathcal{J}_{1\mathcal{C}}(\chi_1, \cdot) \\ \mathcal{J}_{21}(\chi_2, \cdot) & \mathcal{J}_{22}(\chi_2, \cdot) & \dots & \mathcal{J}_{2\mathcal{C}}(\chi_2, \cdot) \\ \vdots & \vdots & \ddots & \vdots \\ \mathcal{J}_{\mathcal{C}1}(\chi_{\mathcal{C}}, \cdot) & \mathcal{J}_{\mathcal{C}2}(\chi_{\mathcal{C}}, \cdot) & \dots & \mathcal{J}_{\mathcal{C}\mathcal{C}}(\chi_{\mathcal{C}}, \cdot) \end{bmatrix}.$$

Several algorithms can be used to assemble it. An example is provided in Algorithm 3.1, which builds the Jacobian by blocks.

Algorithm 3.1 – Jacobian matrix block assembling procedure.

```

1: for  $c_1 = 1, \dots, \mathcal{C}$ 
2:   for  $c_2 = 1, \dots, \mathcal{C}$ 
3:     if  $c_1 = c_2$ 
4:       compute  $\mathcal{J}_{c_1 c_1}(\chi_{c_1}, \cdot)$ 
5:     else
6:       if  $c_1$  is connected to  $c_2$ 
7:         compute  $\mathcal{J}_{c_1 c_2}(\chi_{c_1}, \cdot)$ 
8:       else
9:          $\mathcal{J}_{c_1 c_2} = \mathbf{0}$ 
10:      end
11:    end
12:  end
13: end

```

In the following sections we detail the exact form of the Jacobian matrix blocks for the sets of interface equations introduced in Chapter 2. A practical example of the global resulting matrices together with the corresponding residual forms is presented in Chapter 4.

3.1.1 Matrix blocks: continuity of the mean normal stress

Let us assume that $c_1 \in \mathcal{L}^S$, i.e., continuity of the mean normal stress at the coupling node c_1 . We recall that in this case the form of the unknowns vector χ_{c_1} is given in (2.4), whose size is $\mathcal{L}_{c_1} = n_{c_1}^Q + 1$. The diagonal block element is

$$\mathcal{I}_{c_1 c_1}(\chi_{c_1}, \cdot) = \begin{bmatrix} 1 & 1 & \dots & \dots & 1 & \sum_{i=n_{c_1}^Q+1}^{J_{c_1}} \frac{\partial \mathcal{Q}_{c_1, i}}{\partial \mathcal{S}_{c_1}} \\ \frac{\partial \mathcal{S}_{c_1, 1}}{\partial \mathcal{Q}_{c_1, 1}} & 0 & \dots & \dots & 0 & -1 \\ 0 & \frac{\partial \mathcal{S}_{c_1, 2}}{\partial \mathcal{Q}_{c_1, 2}} & & & \vdots & \vdots \\ \vdots & & \ddots & & \vdots & \vdots \\ \vdots & & & \frac{\partial \mathcal{S}_{c_1, n_{c_1}^Q-1}}{\partial \mathcal{Q}_{c_1, n_{c_1}^Q-1}} & 0 & -1 \\ 0 & \dots & \dots & 0 & \frac{\partial \mathcal{S}_{c_1, n_{c_1}^Q}}{\partial \mathcal{Q}_{c_1, n_{c_1}^Q}} & -1 \end{bmatrix},$$

where in the matrix, for the sake of simplicity, we omit the boundary operator parentheses expressing the dependence on the interface quantities; indeed, all the partial derivatives in the matrix are, in general, non-null entries. The block $\mathcal{I}_{c_1 c_1}(\chi_{c_1}, \cdot)$ is square of size $\mathcal{L}_{c_1} \times \mathcal{L}_{c_1}$.

Regarding the off-diagonal block elements they can take two forms depending on the type of boundary data imposed on the i -th coupling interface, where $1 \leq i \leq J_{c_1}$. More precisely, if the coupling stress is imposed on the i -th interface, then

$$\mathcal{I}_{c_1 c_2}(\chi_{c_1}, \cdot) = \begin{bmatrix} 0 & \dots & 0 & \frac{\partial \mathcal{Q}_{c_1, i}}{\partial [\chi_{c_2}]_\ell} & 0 & \dots & 0 \\ 0 & \dots & 0 & 0 & 0 & \dots & 0 \\ \vdots & & \vdots & \vdots & \vdots & & \vdots \\ 0 & \dots & 0 & 0 & 0 & \dots & 0 \\ 0 & \dots & 0 & 0 & 0 & \dots & 0 \\ 0 & \dots & 0 & 0 & 0 & \dots & 0 \\ \vdots & & \vdots & \vdots & \vdots & & \vdots \\ 0 & \dots & 0 & 0 & 0 & \dots & 0 \end{bmatrix},$$

where we use the notation $[\chi_{c_2}]_\ell$ to refer to the ℓ -th element of the vector χ_{c_2} , with $1 \leq \ell \leq \mathcal{L}_{c_2}$, where \mathcal{L}_{c_2} is the size of the unknowns vector χ_{c_2} . The position of the non-null entry in the matrix is $(1, \ell)$.

In contrast, if the coupling flow is imposed on the i -th interface, then

$$\mathcal{I}_{c_1 c_2}(\chi_{c_1}, \cdot) = \begin{bmatrix} 0 & \dots & 0 & 0 & 0 & \dots & 0 \\ 0 & \dots & 0 & 0 & 0 & \dots & 0 \\ \vdots & & \vdots & \vdots & \vdots & & \vdots \\ 0 & \dots & 0 & 0 & 0 & \dots & 0 \\ 0 & \dots & 0 & \frac{\partial \mathcal{L}_{c_1, i}}{\partial [\chi_{c_2}]_\ell} & 0 & \dots & 0 \\ 0 & \dots & 0 & 0 & 0 & \dots & 0 \\ \vdots & & \vdots & \vdots & \vdots & & \vdots \\ 0 & \dots & 0 & 0 & 0 & \dots & 0 \end{bmatrix},$$

where in this case the position of the non-null entry in the matrix is $(1 + i, \ell)$, with $1 \leq \ell \leq \mathcal{L}_{c_2}$. In both cases the off-diagonal blocks are rectangular of size $\mathcal{L}_{c_1} \times \mathcal{L}_{c_2}$.

3.1.2 Matrix blocks: continuity of the mean total normal stress

Let us consider now the case $c_1 \in \mathcal{L}^J$, i.e., continuity of the mean total normal stress at the coupling node c_1 . We recall that in this case the form of the unknowns vector χ_{c_1} is given in (2.7), whose size is $\mathcal{L}_{c_1} = J_c + 1$. The diagonal block element is

$$\mathcal{I}_{c_1 c_1}(\chi_{c_1}, \cdot) = \begin{bmatrix} 1 & 1 & \dots & 1 & \frac{\partial \mathcal{Q}_{c_1, n_{c_1}^0 + 1}}{\partial \mathcal{S}_{c_1, n_{c_1}^0 + 1}} & \dots & \frac{\partial \mathcal{Q}_{c_1, J_{c_1} - 1}}{\partial \mathcal{S}_{c_1, J_{c_1} - 1}} & \frac{\partial \mathcal{Q}_{c_1, J_{c_1}}}{\partial \mathcal{S}_{c_1, J_{c_1}}} & 0 \\ \frac{\partial \mathcal{T}_{c_1, 1}}{\partial \mathcal{Q}_{c_1, 1}} & 0 & \dots & \dots & \dots & \dots & \dots & 0 & -1 \\ 0 & \frac{\partial \mathcal{T}_{c_1, 2}}{\partial \mathcal{Q}_{c_1, 2}} & & & & & & \vdots & \vdots \\ \vdots & & \ddots & & & & & \vdots & \vdots \\ \vdots & & & \frac{\partial \mathcal{T}_{c_1, n_{c_1}^0}}{\partial \mathcal{Q}_{c_1, n_{c_1}^0}} & & & & \vdots & \vdots \\ \vdots & & & & \frac{\partial \mathcal{T}_{c_1, n_{c_1}^0 + 1}}{\partial \mathcal{S}_{c_1, n_{c_1}^0 + 1}} & & & \vdots & \vdots \\ \vdots & & & & & \ddots & & \vdots & \vdots \\ \vdots & & & & & & \frac{\partial \mathcal{T}_{c_1, J_{c_1} - 1}}{\partial \mathcal{S}_{c_1, J_{c_1} - 1}} & 0 & -1 \\ 0 & \dots & \dots & \dots & \dots & \dots & 0 & \frac{\partial \mathcal{T}_{c_1, J_{c_1}}}{\partial \mathcal{S}_{c_1, J_{c_1}}} & -1 \end{bmatrix},$$

where, as before, we omit to indicate the specific dependence on the interface quantities. The block $\mathcal{I}_{c_1 c_1}(\chi_{c_1}, \cdot)$ is square of size $\mathcal{L}_{c_1} \times \mathcal{L}_{c_1}$.

As in the previous case, the off-diagonal block elements can take two forms depending on the type of boundary data imposed on the i -th coupling interface, where $1 \leq i \leq \mathcal{J}_{c_1}$. More precisely, if the coupling stress is imposed on the i -th interface, then

$$\mathcal{I}_{c_1 c_2}(\boldsymbol{\chi}_{c_1}, \cdot) = \begin{bmatrix} 0 & \dots & 0 & \frac{\partial \mathcal{Q}_{c_1, i}}{\partial [\boldsymbol{\chi}_{c_2}]_\ell} & 0 & \dots & 0 \\ 0 & \dots & 0 & 0 & 0 & \dots & 0 \\ \vdots & & \vdots & \vdots & \vdots & & \vdots \\ 0 & \dots & 0 & 0 & 0 & \dots & 0 \\ 0 & \dots & 0 & \frac{\partial \mathcal{T}_{c_1, i}}{\partial [\boldsymbol{\chi}_{c_2}]_\ell} & 0 & \dots & 0 \\ 0 & \dots & 0 & 0 & 0 & \dots & 0 \\ \vdots & & \vdots & \vdots & \vdots & & \vdots \\ 0 & \dots & 0 & 0 & 0 & \dots & 0 \end{bmatrix},$$

where the positions of the non-null entries in the matrix are $(1, \ell)$ and $(1 + i, \ell)$, with $1 \leq \ell \leq \mathcal{L}_{c_2}$, where \mathcal{L}_{c_2} is the size of the unknowns vector $\boldsymbol{\chi}_{c_2}$.

In contrast, if the coupling flow is imposed on the i -th interface, then

$$\mathcal{I}_{c_1 c_2}(\boldsymbol{\chi}_{c_1}, \cdot) = \begin{bmatrix} 0 & \dots & 0 & 0 & 0 & \dots & 0 \\ 0 & \dots & 0 & 0 & 0 & \dots & 0 \\ \vdots & & \vdots & \vdots & \vdots & & \vdots \\ 0 & \dots & 0 & 0 & 0 & \dots & 0 \\ 0 & \dots & 0 & \frac{\partial \mathcal{T}_{c_1, i}}{\partial [\boldsymbol{\chi}_{c_2}]_\ell} & 0 & \dots & 0 \\ 0 & \dots & 0 & 0 & 0 & \dots & 0 \\ \vdots & & \vdots & \vdots & \vdots & & \vdots \\ 0 & \dots & 0 & 0 & 0 & \dots & 0 \end{bmatrix},$$

where in this case the position of the non-null entry in the matrix is $(1 + i, \ell)$, with $1 \leq \ell \leq \mathcal{L}_{c_2}$. In both cases the off-diagonal blocks are rectangular of size $\mathcal{L}_{c_1} \times \mathcal{L}_{c_2}$.

3.1.3 Matrix blocks: continuity of the vessel area

Finally, let us consider the case $c_1 \in \mathcal{L}^A$, i.e., continuity of the vessel area at the coupling node c_1 . For the six cases described in Table 2.1 the corresponding diagonal block elements are summarized in Table 3.1 where, as before, we omit the boundary operator parentheses expressing the dependence on the interface quantities. The diagonal block elements are square with size dependent on the chosen approach.

Regarding the off-diagonal block elements there are three cases.

1. c_1 and c_2 are connected through a 1-D FSI model: the off-diagonal block elements are those described in Sections 3.1.1 and 3.1.2, with the additional entry $\partial \mathcal{A}_{c_1,1}^{1-D} / \partial [\chi_{c_2}]_\ell$ in the last row of the ℓ -th column, with $1 \leq \ell \leq \mathcal{L}_{c_2}$.
2. c_1 and c_2 are connected through a 3-D FSI model and $c_2 \notin \mathcal{L}^A$: the off-diagonal block elements are those described in Sections 3.1.1 and 3.1.2 without additional entries.
3. c_1 and c_2 are connected through a 3-D FSI model and $c_2 \in \mathcal{L}^A$: the off-diagonal block elements are those described in Sections 3.1.1 and 3.1.2, with some additional entries as described in Table 3.2.

3.2 Matrix entries computation/approximation

The value of each Jacobian entry depends on the corresponding boundary operator to which it is associated. In other words, the computation of a specific Jacobian entry involves only one model and its interfaces. In Leiva et al. (2010) and Blanco et al. (2011) the authors use a finite difference method, which may lead to a good approximation at a reasonable cost. For example, a Jacobian entry corresponding to the partial derivative of the flow rate boundary operator at the i -th interface of the c_1 -th node of the network is given by

$$\frac{\partial \mathcal{Q}_{c_1,i}(\chi_{c_1}, [\chi_{c_2}]_\ell, \cdot)}{\partial [\chi_{c_2}]_\ell} \cong \frac{\mathcal{Q}_{c_1,i}(\chi_{c_1}, [\chi_{c_2}]_\ell + \delta [\chi_{c_2}]_\ell, \cdot) - \mathcal{Q}_{c_1,i}(\chi_{c_1}, [\chi_{c_2}]_\ell, \cdot)}{\delta [\chi_{c_2}]_\ell},$$

where, for the sake of clarity, in the operator we explicitly express the dependence on the unknown quantity $[\chi_{c_2}]_\ell$ and on its perturbation parameter $\delta [\chi_{c_2}]_\ell$, both defined at the c_2 -th node, being $1 \leq \ell \leq \mathcal{L}_{c_2}$. The other entry types can be addressed in a similar way.

The main advantages of this approach are the easy implementation and the abstraction from the original problem, such that it can be applied to black box codes with a very small effort. Nevertheless, the main drawback is that the accuracy of the approximation might affect or compromise the convergence of the Newton method. Moreover, the choice of the magnitude of the perturbation parameter to be applied to the interface quantities is not straightforward; indeed, when not chosen adequately, this might have a severe impact on the global convergence speed of the Newton scheme.

3.2. Matrix entries computation/approximation

Table 3.1: Diagonal block elements corresponding to the imposition of the continuity of the vessel area between a 1-D and a 3-D FSI model. The original residual forms are given in Table 2.1.

$n_{c_1}^Q$	$c_1 \in \mathcal{L}^S \cap \mathcal{L}^A$	$c_1 \in \mathcal{L}^T \cap \mathcal{L}^A$
0	$\begin{bmatrix} \frac{\partial \mathcal{Q}_{c_1,1}^{1-D}}{\partial \mathcal{S}_{c_1}} + \frac{\partial \mathcal{Q}_{c_1,2}^{3-D}}{\partial \mathcal{S}_{c_1}} & \frac{\partial \mathcal{Q}_{c_1,2}^{3-D}}{\partial \mathcal{A}_{c_1}} \\ \frac{\partial \mathcal{A}_{c_1,1}^{1-D}}{\partial \mathcal{S}_{c_1}} & -1 \end{bmatrix}$	$\begin{bmatrix} \frac{\partial \mathcal{Q}_{c_1,1}^{1-D}}{\partial \mathcal{S}_{c_1,1}} & \frac{\partial \mathcal{Q}_{c_1,2}^{3-D}}{\partial \mathcal{S}_{c_1,2}} & 0 & 0 \\ \frac{\partial \mathcal{T}_{c_1,1}^{1-D}}{\partial \mathcal{S}_{c_1,1}} & 0 & -1 & 0 \\ 0 & \frac{\partial \mathcal{T}_{c_1,2}^{3-D}}{\partial \mathcal{S}_{c_1,2}} & -1 & \frac{\partial \mathcal{T}_{c_1,2}^{3-D}}{\partial \mathcal{A}_{c_1}} \\ \frac{\partial \mathcal{A}_{c_1,1}^{1-D}}{\partial \mathcal{S}_{c_1,1}} & 0 & 0 & -1 \end{bmatrix}$
1	$\begin{bmatrix} 1 & \frac{\partial \mathcal{Q}_{c_1,2}^{3-D}}{\partial \mathcal{S}_{c_1}} & \frac{\partial \mathcal{Q}_{c_1,2}^{3-D}}{\partial \mathcal{A}_{c_1}} \\ \frac{\partial \mathcal{T}_{c_1,1}^{1-D}}{\partial \mathcal{Q}_{c_1,1}} & -1 & 0 \\ \frac{\partial \mathcal{A}_{c_1,1}^{1-D}}{\partial \mathcal{Q}_{c_1,1}} & 0 & -1 \end{bmatrix}$	$\begin{bmatrix} 1 & \frac{\partial \mathcal{Q}_{c_1,2}^{3-D}}{\partial \mathcal{S}_{c_1,2}} & 0 & 0 \\ \frac{\partial \mathcal{T}_{c_1,1}^{1-D}}{\partial \mathcal{Q}_{c_1,1}} & 0 & -1 & 0 \\ 0 & \frac{\partial \mathcal{T}_{c_1,2}^{3-D}}{\partial \mathcal{S}_{c_1,2}} & -1 & \frac{\partial \mathcal{T}_{c_1,2}^{3-D}}{\partial \mathcal{A}_{c_1}} \\ \frac{\partial \mathcal{A}_{c_1,1}^{1-D}}{\partial \mathcal{Q}_{c_1,1}} & 0 & 0 & -1 \end{bmatrix}$
2	$\begin{bmatrix} 1 & 1 & 0 & 0 \\ \frac{\partial \mathcal{T}_{c_1,1}^{1-D}}{\partial \mathcal{Q}_{c_1,1}} & 0 & -1 & 0 \\ 0 & \frac{\partial \mathcal{T}_{c_1,2}^{3-D}}{\partial \mathcal{Q}_{c_1,2}} & -1 & \frac{\partial \mathcal{T}_{c_1,2}^{3-D}}{\partial \mathcal{A}_{c_1}} \\ \frac{\partial \mathcal{A}_{c_1,1}^{1-D}}{\partial \mathcal{Q}_{c_1,1}} & 0 & 0 & -1 \end{bmatrix}$	$\begin{bmatrix} 1 & 1 & 0 & 0 \\ \frac{\partial \mathcal{T}_{c_1,1}^{1-D}}{\partial \mathcal{Q}_{c_1,1}} & 0 & -1 & 0 \\ 0 & \frac{\partial \mathcal{T}_{c_1,2}^{3-D}}{\partial \mathcal{Q}_{c_1,2}} & -1 & \frac{\partial \mathcal{T}_{c_1,2}^{3-D}}{\partial \mathcal{A}_{c_1}} \\ \frac{\partial \mathcal{A}_{c_1,1}^{1-D}}{\partial \mathcal{Q}_{c_1,1}} & 0 & 0 & -1 \end{bmatrix}$

Table 3.2: Additional off-diagonal block entries corresponding to the imposition of the continuity of the vessel area between a 1-D and a 3-D FSI model for the case in which c_1 and c_2 are connected through a 3-D FSI model and $c_2 \in \mathcal{L}^A$.

Row	Column	$c_1 \in \mathcal{L}^S \cap \mathcal{L}^A$		$c_1 \in \mathcal{L}^T \cap \mathcal{L}^A$	
		$n_{c_1}^Q < 2$	$n_{c_1}^Q = 2$	$n_{c_1}^Q < 2$	$n_{c_1}^Q = 2$
First	Last	$\frac{\partial \mathcal{Q}_{c_1,2}^{3-D}}{\partial \mathcal{A}_{c_2}}$	0	$\frac{\partial \mathcal{Q}_{c_1,2}^{3-D}}{\partial \mathcal{A}_{c_2}}$	0
Third	Last	0	$\frac{\partial \mathcal{T}_{c_1,2}^{3-D}}{\partial \mathcal{A}_{c_2}}$	$\frac{\partial \mathcal{T}_{c_1,2}^{3-D}}{\partial \mathcal{A}_{c_2}}$	$\frac{\partial \mathcal{T}_{c_1,2}^{3-D}}{\partial \mathcal{A}_{c_2}}$

To overcome the limitations of the finite difference method, we compute the Jacobian entries by solving the exact tangent problem associated to the original model (see, e.g., Sokołowski and Zolésio (1992)). More precisely, we devise a tangent problem formulation for the two FSI models described in Chapter 1. This leads to the exact computation of the Jacobian entries and preserve the quadratic convergence of the Newton method. Moreover, any dependency on the magnitude of the perturbation parameter vanishes.

3.2.1 3-D models

In this section we describe the tangent problem approach for the computation of the Jacobian entries in the case of 3-D problems. Since each Jacobian entry is computed by solving the tangent problem of a single model, hereafter we refer to the model boundary interfaces numeration, i.e., $j = 1, \dots, n_{\text{FS}}^{\Gamma}$, rather than to the node boundary interfaces one, i.e., $i = 1, \dots, \mathcal{J}_c$; indeed, the boundary interfaces of the other models are not relevant at this level.

From the analysis of the Jacobian blocks detailed in Section 3.1 we observe that, beside the constant values, a 3-D problem leads to no more than nine possible entries types, i.e.,

$$\begin{aligned}
 & \frac{\partial \mathcal{Q}_{c_1, j_1}(\boldsymbol{x}_{c_1}, \cdot)}{\partial \mathcal{A}_{c_2, j_2}}, & \frac{\partial \mathcal{S}_{c_1, j_1}(\boldsymbol{x}_{c_1}, \cdot)}{\partial \mathcal{A}_{c_2, j_2}}, & \frac{\partial \mathcal{T}_{c_1, j_1}(\boldsymbol{x}_{c_1}, \cdot)}{\partial \mathcal{A}_{c_2, j_2}}, \\
 & \frac{\partial \mathcal{Q}_{c_1, j_1}(\boldsymbol{x}_{c_1}, \cdot)}{\partial \mathcal{Q}_{c_2, j_2}}, & \frac{\partial \mathcal{S}_{c_1, j_1}(\boldsymbol{x}_{c_1}, \cdot)}{\partial \mathcal{Q}_{c_2, j_2}}, & \frac{\partial \mathcal{T}_{c_1, j_1}(\boldsymbol{x}_{c_1}, \cdot)}{\partial \mathcal{Q}_{c_2, j_2}}, \\
 & \frac{\partial \mathcal{Q}_{c_1, j_1}(\boldsymbol{x}_{c_1}, \cdot)}{\partial \mathcal{S}_{c_2, j_2}}, & \frac{\partial \mathcal{S}_{c_1, j_1}(\boldsymbol{x}_{c_1}, \cdot)}{\partial \mathcal{S}_{c_2, j_2}}, & \frac{\partial \mathcal{T}_{c_1, j_1}(\boldsymbol{x}_{c_1}, \cdot)}{\partial \mathcal{S}_{c_2, j_2}},
 \end{aligned} \tag{3.1}$$

where the indices j_1 and j_2 , which are associated to the coupling nodes c_1 and c_2 , respectively, refer to two boundary interfaces of the same model. In case $c_1 \equiv c_2$ the two boundary interfaces coincide and the fourth and eighth entries in (3.1) are equal to one.

In the following we first make use of the 3-D rigid wall model to describe in detail the procedure for the computation of the Jacobian entries; indeed, 3-D Navier–Stokes equations in fixed domains are simple enough (compared to 3-D FSI problems) to represent a good reference case to write and study the discrete variational form of the associated tangent problem in the most general scenario. Then, we briefly extend the proposed methodology to the 3-D FSI model case, for which the tangent problem is written directly in the discrete matrix form.

3.2.1.1 Rigid wall model

Let us consider first problem (1.3), i.e., 3-D Navier–Stokes equations in a rigid wall domain Ω_{F}^0 . In addition, let $Y^{\mathcal{Q}}$ and $Y^{\mathcal{S}}$ be the local lists of indices associated to the boundary interfaces of Ω_{F}^0 where coupling flow and coupling stress boundary data, respectively, are applied. We remark that, in view of the discussions in Chapter 2, we do not address the case of coupling total stress imposed on the boundary interfaces of the problem.

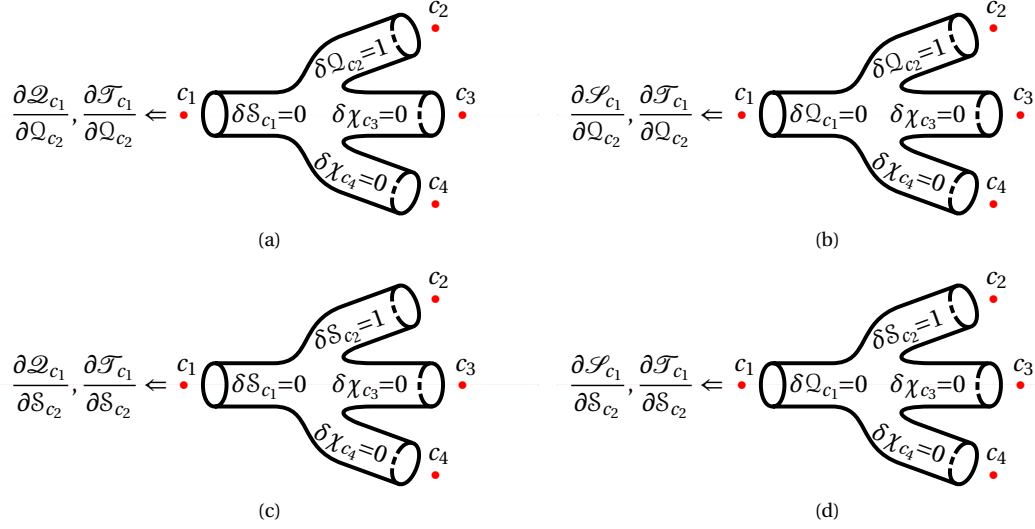


Figure 3.1: Scheme of the computation of the block Jacobian entries $\mathcal{J}_{c_1 c_2}$ for a 3-D rigid wall trifurcation. In each case, a different set of boundary conditions is applied on problem (3.2). (a) Computation of $\frac{\partial \mathcal{Q}_{c_1}}{\partial \mathcal{Q}_{c_2}}$ and $\frac{\partial \mathcal{T}_{c_1}}{\partial \mathcal{Q}_{c_2}}$. (b) Computation of $\frac{\partial \mathcal{S}_{c_1}}{\partial \mathcal{Q}_{c_2}}$ and $\frac{\partial \mathcal{T}_{c_1}}{\partial \mathcal{Q}_{c_2}}$. (c) Computation of $\frac{\partial \mathcal{Q}_{c_1}}{\partial \mathcal{S}_{c_2}}$ and $\frac{\partial \mathcal{T}_{c_1}}{\partial \mathcal{S}_{c_2}}$. (d) Computation of $\frac{\partial \mathcal{S}_{c_1}}{\partial \mathcal{S}_{c_2}}$ and $\frac{\partial \mathcal{T}_{c_1}}{\partial \mathcal{S}_{c_2}}$.

Given $\mathbf{u}_{F,h} \in \mathcal{V}_{F,h}$, $\delta \mathcal{Q}_j$, for all $j \in \Upsilon^\Omega$, and $\delta \mathcal{S}_j$, for all $j \in \Upsilon^S$, the variational form of the associated tangent problem reads: find $(\delta \mathbf{u}_{F,h}, \delta p_{F,h}) \in \mathcal{V}_{F,h}$, and $\delta \lambda_j^\Omega \in \mathbb{R}$, for $j \in \Upsilon^\Omega$, such that

$$\left\{ \begin{array}{l} \int_{\Omega_F^0} \rho_F \frac{\partial \delta \mathbf{u}_{F,h}}{\partial t} \cdot \mathbf{u}_{F,h}^* \, d\Omega - \int_{\Omega_F^0} \delta p_{F,h} \nabla \cdot \mathbf{u}_{F,h}^* \, d\Omega + \int_{\Omega_F^0} \mu_F \nabla \delta \mathbf{u}_{F,h} \cdot \nabla \mathbf{u}_{F,h}^* \, d\Omega \\ + \int_{\Omega_F^0} \rho_F (\delta \mathbf{u}_{F,h} \cdot \nabla) \mathbf{u}_{F,h} \cdot \mathbf{u}_{F,h}^* \, d\Omega + \int_{\Omega_F^0} \rho_F (\mathbf{u}_{F,h} \cdot \nabla) \delta \mathbf{u}_{F,h} \cdot \mathbf{u}_{F,h}^* \, d\Omega \\ + \sum_{j \in \Upsilon^\Omega} \int_{\Gamma_{F,j}^0} \delta \lambda_j^\Omega \mathbf{u}_{F,h}^* \cdot \mathbf{n}_F \, d\Gamma + \sum_{j \in \Upsilon^S} \int_{\Gamma_{F,j}^0} \delta \mathcal{S}_j \mathbf{u}_{F,h}^* \cdot \mathbf{n}_F \, d\Gamma = \mathbf{0} \quad \forall \mathbf{u}_{F,h}^* \in \mathcal{V}_{F,h}^*, \\ \int_{\Omega_F^0} p_{F,h}^* \nabla \cdot \delta \mathbf{u}_{F,h} \, d\Omega = 0 \quad \forall p_{F,h}^* \in \mathcal{V}_{F,h}^*, \\ \int_{\Gamma_{F,j}^0} \delta \mathbf{u}_{F,h} \cdot \mathbf{n}_F \, d\Gamma = \delta \mathcal{Q}_j \quad j \in \Upsilon^\Omega, \end{array} \right. \quad (3.2)$$

where λ_j^Ω are the Lagrange multipliers that enforce the coupling flow on $\Gamma_{F,j}^0$, being $j \in \Upsilon^\Omega$. Note that in $\mathcal{V}_{F,h}$ we consider the essential boundary conditions as given in (1.3). Let us assume that Γ_{F,j_1}^0 and Γ_{F,j_2}^0 are the boundary interfaces associated with the coupling nodes c_1 and c_2 , respectively. The entry types (3.1), which might appear in the generic Jacobian block $\mathcal{J}_{c_1 c_2}$, are computed by solving problem (3.2) as follows:

- $\frac{\partial \mathcal{Q}_{c_1}}{\partial \mathcal{A}_{c_2}}$, $\frac{\partial \mathcal{S}_{c_1}}{\partial \mathcal{A}_{c_2}}$, and $\frac{\partial \mathcal{T}_{c_1}}{\partial \mathcal{A}_{c_2}}$ do not exist in the 3-D rigid wall case, since the area of Γ_{F,j_1}^0 is fixed.

- $\frac{\partial \mathcal{Q}_{c_1}}{\partial \mathcal{Q}_{c_2}}$ and $\frac{\partial \mathcal{S}_{c_1}}{\partial \mathcal{Q}_{c_2}}$ are computed as the flow rate and mean normal stress on Γ_{F,j_1}^0 , resulting from the imposition of a unitary perturbation $\delta \mathcal{Q}_{c_2} = 1$ on Γ_{F,j_2}^0 and homogeneous boundary conditions of the corresponding type on all the other boundaries, i.e., $\delta \mathcal{Q}_j = 0$, $j \in \Upsilon^{\mathcal{Q}}$, $j \neq j_2$ and $\delta \mathcal{S}_j = 0$, $j \in \Upsilon^{\mathcal{S}}$ (see Figures 3.1a and 3.1b). The mean total normal stress entry type is given by

$$\frac{\partial \mathcal{T}_{c_1}}{\partial \mathcal{Q}_{c_2}} = \Theta^{\mathcal{Q}} - \rho_F \frac{1}{|\Gamma_{F,j_1}^0|} \int_{\Gamma_{F,j_1}^0} (\mathbf{u}_{F,h} \cdot \mathbf{n}_F) (\delta \mathbf{u}_{F,h} \cdot \mathbf{n}_F) d\Gamma,$$

where

$$\Theta^{\mathcal{Q}} = \begin{cases} \frac{\partial \mathcal{S}_{c_1}}{\partial \mathcal{Q}_{c_2}} & \text{if } j_1 \in \Upsilon^{\mathcal{Q}}, \\ 0 & \text{otherwise.} \end{cases}$$

- $\frac{\partial \mathcal{Q}_{c_1}}{\partial \mathcal{S}_{c_2}}$ and $\frac{\partial \mathcal{S}_{c_1}}{\partial \mathcal{S}_{c_2}}$, are computed as the flow rate and mean normal stress on Γ_{F,j_1}^0 , resulting from the imposition of a unitary perturbation $\delta \mathcal{S}_{c_2} = 1$ on Γ_{F,j_2}^0 and homogeneous boundary conditions of the corresponding type on all the other boundaries, i.e., $\delta \mathcal{Q}_j = 0$, $j \in \Upsilon^{\mathcal{Q}}$ and $\delta \mathcal{S}_j = 0$, $j \in \Upsilon^{\mathcal{S}}$, $j \neq j_2$ (see Figures 3.1c and 3.1d). The mean total normal stress entry type is given by

$$\frac{\partial \mathcal{T}_{c_1}}{\partial \mathcal{S}_{c_2}} = \Theta^{\mathcal{S}} - \rho_F \frac{1}{|\Gamma_{F,j_1}^0|} \int_{\Gamma_{F,j_1}^0} (\mathbf{u}_{F,h} \cdot \mathbf{n}_F) (\delta \mathbf{u}_{F,h} \cdot \mathbf{n}_F) d\Gamma,$$

where

$$\Theta^{\mathcal{S}} = \begin{cases} \frac{\partial \mathcal{S}_{c_1}}{\partial \mathcal{S}_{c_2}} & \text{if } j_1 \in \Upsilon^{\mathcal{Q}} \text{ and } c_1 \neq c_2, \\ 1 & \text{if } j_1 \in \Upsilon^{\mathcal{S}} \text{ and } c_1 \equiv c_2, \\ 0 & \text{otherwise.} \end{cases}$$

At this point it is clear that the assembly procedure described in Algorithm 3.1 can be further optimized, as in general it leads to perform multiple perturbations of the same interface quantity and hence to perform multiple solutions of the same linear system. For instance, in the examples described in Figures 3.1, the solution of the same tangent problem can be used to compute not only the entries at c_1 , but also the entries at c_3 and c_4 . Indeed, to minimize the computational cost it is convenient to assemble the matrix column by column; in other words, for each perturbed interface we solve the tangent problem associated to that domain only once, computing all the coefficients that appear in the same column of the global Jacobian matrix. This holds independently of the type of model.

Remark 3.1. There exist cases where some Jacobian entries might be trivial, e.g., $\frac{\partial \mathcal{Q}_{c_1}}{\partial \mathcal{Q}_{c_2}} = -1$, if c_1 and c_2 are connected by a 3-D rigid wall pipe or by any 3-D rigid wall geometry with just two interfaces.

3.2.1.2 FSI model

The procedure for the computation of the Jacobian entries (3.1) devised in the previous section can be extended also to the case of a 3-D FSI model. With this aim we can take advantage of the Jacobian computed during the Newton method for the solution of the 3-D FSI problem. Indeed, in Chapter 1 we have described the exact computation of the 3-D FSI Jacobian matrix \mathcal{J}_{FSI} for both the GCE and FI approaches. No matter which time discretization scheme is used, the Jacobian matrix of the FSI

problem serves also for the computation of the Jacobian entries of the interface problems. More precisely, the discrete matrix form of the tangent problem associated to the 3-D FSI model reads:

$$\mathcal{J}_{\text{FSI}}\left(\mathbf{u}_{\text{FSI},h}^k\right)\delta\mathbf{u}_{\text{FSI},h} = \mathbf{b}_{\text{FSI},j_2},$$

where $\mathbf{u}_{\text{FSI},h}^k$ is the solution of the FSI problem obtained during the computation of the residuals vector of the k -th nonlinear Richardson iteration of the interface problem. The entries of $\mathbf{b}_{\text{FSI},j_2}$ are null apart from the contribution given by the unitary perturbation of the interface quantity applied on Γ_{F,j_2}^t such that $\delta\mathbf{u}_{\text{FSI},h}$ is the resulting variation of the global FSI solution vector due to that unitary perturbation. Note that this is equivalent to solve problem (1.14) with a different right-hand side which takes into account the local network topology.

Remark 3.2. From the computational viewpoint, it is necessary to solve one tangent problem for each coupling interface of the 3-D FSI model. However, the Jacobian matrix is the same for all the cases. Moreover, it is already available from the previous Newton iterations of the FSI problem (see equation (1.13)), where it has been computed by using the second last state variable.

Remark 3.3. In the GCE time discretization approach, problem (1.15) is solved just once per time step, at the first nonlinear Richardson iteration of the interface problem. Indeed, it does not depend on any fluid coupling quantity.

The values of the Jacobian entries are then retrieved from the solution of the FSI tangent problem. More precisely, similarly to what has been done in the 3-D rigid wall case, the six partial derivatives of the flow rate and mean normal stress boundary operators with respect to the interface quantities in Γ_{F,j_2}^t (first two columns entries in (3.1)) are computed from $\delta\mathbf{u}_{\text{FSI},h}$ as the resulting flow rate and mean normal stress on Γ_{F,j_1}^t . Regarding the mean total normal stress entry types they are computed as

$$\frac{\partial \mathcal{T}_{c_1}}{\partial Q_{c_2}} = \Theta^{\text{Q}} + \mathcal{K}, \quad \frac{\partial \mathcal{T}_{c_1}}{\partial S_{c_2}} = \Theta^{\text{S}} + \mathcal{K}, \quad \frac{\partial \mathcal{T}_{c_1}}{\partial A_{c_2}} = \Theta^{\text{A}} + \mathcal{K},$$

where Θ^{Q} and Θ^{S} are the same quantities defined in Section 3.2.1.1, while

$$\Theta^{\text{A}} = \begin{cases} \frac{\partial \mathcal{S}_{c_1}}{\partial A_{c_2}} & \text{if } j_1 \in \Upsilon^{\text{Q}}, \\ 0 & \text{otherwise.} \end{cases}$$

Finally, the kinetic term derivative is

$$\begin{aligned} \mathcal{K} = & \frac{1}{2}\rho_{\text{F}} \frac{1}{|\Gamma_{\text{F},j_1}^t|^2} \int_{\Gamma_{\text{F},j_1}^t} \nabla_{\Gamma} \cdot \delta \mathbf{d}_{\text{F},h} \, \text{d}\Gamma \int_{\Gamma_{\text{F},j_1}^t} (\mathbf{u}_{\text{F},h} \cdot \mathbf{n}_{\text{F}})^2 \, \text{d}\Gamma \\ & - \frac{1}{2}\rho_{\text{F}} \frac{1}{|\Gamma_{\text{F},j_1}^t|} \left(\int_{\Gamma_{\text{F},j_1}^t} 2(\mathbf{u}_{\text{F},h} \cdot \mathbf{n}_{\text{F}}) (\delta \mathbf{u}_{\text{F},h} \cdot \mathbf{n}_{\text{F}}) \, \text{d}\Gamma + \int_{\Gamma_{\text{F},j_1}^t} \nabla_{\Gamma} \cdot \delta \mathbf{d}_{\text{F},h} (\mathbf{u}_{\text{F},h} \cdot \mathbf{n}_{\text{F}})^2 \, \text{d}\Gamma \right), \end{aligned}$$

being ∇_{Γ} the divergence operator written on Γ_{F,j_1}^t .

3.2.2 1-D FSI model

In this section we describe the tangent problem to compute the Jacobian entries in the case of a 1-D FSI model. As in the 3-D case, we refer to the model boundary interfaces numeration rather than to the node boundary interfaces one. From the analysis of the Jacobian blocks detailed in Section 3.1 we observe that, beside the constant values, a 1-D problem leads to no more than eight possible types of entries. Moreover, due to the hyperbolic nature of the 1-D problem and to the explicit time discretization scheme chosen in Chapter 1, we can assume that a perturbation on a boundary quantity imposed on a side of the 1-D segment does not have any effect on the other side during a single time step. Indeed, from condition (1.20) we deduce that a pseudo-characteristic which at time t^n has the foot on a boundary interface, thus approaching the first/last finite element, at time t^{n+1} will still be inside the same finite element, being far from the other extremity of the 1-D segment. This amounts to consider a diagonal block structure for the Jacobian matrix (i.e., $\mathcal{J}_{c_1 c_2} = 0$) and reduces the number of different entry types to six, i.e.,

$$\begin{aligned} & \frac{\partial \mathcal{A}_{c_1, j_1}(\mathcal{Q}_{c_1, j_1})}{\partial \mathcal{Q}_{c_1, j_1}}, & \frac{\partial \mathcal{L}_{c_1, j_1}(\mathcal{Q}_{c_1, j_1})}{\partial \mathcal{Q}_{c_1, j_1}}, & \frac{\partial \mathcal{T}_{c_1, j_1}(\mathcal{Q}_{c_1, j_1})}{\partial \mathcal{Q}_{c_1, j_1}}, \\ & \frac{\partial \mathcal{A}_{c_1, j_1}(\mathcal{S}_{c_1, j_1})}{\partial \mathcal{S}_{c_1, j_1}}, & \frac{\partial \mathcal{L}_{c_1, j_1}(\mathcal{S}_{c_1, j_1})}{\partial \mathcal{S}_{c_1, j_1}}, & \frac{\partial \mathcal{T}_{c_1, j_1}(\mathcal{S}_{c_1, j_1})}{\partial \mathcal{S}_{c_1, j_1}}, \end{aligned} \quad (3.3)$$

where j_1 refers to either Γ_L or Γ_R . Note that by choosing an implicit or semi-implicit time discretization scheme the previous assumption is no more valid, such that the number of entry types in (3.3) increases.

In the following, we first devise the exact tangent problem associated to the 1-D FSI model for the computation of the Jacobian entries (3.3). Then we discuss some issues related to the explicit nature of the Taylor–Galerkin scheme described in Chapter 1; these issues are solved by introducing a two-level time step technique. With these we account for an implicit coupling of the entire network while keeping an explicit time discretization in each 1-D segment. Indeed, the implicit treatment at the global level is mandatory to capture the correct flow rate and pressure wave propagation, especially in presence of branching sites and large networks.

3.2.2.1 Exact tangent problem formulation

The entries (3.3) of the diagonal blocks of the Jacobian are computed by setting up the tangent problem boundary data as described in Figure 3.2.

Let us first compute the entries in Figures 3.2a and 3.2b, where flow rate boundary data are applied to the left and right interfaces of the 1-D segment. We remark that in this case the viscoelastic problem (1.21) is closed by a homogeneous Dirichlet boundary condition on the corresponding side, as discussed in Chapter 1; for instance, on the left side of the segment this corresponds to have: $\hat{Q}_L = 0$ and $Q_L \equiv \hat{Q}_L$. We remark that in the following development we take advantage of the chosen explicit time discretization scheme. The analytical expression of the Jacobian entries in the continuous form or for an implicit time discretization scheme is different and is not addressed here.

3.2. Matrix entries computation/approximation

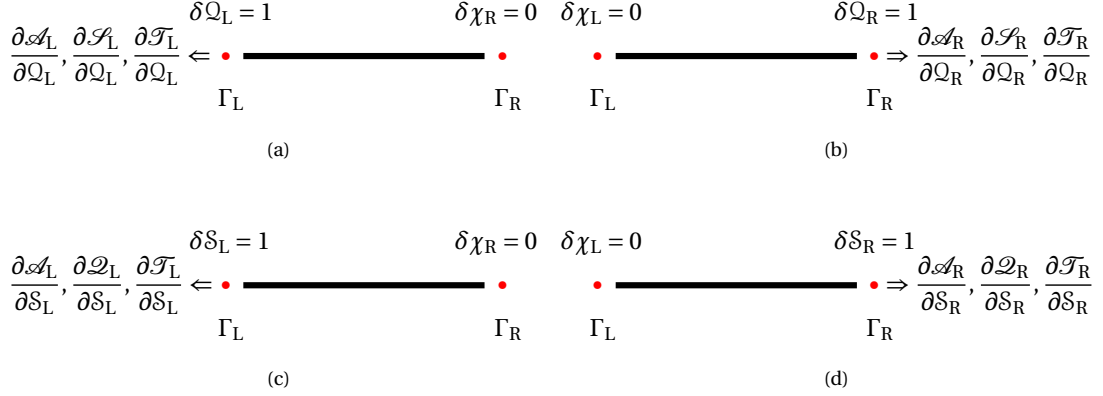


Figure 3.2: Scheme of the computation of the Jacobian entries for a 1-D FSI model. The imposed set of perturbed quantities is shown on top of the coupling nodes. (a) Computation of $\frac{\partial \mathcal{A}_L}{\partial Q_L}$, $\frac{\partial \mathcal{S}_L}{\partial Q_L}$, and $\frac{\partial \mathcal{T}_L}{\partial Q_L}$. (b) Computation of $\frac{\partial \mathcal{A}_R}{\partial Q_R}$, $\frac{\partial \mathcal{S}_R}{\partial Q_R}$, and $\frac{\partial \mathcal{T}_R}{\partial Q_R}$. (c) Computation of $\frac{\partial \mathcal{A}_L}{\partial S_L}$, $\frac{\partial \mathcal{Q}_L}{\partial S_L}$, and $\frac{\partial \mathcal{T}_L}{\partial S_L}$. (d) Computation of $\frac{\partial \mathcal{A}_R}{\partial S_R}$, $\frac{\partial \mathcal{Q}_R}{\partial S_R}$, and $\frac{\partial \mathcal{T}_R}{\partial S_R}$.

The left and right area boundary operators are given by

$$\mathcal{A}_L(Q_L) = \mathcal{E}_{\dot{Q}_L \rightarrow A_L}(-Q_L), \quad \mathcal{A}_R(Q_R) = \mathcal{E}_{\dot{Q}_R \rightarrow A_R}(Q_R), \quad (3.4)$$

being $\mathcal{E}_{\dot{Q}_L \rightarrow A_L}(\cdot)$ and $\mathcal{E}_{\dot{Q}_R \rightarrow A_R}(\cdot)$ the elastic operators that, given the elastic volumetric flow rate on a side of the 1-D FSI segment, return the area at the same side (see problem (1.19) with boundary conditions (1.25)₁ and (1.25)₂, respectively).

By differentiating (3.4) with respect to the coupling flow we get the analytical expression of the first two Jacobian entries

$$\frac{\partial \mathcal{A}_L(Q_L)}{\partial Q_L} = \frac{\partial \mathcal{E}_{\dot{Q}_L \rightarrow A_L}(-Q_L)}{\partial Q_L}, \quad \frac{\partial \mathcal{A}_R(Q_R)}{\partial Q_R} = \frac{\partial \mathcal{E}_{\dot{Q}_R \rightarrow A_R}(Q_R)}{\partial Q_R},$$

where from (1.25)₁ and (1.25)₂ we have

$$\frac{\partial \mathcal{E}_{\dot{Q}_L \rightarrow A_L}(Q_L)}{\partial Q_L} = \frac{L_{22}^n}{L_{21}^n}, \quad \frac{\partial \mathcal{E}_{\dot{Q}_R \rightarrow A_R}(Q_R)}{\partial Q_R} = -\frac{L_{12}^n}{L_{11}^n},$$

which are explicit quantities known from the previous time step.

Being $\psi_L(A) = \psi(A, 0)$, the left mean normal stress boundary operator is

$$\mathcal{S}_L(Q_L) = -\psi_L(\mathcal{A}_L(Q_L)), \quad (3.5)$$

where the contribution on the right side is equivalently defined; for the sake of notation, in the following we refrain from defining both left and right quantities when unnecessary.

Chapter 3. Jacobian matrix for the interface problem

By differentiating (3.5) with respect to the coupling flow we get the analytical expression of the left mean normal stress Jacobian entry

$$\frac{\partial \mathcal{A}_L(Q_L)}{\partial Q_L} = - \frac{\partial \psi_L(A_L^{n+1})}{\partial A_L} \frac{\partial \mathcal{A}_L(Q_L)}{\partial Q_L}.$$

The first term is computed by differentiating (1.17) with respect to the coupling area,

$$\frac{\partial \psi_L(A_L^{n+1})}{\partial A_L} = \frac{\beta_S(0)}{2\sqrt{A^0(0)A_L^{n+1}}} + \frac{\gamma_S(0)}{2\Delta t(A_L^{n+1})^{3/2}} \left(3 \frac{A_L^n}{A_L^{n+1}} - 1 \right),$$

where we approximate the temporal derivative of the area with a first order finite difference.

Finally, the left mean total normal stress boundary operator is

$$\mathcal{F}_L(Q_L) = \mathcal{A}_L(Q_L) - \frac{1}{2} \rho_F \alpha_F \frac{Q_L^2}{\mathcal{A}_L^2(Q_L)},$$

where, as for the mean normal stress, the contribution on the right side is equivalently defined. The analytical expressions of the mean total normal stress Jacobian entries on the left side is

$$\frac{\partial \mathcal{F}_L(Q_L)}{\partial Q_L} = \frac{\partial \mathcal{A}_L(Q_L)}{\partial Q_L} - \rho_F \alpha_F \left(\frac{Q_L}{\mathcal{A}_L^2(Q_L)} - \frac{Q_L^2}{\mathcal{A}_L^3(Q_L)} \frac{\partial \mathcal{A}_L(Q_L)}{\partial Q_L} \right).$$

Therefore, when flow rate boundary data are applied to the left and right interfaces, the computation of the Jacobian entries is extremely cheap and does not require the solution of a finite element problem.

Let us now consider the entries in Figures 3.2c and 3.2d, where mean normal stress boundary data are applied to the left and right interfaces of the 1-D segment.

The left area boundary operator is given by

$$\mathcal{A}_L(S_L) = \psi_L^{-1}(-S_L), \quad (3.6)$$

where ψ_L^{-1} is the inverse of the pressure-area relation evaluated at $z = 0$, i.e., Γ_L . Note that due to the differential form of the viscoelastic term in (1.17), we do not have the analytical expression for the relation $\mathcal{A}(P) = \psi^{-1}(P, z)$, which is solved numerically by using the Newton method. By differentiating (3.6) with respect to the coupling stress we get the analytical expression of the left boundary area Jacobian entry

$$\frac{\partial \mathcal{A}_L(S_L)}{\partial S_L} = \frac{\partial \psi_L^{-1}(-S_L)}{\partial S_L},$$

where, for the aforementioned reasons, the partial derivative of the inverse operator is approximated by finite differences.

The left and right volumetric flow rate boundary operators are given by

$$\mathcal{Q}_L(S_L) = -(\hat{Q}_L(S_L) + \tilde{Q}_L(S_L)), \quad \mathcal{Q}_R(S_R) = \hat{Q}_R(S_R) + \tilde{Q}_R(S_R), \quad (3.7)$$

where the elastic and viscoelastic contributions on the left side are defined as

$$\hat{Q}_L(S_L) = \mathcal{E}_{A_L \rightarrow \hat{Q}_L}(\mathcal{A}_L(S_L)), \quad \tilde{Q}_L(S_L) = \mathcal{V}_{(\hat{Q}, A) \rightarrow \tilde{Q}_L}(\hat{Q}(S_L), A(S_L)),$$

3.2. Matrix entries computation/approximation

being $\mathcal{E}_{A_L \rightarrow \hat{Q}_L}$ the elastic operator that, once given the area on the left side of the 1-D segment, returns the elastic volumetric flow rate at the same side (see problem (1.19) with boundary condition (1.25)₃); similarly, $\mathcal{V}_{(\hat{Q}, A) \rightarrow \hat{Q}_L}(\cdot, \cdot)$ is the viscoelastic operator (see problem (1.21)) that, once given the elastic flow rate and the area along the 1-D segment, returns the viscoelastic flow rate on its left side. In both cases the contributions on the right side are similarly defined.

By differentiating (3.7) with respect to the coupling stress we get the analytical expression of the left and right flow rate Jacobian entries

$$\frac{\partial \mathcal{Q}_L(\mathcal{S}_L)}{\partial \mathcal{S}_L} = - \left(\frac{\partial \hat{Q}_L(\mathcal{S}_L)}{\partial \mathcal{S}_L} + \frac{\partial \tilde{Q}_L(\mathcal{S}_L)}{\partial \mathcal{S}_L} \right), \quad \frac{\partial \mathcal{Q}_R(\mathcal{S}_R)}{\partial \mathcal{S}_R} = \frac{\partial \hat{Q}_R(\mathcal{S}_R)}{\partial \mathcal{S}_R} + \frac{\partial \tilde{Q}_R(\mathcal{S}_R)}{\partial \mathcal{S}_R}.$$

The derivative of the elastic contribution on the left side is

$$\frac{\partial \hat{Q}_L(\mathcal{S}_L)}{\partial \mathcal{S}_L} = \frac{\partial \mathcal{E}_{A_L \rightarrow \hat{Q}_L}(A_L^{n+1})}{\partial A_L} \frac{\partial \mathcal{A}_L(\mathcal{S}_L)}{\partial \mathcal{S}_L}.$$

From (1.25)₃ and (1.25)₄ we compute the derivative of the elastic operators on the left and right side, respectively, such that

$$\frac{\partial \mathcal{E}_{A_L \rightarrow \hat{Q}_L}(A_L^{n+1})}{\partial A_L} = - \frac{L_{21}^n}{L_{22}^n}, \quad \frac{\partial \mathcal{E}_{A_R \rightarrow \hat{Q}_R}(A_R^{n+1})}{\partial A_R} = - \frac{L_{11}^n}{L_{12}^n},$$

which are explicit quantities known from the previous time step. However, the derivative of the viscoelastic contribution on the left side is

$$\frac{\partial \tilde{Q}_L(\mathcal{S}_L)}{\partial \mathcal{S}_L} = \frac{\partial \mathcal{V}_{(\hat{Q}, A) \rightarrow \hat{Q}_L}(\hat{Q}^{n+1}, A^{n+1})}{\partial \hat{Q}} \frac{\partial \hat{Q}(\mathcal{S}_L)}{\partial \mathcal{S}_L} + \frac{\partial \mathcal{V}_{(\hat{Q}, A) \rightarrow \hat{Q}_L}(\hat{Q}^{n+1}, A^{n+1})}{\partial A} \frac{\partial A(\mathcal{S}_L)}{\partial \mathcal{S}_L},$$

where we remark that exploiting the finite element discretization, we have

$$\begin{aligned} \frac{\partial \mathcal{V}_{(\hat{Q}, A) \rightarrow \hat{Q}_L}(\hat{Q}^{n+1}, A^{n+1})}{\partial \hat{Q}} \frac{\partial \hat{Q}(\mathcal{S}_L)}{\partial \mathcal{S}_L} &= \sum_{i=1}^{n_{FE}} \frac{\partial \mathcal{V}_{(\hat{Q}, A) \rightarrow \hat{Q}_L}(\hat{Q}^{n+1}, A^{n+1})}{\partial \hat{Q}_i} \frac{\partial \mathcal{E}_{A_L \rightarrow \hat{Q}_i}(A_L^{n+1})}{\partial A_L} \frac{\partial \mathcal{A}_L(\mathcal{S}_L)}{\partial \mathcal{S}_L}, \\ \frac{\partial \mathcal{V}_{(\hat{Q}, A) \rightarrow \hat{Q}_L}(\hat{Q}^{n+1}, A^{n+1})}{\partial A} \frac{\partial A(\mathcal{S}_L)}{\partial \mathcal{S}_L} &= \sum_{i=1}^{n_{FE}} \frac{\partial \mathcal{V}_{(\hat{Q}, A) \rightarrow \hat{Q}_L}(\hat{Q}^{n+1}, A^{n+1})}{\partial A_i} \frac{\partial \mathcal{E}_{A_L \rightarrow A_i}(A_L^{n+1})}{\partial A_L} \frac{\partial \mathcal{A}_L(\mathcal{S}_L)}{\partial \mathcal{S}_L}, \end{aligned}$$

being $\mathcal{E}_{A_L \rightarrow \hat{Q}_i}$ and $\mathcal{E}_{A_L \rightarrow A_i}$ the elastic operators that, given the area on the left side of the 1-D segment, return the elastic volumetric flow rate and the area, respectively, at the i -th finite element node, $i = 1, \dots, n_{FE}$. Therefore, the computation of this Jacobian entry requires the solution of the finite element problem and is not as cheap as in the case of flow rate boundary data applied on the interfaces.

Finally, the left mean total normal stress boundary operator is

$$\mathcal{F}_L(\mathcal{S}_L) = \mathcal{S}_L - \frac{1}{2} \rho_F \alpha_F \frac{\mathcal{Q}_L^2(\mathcal{S}_L)}{\mathcal{A}_L^2(\mathcal{S}_L)},$$

thus the analytical expression of the mean total normal stress Jacobian entries becomes

$$\frac{\partial \mathcal{T}_L(S_L)}{\partial S_L} = 1 - \rho_F \alpha_F \left(\frac{\mathcal{Q}_L(S_L)}{\mathcal{A}_L^2(S_L)} \frac{\partial \mathcal{Q}_L(S_L)}{\partial S_L} - \frac{\mathcal{Q}_L^2(S_L)}{\mathcal{A}_L^3(S_L)} \frac{\partial \mathcal{A}_L(S_L)}{\partial S_L} \right).$$

The contribution on the right side is equivalently defined.

3.2.2.2 Two-level time step technique

In Chapter 1 we briefly discussed the limitation imposed on the time step by the stability condition (1.20). This limitation is particularly severe when dealing with large networks of elements and, in particular, for the coupling of 1-D FSI models with computationally expensive 3-D FSI ones. In fact, to perform the nonlinear Richardson iterations on the global coupled problem, all the elements in the network must use the same time step; hence the element that requires the smallest time step forces the entire system to advance the computations at its own time step (including all the connected 3-D FSI problems). For instance, when solving the blood flow in an arterial network, the time step required for the solution of the 1-D FSI segments in the circle of Willis may be around two orders of magnitude smaller than the one needed by a 3-D FSI vessel embedded in the arterial tree.

To satisfy condition (1.20) in each 1-D FSI model without imposing a global limitation on the time discretization of the other models, we devise a two-level time step technique: the inner time step meets the local 1-D stability requirements, being different for each 1-D FSI model; the outer time step is used for the global coupling between the models, i.e., the sets of interface equations devised in Chapter 2 are satisfied just at this outer level. This allows to choose the outer global time step according to the requirements of the 3-D FSI problems in the network. In addition, in a full network of 1-D problems, it can be used to relax the coupling among the subproblems to reduce the computational cost.

Despite its simplicity, the two-level time step technique introduces a couple of issues related to the solution of the inner time steps and to the computation of the Jacobian entries. Both these problems are addressed in the following paragraphs.

Inner time step interpolation In the two-level time step approach the interface equations are satisfied at the outer time level. A possible way to provide the boundary conditions at the inner, and finer, time level for the 1-D FSI problems is to use interpolation. In particular, in this work we use Lagrange polynomial interpolation, whose order can be tuned to improve the final result (see Figure 3.3).

In general, in presence of large ratios between global and local time steps, it is expected that a linear interpolation polynomial is able to capture well long wavelengths (typical of the arterial tree). However, for short wavelengths, an inaccurate approximation of the shape of the wave during the inner time steps can generate some spurious numerical reflections at the coupling interfaces. This is due to the fact that the sets of interface equations devised in Chapter 2 are satisfied just for the outer global time steps. An alternative is either to reduce the outer time step (i.e., reduce the ratio with respect to the inner time step) or to use higher order interpolation polynomials, as described with a schematic example in Figure 3.3. Further discussions and analysis about the numerical reflections are postponed to Chapter 4.

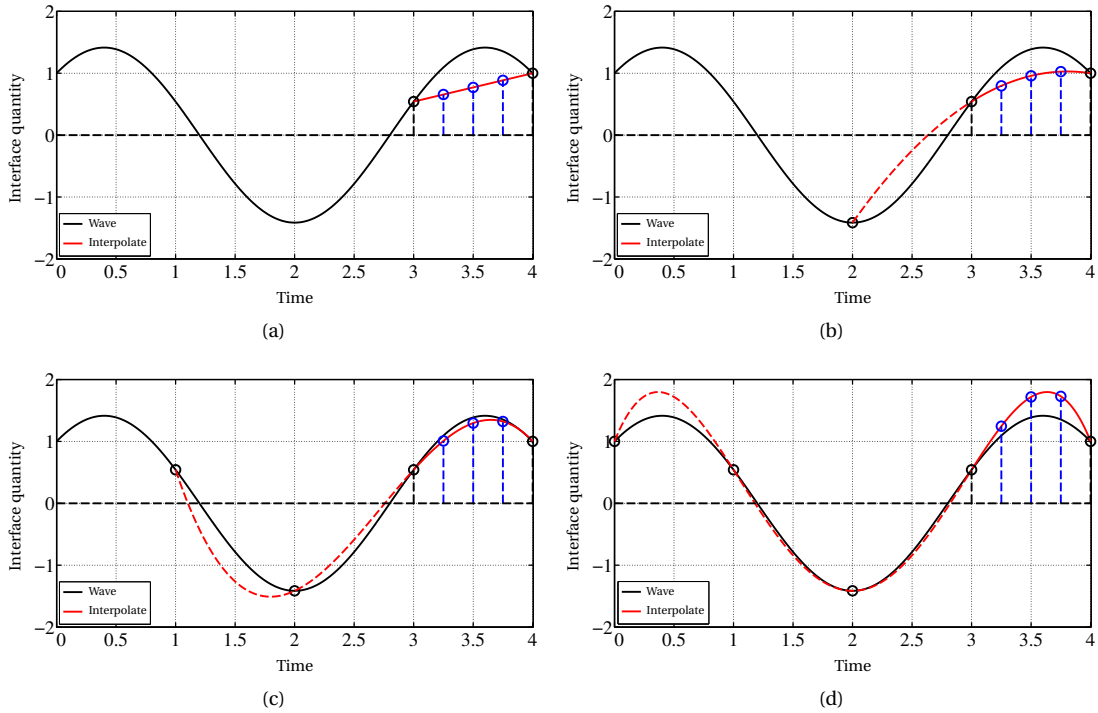


Figure 3.3: Two-level time step technique interpolation example: four local inner time steps (vertical dashed blue lines; 0.25 time units) are performed inside the global outer time step (vertical dashed black lines; 1.0 time unit). The blue circles represent the boundary conditions imposed on the 1-D segment at each inner time step. (a) The linear interpolation does not capture the shape of the short wavelength. (b) The quadratic interpolation improves the results compared to the linear case. (c) The cubic interpolation almost capture the true shape of the wave. (d) Increasing too much the order of the interpolation may be counter-productive, as in this case for the quartic interpolation.

Jacobian entries approximation The presence of inner time steps in the 1-D FSI model introduces additional difficulties in the calculation of the Jacobian entries. The finite difference approximation described at the beginning of Section 3.2 is still valid, since the local inner time steps are hidden behind the boundary operators. In contrast, the analytical formulation of the tangent problem derived in Section 3.2.2.1 does not hold anymore, since it does not keep into account the recursion of the problem at each inner time step.

The derivation of the analytical form of the tangent problem in presence of the two-level time step technique is complex and computationally expensive. In our approach we use an approximated version of the tangent problem by neglecting all the recursions present in the formulation, assuming a single global time step for the approximation of the Jacobian coefficients. This is equivalent to the approach described in Section 3.2.2.1 with a fictitious larger time step.

As we will show in Chapter 4, both the finite difference approach and the approximated tangent lead to convergent inexact-Newton schemes in simple academic cases. However, in more complex and general scenarios, like the one presented in Chapter 5, the latter approach might not converge for large outer time steps.

Alternative methods Other strategies can be followed to avoid the issues introduced by the two-level time step technique without imposing a restriction on the global time step. A first possibility is to suppress (or reduce) the constraint on the time step resulting from the von Neumann stability analysis (see condition (1.20)), by integrating the 1-D FSI equations implicitly. This has been done, for instance, in Blanco et al. (2007) and Reymond et al. (2009). The main drawback of this approach is the increased computational cost for the solution of the 1-D FSI problem, which however is still negligible when compared to the one of a 3-D FSI model.

Another possibility is to use algorithms similar to those developed for heterogeneous multiscale problems, where the macro and micro scales require different time steps. For instance, in Abdulle et al. (2012, Figure 3.1) the authors propose an approach where two heterogeneous models advance with their own time step; the data between the different time scales is exchanged through a couple of ad-hoc operators, namely reconstruction and compression. In a similar way, the 1-D and 3-D FSI model might be seen as the micro and macro scale models, respectively, where the reconstruction and compression operators entail the interface equations between the dimensionally-heterogeneous problems.

Despite the fact that both these alternatives solve a priori the problem of the possible generation of spurious numerical reflections at the boundary interfaces, they might still require an additional effort for the computation of the exact Jacobian entries. In addition, in Chapter 4 we show that the two-level time step technique performs effectively for cardiovascular problems, thus representing a valid solution to the considered problem.

Main references of the chapter:

- ☆ A. C. I. Malossi, P. J. Blanco, S. Deparis, and A. Quarteroni. Algorithms for the partitioned solution of weakly coupled fluid models for cardiovascular flows. *Int. J. Num. Meth. Biomed. Engng.*, 27(12):2035–2057, 2011.
- ☆ A. C. I. Malossi, P. J. Blanco, and S. Deparis. A two-level time step technique for the partitioned solution of one-dimensional arterial networks. *Comp. Meth. Appl. Mech. Engrg.*, 237–240:212–226, 2012.
- ☆ A. C. I. Malossi, P. J. Blanco, P. Crosetto, S. Deparis, and A. Quarteroni. Implicit coupling of one-dimensional and three-dimensional blood flow models with compliant vessels. Submitted, 2012.
- ☆ P. J. Blanco, S. Deparis, and A. C. I. Malossi. On the continuity of mean total normal stress in geometrical multiscale cardiovascular problems. In preparation, 2012.

Examples and cardiovascular simulations

Part II

4 Benchmark examples

In this chapter we set up several benchmark cases to test and, somehow, validate the methodology devised in Part I. More precisely, the aim is to use simple examples to study critical aspects of the interface problem, such as the entity of the numerical spurious reflections at the coupling interfaces or the number of iterations required to achieve the convergence in the network.

The layout of the chapter is the following: in Section 4.1 we present a 3-D steady Stokes benchmark case, with the aim to test the proposed methodology in a simple closed loop problem and, at the same time, to provide more details about the solution of the interface problem writing the exact expression of the residual form and the Jacobian matrix for different configurations. Then, in Section 4.2 we address the partitioned solution of a Womersley fluid flow in a 3-D cylindrical domain. This example serves to study the effect of the approximation introduced by the averaged/integrated interface quantities on a 3-D boundary interface orthogonal to the flow. Finally, the last two sections are mainly focused on the study of the numerical reflections at the boundary interfaces in different configurations. More precisely, in Section 4.3 we analyze the effect of the ratio between the number of inner and the outer time steps, introduced by the two-level time step technique described in Chapter 3, on a simple network of two 1-D pipes. Then, in Section 4.4 we address the case of the coupling of two heterogeneous FSI pipes, comparing the reflection amplitude as a function of the main parameters of the problem and of the different set of interface equations described in Chapter 2.

4.1 Seven 3-D rigid wall pipes in a steady Stokes regime

The first example we propose is a dimensionless 3-D rigid wall steady Stokes problem, whose domain consists in a set of seven cylinders connected by four coupling interfaces, as shown in Figure 4.1a. All the cylinders have the same geometrical dimensions (diameter 0.16; length 0.4). A unitary flow rate is imposed on the inflow on the leftmost side, while a homogeneous Neumann boundary condition is applied on the rightmost outflow. The value of the fluid physical quantities is chosen in order to obtain a global pressure drop of 100000 along the network; more precisely, $\rho_F = 1.0$ and $\mu_F = 0.100531$. The resulting velocity magnitude and flow distribution is shown in Figure 4.1b. Note that the computed flow rate is exact up to the imposed tolerance for the Stokes solver. Regarding the pressure field and the stress boundary quantities, the solution changes as a function of the chosen set of interface equations, as shown in Figure 4.2 and Table 4.1, respectively. The convergence of the boundary pressure with respect to the mesh size is shown in Figure 4.3. We remark that the Aitken method (see Section 2.4.1) does not converge because of the complex pattern of the network, while the Newton method converges in one iteration in both cases, since the fluid flow problem defined inside each pipe is linear.

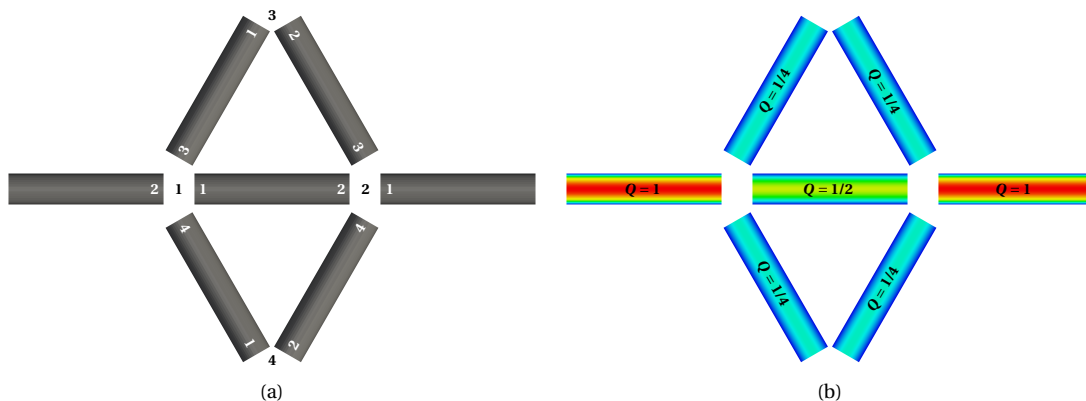


Figure 4.1: Configuration and velocity magnitude of seven 3-D rigid wall pipes in a steady Stokes regime. (a) Nodes and interfaces numeration: black and white numbers indicate the coupling nodes and the local numeration of the boundary interfaces, respectively. (b) Velocity magnitude: the color bar ranges from blue (0) to red (400).

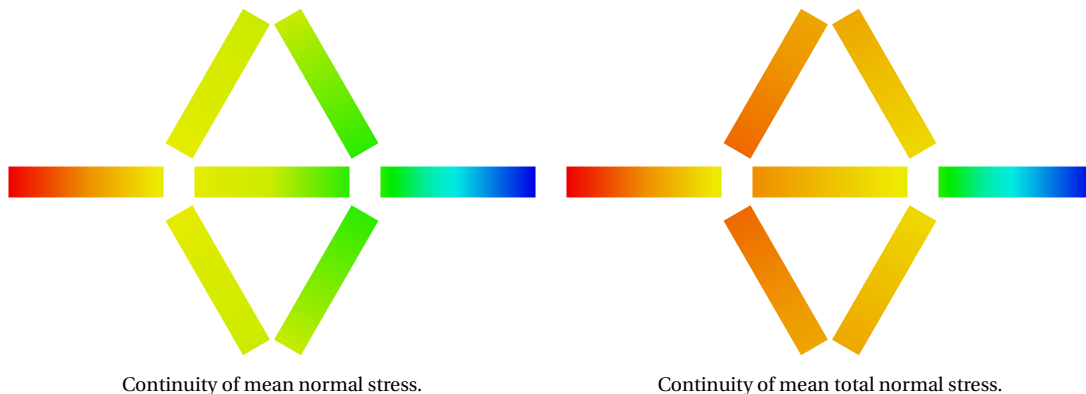


Figure 4.2: Pressure field of seven 3-D rigid wall pipes in a steady Stokes regime, as a function of the chosen set of interface equations. The color bar ranges from blue (0) to red (100000). Note that in the case of continuity of the mean total normal stress the pressure is not continuous.

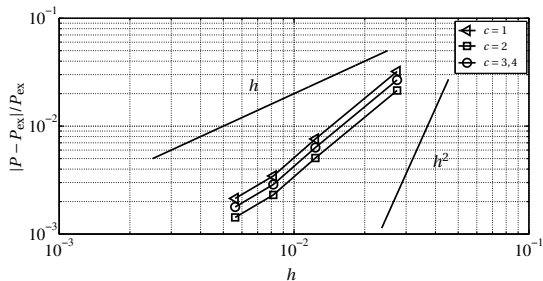


Figure 4.3: Normalized boundary pressure error at the four coupling nodes of the example in Figure 4.1a; P_{ex} is the exact solution. The two sets of interface equations (continuity of mean normal stress and continuity of mean total normal stress) lead to very similar results.

4.1. Seven 3-D rigid wall pipes in a steady Stokes regime

Table 4.1: Coupling stress and coupling total stress at the coupling interfaces of the of seven 3-D rigid wall pipes in a steady Stokes regime.

c	i	$c \in \mathcal{L}^S$		$c \in \mathcal{L}^T$	
		$\mathcal{S}_{c,i}$	$\mathcal{T}_{c,i}$	$\mathcal{S}_{c,i}$	$\mathcal{T}_{c,i}$
1	1	-60759.84	-67554.20	-81142.62	-87937.01
1	2	-60759.84	-87937.01	-60759.84	-87937.01
1	3	-60759.84	-62458.42	-86238.39	-87937.01
1	4	-60759.84	-62458.42	-86238.39	-87937.01
2	1	-40506.39	-67684.14	-40506.39	-67684.14
2	2	-40506.39	-47300.71	-60889.90	-67684.14
2	3	-40506.39	-42205.22	-65985.52	-67684.14
2	4	-40506.39	-42205.22	-65985.52	-67684.14
3	1	-50633.21	-52331.78	-76111.96	-77810.54
3	2	-50633.21	-52331.78	-76111.96	-77810.54
4	1	-50633.21	-52331.78	-76111.96	-77810.54
4	2	-50633.21	-52331.78	-76111.96	-77810.54

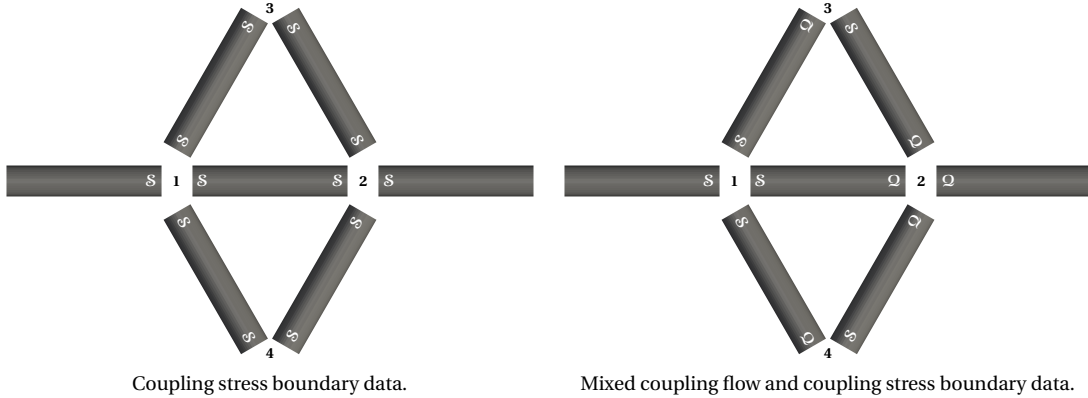


Figure 4.4: Coupling quantities benchmark configurations.

We make use of this simple benchmark example to provide more details about the solution of the interface problem addressing both the continuity of the mean normal stress and the continuity of the mean total normal stress cases. In particular, we consider the two configurations described in Figure 4.4: on the left, stress boundary data are applied on all the interfaces, such that $n_c^Q = 0$, $c = 1, \dots, 4$; on the right, $n_1^Q = 0$ and $n_c^Q > 0$, $c = 2, \dots, 4$. For both configurations we provide the detailed expression of the unknowns and residuals vectors, as well as that of the exact Jacobian matrix needed by the Newton method. Note that, as remarked in Chapter 2, the solution of the problem is the same independently of the value of n_c^Q , $c = 1, \dots, C$. However, in presence of rigid wall models, the imposition of flow rate boundary data on all the interfaces of the same model must be avoided, otherwise the well-posedness of the subproblems can be compromised. For this reason, in the second configuration we choose the interface quantities such that at least one side of each pipe takes a Neumann boundary condition.

4.1.1 Interface problem: continuity of mean normal stress

The first case we address is the set up of the interface problem in the case $c \in \mathcal{L}^S$, $c = 1, \dots, 4$, i.e., continuity of mean normal stress imposed at all the coupling interfaces. The unknowns and residuals vectors of the first configuration (see Figure 4.4a) are

$$\chi_{\mathcal{G}} = \begin{pmatrix} \mathcal{S}_1 \\ \mathcal{S}_2 \\ \mathcal{S}_3 \\ \mathcal{S}_4 \end{pmatrix}, \quad \mathcal{R}_{\mathcal{G}}(\chi_{\mathcal{G}}) = \begin{pmatrix} \frac{\mathcal{Q}_{1,1}(\mathcal{S}_1, \mathcal{S}_2) + \mathcal{Q}_{1,2}(\mathcal{S}_1) + \mathcal{Q}_{1,3}(\mathcal{S}_1, \mathcal{S}_3) + \mathcal{Q}_{1,4}(\mathcal{S}_1, \mathcal{S}_4)}{\mathcal{Q}_{2,1}(\mathcal{S}_2) + \mathcal{Q}_{2,2}(\mathcal{S}_1, \mathcal{S}_2) + \mathcal{Q}_{2,3}(\mathcal{S}_2, \mathcal{S}_3) + \mathcal{Q}_{2,4}(\mathcal{S}_2, \mathcal{S}_4)} \\ \frac{\mathcal{Q}_{3,1}(\mathcal{S}_1, \mathcal{S}_3) + \mathcal{Q}_{3,2}(\mathcal{S}_2, \mathcal{S}_3)}{\mathcal{Q}_{4,1}(\mathcal{S}_1, \mathcal{S}_4) + \mathcal{Q}_{4,2}(\mathcal{S}_2, \mathcal{S}_4)} \end{pmatrix},$$

where we remark that the size of the vectors is four, since $n_c^Q = 0$, $c = 1, \dots, 4$.

The associated Jacobian matrix is

$$\mathcal{J}_{\mathcal{G}} = \begin{bmatrix} \sum_{i=1}^4 \frac{\partial \mathcal{Q}_{1,i}}{\partial \mathcal{S}_1} & \frac{\partial \mathcal{Q}_{1,1}}{\partial \mathcal{S}_2} & \frac{\partial \mathcal{Q}_{1,3}}{\partial \mathcal{S}_3} & \frac{\partial \mathcal{Q}_{1,4}}{\partial \mathcal{S}_4} \\ \frac{\partial \mathcal{Q}_{2,2}}{\partial \mathcal{S}_1} & \sum_{i=1}^4 \frac{\partial \mathcal{Q}_{2,i}}{\partial \mathcal{S}_2} & \frac{\partial \mathcal{Q}_{2,3}}{\partial \mathcal{S}_3} & \frac{\partial \mathcal{Q}_{2,4}}{\partial \mathcal{S}_4} \\ \frac{\partial \mathcal{Q}_{3,1}}{\partial \mathcal{S}_1} & \frac{\partial \mathcal{Q}_{3,2}}{\partial \mathcal{S}_2} & \sum_{i=1}^2 \frac{\partial \mathcal{Q}_{3,i}}{\partial \mathcal{S}_3} & 0 \\ \frac{\partial \mathcal{Q}_{4,1}}{\partial \mathcal{S}_1} & \frac{\partial \mathcal{Q}_{4,2}}{\partial \mathcal{S}_2} & 0 & \sum_{i=1}^2 \frac{\partial \mathcal{Q}_{4,i}}{\partial \mathcal{S}_4} \end{bmatrix}.$$

Note the presence of only one type of entry, namely the partial derivative of the flow rate boundary operator with respect to the coupling stress boundary data. By using an optimal algorithm for the computation of the Jacobian entries (see end of Section 3.2.1.1), we need twelve evaluations of problem (3.2) to fill the Jacobian matrix, each one corresponding to the perturbation of one boundary interface of the global problem. Indeed, in a general geometrical multiscale problem, at each Newton iteration we need to perform $\sum_{c=1}^C \mathcal{J}_c$ evaluations of the tangent problem to update $\chi_{\mathcal{G}}$, plus \mathcal{M} evaluations of the real problem to evaluate the new residual $\mathcal{R}_{\mathcal{G}}$. These operations can be done completely in parallel, as detailed in Chapter 2.

4.1. Seven 3-D rigid wall pipes in a steady Stokes regime

When considering the second configuration (see Figure 4.4b), both coupling stress and coupling flow boundary data are used in the network. The resulting unknowns and residuals vectors are

$$\boldsymbol{\chi}_{\mathcal{G}} = \begin{pmatrix} \mathcal{S}_1 \\ \mathcal{Q}_{2,1} \\ \mathcal{Q}_{2,2} \\ \mathcal{Q}_{2,3} \\ \mathcal{Q}_{2,4} \\ \mathcal{S}_2 \\ \mathcal{Q}_{3,1} \\ \mathcal{S}_3 \\ \mathcal{Q}_{4,1} \\ \mathcal{S}_4 \end{pmatrix}, \quad \mathcal{R}_{\mathcal{G}}(\boldsymbol{\chi}_{\mathcal{G}}) = \begin{pmatrix} \mathcal{Q}_{2,1}(\mathcal{S}_1, \mathcal{Q}_{2,2}) + \mathcal{Q}_{2,2}(\mathcal{S}_1) + \mathcal{Q}_{2,3}(\mathcal{S}_1, \mathcal{Q}_{3,1}) + \mathcal{Q}_{2,4}(\mathcal{S}_1, \mathcal{Q}_{4,1}) \\ \mathcal{Q}_{2,1} + \mathcal{Q}_{2,2} + \mathcal{Q}_{2,3} + \mathcal{Q}_{2,4} \\ \mathcal{S}_{2,1}(\mathcal{Q}_{2,1}) - \mathcal{S}_2 \\ \mathcal{S}_{2,2}(\mathcal{S}_1, \mathcal{Q}_{2,2}) - \mathcal{S}_2 \\ \mathcal{S}_{2,3}(\mathcal{Q}_{2,3}, \mathcal{S}_3) - \mathcal{S}_2 \\ \mathcal{S}_{2,4}(\mathcal{Q}_{2,4}, \mathcal{S}_4) - \mathcal{S}_2 \\ \mathcal{Q}_{3,1} + \mathcal{Q}_{3,2}(\mathcal{Q}_{2,3}, \mathcal{S}_3) \\ \mathcal{S}_{3,1}(\mathcal{S}_1, \mathcal{Q}_{3,1}) - \mathcal{S}_3 \\ \mathcal{Q}_{4,1} + \mathcal{Q}_{4,2}(\mathcal{Q}_{2,4}, \mathcal{S}_4) \\ \mathcal{S}_{4,1}(\mathcal{S}_1, \mathcal{Q}_{4,1}) - \mathcal{S}_4 \end{pmatrix}.$$

The size of the problem is increased to ten since $n_1^{\mathcal{Q}} = 0$, $n_2^{\mathcal{Q}} = 4$, $n_3^{\mathcal{Q}} = 1$, and $n_4^{\mathcal{Q}} = 1$.

The associated Jacobian matrix is

$$\mathcal{J}_{\mathcal{G}} = \begin{pmatrix} \sum_{i=1}^4 \frac{\partial \mathcal{Q}_{1,i}}{\partial \mathcal{S}_1} & 0 & \frac{\partial \mathcal{Q}_{1,1}}{\partial \mathcal{Q}_{2,2}} & 0 & 0 & 0 & \frac{\partial \mathcal{Q}_{1,3}}{\partial \mathcal{Q}_{3,1}} & 0 & \frac{\partial \mathcal{Q}_{1,4}}{\partial \mathcal{Q}_{4,1}} & 0 \\ 0 & 1 & 1 & 1 & 1 & 0 & 0 & 0 & 0 & 0 \\ 0 & \frac{\partial \mathcal{S}_{2,1}}{\partial \mathcal{Q}_{2,1}} & 0 & 0 & 0 & -1 & 0 & 0 & 0 & 0 \\ \frac{\partial \mathcal{S}_{2,2}}{\partial \mathcal{S}_1} & 0 & \frac{\partial \mathcal{S}_{2,2}}{\partial \mathcal{Q}_{2,2}} & 0 & 0 & -1 & 0 & 0 & 0 & 0 \\ 0 & 0 & 0 & \frac{\partial \mathcal{S}_{2,3}}{\partial \mathcal{Q}_{2,3}} & 0 & -1 & 0 & \frac{\partial \mathcal{S}_{2,3}}{\partial \mathcal{S}_3} & 0 & 0 \\ 0 & 0 & 0 & 0 & \frac{\partial \mathcal{S}_{2,4}}{\partial \mathcal{Q}_{2,4}} & -1 & 0 & 0 & 0 & \frac{\partial \mathcal{S}_{2,4}}{\partial \mathcal{S}_4} \\ 0 & 0 & 0 & \frac{\partial \mathcal{Q}_{3,2}}{\partial \mathcal{Q}_{2,3}} & 0 & 0 & 1 & \frac{\partial \mathcal{Q}_{3,2}}{\partial \mathcal{S}_3} & 0 & 0 \\ \frac{\partial \mathcal{S}_{3,1}}{\partial \mathcal{S}_1} & 0 & 0 & 0 & 0 & 0 & \frac{\partial \mathcal{S}_{3,1}}{\partial \mathcal{Q}_{3,1}} & -1 & 0 & 0 \\ 0 & 0 & 0 & 0 & \frac{\partial \mathcal{Q}_{4,2}}{\partial \mathcal{Q}_{2,4}} & 0 & 0 & 0 & 1 & \frac{\partial \mathcal{Q}_{4,2}}{\partial \mathcal{S}_4} \\ \frac{\partial \mathcal{S}_{4,1}}{\partial \mathcal{S}_1} & 0 & 0 & 0 & 0 & 0 & 0 & 0 & \frac{\partial \mathcal{S}_{4,1}}{\partial \mathcal{Q}_{3,1}} & -1 \end{pmatrix}.$$

Independently from the new size of the interface problem, the Jacobian matrix is still filled by the same twelve evaluations of problem (3.2), as in the first configuration. Indeed, the number of non-constant entries is twenty-two as before. Nevertheless, this time we have four different types of entries, corresponding to the partial derivatives of the flow rate and mean normal stress boundary operators with respect to the coupling flow and to the coupling stress boundary data.

4.1.2 Interface problem: continuity of mean total normal stress

We consider now the set up of the interface problem in the case $c \in \mathcal{L}^{\mathcal{T}}$, $c = 1, \dots, 4$, i.e., continuity of mean total normal stress imposed at all the coupling interfaces. The unknowns and residuals vectors of the first configuration (see Figure 4.4a) are

$$\chi_g = \begin{pmatrix} \mathcal{S}_{1,1} \\ \mathcal{S}_{1,2} \\ \mathcal{S}_{1,3} \\ \mathcal{S}_{1,4} \\ \mathcal{T}_1 \\ \hline \mathcal{S}_{2,1} \\ \mathcal{S}_{2,2} \\ \mathcal{S}_{2,3} \\ \mathcal{S}_{2,4} \\ \mathcal{T}_2 \\ \hline \mathcal{S}_{3,1} \\ \mathcal{S}_{3,2} \\ \mathcal{T}_3 \\ \hline \mathcal{S}_{4,1} \\ \mathcal{S}_{4,2} \\ \mathcal{T}_4 \end{pmatrix}, \quad \mathcal{R}_g(\chi_g) = \begin{pmatrix} \mathcal{Q}_{1,1}(\mathcal{S}_{1,1}, \mathcal{S}_{2,2}) + \mathcal{Q}_{1,2}(\mathcal{S}_{1,2}) + \mathcal{Q}_{1,3}(\mathcal{S}_{1,3}, \mathcal{S}_{3,1}) + \mathcal{Q}_{1,4}(\mathcal{S}_{1,4}, \mathcal{S}_{4,1}) \\ \mathcal{T}_{1,1}(\mathcal{S}_{1,1}, \mathcal{S}_{2,2}) - \mathcal{T}_1 \\ \mathcal{T}_{1,2}(\mathcal{S}_{1,2}) - \mathcal{T}_1 \\ \mathcal{T}_{1,3}(\mathcal{S}_{1,3}, \mathcal{S}_{3,1}) - \mathcal{T}_1 \\ \mathcal{T}_{1,4}(\mathcal{S}_{1,4}, \mathcal{S}_{4,1}) - \mathcal{T}_1 \\ \hline \mathcal{Q}_{2,1}(\mathcal{S}_{2,1}) + \mathcal{Q}_{2,2}(\mathcal{S}_{1,1}, \mathcal{S}_{2,2}) + \mathcal{Q}_{2,3}(\mathcal{S}_{2,3}, \mathcal{S}_{3,2}) + \mathcal{Q}_{2,4}(\mathcal{S}_{2,4}, \mathcal{S}_{4,2}) \\ \mathcal{T}_{2,1}(\mathcal{S}_{2,1}) - \mathcal{T}_2 \\ \mathcal{T}_{2,2}(\mathcal{S}_{1,1}, \mathcal{S}_{2,2}) - \mathcal{T}_2 \\ \mathcal{T}_{2,3}(\mathcal{S}_{2,3}, \mathcal{S}_{3,2}) - \mathcal{T}_2 \\ \mathcal{T}_{2,4}(\mathcal{S}_{2,4}, \mathcal{S}_{4,2}) - \mathcal{T}_2 \\ \hline \mathcal{Q}_{3,1}(\mathcal{S}_{1,3}, \mathcal{S}_{3,1}) + \mathcal{Q}_{3,2}(\mathcal{S}_{2,3}, \mathcal{S}_{3,2}) \\ \mathcal{T}_{3,1}(\mathcal{S}_{1,3}, \mathcal{S}_{3,1}) - \mathcal{T}_3 \\ \mathcal{T}_{3,2}(\mathcal{S}_{2,3}, \mathcal{S}_{3,2}) - \mathcal{T}_3 \\ \hline \mathcal{Q}_{4,1}(\mathcal{S}_{1,4}, \mathcal{S}_{4,1}) + \mathcal{Q}_{4,2}(\mathcal{S}_{2,4}, \mathcal{S}_{4,2}) \\ \mathcal{T}_{4,1}(\mathcal{S}_{1,4}, \mathcal{S}_{4,1}) - \mathcal{T}_4 \\ \mathcal{T}_{4,2}(\mathcal{S}_{2,4}, \mathcal{S}_{4,2}) - \mathcal{T}_4 \end{pmatrix},$$

where we remark that the size of the vector is sixteen.

4.1. Seven 3-D rigid wall pipes in a steady Stokes regime

The associated Jacobian matrix is

$$\mathcal{J}_g = \begin{bmatrix}
 \frac{\partial \mathcal{Q}_{1,1}}{\partial \mathcal{S}_{1,1}} & \frac{\partial \mathcal{Q}_{1,2}}{\partial \mathcal{S}_{1,2}} & \frac{\partial \mathcal{Q}_{1,3}}{\partial \mathcal{S}_{1,3}} & \frac{\partial \mathcal{Q}_{1,4}}{\partial \mathcal{S}_{1,4}} & 0 & 0 & \frac{\partial \mathcal{Q}_{1,1}}{\partial \mathcal{S}_{2,2}} & 0 & 0 & 0 & \frac{\partial \mathcal{Q}_{1,3}}{\partial \mathcal{S}_{3,1}} & 0 & 0 & \frac{\partial \mathcal{Q}_{1,4}}{\partial \mathcal{S}_{4,1}} & 0 & 0 \\
 \frac{\partial \mathcal{T}_{1,1}}{\partial \mathcal{S}_{1,1}} & 0 & 0 & 0 & -1 & 0 & \frac{\partial \mathcal{T}_{1,1}}{\partial \mathcal{S}_{2,2}} & 0 & 0 & 0 & 0 & 0 & 0 & 0 & 0 & 0 \\
 0 & \frac{\partial \mathcal{T}_{1,2}}{\partial \mathcal{S}_{1,2}} & 0 & 0 & -1 & 0 & 0 & 0 & 0 & 0 & 0 & 0 & 0 & 0 & 0 & 0 \\
 0 & 0 & \frac{\partial \mathcal{T}_{1,3}}{\partial \mathcal{S}_{1,3}} & 0 & -1 & 0 & 0 & 0 & 0 & 0 & \frac{\partial \mathcal{T}_{1,3}}{\partial \mathcal{S}_{3,1}} & 0 & 0 & 0 & 0 & 0 \\
 0 & 0 & 0 & \frac{\partial \mathcal{T}_{1,4}}{\partial \mathcal{S}_{1,4}} & -1 & 0 & 0 & 0 & 0 & 0 & 0 & 0 & 0 & \frac{\partial \mathcal{T}_{1,4}}{\partial \mathcal{S}_{4,1}} & 0 & 0 \\
 \hline
 \frac{\partial \mathcal{Q}_{2,2}}{\partial \mathcal{S}_{1,1}} & 0 & 0 & 0 & 0 & \frac{\partial \mathcal{Q}_{2,1}}{\partial \mathcal{S}_{2,1}} & \frac{\partial \mathcal{Q}_{2,2}}{\partial \mathcal{S}_{2,2}} & \frac{\partial \mathcal{Q}_{2,3}}{\partial \mathcal{S}_{2,3}} & \frac{\partial \mathcal{Q}_{2,4}}{\partial \mathcal{S}_{2,4}} & 0 & 0 & \frac{\partial \mathcal{Q}_{2,3}}{\partial \mathcal{S}_{3,2}} & 0 & 0 & \frac{\partial \mathcal{Q}_{2,4}}{\partial \mathcal{S}_{4,2}} & 0 \\
 0 & 0 & 0 & 0 & 0 & \frac{\partial \mathcal{T}_{2,1}}{\partial \mathcal{S}_{2,1}} & 0 & 0 & 0 & -1 & 0 & 0 & 0 & 0 & 0 & 0 \\
 \frac{\partial \mathcal{T}_{2,2}}{\partial \mathcal{S}_{1,1}} & 0 & 0 & 0 & 0 & 0 & \frac{\partial \mathcal{T}_{2,2}}{\partial \mathcal{S}_{2,2}} & 0 & 0 & -1 & 0 & 0 & 0 & 0 & 0 & 0 \\
 0 & 0 & 0 & 0 & 0 & 0 & 0 & \frac{\partial \mathcal{T}_{2,3}}{\partial \mathcal{S}_{2,3}} & 0 & -1 & 0 & \frac{\partial \mathcal{T}_{2,3}}{\partial \mathcal{S}_{3,2}} & 0 & 0 & 0 & 0 \\
 0 & 0 & 0 & 0 & 0 & 0 & 0 & 0 & \frac{\partial \mathcal{T}_{2,4}}{\partial \mathcal{S}_{2,4}} & -1 & 0 & 0 & 0 & 0 & \frac{\partial \mathcal{T}_{2,4}}{\partial \mathcal{S}_{4,2}} & 0 \\
 \hline
 0 & 0 & \frac{\partial \mathcal{Q}_{3,1}}{\partial \mathcal{S}_{1,3}} & 0 & 0 & 0 & 0 & \frac{\partial \mathcal{Q}_{3,2}}{\partial \mathcal{S}_{2,3}} & 0 & 0 & \frac{\partial \mathcal{Q}_{3,1}}{\partial \mathcal{S}_{3,1}} & \frac{\partial \mathcal{Q}_{3,2}}{\partial \mathcal{S}_{3,2}} & 0 & 0 & 0 & 0 \\
 0 & 0 & \frac{\partial \mathcal{T}_{3,1}}{\partial \mathcal{S}_{1,3}} & 0 & 0 & 0 & 0 & 0 & 0 & 0 & \frac{\partial \mathcal{T}_{3,1}}{\partial \mathcal{S}_{3,1}} & 0 & -1 & 0 & 0 & 0 \\
 0 & 0 & 0 & 0 & 0 & 0 & 0 & \frac{\partial \mathcal{T}_{3,2}}{\partial \mathcal{S}_{2,3}} & 0 & 0 & 0 & \frac{\partial \mathcal{T}_{3,2}}{\partial \mathcal{S}_{3,2}} & -1 & 0 & 0 & 0 \\
 \hline
 0 & 0 & 0 & \frac{\partial \mathcal{Q}_{4,1}}{\partial \mathcal{S}_{1,4}} & 0 & 0 & 0 & 0 & \frac{\partial \mathcal{Q}_{4,2}}{\partial \mathcal{S}_{2,4}} & 0 & 0 & 0 & 0 & \frac{\partial \mathcal{Q}_{4,1}}{\partial \mathcal{S}_{4,1}} & \frac{\partial \mathcal{Q}_{4,2}}{\partial \mathcal{S}_{4,2}} & 0 \\
 0 & 0 & 0 & \frac{\partial \mathcal{T}_{4,1}}{\partial \mathcal{S}_{1,4}} & 0 & 0 & 0 & 0 & 0 & 0 & 0 & 0 & 0 & \frac{\partial \mathcal{T}_{4,1}}{\partial \mathcal{S}_{4,1}} & 0 & -1 \\
 0 & 0 & 0 & 0 & 0 & 0 & 0 & 0 & \frac{\partial \mathcal{T}_{4,2}}{\partial \mathcal{S}_{2,4}} & 0 & 0 & 0 & 0 & 0 & \frac{\partial \mathcal{T}_{4,2}}{\partial \mathcal{S}_{4,2}} & -1
 \end{bmatrix}.$$

We observe the presence of two types of entries: the partial derivatives of the flow rate boundary operator and that of the mean total normal stress boundary operator, both with respect to the coupling stress boundary data. Despite the fact that the number of entries is doubled compared to the previous cases, the Jacobian matrix is still filled by twelve evaluations of problem (3.2). In fact, the additional partial derivatives of the mean total normal stress boundary operator are computed at the same time of the corresponding flow rate boundary operators derivatives; hence, the global computational cost of the problem does not increase.

Chapter 4. Benchmark examples

We consider now the second configuration (see Figure 4.4b), where both coupling stress and coupling flow boundary data are used in the network. The resulting unknowns and residuals vectors are

$$\chi_g = \begin{pmatrix} \mathcal{S}_{1,1} \\ \mathcal{S}_{1,2} \\ \mathcal{S}_{1,3} \\ \mathcal{S}_{1,4} \\ \mathcal{T}_1 \\ \hline \mathcal{Q}_{2,1} \\ \mathcal{Q}_{2,2} \\ \mathcal{Q}_{2,3} \\ \mathcal{Q}_{2,4} \\ \mathcal{T}_2 \\ \hline \mathcal{Q}_{3,1} \\ \mathcal{S}_{3,2} \\ \mathcal{T}_3 \\ \hline \mathcal{Q}_{4,1} \\ \mathcal{S}_{4,2} \\ \mathcal{T}_4 \end{pmatrix}, \quad \mathcal{R}_g(\chi_g) = \begin{pmatrix} \mathcal{Q}_{1,1}(\mathcal{S}_{1,1}, \mathcal{Q}_{2,2}) + \mathcal{Q}_{1,2}(\mathcal{S}_{1,2}) + \mathcal{Q}_{1,3}(\mathcal{S}_{1,3}, \mathcal{Q}_{3,1}) + \mathcal{Q}_{1,4}(\mathcal{S}_{1,4}, \mathcal{Q}_{4,1}) \\ \mathcal{T}_{1,1}(\mathcal{S}_{1,1}, \mathcal{Q}_{2,2}) - \mathcal{T}_1 \\ \mathcal{T}_{1,2}(\mathcal{S}_{1,2}) - \mathcal{T}_1 \\ \mathcal{T}_{1,3}(\mathcal{S}_{1,3}, \mathcal{Q}_{3,1}) - \mathcal{T}_1 \\ \mathcal{T}_{1,4}(\mathcal{S}_{1,4}, \mathcal{Q}_{4,1}) - \mathcal{T}_1 \\ \hline \mathcal{Q}_{2,1} + \mathcal{Q}_{2,2} + \mathcal{Q}_{2,3} + \mathcal{Q}_{2,4} \\ \mathcal{T}_{2,1}(\mathcal{Q}_{2,1}) - \mathcal{T}_2 \\ \mathcal{T}_{2,2}(\mathcal{S}_{1,1}, \mathcal{Q}_{2,2}) - \mathcal{T}_2 \\ \mathcal{T}_{2,3}(\mathcal{Q}_{2,3}, \mathcal{S}_{3,2}) - \mathcal{T}_2 \\ \mathcal{T}_{2,4}(\mathcal{Q}_{2,4}, \mathcal{S}_{4,2}) - \mathcal{T}_2 \\ \hline \mathcal{Q}_{3,1} + \mathcal{Q}_{3,2}(\mathcal{Q}_{2,3}, \mathcal{S}_{3,2}) \\ \mathcal{T}_{3,1}(\mathcal{S}_{1,3}, \mathcal{Q}_{3,1}) - \mathcal{T}_3 \\ \mathcal{T}_{3,2}(\mathcal{Q}_{2,3}, \mathcal{S}_{3,2}) - \mathcal{T}_3 \\ \hline \mathcal{Q}_{4,1} + \mathcal{Q}_{4,2}(\mathcal{Q}_{2,4}, \mathcal{S}_{4,2}) \\ \mathcal{T}_{4,1}(\mathcal{S}_{1,4}, \mathcal{Q}_{4,1}) - \mathcal{T}_4 \\ \mathcal{T}_{4,2}(\mathcal{Q}_{2,4}, \mathcal{S}_{4,2}) - \mathcal{T}_4 \end{pmatrix}.$$

The size of the problem is again sixteen, independently of the different value of n_c^Q , $c = 1, \dots, 4$.

The associated Jacobian matrix is

$$\mathcal{J}_g = \begin{bmatrix}
 \frac{\partial \mathcal{Q}_{1,1}}{\partial \mathcal{S}_{1,1}} & \frac{\partial \mathcal{Q}_{1,2}}{\partial \mathcal{S}_{1,2}} & \frac{\partial \mathcal{Q}_{1,3}}{\partial \mathcal{S}_{1,3}} & \frac{\partial \mathcal{Q}_{1,4}}{\partial \mathcal{S}_{1,4}} & 0 & 0 & \frac{\partial \mathcal{Q}_{1,1}}{\partial \mathcal{Q}_{2,2}} & 0 & 0 & 0 & \frac{\partial \mathcal{Q}_{1,3}}{\partial \mathcal{Q}_{3,1}} & 0 & 0 & \frac{\partial \mathcal{Q}_{1,4}}{\partial \mathcal{Q}_{4,1}} & 0 & 0 \\
 \frac{\partial \mathcal{T}_{1,1}}{\partial \mathcal{S}_{1,1}} & 0 & 0 & 0 & -1 & 0 & \frac{\partial \mathcal{T}_{1,1}}{\partial \mathcal{Q}_{2,2}} & 0 & 0 & 0 & 0 & 0 & 0 & 0 & 0 & 0 \\
 0 & \frac{\partial \mathcal{T}_{1,2}}{\partial \mathcal{S}_{1,2}} & 0 & 0 & -1 & 0 & 0 & 0 & 0 & 0 & 0 & 0 & 0 & 0 & 0 & 0 \\
 0 & 0 & \frac{\partial \mathcal{T}_{1,3}}{\partial \mathcal{S}_{1,3}} & 0 & -1 & 0 & 0 & 0 & 0 & 0 & \frac{\partial \mathcal{T}_{1,3}}{\partial \mathcal{Q}_{3,1}} & 0 & 0 & 0 & 0 & 0 \\
 0 & 0 & 0 & \frac{\partial \mathcal{T}_{1,4}}{\partial \mathcal{S}_{1,4}} & -1 & 0 & 0 & 0 & 0 & 0 & 0 & 0 & 0 & \frac{\partial \mathcal{T}_{1,4}}{\partial \mathcal{Q}_{4,1}} & 0 & 0 \\
 \hline
 0 & 0 & 0 & 0 & 0 & 1 & 1 & 1 & 1 & 0 & 0 & 0 & 0 & 0 & 0 & 0 \\
 0 & 0 & 0 & 0 & 0 & \frac{\partial \mathcal{T}_{2,1}}{\partial \mathcal{Q}_{2,1}} & 0 & 0 & 0 & -1 & 0 & 0 & 0 & 0 & 0 & 0 \\
 \frac{\partial \mathcal{T}_{2,2}}{\partial \mathcal{S}_{1,1}} & 0 & 0 & 0 & 0 & 0 & \frac{\partial \mathcal{T}_{2,2}}{\partial \mathcal{Q}_{2,2}} & 0 & 0 & -1 & 0 & 0 & 0 & 0 & 0 & 0 \\
 0 & 0 & 0 & 0 & 0 & 0 & 0 & \frac{\partial \mathcal{T}_{2,3}}{\partial \mathcal{Q}_{2,3}} & 0 & -1 & 0 & \frac{\partial \mathcal{T}_{2,3}}{\partial \mathcal{S}_{3,2}} & 0 & 0 & 0 & 0 \\
 0 & 0 & 0 & 0 & 0 & 0 & 0 & 0 & \frac{\partial \mathcal{T}_{2,4}}{\partial \mathcal{Q}_{2,4}} & -1 & 0 & 0 & 0 & 0 & \frac{\partial \mathcal{T}_{2,4}}{\partial \mathcal{S}_{4,2}} & 0 \\
 \hline
 0 & 0 & 0 & 0 & 0 & 0 & 0 & \frac{\partial \mathcal{Q}_{3,2}}{\partial \mathcal{Q}_{2,3}} & 0 & 0 & 1 & \frac{\partial \mathcal{Q}_{3,2}}{\partial \mathcal{S}_{3,2}} & 0 & 0 & 0 & 0 \\
 0 & 0 & \frac{\partial \mathcal{T}_{3,1}}{\partial \mathcal{S}_{1,3}} & 0 & 0 & 0 & 0 & 0 & 0 & 0 & \frac{\partial \mathcal{T}_{3,1}}{\partial \mathcal{Q}_{3,1}} & 0 & -1 & 0 & 0 & 0 \\
 0 & 0 & 0 & 0 & 0 & 0 & 0 & \frac{\partial \mathcal{T}_{3,2}}{\partial \mathcal{Q}_{2,3}} & 0 & 0 & 0 & \frac{\partial \mathcal{T}_{3,2}}{\partial \mathcal{S}_{3,2}} & -1 & 0 & 0 & 0 \\
 \hline
 0 & 0 & 0 & 0 & 0 & 0 & 0 & 0 & \frac{\partial \mathcal{Q}_{4,2}}{\partial \mathcal{Q}_{2,4}} & 0 & 0 & 0 & 0 & 1 & \frac{\partial \mathcal{Q}_{4,2}}{\partial \mathcal{S}_{4,2}} & 0 \\
 0 & 0 & 0 & \frac{\partial \mathcal{T}_{4,1}}{\partial \mathcal{S}_{1,4}} & 0 & 0 & 0 & 0 & 0 & 0 & 0 & 0 & 0 & \frac{\partial \mathcal{T}_{4,1}}{\partial \mathcal{Q}_{4,1}} & 0 & -1 \\
 0 & 0 & 0 & 0 & 0 & 0 & 0 & \frac{\partial \mathcal{T}_{4,2}}{\partial \mathcal{Q}_{2,4}} & 0 & 0 & 0 & 0 & 0 & 0 & \frac{\partial \mathcal{T}_{4,2}}{\partial \mathcal{S}_{4,2}} & -1
 \end{bmatrix}.$$

Four types of entries are present in the matrix: the partial derivatives of the flow rate boundary operator and that of the mean total normal stress boundary operator, both with respect to the coupling flow and to the coupling stress boundary data. The total number of Jacobian entries is thirty-three and, as before, require twelve evaluations of problem (3.2).

4.2 Five 3-D rigid wall pipes in a Womersley regime

The second example we propose is the partitioned solution of a Womersley fluid flow (see Womersley (1957)) in a 3-D cylindrical domain. More precisely, we partition the original domain into five pipes of equal size and shape (see Figure 4.5) and discretized by the same unstructured mesh (with $h/D = 0.15415$, where D is the diameter). At the four coupling nodes the set of equations (2.2) is imposed through coupling stress boundary data on all the interfaces (i.e., $n_c^Q = 0$, $c = 1, \dots, 4$). The imposed

Chapter 4. Benchmark examples

tolerance ε for the interface problem (see equation (2.10)) is 10^{-6} . On the leftmost inflow we impose a sinusoidal flow rate $\mathcal{Q}(t) = -A_w \sin(2\pi t/T_w)$, while a homogeneous Neumann boundary condition is applied on the rightmost outflow. The amplitude A_w , the period T_w , and all the dimensionless physical quantities are chosen in order to obtain a Womersley number of 5 and a Reynolds number of 600, which represent typical values in a human carotid. The time step Δt is given by $T_w/256$.

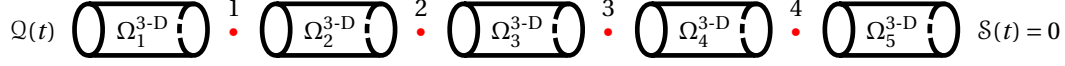


Figure 4.5: Scheme of the serial network made of five rigid wall pipes connected by four coupling nodes.

The interface problem is solved by using the Newton method, which converges in one iteration since the fluid flow problem inside each pipe is linear. More specifically, for this problem each iteration of the Newton method requires eight evaluations of the tangent problem (3.2) to fill the Jacobian matrix, plus five evaluations of the Navier–Stokes problem (1.3) to compute the solution in the 3-D domains and evaluate the residual.

In Figure 4.6, we show a comparison between the magnitude of the computed velocity profiles and the analytical solution at selected times. From these graphs we observe that, despite the approximation introduced at the coupling interfaces, the velocity profiles follow the shape of the exact solution. This confirms that the use of averaged/integrated quantities for the coupling of 3-D models (together with the tangential homogeneous Neumann boundary conditions defined in *Remark 2.4*) is a reasonable approximation if the flow is fully developed and orthogonal to the plane. In the first network described in Chapter 5 we study a case in which the cutting section is placed by a bifurcation, where the hypotheses in *Remark 2.4* are far from being satisfied.

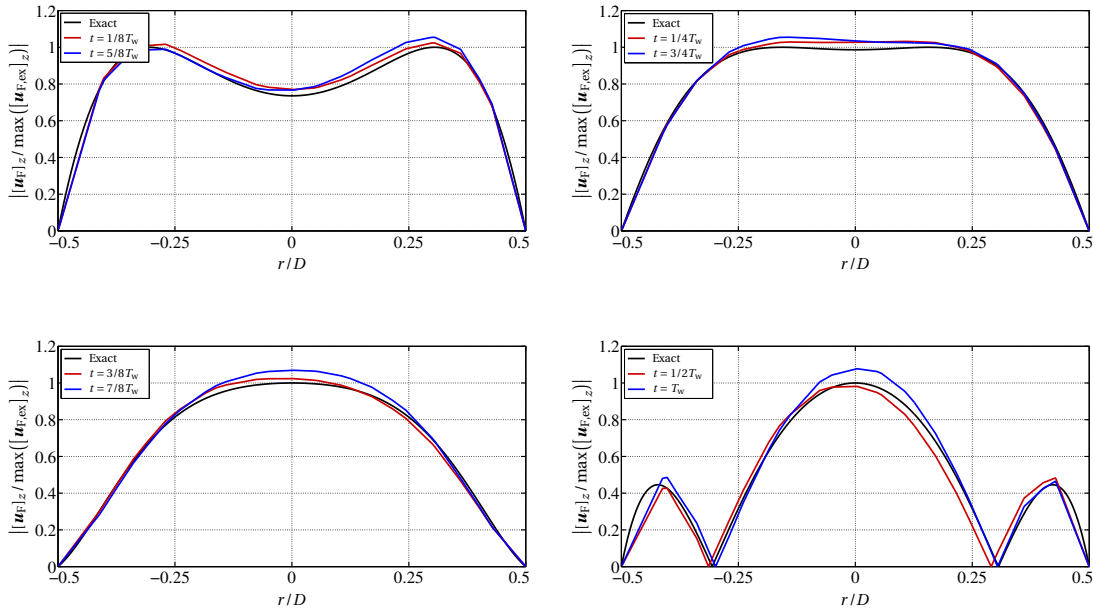


Figure 4.6: Womersley velocity profiles: on the x -axis we show the ratio between the radial coordinate and the diameter, while on the y -axis we display the modulus of the axial velocity, normalized on the maximum value of the exact solution $\|\mathbf{u}_{F,ex}\|_z$.

4.3 Two 1-D FSI pipes

In this section we use simple examples to analyze the behaviour of the two-level time step technique introduced at the end of Chapter 3. To carry out these analyses, we consider the setting described in Figure 4.7, where two 1-D segments are coupled together by imposing the set of equations (2.2) through coupling stress boundary data on both sides (i.e., $n_c^Q = 0$, $c = 1$). The imposed tolerance ε for the interface problem (see equation (2.10)) is 10^{-9} .

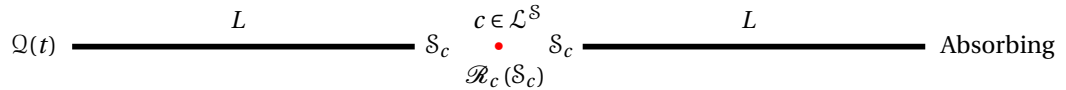


Figure 4.7: Scheme of the serial network made of two 1-D FSI pipes connected by a single coupling node.

On the inflow on the leftmost side we impose a given volumetric flow rate $Q(t)$, while on the rightmost outflow an absorbing boundary condition (see Sherwin et al. (2003)). The dimensionless parameters that define the problem are: $\rho_F = 1$, $\mu_F = 0$ (i.e., $\kappa_F = 0$), $\alpha_F = 1.1$, $P_{\text{ext}} = 0$, $A^0 = \pi$, $h_S = 0.1$, $E_S = 3000000$, $\nu_S = 0.5$ (i.e., $\beta_S = 400000$), and $\gamma_S = 0$. The spatial discretization h is set equal to 0.01, independently of the length L of the elements, which ranges between 3 and 75. In all the simulated cases, the inner time step is fixed to 10^{-6} and the outer time step is chosen accordingly to the desired number of inner time steps to be performed per each outer time step.

Remark 4.1. In this benchmark example, where the two 1-D pipes have the same material properties and geometrical dimensions, the solution of the problem is the same independently of the chosen set of interface equations. Indeed problem (2.2) and (2.5) lead to the same solution, such that the continuity of mean normal stress imply also the continuity of mean total normal stress and vice versa.

4.3.1 Iterations analysis

First of all, we study the sensitivity of the number of iterations required for the solution of the coupled problem with respect to the number of inner time steps, the order of the Lagrange polynomial interpolation, and the applied numerical method. For this analysis we impose a periodic flow rate wave $Q(t) = -\sin(2\pi t/T_w)$, where $T_w = 0.00512$ is the chosen wave period. The length of each 1-D segment is set equal to 3.

The number of nonlinear iterations is shown in Figure 4.8. We can observe that, for the selected example, there is no evident dependence of the average number of iterations on the chosen iterative method. The Broyden method and both versions of the inexact-Newton algorithm behave similarly. In all the three cases, for a small number of inner time steps per outer time step, increasing the order of the Lagrange polynomial decreases the average number of iterations. However, when the number of inner time steps per outer time step is larger than 8, the curves cross each others more than once. Finally, we can observe a slight increase of the average number of iterations with respect to the increase in the ratio between outer and inner time steps. This behavior is mainly due to the approximations introduced in the Jacobian matrix. In particular, the accuracy of the Jacobian entries computed with the three approaches decreases by increasing the ratio between the outer and the inner time steps. However, even in the worse presented case (128 inner time steps per outer time step), the average number of iterations is quite small (between three and four).

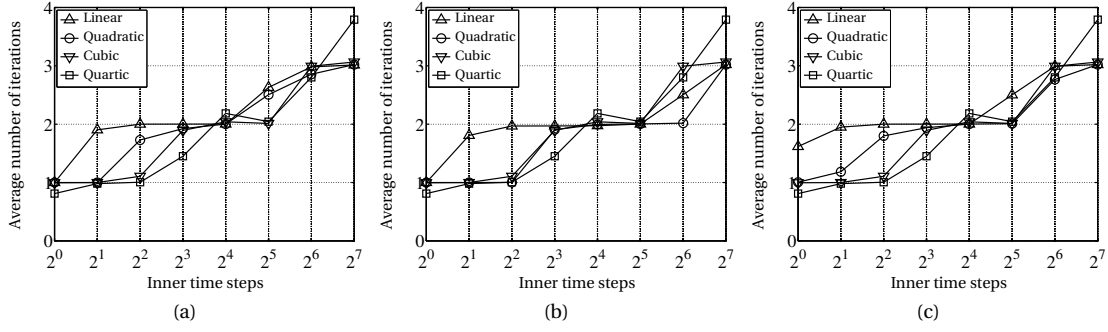


Figure 4.8: Average number of nonlinear Richardson iterations as a function of the number of inner time steps and of the Lagrange interpolation order. (a) Approximated tangent problem formulation. (b) Finite difference approximation. (c) Broyden method.

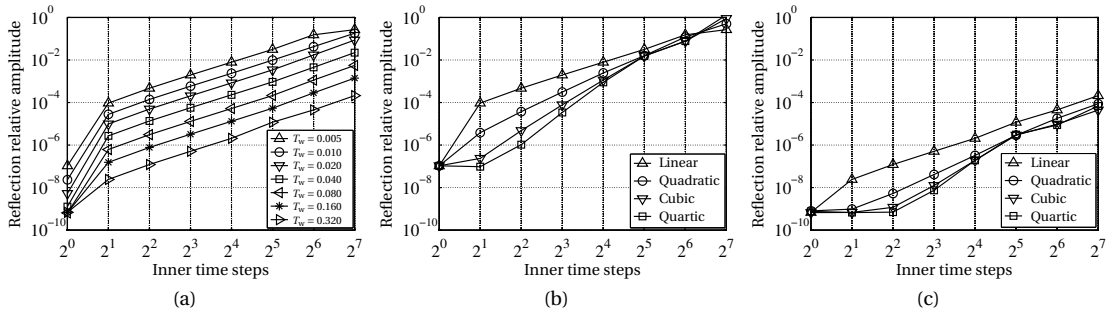


Figure 4.9: Maximum reflection relative amplitude as a function of the number of inner time steps, of the wave period, and of the Lagrange interpolation order. (a) Linear Lagrange polynomial interpolation for different wave periods. (b) Shorter tested wave period ($T_w = 0.005$) for different Lagrange interpolation orders. (c) Longer tested wave period ($T_w = 0.320$) for different Lagrange interpolation orders.

4.3.2 Reflections analysis

A second study regards the possible presence of numerical reflections at the coupling interfaces, which are due to the interpolation at the level of the inner time steps. For this analysis we impose a single flow rate wave defined as

$$Q(t) = \begin{cases} -\sin\left(\frac{2\pi t}{T_w}\right)^2 & t < \frac{T_w}{2}, \\ 0 & \text{otherwise.} \end{cases} \quad (4.1)$$

The length of each 1-D element is set equal to 75, which ensures that the longest considered wave fits in a single 1-D segment. This choice allows to easily identify the reflected wave in the first segment, once the end of the prescribed wave crosses the coupling interface.

In Figure 4.9a we can observe a clear dependence of the amplitude of the reflection with respect to the wavelength and the number of inner time steps performed per outer time step. As expected, the longest the wave, the smallest the numerical reflection. Note that the longest considered wave has a period similar to the one of the human systolic phase. Hence, as we show in Chapter 5, in a cardiovascular setting the magnitude of the numerical reflections is negligible when considering up to 128 inner time steps (which corresponds to an outer time step of approximately 10^{-3} s). Finally, in Figures 4.9b

and 4.9c we can observe that, as for the number of coupling iterations, the benefits of a higher order Lagrange polynomial are visible only when the inner time step is close to the outer time step.

4.4 Wave reflection analysis in a series of heterogeneous FSI pipes

In this section, we use simple examples to compare the behavior of the three proposed solid ring interface conditions introduced in Chapter 1 for the closure of the 3-D solid problem. In particular, we focus our analysis on the spurious backward wave reflections that might be generated at the coupling interfaces between two dimensionally-heterogeneous pipes. In order to have a full overview of the phenomena we analyze both the case of a 1-D wave flow that enters a 3-D pipe, and the inverse one, i.e., a 3-D wave flow entering a 1-D pipe. In both cases, on the leftmost inflow side we impose (4.1), being $T_w = 0.005$ the chosen wave period. On the rightmost outflow, an appropriate absorbing boundary condition is applied (see Sherwin et al. (2003) and Nobile and Vergara (2008) for 1-D and 3-D problems, respectively). The interface problem is defined through the set of equations (2.2) and by imposing mean normal stress boundary data on the coupling interfaces (i.e., $n_c^0 = 0$, $c = 1$). In the following, unless otherwise specified, the reference dimensionless parameters that define the problem are: $\rho_F = 1$, $\mu_F = 0.035$, $\alpha_F = 1.1$, $A^0 = \pi$, $h_S = 0.1$, $E_S = 3000000$, $\rho_S = 0$, and $\gamma_S = 0$. Note that with this choice of ρ_S and γ_S , the inertia and the viscoelastic effects of the wall are neglected in both the FSI models; indeed, we aim to study the reflections generated by the dimensional heterogeneity of the models, thus we need to exclude other possible sources of reflections, such as heterogeneous physical modeling features. The Poisson's ratio ν_S is 0.5 for the 1-D FSI model and 0.475 for the 3-D FSI model. The length L of each pipe is equal to 3. On the solid external wall $\Gamma_{S,ext}^0$ of the 3-D FSI problem we apply a homogeneous Neumann boundary condition, while we set $P_{ext} = 0$ in the 1-D FSI problem.

The imposed tolerance ε for the interface problem (see equation (2.10)) is 10^{-6} , while the one for the 3-D FSI problem is 10^{-7} . The mesh of the fluid part of the 3-D pipe consists of 137712 tetrahedral elements with 25077 vertices, while the solid part is made of 51984 tetrahedral elements with 11856 vertices. The corresponding average space discretization for the fluid and solid problems are 0.094 and 0.092, respectively. Regarding the 1-D FSI pipe, we use a uniform space discretization of 0.1, corresponding to 31 vertices. The global time step is set equal to 10^{-5} ; since this is quite a small value, we use the GCE time discretization scheme to solve the 3-D FSI problem. All the simulations last 1500 time steps ($T = 0.0015$), which is the time needed by the wave flow to reach the rightmost side of the problems.

4.4.1 From 1-D to 3-D wave flow propagation

The first case we analyze is described in Figure 4.10a: a wave propagates from a 1-D FSI segment (on the left) to a 3-D FSI pipe (on the right). As a reference case we consider the solution computed by solving the problem with a single 1-D segment of length 6 (see Figure 4.10b). By comparing the solution of the two problems we study the reflection amplitude generated at the coupling interfaces due to the heterogeneity of the models.

The results are summarized in Figure 4.11. On the x -axis we represent the normalized time, while on the y -axis we show the difference between the volumetric flow rate in the heterogeneous case (see Figure 4.10a) and the one given by the reference case (see Figure 4.10b), namely ΔQ , normalized over the maximum amplitude of the inflow wave. This quantity coincides with the normalized reflection wave generated at the coupling interface. Note that a similar analysis done in terms of pressure waves (which for brevity is not presented here) leads to the same conclusions.

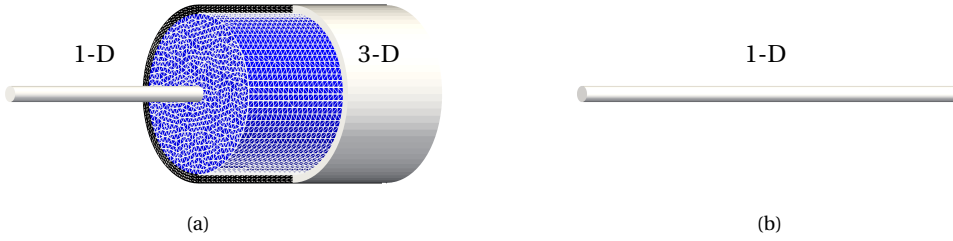


Figure 4.10: Schematic representation of the benchmark case. (a) The wave flow propagates from the 1-D FSI model to the 3-D FSI one. The length of each pipe is equal to 3. (b) The reference case: a single 1-D FSI pipe of length 6.

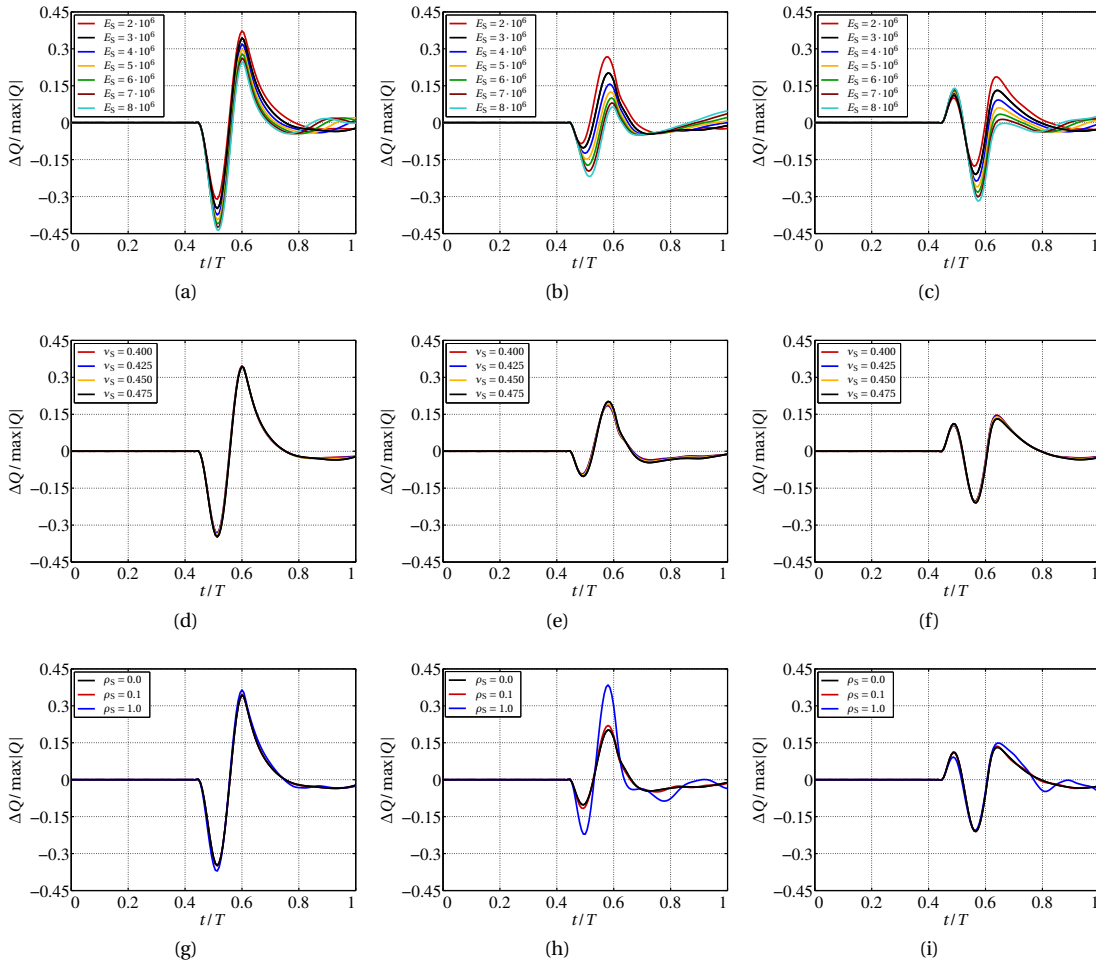


Figure 4.11: Volumetric flow rate wave reflection at the coupling interfaces for different values of the main 3-D solid parameters. In all the figures, the black curve corresponds to the reference parameters. (a,b,c) Varying Young's modulus. (d,e,f) Varying Poisson's ratio. (g,h,i) Varying solid density. (a,d,g) Fixed area boundary condition on the 3-D solid ring. (b,e,h) Free area boundary condition on the 3-D solid ring. (c,f,i) Continuity of the area at the coupling interfaces ($c \in \mathcal{L}^A$).

4.4. Wave reflection analysis in a series of heterogeneous FSI pipes

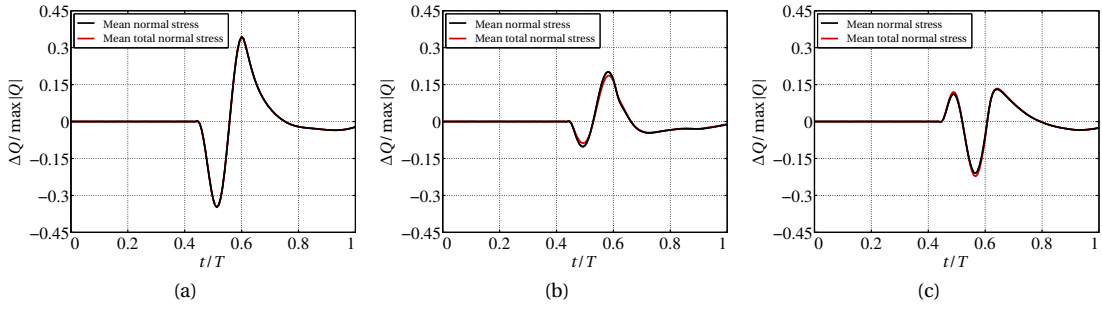


Figure 4.12: Volumetric flow rate wave reflection at the coupling interfaces for different sets of interface equations. (a) Fixed area boundary condition on the 3-D solid ring. (b) Free area boundary condition on the 3-D solid ring. (c) Continuity of the area at the coupling interfaces ($c \in \mathcal{L}^A$).

First of all we observe that, as expected, the amplitude of the reflection is always larger when the 3-D solid ring is fixed. More precisely, the reflection generated by using such a constraining boundary condition is around twice the size of the one observed when the other two approaches are employed, motivating the need of such more relaxed conditions on the coupling interface. In contrast, there is no clear advantage in prescribing the continuity of the area of the pipes, compared to letting the deformation of the 3-D boundary solid ring free. Indeed, such behavior depends upon the specific case (see Figures 4.11b and 4.11c for varying Young's modulus).

Regarding the sensitivity analysis with respect to the main 3-D solid parameters, we observe that the value of the Young's modulus has an impact on the reflection, even if the shape of the wave does not change significantly. The vertical difference between the subsequent peaks in the wave is nearly constant, such that the amplitude of the reflection is almost the same. In contrast, the Poisson's ratio does not have any effect on the reflection. Finally, we observe that modeling the inertia of the 3-D solid wall leads to significant differences only in presence of the free solid ring boundary condition. More precisely, the reflection amplifies probably due to the additional modeling heterogeneity introduced in this specific case (we recall that our 1-D FSI model does not account for the inertia of the wall). By applying the other two solid ring boundary conditions the displacement of the ring is controlled by the boundary data, such that the boundary inertial effects are smoothed out.

The comparison between the imposition of the continuity of the mean normal stress (see problem (2.2)), with that of the mean total normal stress (see problem (2.5)) is presented in Figure 4.12. The difference between the results in the two cases is very small because, for the chosen set of values of the parameters (which characterizes blood and arteries), the kinetic contribution is almost negligible. In Blanco et al. (2012) we will extend this analysis to regimes where the kinetic term cannot be neglected.

Finally, in Figure 4.13 we show the reflection amplitude as a function of the 3-D mesh size. The first row of images shows an opposite behavior between the case where the continuity of the area is imposed and the other two types of boundary conditions. More precisely, a refinement of the mesh leads to a progressive reduction of the reflection amplitude in the former case and an increase in the latter. In the second row of images we compare the reflection amplitude as a function of the interface condition for fixed values of the 3-D mesh size. From the images it is evident that, in contrast with the coarse mesh results, with the finer mesh the reflection amplitude of the case where the continuity of the area is imposed is smaller with respect to one obtained by using the other two interface conditions. By assuming that the result provided by the finer mesh is the most accurate, we might conclude that

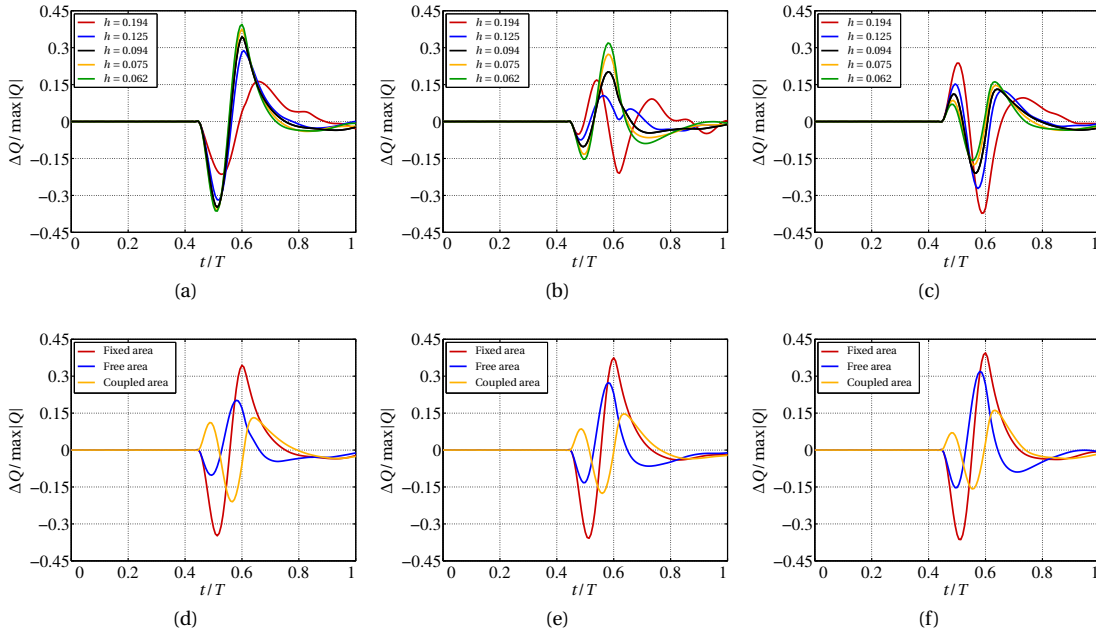


Figure 4.13: Volumetric flow rate wave reflection at the coupling interfaces for different values of the fluid mesh size (note that also the solid mesh size changes accordingly). As in Figure 4.11, the black curve corresponds to the reference parameters. (a) Fixed area boundary condition on the 3-D solid ring. (b) Free area boundary condition on the 3-D solid ring. (c) Continuity of the area at the coupling interfaces ($c \in \mathcal{L}^A$). (d) $h = 0.094$. (e) $h = 0.075$. (f) $h = 0.062$.

the continuity of the area represents the most suitable interface condition between the considered heterogeneous models. Nevertheless, further analyses should be performed to confirm this behavior in more general cases. Note also that a similar analysis with respect to the 1-D mesh size does not produce any significant difference. In particular, below a certain mesh size, the results in the 1-D segment are almost the same.

4.4.2 From 3-D to 1-D wave flow propagation

In the second case, described in Figure 4.14, we study the reflection amplitude generated at the coupling interfaces when a wave propagates from a 3-D FSI pipe (on the left) to a 1-D FSI segment (on the right), see Figure 4.14a. As a reference case we consider the solution computed by solving the problem with a single 3-D FSI pipe of length 6 (see Figure 4.14b).

Figure 4.15 shows the same quantities as in Figure 4.11 with the inverted configuration. Now the amplitude of the reflection is much smaller, around one-third of the previous case. This can be explained by observing that the 1-D problem is hyperbolic and at the coupling interface it behaves as a passive element which absorbs the flow generated by the 3-D pipe. By way of contrast, in the previous case, the flow generated by the 1-D segment is passed to a non-hyperbolic model which reflects an active feedback to the connected 1-D segment.

4.4. Wave reflection analysis in a series of heterogeneous FSI pipes

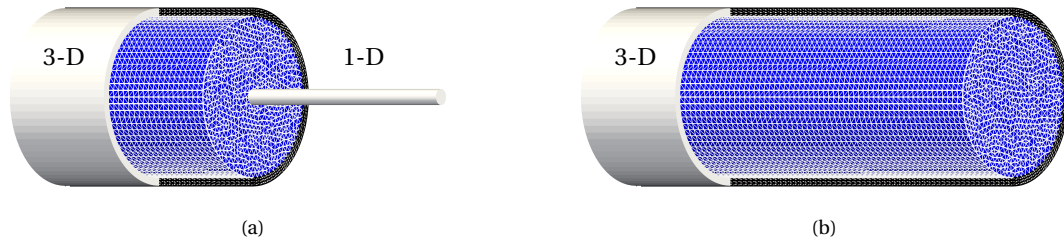


Figure 4.14: Schematic representation of the benchmark case. (a) The wave flow propagates from the 3-D FSI model to the 1-D FSI one. The length of each pipe is equal to 3. (b) The reference case: a single 3-D FSI pipe of length 6.

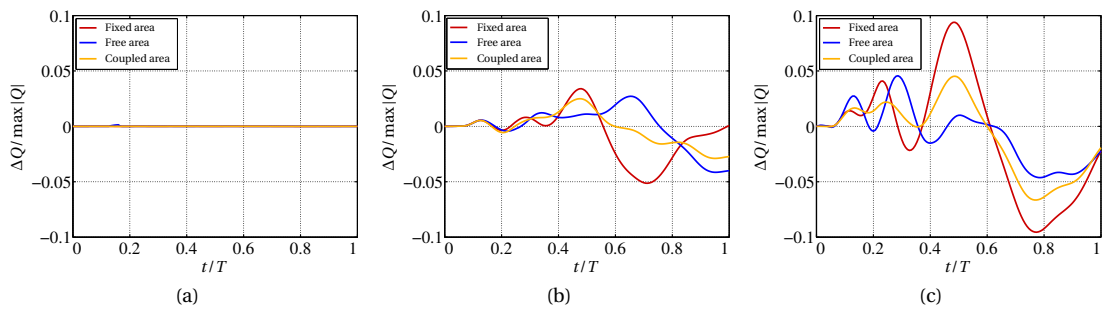


Figure 4.15: Volumetric flow rate wave reflection at different locations of the 3-D FSI pipe. (a) Left inlet. (b) Half section. (c) Right outlet (coupling interface).

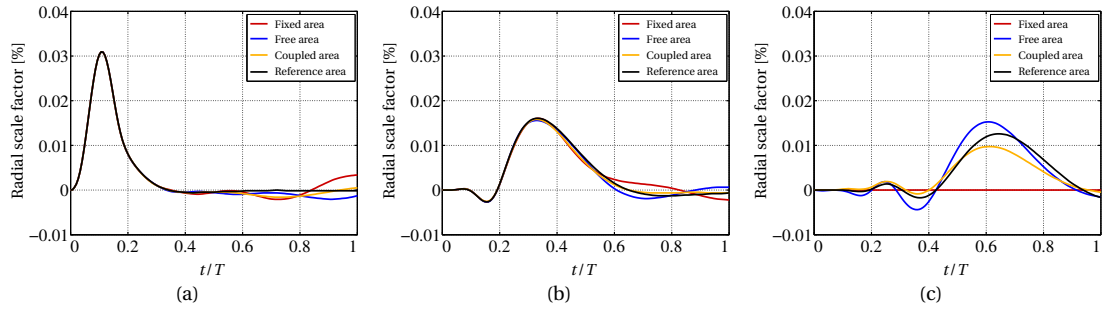


Figure 4.16: Radial scale factor of the 3-D FSI pipe in Figure 4.14a at different locations. The black line is the reference value (see Figure 4.14b). (a) Left inlet. (b) Half section. (c) Right outlet (coupling interface).

An additional comparison is presented in Figure 4.16, where on the y-axis we show the radial scale factor (in percentage units) whose definition is given in (1.10). This result leads to the same conclusions discussed in Section 4.4.1. In particular, the amplitude of the reflection is always larger when the 3-D solid ring is fixed, while the other two approaches yield better results. Moreover, we notice that prescribing the continuity of the area of the pipes produces a slightly better result with respect to letting the deformation of the 3-D boundary solid ring free.

Chapter 4. Benchmark examples

Finally, a further comparison (which for brevity is not presented here) between the two sets of interface equations (see problems (2.2) and (2.5)), shows no significant differences between the two cases, as already observed in the inverted problem (see Figure 4.12).

Main references of the chapter:

- ☆ A. C. I. Malossi, P. J. Blanco, S. Deparis, and A. Quarteroni. Algorithms for the partitioned solution of weakly coupled fluid models for cardiovascular flows. *Int. J. Num. Meth. Biomed. Engng.*, 27(12):2035–2057, 2011.
- ☆ A. C. I. Malossi, P. J. Blanco, and S. Deparis. A two-level time step technique for the partitioned solution of one-dimensional arterial networks. *Comp. Meth. Appl. Mech. Engrg.*, 237–240:212–226, 2012.
- ☆ A. C. I. Malossi, P. J. Blanco, P. Crosetto, S. Deparis, and A. Quarteroni. Implicit coupling of one-dimensional and three-dimensional blood flow models with compliant vessels. Submitted, 2012.

5 Cardiovascular networks

In this chapter we perform several numerical simulations of different cardiovascular networks, to which the algorithms devised in Part I are applied. More precisely, the aim of this chapter is twofold: on the one hand, we use the cardiovascular problems as a benchmark to further investigate some interesting numerical aspects, such as the iterations number and the CPU time required to solve realistic cardiovascular problems. On the other hand, we simulate the blood flow in large networks of arteries modeled through dimensionally-heterogeneous FSI models, such as those described in Chapter 1; in this regard, we perform several numerical comparisons to study the dynamic of the flow with respect to both published data and simplified models, where the simplifications take place at either the level of the specific model or that of the global network of elements.

The layout of the chapter is the following: in Section 5.1 we present a numerical comparison between two 3-D rigid wall geometries representing a carotid bifurcation. Then, in Section 5.2 we compare the results given by a network of 1-D FSI models with the *in vitro* and numerical simulations data published by Matthys et al. (2007) and Alastruey et al. (2011). To do that we also describe a lumped parameters model to account for the cumulative effects of the distal vessels, which is later employed in all the simulated global cardiovascular networks. After that, in Section 5.3 we make use of the data provided by Reymond et al. (2009) to set up several numerical simulations in a human arterial network, with the aim of both reproduce the results of the reference work and also further investigate some critical modeling and numerical aspects of the proposed methods, with a particular focus on the two-level time step technique introduced in Chapter 3. Then, in Section 5.4 we present several comparisons among different dimensionally-heterogeneous geometrical multiscale models. The purpose of these comparisons is manifold. On the one hand, we study the interaction between 3-D patient specific geometries and a global arterial network of 1-D models. These results are compared both with a full 1-D network of arteries, and a stand-alone 3-D simulation with boundary data taken from the same full 1-D network. On the other hand, we also analyze the effect of the 3-D solid boundary conditions on the simulations. In particular, we perform a sensitivity analysis of the external tissues parameters, and we also compare results of configurations where the area at the interfaces is fixed, with those where it is scaled to have the continuity of the vessels size with the surrounding 1-D arteries. Finally, in Section 5.5 we assess the computational efficiency of our methodology through several simulations in a 3-D abdominal aorta geometry coupled with a variable number of 1-D arterial vessels.

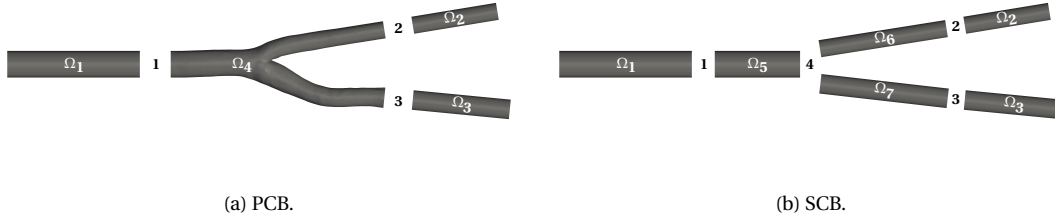


Figure 5.1: Carotid bifurcation schemes. The area of the cylindrical subdomains Ω_1 , Ω_2 , and Ω_3 is the same of the corresponding interfaces of the PCB Ω_4 , while their radius/length ratio is equal to 0.1. (a) The central element is the PCB Ω_4 . The inlet area is 0.351 cm^2 , while the internal and external outlet carotid areas are 0.147 cm^2 and 0.190 cm^2 , respectively. (b) The central element is modeled by a SCB composed by three cylinders: Ω_5 , Ω_6 , and Ω_7 . The area of the cylinders match the ones of the three interfaces of the PCB Ω_4 .

5.1 Numerical comparison of 3-D rigid wall carotid bifurcation geometries

The first cardiovascular example we propose is a numerical comparison between two 3-D rigid wall geometries representing a carotid bifurcation. We compare the solution obtained in a physiological carotid bifurcation (PCB) network (see Figure 5.1a), with the one given by a synthetic carotid bifurcation (SCB) network (see Figure 5.1b).

The fluid in the rigid domains is governed by the unsteady Navier–Stokes equations (1.3). The time step is chosen equal to 10^{-3} s, which is a typical value for arterial flow problems. To set up the two networks we impose the set of equations (2.2) at all the coupling nodes through coupling stress boundary data on all the interfaces (i.e., $n_c^Q = 0$ with $c \in \mathcal{L}^S$, $c = 1, \dots, 4$). It is worth pointing out that the two configurations feature a different number of coupling interfaces. Therefore for the PCB each subiteration of the Newton method requires six evaluations of problem (3.2), plus four evaluations of problem (1.3), while for the SCB it requires nine evaluations of problem (3.2), plus six evaluations of problem (1.3). The imposed tolerance for the interface problem is 10^{-6} ; in any case, convergence is reached in one iteration since the fluid flow problem defined inside each domain is linear. At the inlet of Ω_1 a heart systole-diastole flow rate cycle (corresponding to 75 beats per minute) is imposed, while homogeneous Neumann boundary conditions are applied on the outflow of Ω_2 and Ω_3 . The physical quantities that define the problem are: $\rho_F = 1 \text{ g/cm}^3$ and $\mu_F = 0.035 \text{ g/cm/s}$.

The aim of this example is on the application of the decomposition strategy devised in Chapter 2, which may give insights on the differences in global quantities (e.g., coupling flow and coupling stress) that should be expected when using a simple version of a bifurcation (such as the SCB), when compared with a real geometry (such as the PBC). In particular, for the two configurations we compare the flow division and the coupling stress at the different coupling interfaces. In addition, we also compare the velocity profiles inside the two carotids. Indeed, we remark that we are by no means interested in trying to recover the 3-D features of the flow computed in the PCB with the SCB.

5.1. Numerical comparison of 3-D rigid wall carotid bifurcation geometries

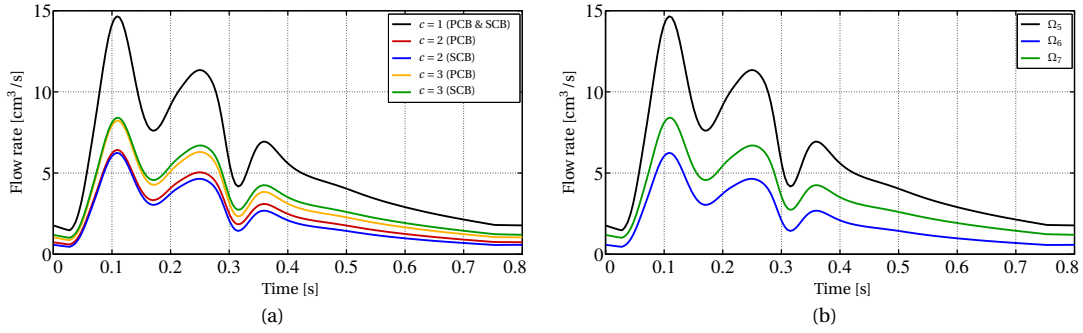


Figure 5.2: Flow rate splitting at the coupling nodes of the two carotid bifurcation networks. (a) Flow rate comparison at the main coupling interfaces of the PCB and SCB. (b) Flow rate splitting at $c = 4$ of the SCB.

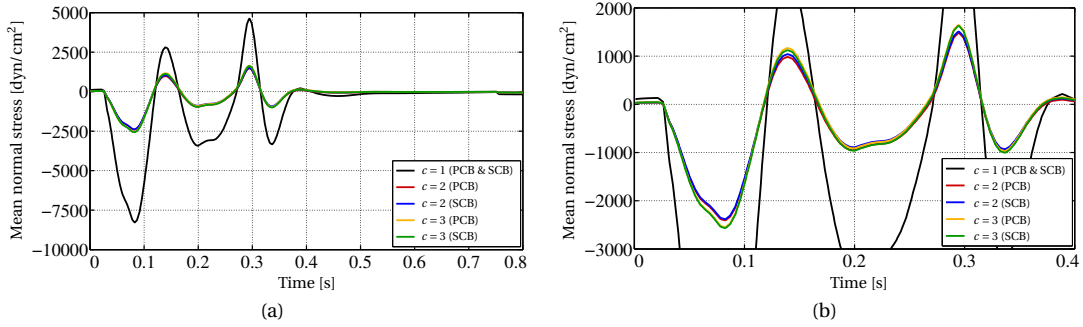


Figure 5.3: (a) Coupling stress comparison at the main coupling interfaces of the PCB and SCB. (b) Enlarged view of the left image.

In Figure 5.2 the evolution of the flow rate during one heart beat is shown. The small difference (approximately ten percent) between the flow rates of the PCB with respect to the ones of the SCB (see coupling nodes $c = 2$ and $c = 3$ in Figure 5.2a) is due to the different model used to represent the bifurcation, which in the case of the SCB neglects the effects of the 3-D geometry. Nevertheless, we obtain a good separation of the flows in the SCB when compared to the PCB. Regarding the coupling stress (Figure 5.3), we observe no significant differences between the PCB and the SCB cases, as this quantity mainly depends on the global length of the geometrical model (which is the same in the two cases), rather than on the 3-D geometry of the bifurcation.

Finally, in Figure 5.4 we show a qualitative comparison between the velocity profiles of the two carotids, at selected times. As expected, in the SCB the velocity assumes a Womersley-like profile, which is not the case of the PCB, where the shape of the 3-D bifurcation produces asymmetries in the solution. Nevertheless, the magnitude of the velocity in the two cases is nearly the same (see the colors in Figure 5.4). In addition, we observe that the velocity profiles at the coupling interfaces agree well in both cases.

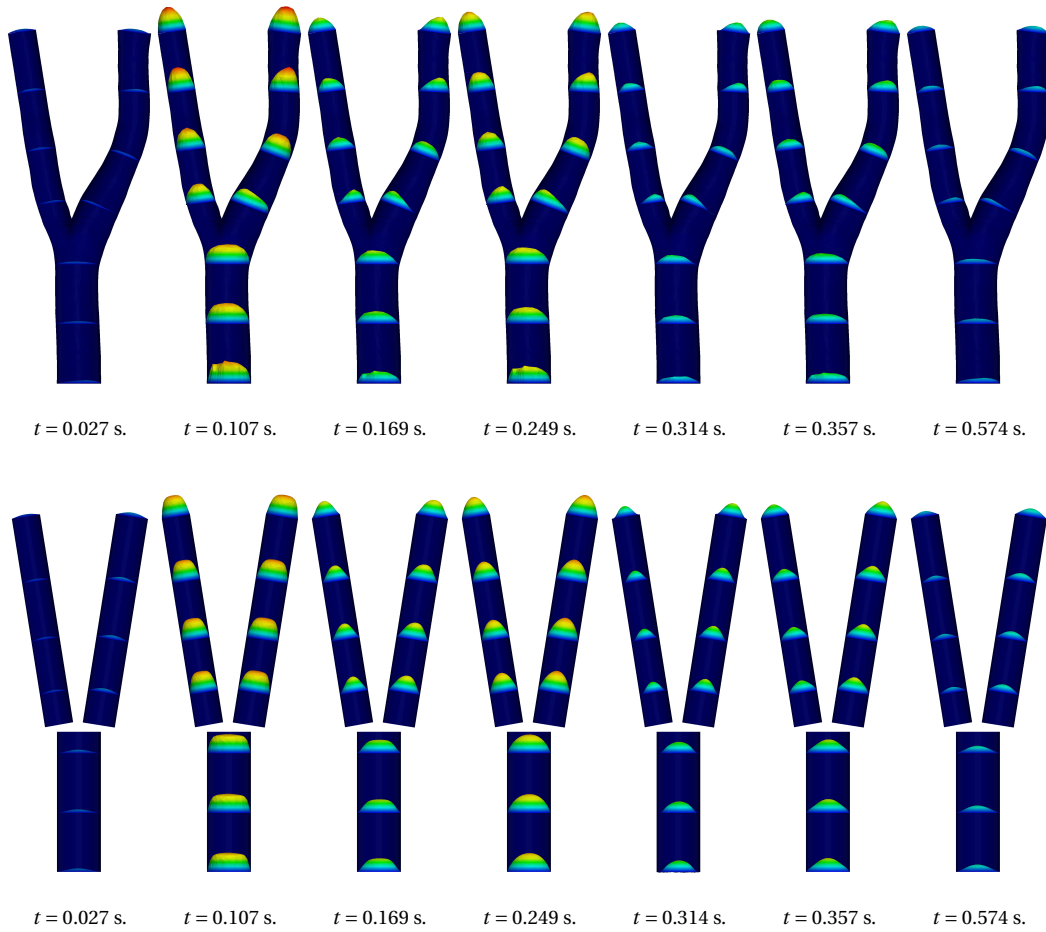


Figure 5.4: Comparison between the velocity profiles of the PCB (first line), with the ones obtained for the SCB (second line). The color bar ranges from blue (0.0 cm/s) to red (79.6 cm/s).

5.2 Assessment of 1-D FSI numerical simulations against published data

In this section we compare the results given by a network of 1-D FSI models with both *in vitro* and *in silico* published data. The aim is to assess and, somehow, validate the methodology devised in Part I for the modeling of reduced order cardiovascular networks. As reference data we use the results given by Matthys et al. (2007), which have later been extended in Alastruey et al. (2011) to include also the viscoelastic effects in the numerical model.

In the following, first we briefly recall from the aforementioned works the experimental setting and the numerical model used to produce the benchmark results. Then, we describe a simple lumped parameters model to account for the peripheral circulation in the arterial network. Finally, we provide a series of comparisons between our numerical simulations and both the experimental and numerical reference data.

5.2.1 Reference experimental and numerical setting

The experimental model is an *in vitro* 1:1 replica of the 37 largest conduit arteries of the systemic circulation (see Matthys et al. (2007, Fig. 1)). The closed loop hydraulic system is set up through a Harvard pulsatile pump, which provides a periodic flow rate at the very inflow of the network. More precisely, the settings of the pump are: 70 beats per minute, with a systole-to-diastole ratio of 35/65 leading to $T_S = 0.4615$ s (see Matthys et al. (2007, Fig. 2)), and a stroke volume of 70 cm^3 , such that the mean pressure at the aortic root is approximately 133000 dyn/cm^2 . Outflow boundary conditions are set up through passive resistance elements made of a single flexible plastic tube (length 25 cm; diameter 0.2 cm) and an overflow reservoir inducing a back pressure of approximately 4300 dyn/cm^2 . The peripheral compliance is not included in the experimental model.

The network of elements is manufactured by using a two-component incompressible silicone material¹, characterized by a Young's modulus of $12 \cdot 10^6 \text{ dyn/cm}^2$, a Poisson's ratio of 0.5, and a viscosity φ_S of $30000 \text{ dyn}\cdot\text{s/cm}^2$. In our analysis, the last parameter is used to recover the value of the viscoelastic angle: indeed, from (1.17) and Alastruey et al. (2011, equation (5)) we get

$$\phi_S = \arctan\left(\frac{8\pi(1-\nu_S^2)}{3E_S T_S} \varphi_S\right),$$

such that $\phi_S = 1.9494^\circ$. To mimic the density and viscous properties of blood a 65-35 % water-glycerol mixture with density 1.05 g/cm^3 and viscosity 0.025 g/cm/s is used. The flow rate is measured by using an ultrasonic volume flow meter², while the pressure is obtained by means of two micro-tip catheter pressure transducers³. Both pressure and flow rate are measured at 70 locations along the experimental network. The geometrical properties (length, cross-section radius at inlet and outlet locations, and average wall thickness) and the values of the peripheral resistance are given in Matthys et al. (2007, Table 1) for each segment and terminal.

Regarding the mathematical model, the same governing equations described in Chapter 1 for continuity of mass and momentum, as well as for the pressure-area relation, are used in the reference works. Nevertheless, at the discrete level, Matthys et al. (2007) and Alastruey et al. (2011) use a spectral discontinuous Galerkin scheme, which involves the solution of Riemann problems at the interfaces between arteries. An explicit second order Adams–Bashforth scheme is used for the time integration, with a time step ranging from $2 \cdot 10^{-5}$ s (in the viscoelastic wall case) to 10^{-4} s (in the purely elastic wall case). More details on this algorithm can be found in Sherwin et al. (2003) and Karniadakis and Sherwin (2005).

The numerical simulations are set up by imposing the conservation of flow rate and the continuity of mean total normal stress at the coupling interfaces. At the inlet of the ascending aorta the flow rate measured in the experiment is imposed, while a three-element windkessel model, whose details are given in the next section, is connected to the outflow of each terminal 1-D model. The energy losses have not been considered at the arterial junctions, since these are negligible in large healthy arteries, as shown in Matthys et al. (2007, Section 3.2).

For more details about the reference experimental and numerical results see Matthys et al. (2007) and Alastruey et al. (2011).

¹Baysilone LSR2050, General Electric, Fairfield, CT, USA.

²Dual Channel Flowmeter, Transonic Systems Inc., Ithaca, NY, USA.

³Millar Instruments, Houston, TX, USA.

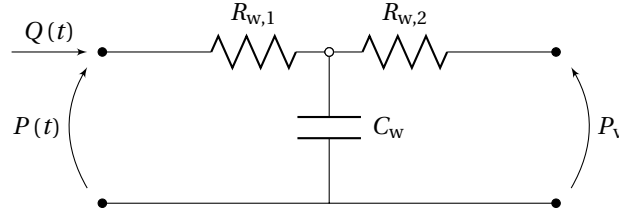


Figure 5.5: Three-element windkessel model scheme.

5.2.2 Three-element windkessel terminal lumped parameters model

To account for the cumulative effects of the distal vessels (small arteries, arterioles, and capillaries), the peripheral 1-D arterial elements are generally terminated by lumped parameters models. Among the others, one of the most simple and effective model is the three-element windkessel (see Frank (1899)), which accounts for the wall compliance and the blood viscosity (friction) through a capacitor C_w and two resistances $R_{w,1}$ and $R_{w,2}$, respectively, as shown in Figure 5.5; the values of these parameters can be obtained by *in vivo* measurements and reasonable assumptions (see, e.g., Avolio (1980) and Reymond et al. (2009)).

By exploiting the electrical analogy, the windkessel model leads to a differential relation between the pressure and the volumetric flow rate in the time domain, namely

$$P(t) - P_v + C_w R_{w,2} \frac{dP(t)}{dt} = (R_{w,1} + R_{w,2}) Q(t) + C_w R_{w,1} R_{w,2} \frac{dQ(t)}{dt}, \quad t \in (0, T], \quad (5.1)$$

where $P(t)$ and $Q(t)$ are the pressure and the volumetric flow rate at the corresponding terminal node and P_v is the venous pressure. Equation (5.1) can be solved for either the pressure or the volumetric flow rate. In the first case, by introducing the approximation

$$\left\{ \begin{array}{l} Q(t) \approx Q^n + \frac{Q^{n+1} - Q^n}{\Delta t} (t - t^n), \\ \frac{dQ(t)}{dt} = \frac{Q^{n+1} - Q^n}{\Delta t}, \end{array} \right.$$

we can rewrite (5.1) as

$$\frac{dP(t)}{dt} + K_1^Q P(t) = K_2^Q (Q^{n+1}) t + K_3^Q (Q^{n+1}), \quad t \in [t^n, t^{n+1}], \quad (5.2)$$

being

$$\begin{aligned} K_1^P &= \frac{1}{C_w R_{w,2}}, & K_2^P (Q^{n+1}) &= \frac{R_{w,1} + R_{w,2}}{C_w R_{w,2}} \frac{Q^{n+1} - Q^n}{\Delta t}, \\ K_3^P (Q^{n+1}) &= \frac{R_{w,1} + R_{w,2}}{C_w R_{w,2}} \left(Q^n + \frac{Q^{n+1} - Q^n}{\Delta t} \left(\frac{C_w R_{w,1} R_{w,2}}{R_{w,1} + R_{w,2}} - t^n \right) + \frac{P_v}{R_{w,1} + R_{w,2}} \right), \end{aligned}$$

where, for the sake of clarity, we put in evidence the dependence of some of the parameters on Q^{n+1} .

5.2. Assessment of 1-D FSI numerical simulations against published data

Equation (5.2) is integrated analytically at each time step

$$P(t^{n+1}) = \exp(-K_1^P \Delta t) \left(P(t^n) + \int_{t^n}^{t^{n+1}} (K_2^P(Q^{n+1})t + K_3^P(Q^{n+1})) \exp(K_1^P(t-t^n)) dt \right),$$

such that the new value of the pressure is given by the following algebraic expression

$$P(t^{n+1}) = P(t^n) \exp(-K_1^P \Delta t) + \mathcal{F}(K_1^P, K_2^P(Q^{n+1}), K_3^P(Q^{n+1})),$$

being

$$\mathcal{F}(K_1, K_2, K_3) = \frac{1}{K_1} \left(\left(K_3 - \frac{K_2}{K_1} \right) (1 - \exp(-K_1 \Delta t)) + K_2 (t^{n+1} - t^n \exp(-K_1 \Delta t)) \right). \quad (5.3)$$

The same approach holds when solving for the volumetric flow rate. More precisely, in that case we get

$$Q(t^{n+1}) = Q(t^n) \exp(-K_1^Q \Delta t) + \mathcal{F}(K_1^Q, K_2^Q(P^{n+1}), K_3^Q(P^{n+1})),$$

with

$$K_1^Q = \frac{R_{w,1} + R_{w,2}}{C_w R_{w,1} R_{w,2}}, \quad K_2^Q(P^{n+1}) = \frac{1}{C_w R_{w,1} R_{w,2}} \frac{P^{n+1} - P^n}{\Delta t},$$

$$K_3^Q(P^{n+1}) = \frac{1}{C_w R_{w,1} R_{w,2}} \left(P^n - \frac{P^{n+1} - P^n}{\Delta t} t^n - P_v \right) + \frac{1}{R_{w,1}} \frac{P^{n+1} - P^n}{\Delta t}.$$

The three-element windkessel model can be coupled with the other elements in the network by using the same approach devised in Chapters 2 and 3. First of all, similarly to what has been done in Section 2.2 for the FSI models described in Chapter 1, we define the interface quantities as

$$\Omega_w = -Q, \quad \mathcal{S}_w = -P,$$

where we remark that the area and, consequently, the mean total normal stress cannot be defined at the boundary interface. In view of this, the only available set of interface equations is (2.2), i.e, conservation of flow rate and continuity of mean normal stress. The Jacobian entries are computed through the exact tangent problem; the analytical expression of the boundary operator partial derivatives reads

$$\frac{\partial \mathcal{Q}_w(\mathcal{S}_w)}{\partial \mathcal{S}_w} = \frac{\partial \mathcal{F}(K_1^Q, K_2^Q(-\mathcal{S}_w), K_3^Q(-\mathcal{S}_w))}{\partial \mathcal{S}_w}, \quad \frac{\partial \mathcal{S}_w(\Omega_w)}{\partial \Omega_w} = \frac{\partial \mathcal{F}(K_1^P, K_2^P(-\Omega_w), K_3^P(-\Omega_w))}{\partial \Omega_w},$$

where the derivatives of (5.3) are straightforward.

Table 5.1: Main parameters of the 1-D network of arteries. For the geometrical properties (length, proximal/distal areas, wall thickness) of the vessels and the data of the terminals see Matthys et al. (2007, Figure 1 and Table 1).

ρ_F	Blood density	1.05 g/cm ³
μ_F	Blood viscosity	0.025 g/cm/s
κ_F	Friction coefficient	1.6456 cm ² /s
α_F	Coriolis coefficient	1.1
P_{ext}	Reference external pressure	100000 dyn/cm ²
P_V	Venous pressure	4300 dyn/cm ²
E_S	Young's modulus	$12 \cdot 10^6$ dyn/cm ²
ν_S	Poisson's ratio	0.50
ϕ_S	Viscoelastic angle	1.9494 degrees
T_S	Systolic period	0.4615 s
	Heart rate	70 bpm

5.2.3 Elastic wall simulations

In this section we compare the results of our numerical simulations with the experimental and the numerical reference data provided in Matthys et al. (2007). There, in the numerical setting, the authors consider a purely elastic wall model, which in our case corresponds to assume $\gamma_S = 0$. To set up the comparison we imported in our framework the data given in Matthys et al. (2007, Figure 1 and Table 1), together with the other parameters required by the numerical setting, here summarized in Table 5.1; for the sake of completeness, in the table we also provide the viscoelastic parameters, which are used in the next section.

In accordance with the approach used in Matthys et al. (2007) the coupling of the elements in the network is enforced by imposing the conservation of volumetric flow rate and the continuity of the mean total normal stress at the interfaces between the 1-D segments. The latter condition is replaced by the continuity of mean normal stress at the interfaces between the 1-D elements and 0-D terminals.

In all the simulations we run ten heart beats to reach the periodic state. Then, for each considered segment we plot both the reference data and our numerical results on the same image. In this regard, in the following we denote by “Exp.” and “Num.” the experimental and the numerical results, respectively, and we add the suffix “Ref.” when displaying the reference data from Matthys et al. (2007). Moreover, in the figures we use dashed lines to draw reference data and solid lines to represent our results.

Remark 5.1. In the reference works, during the post-processing the authors have translated the flow rate and pressure curves in time to match the onset of the experimental and numerical systolic ejections in all the segments. In order to compare our results with their reference data, we have applied a similar translation to our curves.

In Figure 5.6 we compare the volumetric flow rate waveforms in different arterial segments. We remark that the terminal elements in both the experimental and numerical settings are purely resistive. From the analysis of the images we observe that the results of our numerical simulation are in good agreement with the numerical data in Matthys et al. (2007). However, there is a significant difference between the experimental curves and the two numerical results. This mismatch is less evident in the pressure waveform curves shown in Figure 5.7.

5.2. Assessment of 1-D FSI numerical simulations against published data

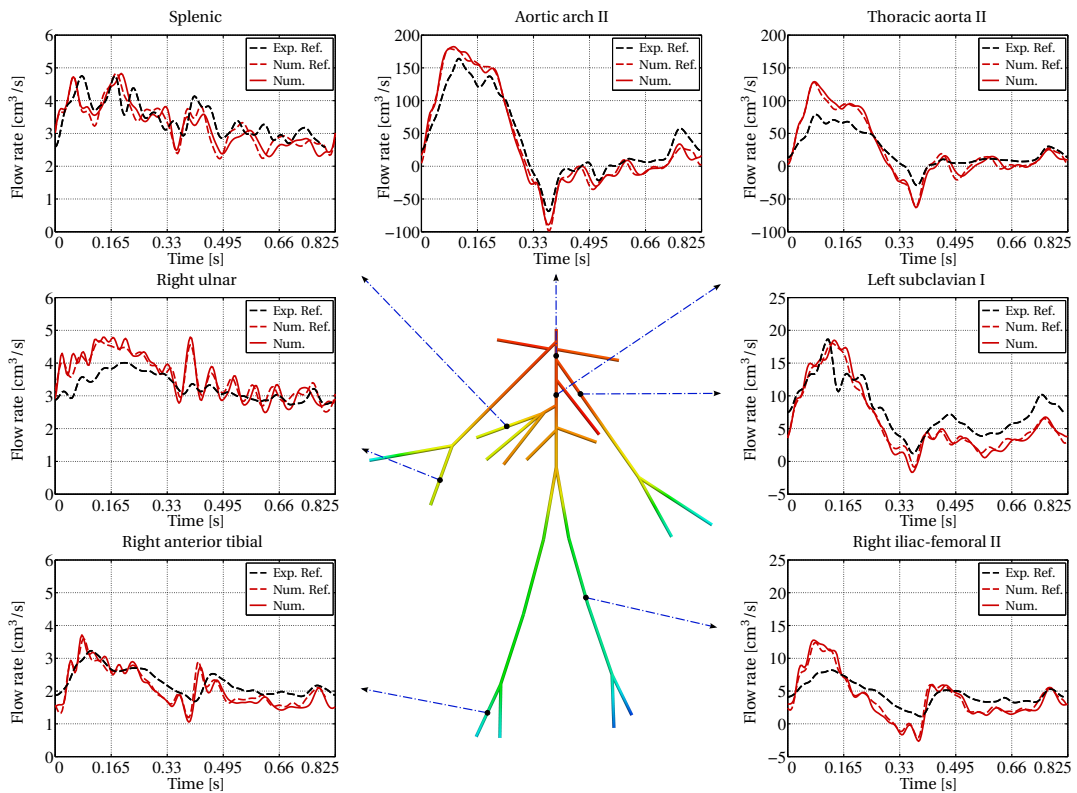


Figure 5.6: Periodic flow rate comparison in seven different arterial segments. In the numerical models (red lines) the viscoelastic effects of the arterial wall have been neglected, as well as the peripheral compliance. The color in the central image represents the pressure field at the end-systole, where the color bar ranges from blue (85000 dyn/cm^2) to red (130000 dyn/cm^2). Positioning of 1-D network elements is purely visual.

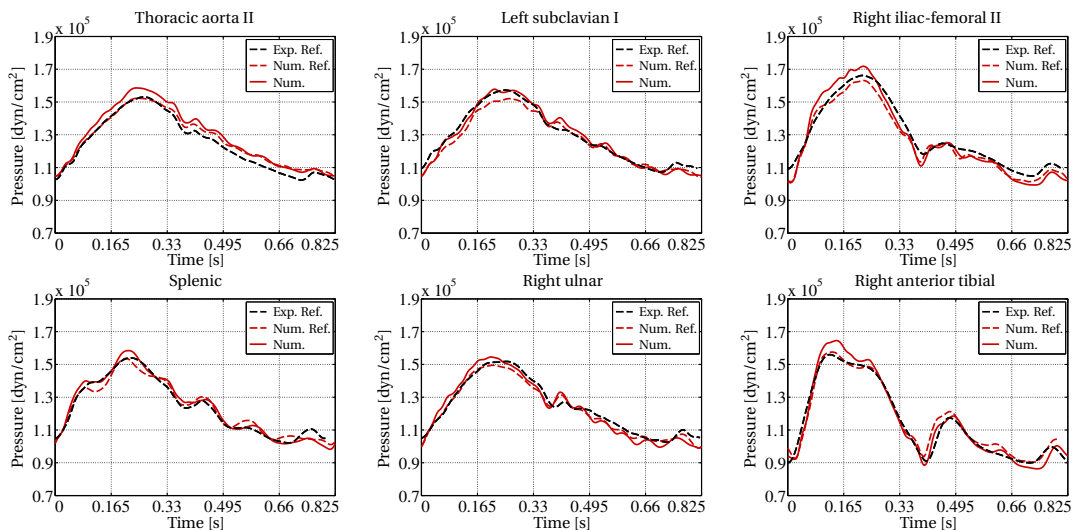


Figure 5.7: Pressure wave comparison for six of the seven segments shown in Figure 5.6. In the numerical models (red lines) the viscoelastic effects of the arterial wall have been neglected, as well as the peripheral compliance.

Table 5.2: Relative percentage errors (see equations (5.4)) between the numerical results obtained by using the methodology described in this work and the reference experimental (Exp.) and numerical (Num.) data, for a significant subset of the 37 1-D arterial segments. In the numerical models the viscoelastic effects of the arterial wall have been neglected, as well as the peripheral compliance.

Arterial segment	$\mathcal{E}_Q^{\text{mean}}$ [%]		$\mathcal{E}_Q^{\text{max}}$ [%]		$\mathcal{E}_P^{\text{mean}}$ [%]		$\mathcal{E}_P^{\text{max}}$ [%]	
	Exp.	Num.	Exp.	Num.	Exp.	Num.	Exp.	Num.
Aortic arch II	11.0	2.8	32.0	7.8	2.5	1.8	6.1	4.2
Thoracic aorta II	21.3	3.7	69.9	9.8	3.7	1.9	6.0	4.2
Abdominal aorta III	24.9	5.7	83.1	24.0	4.9	2.4	10.5	7.4
Left subclavian I	13.6	3.3	38.2	12.5	1.8	2.0	5.5	4.9
Right ulnar	10.7	3.7	36.7	13.5	2.7	1.8	6.2	4.3
Left ulnar	12.2	3.9	30.1	18.6	2.0	2.0	5.9	4.9
Splenic	7.8	4.1	23.7	10.5	1.8	2.0	5.7	4.8
Left renal	13.0	8.1	36.0	32.4	4.3	2.5	9.2	5.7
Right iliac-femoral II	23.2	3.8	70.3	15.1	3.7	2.4	8.9	6.5
Right anterior tibial	10.0	3.1	27.2	13.8	2.9	3.1	8.7	8.5

To quantify more precisely this difference we calculate the relative error between our numerical result and both the experimental and numerical reference data by computing the quantities

$$\mathcal{E}_Q^{\text{mean}} = \text{mean}(\mathcal{E}_Q), \quad \mathcal{E}_Q^{\text{max}} = \max(\mathcal{E}_Q), \quad \mathcal{E}_P^{\text{mean}} = \text{mean}(\mathcal{E}_P), \quad \mathcal{E}_P^{\text{max}} = \max(\mathcal{E}_P), \quad (5.4)$$

with

$$\mathcal{E}_{Q,\text{Ref}}^n = \left| \frac{Q_{\text{Ref}}^n - Q^n}{\max(Q_{\text{Ref}})} \right|, \quad \mathcal{E}_{P,\text{Ref}}^n = \left| \frac{P_{\text{Ref}}^n - P^n}{P_{\text{Ref}}^n} \right|.$$

where the operators $\text{mean}(\cdot)$ and $\max(\cdot)$ calculate the mean and maximum values, respectively, over all the performed time steps of the last cardiac beat, while Q_{Ref} and P_{Ref} can be either experimental or numerical reference data.

From the analysis of the values in Table 5.2 we observe that the numerical average errors are approximately between 2% and 3%, for the pressure, and between 3% and 4%, for the flow rate, with a peak of 8% in the left renal artery. This confirms the preliminary impression that the two numerical models are in good agreement with each other, despite the fact that the numerical schemes used for the solution of problem (1.16) are different. Regarding the experimental comparison, the average pressure error is still quite small, between 2% and 5%. However, the mean flow rate error ranges approximately from 7% to 25%, which is quite severe. On the one hand, these differences are justified in Matthys et al. (2007) by the fact that the experimental flow measurements are less precise than experimental pressure ones. On the other hand, these discrepancies are also due to the simplifications in the 1-D model, where for instance the viscoelastic term has been neglected. Indeed, among the positive aspects we observe that the frequency of the numerical oscillations mimics the experimental results (see, e.g., the splenic artery in Figure 5.6).

5.2. Assessment of 1-D FSI numerical simulations against published data

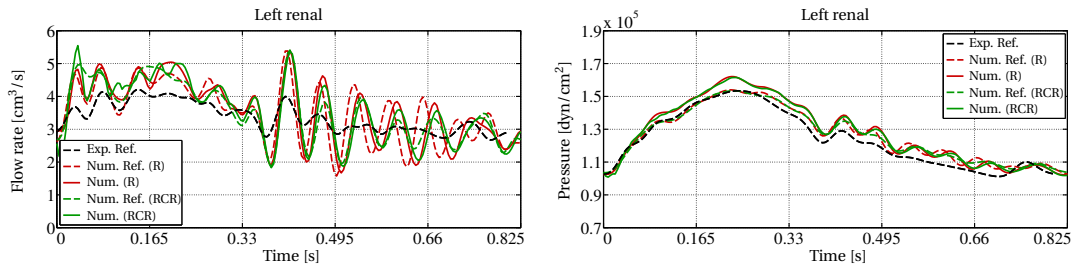


Figure 5.8: Periodic flow rate and pressure comparison at the left renal artery. Red and green lines represent numerical results with purely resistive (R) and resistive-compliant (RCR), respectively, terminals. In both cases the viscoelastic effects of the arterial wall have been neglected.

Finally, with the aim of studying the effect of the peripheral compliance on the global network, we replaced the purely resistive terminals with the three-element windkessel model described in Section 5.2.2, where the compliance of all the terminals is set equal to $10^{-6} \text{ cm}^5/\text{dyn}$. The results of this comparison for the left renal artery is shown in Figure 5.8, where we observe that the effect of the compliance on the waveform is almost negligible, even if a slightly decrease in the amplitude of the non-physical oscillations is visible.

5.2.4 Viscoelastic wall simulations

In the previous section we have shown the ability of the purely elastic nonlinear 1-D model to capture the main features of pressure and flow rate waveforms measured in the experimental setting. Nevertheless, the lack of viscoelasticity in the model introduces some non-physical oscillations, especially in the vessels close to the terminal nodes. For this reason in this section we extend our results by including the viscoelastic effects in the wall model, comparing our numerical simulations with both the same experimental setting and the numerical reference data provided in Alastruey et al. (2011). The set up of the simulation is the same as before and the viscoelastic parameters are given in Table 5.1.

In Figure 5.9 we compare the flow rate and pressure waveforms in the four arterial segments shown in Alastruey et al. (2011, Figure 1). As before, we remark that the terminal elements in both the experimental and numerical settings are purely resistive. First of all, the results of our numerical simulations are again in good agreement with the reference numerical results. In addition, comparing the elastic (red lines) and the viscoelastic (green lines) wall models we observe that the presence of viscoelasticity provides, as expected, a significative reduction of the non-physical oscillation, especially in the small distal vessels (see, e.g., the left renal artery in Figure 5.9); indeed, this is in agreement with the increase of the viscoelastic in term (1.17) when decreasing the cross-section area of the vessel.

Regarding the error analysis reported in Table 5.3 we have an evident reduction of the average and maximum flow rate errors. In particular the numerical average errors are now approximately between 2% and 3%, with a peak of 5.6% in the right carotid artery, while the experimental average error ranges from 8% to 14%. Also the pressure shows a small error reduction compared to the previous case.

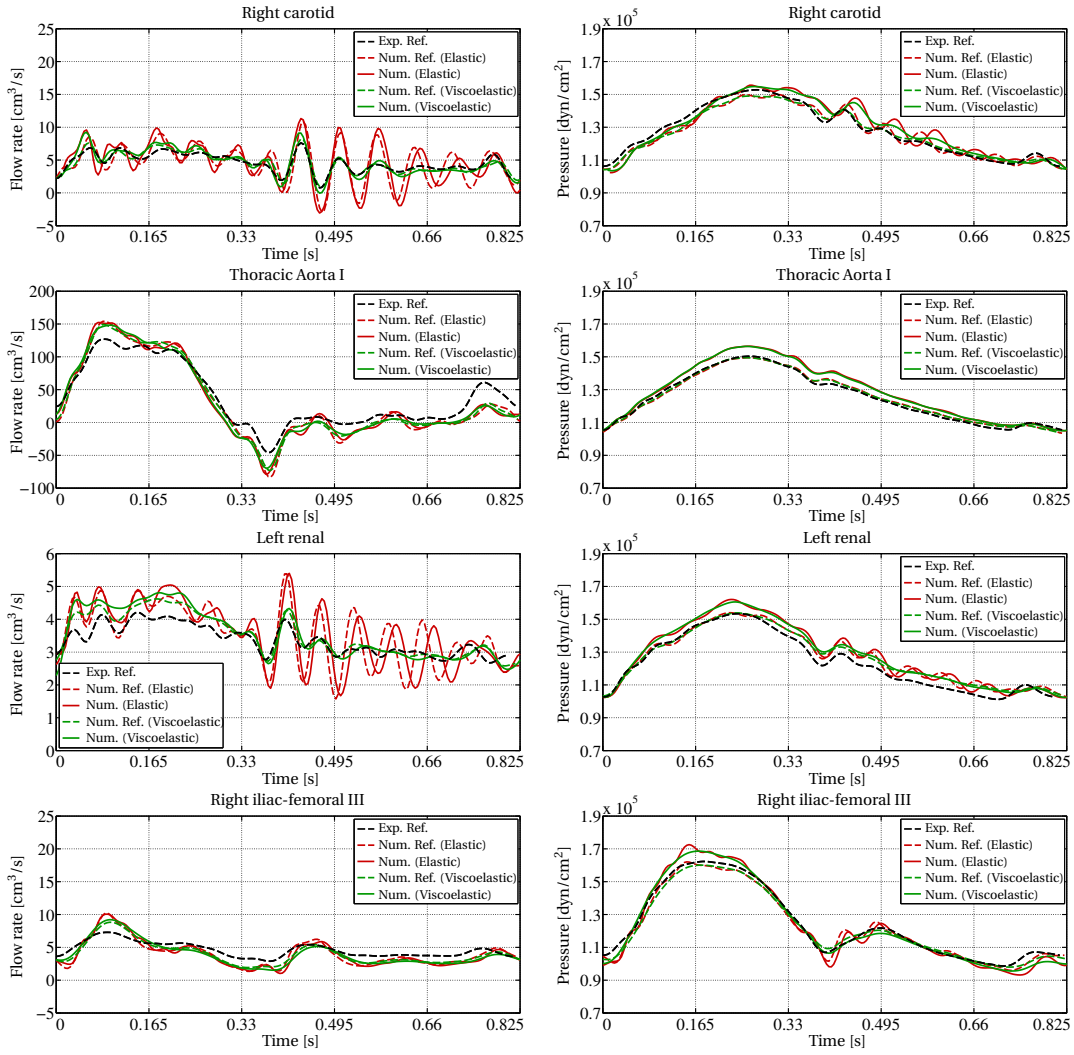


Figure 5.9: Periodic flow rate and pressure comparison at four different arterial segments. Red and green lines are numerical results with elastic and viscoelastic, respectively, arterial wall models. In both cases the terminals are purely resistive elements.

Table 5.3: Relative percentage errors (see equations (5.4)) between the numerical results obtained by using the methodology described in this work and the reference experimental (Exp.) and numerical (Num.) data, for the 1-D arterial segments shown in Figure 5.9. In the numerical models the viscoelastic effects of the arterial wall have been considered.

Arterial segment	$\mathcal{E}_Q^{\text{mean}}$ [%]		$\mathcal{E}_Q^{\text{max}}$ [%]		$\mathcal{E}_P^{\text{mean}}$ [%]		$\mathcal{E}_P^{\text{max}}$ [%]	
	Exp.	Num.	Exp.	Num.	Exp.	Num.	Exp.	Num.
Right carotid	7.8	5.7	36.7	25.4	2.9	2.3	9.7	8.0
Thoracic aorta I	11.4	3.0	28.2	11.2	3.1	2.8	5.3	4.6
Left renal	7.9	2.5	26.4	10.2	4.2	1.8	7.1	4.7
Right iliac-femoral III	13.7	3.4	26.7	6.3	2.2	2.5	7.9	5.5

5.3 1-D modeling of the human arterial tree

In this section we present several numerical simulations of a full human arterial tree, whose data are provided in Reymond et al. (2009). The aim is to use this complex network to set up different analyses regarding both the modeling and the algorithmic aspects. One of the main focus of this study concerns the behavior of the two-level time step technique introduced in Chapter 3 when applied to 1-D networks of arteries. In addition, we also compare the solution of the problem for different configurations and interface equations.

5.3.1 Model predictions

The arterial network provided in Reymond et al. (2009, Figure 2 and Table 2) is composed by 103 elements (24 aortic, 4 coronary, 51 cerebral, 10 upper limbs, and 14 lower limbs) and includes all the values of the parameters required to describe the blood flow, such as the data for the terminals, which are modeled as three-element windkessel elements (see Section 5.2.2), and the geometrical properties of the vessels (length and proximal/distal areas). These values have been obtained from both *in vivo* measurements and averaged data from the literature. We remark that the proximal/distal areas data are used to impose a linear variation of the reference radius along the vessels.

Regarding the parameters of the wall, since we use a different model with respect to that used in Reymond et al. (2009), we estimate these values from other sources. In particular, the value of the Young's modulus for each arterial segment has been taken from Avolio (1980) (for the body and the cerebral parts) and from Huo and Kassab (2007) (for the coronaries). The Poisson's ratio has been set equal to 0.5, as the arterial wall is assumed to be incompressible. The thickness of the vessels wall has been estimated to be equal to five percent of the local lumen diameter, which is a commonly accepted approximation (see, e.g., Langewouters (1982)), leading to a non-uniform distribution of the coefficient β_S along the narrowed segments. Regarding the viscoelastic properties, we set the viscoelastic angle equal to 10° for all the vessels, while the systolic period (for the prescribed flow) is equal to 0.24 s. Note that, to enhance the comparison with the results presented in Reymond et al. (2009), we impose the same time-dependent volumetric flow rate at the inflow of the arterial network.

Finally, the other parameters that define the problem are: $\rho_F = 1.04 \text{ g/cm}^3$, $\mu_F = 0.035 \text{ g/cm/s}$, $P_{\text{ext}} = 100000 \text{ dyn/cm}^2$, and $P_V = 6666 \text{ dyn/cm}^2$; these are typical values in blood flow simulations. The power law coefficient θ is set equal to 9, leading to a constant in time velocity profile characterized by a Coriolis coefficient α_F equal to 1.1. The value of the main parameters of the 1-D network of arteries is summarized in Table 5.4.

Regarding the time discretization, the outer time step is set equal to 10^{-3} s, while the inner time step is computed to meet the local stability requirements, and is different in each segment; more precisely, the ratio between inner and outer time steps ranges approximately from 0.1 to 0.02. At the 99 coupling nodes of the network (52 to connect the 1-D arterial segments, plus 47 to connect the windkessel terminals) the set of equations (2.2) is imposed through mean normal stress boundary data on all the coupling interfaces (i.e., $n_c^Q = 0$, $c = 1, \dots, 99$).

Figures 5.10 and 5.11 show the global and the cerebral views of the result obtained for the full 1-D arterial tree. The results refer to the last of seven cardiac cycles, when the periodic regime has been reached. From the analysis of the images, we can observe that the results of our simulation match the ones given in Reymond et al. (2009, Figures 4 and 5), even if some differences are present due to the

Table 5.4: Main parameters of the 1-D network of arteries. For the geometrical properties of the vessels and the data of the terminals see Reymond et al. (2009, Figure 2 and Table 2).

ρ_F	Blood density	1.04 g/cm ³
μ_F	Blood viscosity	0.035 g/cm/s
κ_F	Friction coefficient	2.326 cm ² /s
α_F	Coriolis coefficient	1.1
P_{ext}	Reference external pressure	100000 dyn/cm ²
P_V	Venous pressure	6666 dyn/cm ²
h_S/D_F	Wall thickness / lumen diameter	0.05
E_S	Young's modulus	$3 - 12 \cdot 10^6$ dyn/cm ²
ν_S	Poisson's ratio	0.50
ϕ_S	Viscoelastic angle	10 degrees
T_S	Systolic period	0.24 s
	Heart rate	75 bpm

different choice of the arterial wall model. Nevertheless, the predictions of our model are accurate, especially when compared with the averaged *in vivo* measurements. Since the validation of this model is not a matter of this work, no further comments are added here: indeed, a patient-specific validation of the network is given in Reymond et al. (2011).

5.3.2 Error analysis

To assess the accuracy of the numerical predictions of volumetric flow rate and pressure when using the two-level time step technique, we make a comparison with the solution of the same problem when the outer time step is equal to the inner time step, i.e., no inner time steps are performed. Note that in the former case the required number of inner time steps is different for each 1-D segment, since it is computed automatically on the basis of the local stability condition (see equation (1.20)) and of the local properties of the element. Therefore, to avoid performing inner time steps in all the segments, the outer time step must be small enough to satisfy the stability condition in the most restricting vessel of the network. Being $\Delta t_{2\text{-level}} = 10^{-3}$ s the global time step used for the case when the inner time step differs from the outer time step, and $\Delta t_{1\text{-level}} = 10^{-5}$ s the one chosen in order to have the outer time step equal to the most restrictive inner time step, we calculate the relative error between the two cases at each time $t_{2\text{-level}}^n = n\Delta t_{2\text{-level}}$, $n = 0, 1, 2, \dots$, by using the quantities (5.4) with

$$\mathcal{E}_Q^n = \left| \frac{Q_{2\text{-level}}^n - Q_{1\text{-level}}^n}{\max(Q_{1\text{-level}})} \right|, \quad \mathcal{E}_P^n = \left| \frac{P_{2\text{-level}}^n - P_{1\text{-level}}^n}{P_{1\text{-level}}^n} \right|.$$

From the analysis of the values in Table 5.5, we can observe that the average pressure error $\mathcal{E}_P^{\text{mean}}$ and the maximum pressure error $\mathcal{E}_P^{\text{max}}$ are always less than 0.5% and 1.0%, respectively. Regarding volumetric flow rate, the average error $\mathcal{E}_Q^{\text{mean}}$ is less than 0.5% in most of the segments, and never above 2.0%. The maximum error $\mathcal{E}_Q^{\text{max}}$ is in general around 1.0%, with a maximum of 2.5%. Increasing the order of the interpolation, the magnitude of the value does not change significantly. In view of these values, we confirm the preliminary result in Section 4.3.2, i.e., in a cardiovascular setting, where the wavelengths are long, a linear interpolation at the level of the inner time steps leads to accurate results without significant numerical reflections.

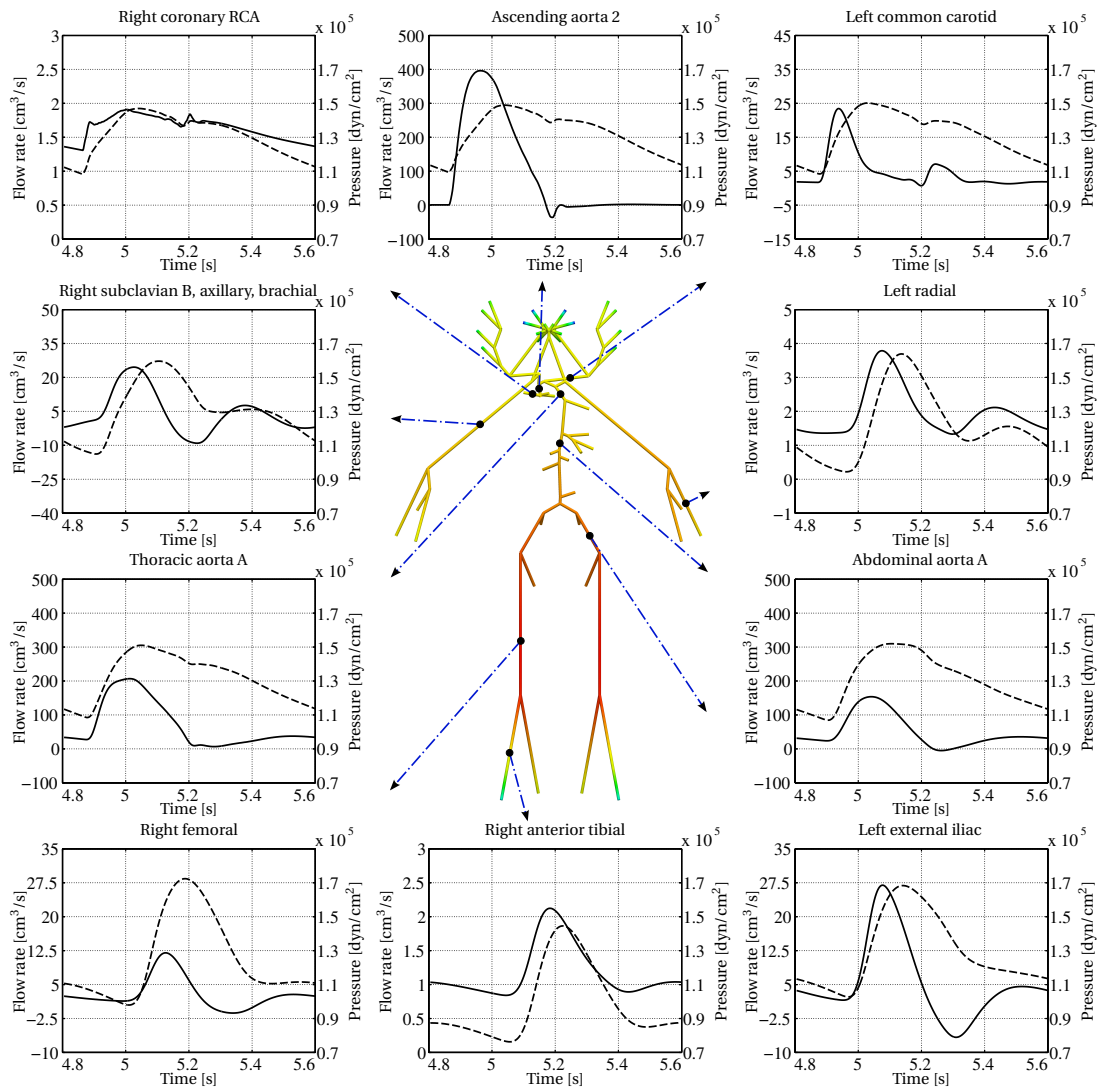


Figure 5.10: Periodic flow rate (solid line) and pressure (dashed line) results in ten different arterial segments. The color in the central image represents the pressure field at the end-systole of the seventh heart beat ($t = 5.2$ s), where the color bar ranges from blue (80000 dyn/cm^2) to red (175000 dyn/cm^2). Positioning of 1-D network elements is purely visual.

5.3.3 Modeling analysis

As we already discussed in Chapter 1, the inclusion of the viscoelastic effect and of the local variation of the radius (and eventually of other properties) along the vessel, leads to an increase of the complexity of the model. In particular, the differential nature of the viscoelastic term requires the introduction of an operator splitting technique for the solution of the numerical problem (see Section 1.2.3), while the axial dependence of the reference area leads to a more complex formulation for the compatibility conditions (see Section 1.2.4). In view of these considerations, we may wonder if these enrichments are really necessary to capture the true physics of the cardiovascular circulation.

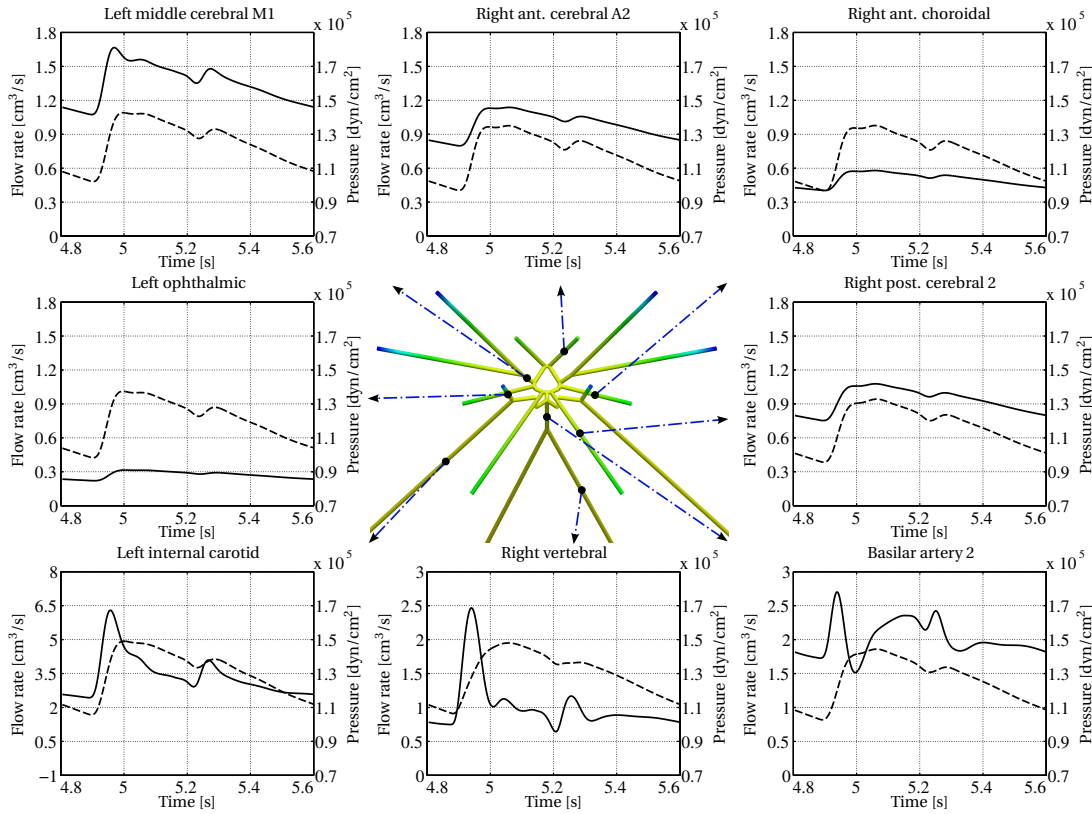


Figure 5.11: Enlarged view on the cerebral region in Figures 5.10 showing the periodic flow rate (solid line) and pressure (dashed line) results in eight different cerebral arterial segments. The color in the central image represents the pressure field at the end-systole of the seventh heart beat ($t = 5.2$ s), where the color bar ranges from blue (80000 dyn/cm^2) to red (175000 dyn/cm^2). Positioning of 1-D network elements is purely visual.

To answer this question, we perform a comparison between the results presented in Section 5.3.1 and the ones obtained by removing these features from the model. In particular, we set up three models corresponding to three different configurations.

Model 1: the segments in the 1-D network include both the elastic and viscoelastic wall effects. An axial linear variation of the reference radius and, consequently, of the wall thickness is present on most of the vessels, using the data in Reymond et al. (2009).

Model 2: the segments in the 1-D network include only the elastic wall effect. An axial linear variation of the reference radius and, consequently, of the wall thickness is present on most of the vessels, using the data in Reymond et al. (2009).

Model 3: the segments in the 1-D network include only the elastic wall effects. In each segment the radius and the wall thickness are averaged and considered constant along the vessel.

The results of this comparison are shown in Figures 5.12 and 5.13. As we can see, a purely elastic model of the wall (red lines) induces additional reflections along the segments, which are not damped by the viscoelastic behavior. These reflections are further amplified when the narrowed elements are replaced by equivalent segments with a uniform reference area (blue lines). Neglecting the variation

Table 5.5: Relative percentage errors (see equations (5.4)) between the results obtained by using the two-level time step technique (with a model dependent number of inner time steps per outer time step), with respect to those where the outer time step is equal to the inner time step, i.e., no inner time steps are performed. The errors are computed for all the 1-D arterial segments presented in Figures 5.10 and 5.11. A linear interpolation is used for the inner time steps.

Arterial segment	$\varepsilon_Q^{\text{mean}}$ [%]	$\varepsilon_Q^{\text{max}}$ [%]	$\varepsilon_P^{\text{mean}}$ [%]	$\varepsilon_P^{\text{max}}$ [%]
Ascending aorta 2	0.0	0.1	0.4	0.5
Thoracic aorta A	0.2	0.5	0.3	0.4
Abdominal aorta A	0.2	0.5	0.3	0.3
Left common carotid	0.2	0.7	0.3	0.4
Right coronary RCA	0.3	0.6	0.3	0.5
Right subclavian B, axillary, brachial	0.2	0.6	0.1	0.2
Left radial	0.1	0.3	0.2	0.3
Left external iliac	0.3	1.0	0.2	0.3
Right femoral	0.3	0.9	0.2	0.4
Right anterior tibial	0.2	0.6	0.2	0.4
Left internal carotid	0.5	1.0	0.2	0.4
Right vertebral	0.9	1.8	0.2	0.3
Basilar artery 2	1.4	2.5	0.1	0.2
Right ant. cerebral A2	0.2	0.6	0.2	0.6
Left middle cerebral M1	0.3	0.6	0.2	0.4
Right post. cerebral 2	0.2	0.5	0.2	0.5
Right ant. choroidal	0.2	0.6	0.2	0.5
Left ophthalmic	1.8	2.0	0.2	0.6

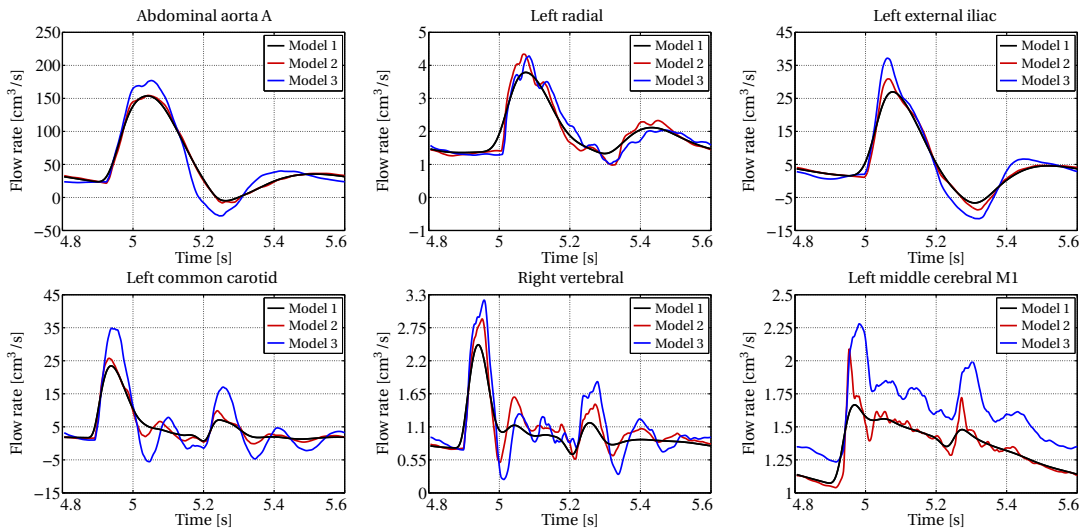


Figure 5.12: Flow rate comparison between Model 1 (same as in Figures 5.10 and 5.11), Model 2, and Model 3 in six selected 1-D segments.

of the vessels radius (Model 3) produces the largest differences in term of flow rate and, at the left external iliac, an overshoot of the pressure. We thus conclude that both ingredients are mandatory for the correct prediction of the physical quantities, as already stated in Reymond et al. (2009).

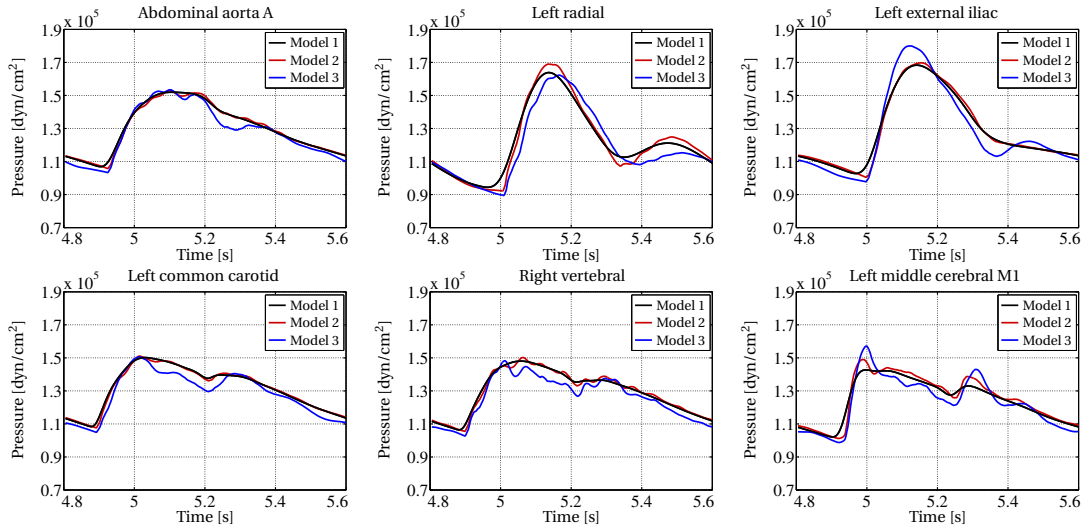


Figure 5.13: Pressure comparison between Model 1 (same as in Figures 5.10 and 5.11), Model 2, and Model 3 in six selected 1-D segments.

5.3.4 Iterations and CPU time analyses

To assess the efficiency of the methodology presented here, we compare the number of iterations and the CPU time required by the different algorithms to solve the full 1-D arterial network. Since all the 99 local interface problems are written in terms of conservation of flow rate and continuity of mean normal stress, and in addition $n_c^Q = 0$, $c = 1, \dots, 99$, the resulting global coupled problem is composed of 99 interface variables. Even if this number is relatively small, it represents the implicit coupling of 150 models (103 1-D segments plus 47 windkessel terminals) in a complex network topology (which includes bifurcations and closed loops).

The 1-D FSI segments are uniformly discretized in space. In most of the vessels the mesh size is 0.1 cm, while in the shortest elements ($L \leq 0.5$ cm) it is further reduced to have at least 5 nodes in each segment. All the simulations presented in this section have been performed on one cluster node with two Intel[®] Xeon[®] processors X5550 (quad core, 8 MB cache, 2.66 GHz CPU). We remark that the number of processors and nodes used to solve the global problem does not have any effect on the amount of nonlinear Richardson iterations required for the convergence (obviously).

First of all, in Figure 5.14 we observe that the number of iterations required for the convergence to the solution of the global problem (up to an imposed tolerance of 10^{-6} , see equation (2.10)) is always higher in the graphs in the second line (two-level time step technique, using an outer time step equal to 10^{-3} s) with respect to the ones in the first line (no inner time steps, using an outer time step equal to 10^{-5} s). This behavior is more evident for the Broyden method rather than for the Newton one. Moreover, when the inner time step is different from the outer time step, the approximated 1-D tangent problem worsen the accuracy of the Jacobian matrix and the convergence is compromised.

In the second place, we also compare the results given by simplifying the model, first neglecting the viscoelastic effect (second column) and then averaging the radius along the narrowed vessels (third column). The first approximation should decrease the number of iterations, since the nonlinearities of the viscoelastic term disappear. However, comparing Figure 5.14d with Figure 5.14e we observe this behavior only during the systolic phase, while in the diastolic one the number of iterations increases.

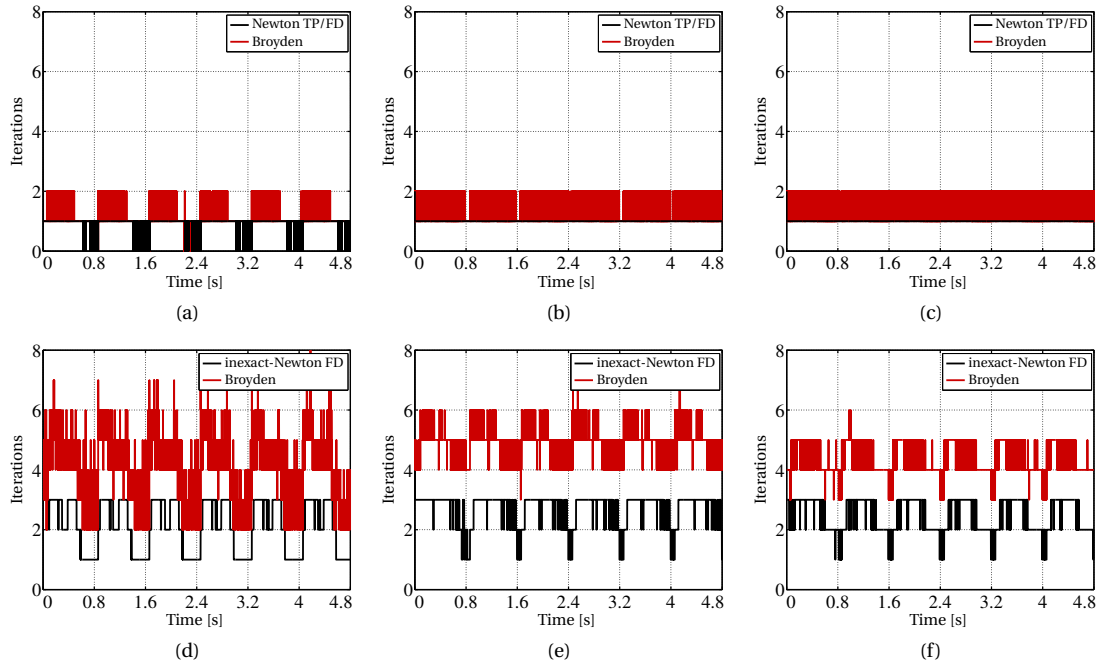


Figure 5.14: Comparison, in terms of number of iterations, of different algorithms for the coupling of the full 1-D arterial network. The acronyms FD and TP stand for finite difference and tangent problem, respectively, and refer to the methods used for the computation of the 1-D Jacobian entries. In both cases, the entries related to the windkessel elements are computed analytically. The first six heart beats are shown. (a,b,c) Cases without inner time steps. (d,e,f) Cases with inner time steps. (a,d) Model 1. (b,e) Model 2. (c,f) Model 3.

Table 5.6: Average number of iterations over six heart beats for different models and numerical algorithms (see Figure 5.14 for more details). Note that the average number of iterations is less than one for the case of the one-level time step technique applied to Model 1. This is due to the fact that, with such a small time step, it may happen that the tolerance is satisfied without any implicit iteration over the coupling quantities.

Model	One-level time step			Two-level time step		
	TP	FD	Broyden	TP	FD	Broyden
1	0.87	0.87	0.94	–	2.11	4.02
2	1.00	1.00	1.20	–	2.70	4.82
3	1.00	1.00	1.25	–	2.49	4.37

This can be justified by observing the curves in Figures 5.12 and 5.13, where the lack of viscoelastic effects leads to the introduction of some oscillations along the network. On the contrary, averaging the radius along the vessels seems to slightly speed up the convergence.

The results of these comparisons can be further summarized by averaging the number of iterations over the entire simulation, as done in Table 5.6. More precisely, comparing the results of Table 5.6 with the ones presented in Figure 4.8 we observe that, even if the simulated cardiovascular network of arteries is composed by more than 100 elements, the average number of iterations required for the solution of the global problem is almost the same of the very simple case with just two elements.

Table 5.7: Relative CPU time over six heart beats for different models and numerical algorithms (see Figure 5.14 for more details).

Model	One-level time step			Two-level time step		
	TP	FD	Broyden	TP	FD	Broyden
1	1.00	1.45	0.85	–	0.28	0.20
2	1.00	1.46	0.92	–	0.29	0.20
3	1.01	1.45	0.96	–	0.27	0.18

Finally, in Table 5.7 we compare the CPU time of the same simulations normalized over the CPU time needed by the reference case, i.e., Model 1 solved without the two-level time step technique and using the exact tangent problem method. First of all, it is evident that the two-level time step technique leads to a sensible reduction of the CPU time required for the solution of the global problem. This is due to the fact that each 1-D segment chooses its local time step according to the local stability requirements, rather than advancing with the time step imposed by needs of the global network of elements. Moreover, despite the higher average number of iterations (see Table 5.6), the Broyden method is faster than the finite difference approximation. Indeed, the update of the Jacobian matrix with the Broyden method is very cheap as shown in Algorithm 2.2, thus reducing the time for each iteration. Regarding the one-level time step approach, we notice that the Broyden method is still the fastest. Nevertheless, in this case the difference between the exact tangent problem approach and the Broyden method is not so evident.

5.3.5 Interface equations comparison

The last analysis we present is a numerical comparison between the results obtained by imposing the continuity of the mean normal stress at all the coupling nodes, with respect to those given by enforcing the continuity of the mean total normal stress at the interfaces between the 1-D segments. Note that, in both configurations, the continuity of the mean normal stress is imposed at the 47 coupling nodes between the distal 1-D segments and the corresponding windkessel terminals.

The results of this comparison are shown in Figure 5.15. From the images it is evident that the contribution of the kinetic term in the interface equations is negligible in cardiovascular problems. The most significant difference is visible in the right vertebral artery. However, even there the two solutions are very similar. By using the quantities (5.4) we can quantify the difference between the two cases. In particular, by assuming as a reference case the continuity of mean total normal stress, we define the following relative error quantities

$$\varepsilon_Q^n = \left| \frac{Q_S^n - Q_{\mathcal{T}}^n}{\max(Q_{\mathcal{T}}^n)} \right|, \quad \varepsilon_P^n = \left| \frac{P_S^n - P_{\mathcal{T}}^n}{P_{\mathcal{T}}^n} \right|,$$

where, with an abuse of notation, the subscripts \mathcal{S} and \mathcal{T} refer to the imposed set of interface equations.

From the analysis of the data in Table 5.8 we can observe that the average flow rate and pressure relative differences are very small, i.e., less than 1.0% and 0.5%, respectively, in most of the segments. Regarding the maximum differences they are also bounded; for instance, in the right vertebral artery we have a maximum difference of approximately 4.5%, which corresponds to the difference in the systolic peak observed in Figure 5.15. From these results we can conclude that continuity of mean normal stress (together with conservation of flow rate) is a sufficient condition at the network junctions to correctly predict the flow and pressure wave propagation in a network of 1-D arteries. This result is later extended in Section 5.4.2.5 to the case of heterogeneous FSI cardiovascular problems.

5.3. 1-D modeling of the human arterial tree

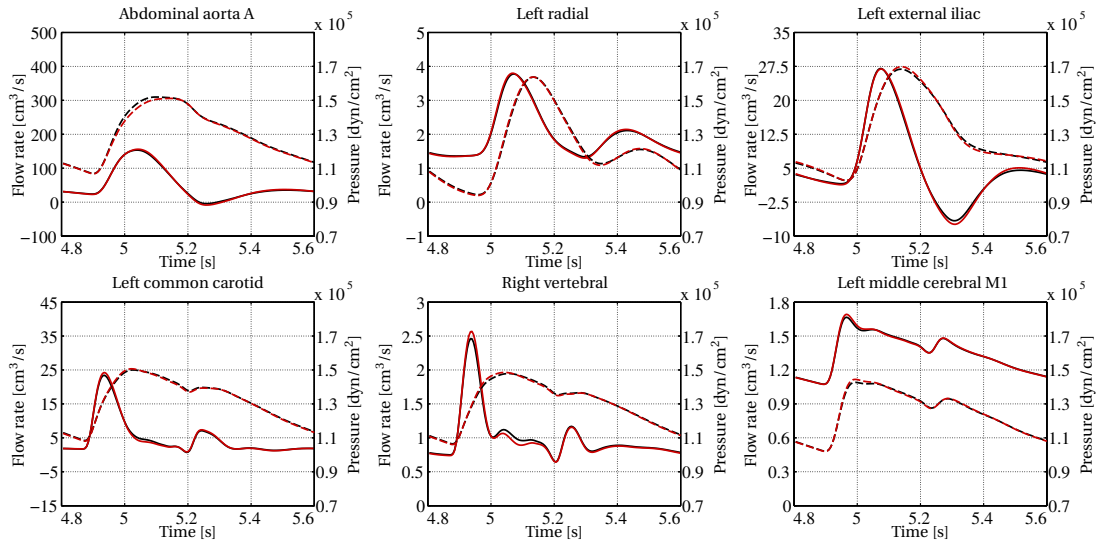


Figure 5.15: Comparison, in terms of flow rate (solid lines) and pressure (dashed lines), between the results obtained by imposing the continuity of the mean normal stress at all the coupling nodes (black lines: same as in Figures 5.12 and 5.13), with respect to those given by enforcing the continuity of the mean total normal stress at the interfaces between the 1-D segments (red lines).

Table 5.8: Relative percentage errors (see equations (5.4)) between the results obtained by imposing the continuity of the mean normal stress at all the coupling nodes, with respect to those given by enforcing the continuity of the mean total normal stress at the interfaces between the 1-D segments. The errors are computed for all the 1-D arterial segments presented in Figures 5.10 and 5.11. The two-level time step technique (with linear interpolation) is used in both cases.

Arterial segment	$\mathcal{E}_Q^{\text{mean}}$ [%]	$\mathcal{E}_Q^{\text{max}}$ [%]	$\mathcal{E}_P^{\text{mean}}$ [%]	$\mathcal{E}_P^{\text{max}}$ [%]
Ascending aorta 2	0.1	0.2	0.3	0.6
Thoracic aorta A	0.9	2.1	0.4	0.7
Abdominal aorta A	1.1	2.7	0.5	2.1
Left common carotid	0.9	3.7	0.3	0.7
Right coronary RCA	0.4	0.9	0.4	0.7
Right subclavian B, axillary, brachial	1.2	2.6	0.4	1.0
Left radial	0.7	2.2	0.5	1.1
Left external iliac	1.2	2.9	0.5	1.2
Right femoral	1.2	2.8	0.6	1.6
Right anterior tibial	0.6	1.5	0.7	1.9
Left internal carotid	0.5	1.8	0.3	0.9
Right vertebral	1.0	4.5	0.4	1.2
Basilar artery 2	0.9	3.2	0.4	1.3
Right ant. cerebral A2	0.5	0.9	0.5	0.9
Left middle cerebral M1	0.3	1.6	0.3	1.2
Right post. cerebral 2	0.4	1.1	0.4	1.0
Right ant. choroidal	0.3	1.0	0.4	0.9
Left ophthalmic	0.5	0.9	0.5	0.9

5.4 Numerical comparison and calibration of geometrical multiscale models

Despite the geometrical multiscale modeling idea is rather established, so far the greatest part of the existing literature has focused mainly on the mathematical and methodological aspects rather than on the application to patient-specific cardiovascular problems. In addition, at the best of our knowledge, evidence of the benefit of such a more complex model with respect to simplified problems, e.g., stand-alone 3-D FSI simulations of local compartments, has been neither directly investigated nor quantified by numerical comparisons in real cardiovascular problems.

To fill this gap, we provide several numerical comparisons of geometrical multiscale models with the aim of proving, and somehow quantifying, the benefits of such complex dimensionally-heterogeneous problems with respect to other simpler approaches. The geometrical multiscale models are set up by coupling one or more 3-D patient-specific geometries with the full network of 1-D models described in Section 5.3 (see Table 5.4 for the main parameters), which represents the global circulation of an average healthy patient. In particular, since the analysis of pathological scenarios is not considered here, we select two healthy 3-D geometries corresponding to the aorta and the iliac arteries. The results of these models are compared with both a full 1-D network of arteries and stand-alone 3-D FSI simulations, where, for the latter, the data at the inlet and outlet boundary interfaces are taken from a precomputed full 1-D network simulation. The comparisons are performed mainly in terms of flow rate and pressure waveforms. In addition, we also analyze the 3-D solid wall displacement magnitude.

On a slightly different context, we also focus on the calibration of cardiovascular simulations. Indeed, as discussed in Chapter 1 one critical aspect to get physiological results is the tuning of the problem parameters, especially for modeling 3-D FSI arteries. In this regard, it is essential to account for the correct boundary data on the the solid wall geometries. This problem has been already addressed in Crosetto et al. (2011b) and Moireau et al. (2012) for the external surface of the arterial wall (see Section 1.1.2), where Robin boundary conditions have been successfully used to account for the elastic and viscoelastic responses of the external tissues. Nevertheless, the values of the empirical tissue parameters appearing at the boundaries is rather difficult to estimate, and neither calibration procedures nor sensitivity analysis to show the effect of the variation of the parameters on the main quantities of interest were provided. Regarding the interface boundary rings of the arterial wall, Formaggia et al. (2007) proposes a method to prescribe the continuity of the vessel area with surrounding models (see Section 1.1.3). However, its impact on cardiovascular simulations compared to fixed area configurations has never been investigated, apart from few benchmark tests in simple geometries, such as those described in Chapter 4.

With the aim of covering the aspects mentioned above, in the following we also provide several comparisons and sensitivity analysis focused both on the calibration of the tissue parameters (extending the preliminary results in Malossi et al. (2011a)) and on the analysis of the impact of different interface ring boundary conditions on the main quantities of interest.

5.4.1 Geometry reconstruction and mesh generation

To set up the geometrical multiscale models we select two main patient-specific arteries: the aorta and the iliac of two healthy patients. These geometries have several bifurcations and some severe bends, such that the 3-D dynamics of the blood is not negligible.

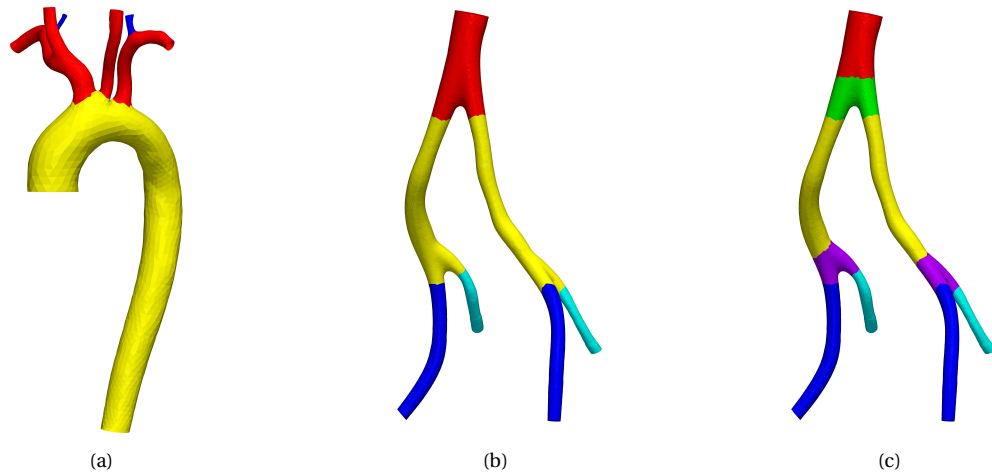


Figure 5.16: View of the aorta and iliac geometries with wall regions. (a) The aorta is divided in three regions: aortic arch (yellow), carotids and subclavians (red), and vertebrals (blue). (b) The iliac is divided in four regions: abdominal aorta (red), common iliac (yellow), external iliac (blue), and inner iliac (cyan). (c) Same as (b) with two additional regions at the bifurcations: abdominal aorta bifurcation (green) and common iliac bifurcations (magenta).

Table 5.9: Wall parameters of the 3-D FSI arteries. The Young's modulus of the 3-D FSI aorta and iliac is 3000000 dyn/cm^2 in all the branches apart from the vertebral arteries, where it is 6000000 dyn/cm^2 , and inner iliac arteries, where it is $12000000 \text{ dyn/cm}^2$.

ρ_S	Wall density	1.2 g/cm^3
h_S/D_F	Wall thickness / lumen diameter	0.05
E_S	Young's modulus	$3 - 12 \cdot 10^6 \text{ dyn/cm}^2$
ν_S	Poisson's ratio	0.48

The segmentation of the aorta was obtained through MRI Time of Flight acquisition on a 3T MRI scanner (Siemens Trio-Tim 3T System); details on the used sequences are given in Reymond et al. (2011). Then, the arterial lumen was reconstructed in 3-D from MRI magnitude data (ITK Snap software). Since the thickness of the wall is not visible in MRI data, it had to be synthetically reconstructed. In particular, it has been estimated to be equal to five percent of local lumen diameter, which is a commonly accepted approximation (see, e.g., Langewouters (1982)). Regarding the iliac, the geometry of the lumen has been taken from the Simtk website⁴, and the thickness of the wall has been reconstructed with the same assumptions used for the aorta.

To correctly model the different material properties of the arterial wall and of the external tissues, we divide the solid domains into several regions, which are schematically shown in Figure 5.16. Note that for the iliac geometry we provide two different configurations, which are later used in Section 5.4.2.2 for a numerical comparison of the results as a function of the tissue parameters at the bifurcations. The main wall parameters that define the 3-D problems are summarized in Table 5.9.

⁴<http://simtk.org>.

Finally, for each arterial vessel two separate conforming fluid and solid geometries have been generated using the VTK⁵, VMTK⁶, and ITK⁷ libraries, as detailed in Faggiano et al. (2012). The resulting mesh of the fluid part of the 3-D aorta consists of 280199 unstructured tetrahedral elements with 50866 vertices, while the solid part is made of 278904 structured tetrahedral elements with 58565 vertices. The corresponding average space discretizations for both the fluid and solid problems is 0.158 cm. Regarding the 3-D iliac, the mesh of the fluid part consists of 350376 unstructured tetrahedral elements with 63716 vertices, while the solid part is made of 359256 structured tetrahedral elements with 60788 vertices. In this case, the corresponding average space discretizations for both the fluid and solid problems is 0.076 cm. All the simulations presented in the following sections have been performed on several cluster nodes with two Intel[®] Xeon[®] processors X5550 (quad core, 8 MB cache, 2.66 GHz CPU) each, interconnected by a 20 Gb/s InfiniBand[®] architecture.

5.4.2 Geometrical multiscale modeling

In this section we set up three different geometrical multiscale models where the 3-D patient-specific vessels in Figure 5.16 are embedded in the 1-D network described in Section 5.3, which represents an average healthy patient. To set up the models we use the following procedure. First of all, we identify the 1-D elements of the network to be removed or cut, since they overlap with some regions of the 3-D patient-specific geometries. This is done by measuring the length of the different branches of the 3-D vessels and comparing these data with the one of the 1-D network. Obviously, this phase presents several degrees of freedom and arbitrariness. The degree of precision of this step also depends on the region of interest and the required level of accuracy (e.g., rough evaluation of flow versus precise local quantification for surgery planning). In a clinical context this operation should be supervised by the clinician in order to immediately determine the crucial regions for the numerical simulations. Once the 1-D elements are cut, the second step consists in changing the reference area and the wall thickness of the 1-D arteries to match the one of the nearby 3-D interfaces. Since the 3-D geometries are not symmetric, it is possible that some asymmetries are introduced also in the 1-D networks (e.g., between the left and right external iliac arteries). Moreover, it is important to check that the resulting distal area is always smaller or equal than the proximal one. If it is not the case, some further adjustments to the 1-D elements are required to avoid non-physiological pressure wave reflections in those arteries. Finally, the coupling among the vessels is set up through one of the sets of interface equations described in Chapter 2, with $n_c^Q = 0$, $c = 0, 1, 2, \dots$; unless otherwise specified, at the interfaces between the models we impose conservation of flow rate and continuity of mean normal stress.

5.4.2.1 External tissues parameters comparisons: 3-D aorta

In this section we focus on the study of the external tissues parameters k_s and c_s introduced by the Robin boundary condition on the arterial wall of the 3-D FSI problem, as described in Section 1.1.2. For this analysis, we consider a geometrical multiscale model assembled by coupling the 3-D aorta in Figure 5.16a with the 1-D arterial tree described in Section 5.3. For the sake of simplicity, the results presented in this section are obtained by fixing the position of the boundary solid rings of the 3-D arterial wall of the aorta, i.e., by imposing (1.6) for $j = 1, \dots, n_{FS}^F$.

⁵<http://www.vtk.org>.

⁶<http://www.vmtk.org>.

⁷<http://www.itk.org>.

5.4. Numerical comparison and calibration of geometrical multiscale models

The first study we perform consists of a sensitivity analysis of the main quantities of interest with respect to a variation of the elastic parameter k_S . This is done by assuming $c_S = 0$ and choosing five sets of values for the coefficient k_S at the different branches of the aorta, as detailed in Table 5.10. Note that the values of the different cases are chosen as multiples of those of case E_1^A .

The results of this comparison, at the most significant coupling interfaces between the 3-D aorta and the 1-D network, are summarized in Figure 5.17, where we also plot the result of the full 1-D arterial network as an indicative reference case. First of all, we observe that the behavior of the flow rate is quite different in each of the five considered cases. At the thoracic aorta the elastic tissues parameters of case E_1^A seem to be not stiff enough to correctly capture the cardiovascular wave pulse. This is confirmed by the analysis of the displacement magnitude field of the 3-D arterial wall of the aorta at the second heart beat (see Figure 5.18), where we observe a small overinflation of the thoracic aorta in case E_1^A and severe overinflations of the left common carotid artery for the first three sets of coefficients in Table 5.10.

The analysis of the flow rate profiles in the other branches displayed in Figure 5.17 shows that all the considered cases present spurious high-frequency oscillations at the vertebral arteries, which are probably the cause of the numerical breakdown in cases E_2^A and E_4^A . In case E_5^A , which represents the stiffest artery, the oscillations do not appear in the left vertebral artery, suggesting that this phenomenon might be related to the stiffness of the external tissues parameters. In particular, the two vertebral arteries are the smallest branches of the considered geometry, which in turn means that the wall thickness there is considerably smaller than in the other branches (we recall that the thickness of the solid domain is chosen to be proportional to the local lumen of the vessel). This could explain the fact that the high-frequency oscillations are not present in the other branches of the same geometry.

Further comments about the high-frequency oscillations observed in the purely elastic case can be performed by studying the results of a second set of simulations in which we introduce the viscoelastic response of the tissues through the parameter c_S (see equation (1.5)). As previously done for the elastic parameter, we select several sets of values for the coefficient c_S at the different branches of the aorta, as detailed in Table 5.11. Regarding the elastic parameter, we choose the set of values E_4^A , which has proven to be stiff enough to prevent overinflations in all the branches of the 3-D geometry.

The results of this comparison, at the same interfaces of the previous one, are summarized in Figure 5.19. First of all, we observe that the spurious high-frequency oscillations disappear at all the boundary interfaces and independently from the chosen set of values for the parameter c_S . This behavior confirms the importance of including the viscoelastic effects in the model of the arterial wall, not only in 1-D FSI simulations, as already proven in Section 5.3.3, but also in 3-D FSI problems, as claimed in Moireau et al. (2012). Moreover, this result suggests that the high-frequency oscillations observed in Figure 5.17 might be related mainly to the model chosen for the structure of the arterial wall. In particular, we recall that in our simulations we use a linear elastic isotropic model, which does not include any damping effect.

Further investigations should be performed to confirm this preliminary analysis. A possible strategy to do this is to try to reproduce the high-frequency oscillations on a simpler geometrical configuration, e.g., a cylindrical benchmark case where the radius, the material properties, and the inflow wave are chosen to be similar to those at the simulated vertebral arteries. In addition, further sets of simulations can be performed on the 3-D geometry of the aorta by varying, for instance, the local thickness of the wall or by including a more accurate model for the structure. Since the focus of the present work is on the algorithms for the coupling of the dimensionally-heterogeneous models, no further comments are added here.

Table 5.10: Empirical external tissues coefficients at the different wall regions of the 3-D aorta (see Figure 5.16a). We define five cases for the sets of values of the elastic coefficient.

Artery	k_S [dyn/cm ³]					c_S [dyn·s/cm ³]
	E_1^A	E_2^A	E_3^A	E_4^A	E_5^A	
Aortic arch	15000	30000	45000	60000	75000	0.0
Left / right carotid and subclavian	22500	45000	67500	90000	112500	0.0
Left / right vertebral	30000	60000	90000	120000	150000	0.0

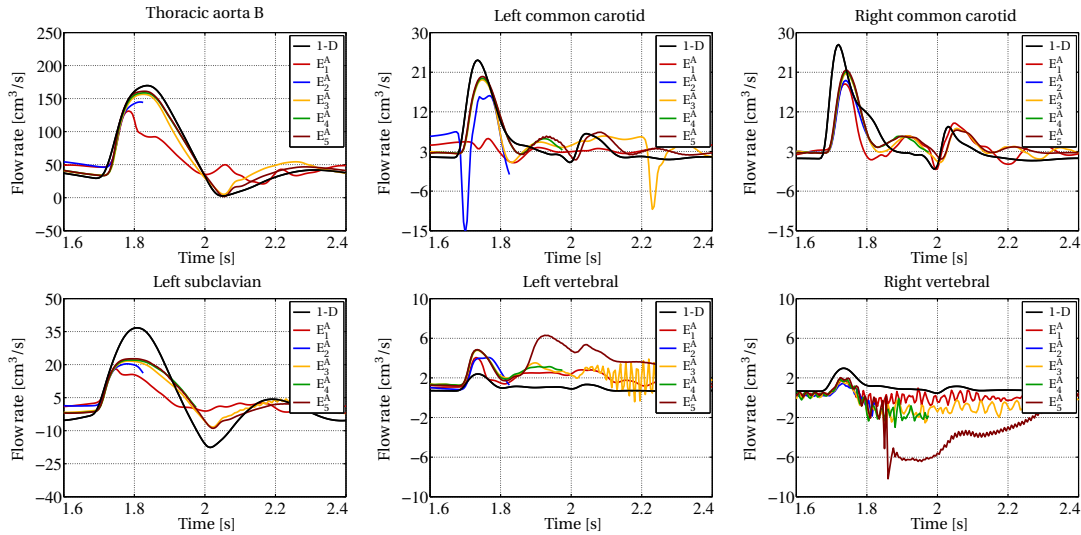


Figure 5.17: Flow rate comparison, at the third heart beat, for the sets of values given in Table 5.10 (elastic behavior of the external tissues), at the most significant coupling interfaces between the 3-D aorta (see Figure 5.16a) and the 1-D network. The black line is the solution of the full 1-D network.

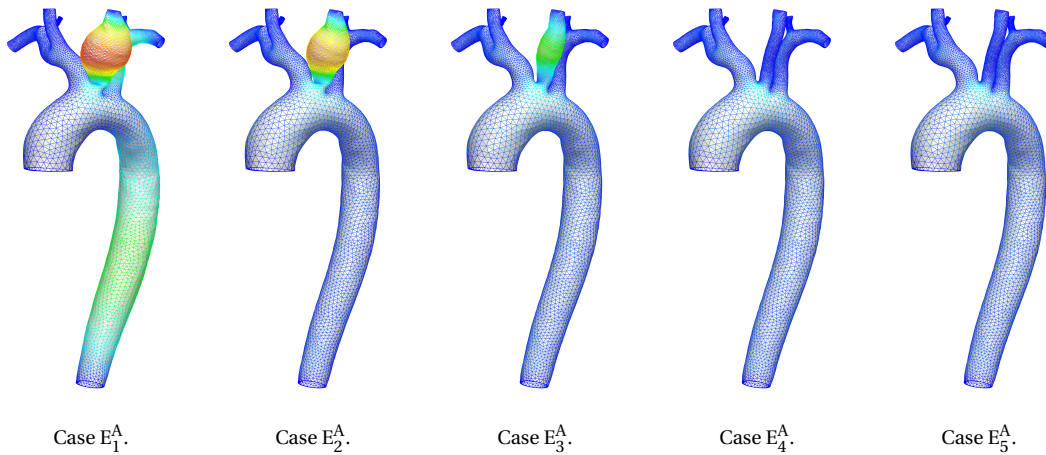


Figure 5.18: Wall displacement magnitude comparison, at the end-systole of the second heart beat ($t = 1.2$ s), for the sets of values given in Table 5.10 (elastic behavior of the external tissues) of the 3-D aorta (see Figure 5.16a) coupled with the 1-D network (not shown). The color bar ranges from blue (0.0 cm) to red (1.8 cm).

5.4. Numerical comparison and calibration of geometrical multiscale models

Table 5.11: Empirical external tissues coefficients at the different wall regions of the 3-D aorta (see Figure 5.16a). We define six cases for the sets of values of the viscoelastic coefficient.

Artery	k_S [dyn/cm ³]			c_S [dyn·s/cm ³]			
	E_4^A	V_1^A	V_2^A	V_3^A	V_4^A	V_5^A	V_6^A
Aortic arch	60000	500	1000	5000	10000	50000	100000
Left / right carotid and subclavian	90000	500	1000	5000	10000	50000	100000
Left / right vertebral	120000	500	1000	5000	10000	50000	100000

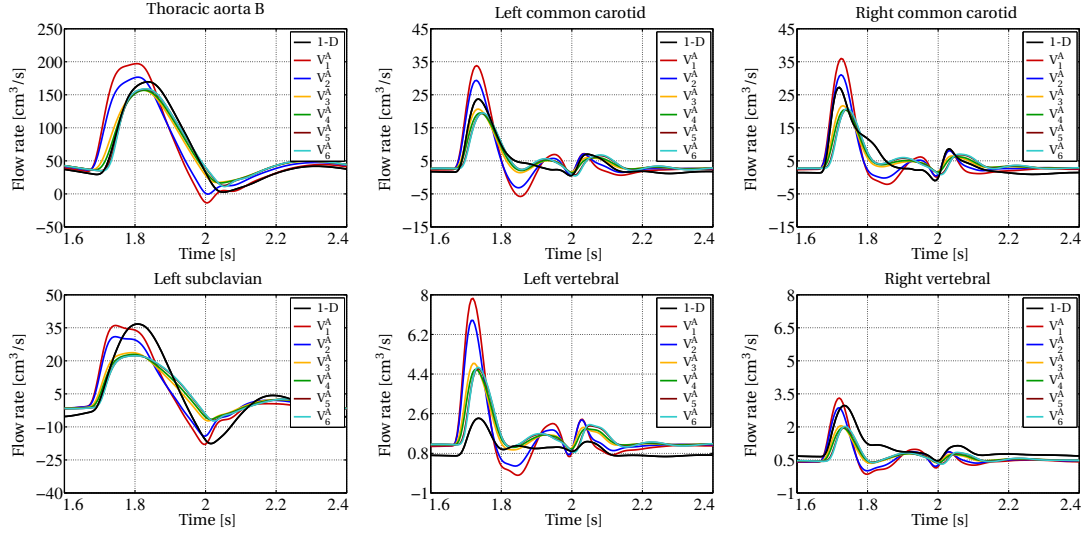


Figure 5.19: Flow rate comparison, at the third heart beat, for the sets of values given in Table 5.11 (elastic and viscoelastic behavior of the external tissues), at the most significant coupling interfaces between the 3-D aorta (see Figure 5.16a) and the 1-D network. The black line is the solution of the full 1-D network.

Regarding the value of the viscoelastic parameter, we observe that the flow rate waveforms change significantly among the simulated cases. More precisely, the sets of values V_1^A and V_2^A are not high enough to smooth the low-frequency oscillations of the 3-D FSI elastic wall. On the contrary, the results given by the other four sets of values are all very similar and belong to the physiological regime. In particular, we observe a sort of limit behavior of the viscoelastic parameter, such that above a certain threshold the sensitivity of the flow rate waveform to a variation of the parameter c_S becomes very small. In view of these results, hereafter we compute the value of the viscoelastic parameter as one tenth of the value of the corresponding elastic one. This rule provides a reliable and easy way to calibrate the viscoelastic parameter of the Robin boundary condition for the external tissues.

5.4.2.2 External tissues parameters comparisons: 3-D iliac

In this section we further extend the study of the external tissues parameters k_S and c_S by considering a different problem. We set up a geometrical multiscale model composed by the 3-D patient-specific iliac in Figure 5.16b coupled with the 1-D arterial tree described in Section 5.3, which represents an average healthy patient. For the sake of simplicity, the results presented in this section are obtained by fixing the position of the boundary solid rings of the 3-D arterial wall of the iliac, i.e., by imposing (1.6) for $j = 1, \dots, n_{FS}^\Gamma$.

Table 5.12: Empirical external tissues coefficients at the different wall regions of the 3-D iliac (see Figure 5.16b). We define five cases for the sets of values of the coefficients.

Artery	k_S [dyn/cm ³]					c_S [dyn·s/cm ³]
	E_1^I	E_2^I	E_3^I	E_4^I	E_5^I	
Abdominal aorta E	25000	50000	75000	100000	125000	$k_S/10$
Left / right common iliac	35000	70000	105000	140000	112500	$k_S/10$
Left / right external iliac	37500	75000	112500	150000	187500	$k_S/10$
Left / right inner iliac	42500	85000	127500	170000	212500	$k_S/10$

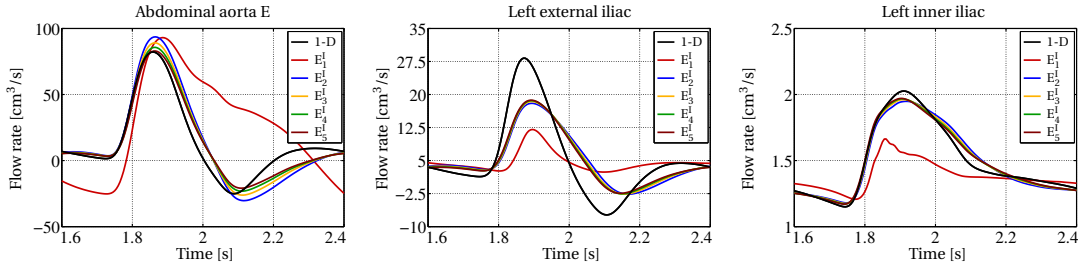


Figure 5.20: Flow rate comparison, at the third heart beat, for the sets of values given in Table 5.12 (elastic and viscoelastic behavior of the external tissues), at the most significant coupling interfaces between the 3-D iliac (see Figure 5.16b) and the 1-D network. The black line is the solution of the full 1-D network.

First of all, we perform a sensitivity analysis of the main quantities of interest with respect to a variation of the external tissues parameters. In view of the results achieved in the previous section, we directly consider both the elastic and viscoelastic coefficients. For the first one, we choose five sets of values at the different branches of the iliac, as detailed in Table 5.12. Note that the values of the different cases are chosen as multiples of the ones of case E_1^I . Then, following the result of the previous section, the viscoelastic parameter is obtained from the relation: $c_S = k_S/10$.

The results of this comparison, at the most significant coupling interfaces between the 3-D iliac and the 1-D network, are summarized in Figure 5.20, where we also plot the result of the full 1-D arterial network as an indicative reference case. From the images we observe that, apart from case E_1^I , whose tissues are clearly not stiff enough, all the other cases lead to results similar to those of the full 1-D network of arteries, thus in a physiological regime. Moreover, there are no significant differences among the last four cases, even if the parameters change considerably. We can therefore conclude that, above a certain threshold, the sensitivity of the flow rate waveform to a variation of the external tissues parameters is very small when considering both the elastic and viscoelastic components. In particular, we remark that the high sensitivity observed in Figure 5.17 for the aorta was mainly due to the numerical instabilities and, consequently, to the high-frequency oscillations in the solution, rather than to a true sensitivity to the elastic parameter k_S .

Regarding the displacement of the 3-D arterial wall, similarly to the previous section, we observe a gradual decrease in the displacement magnitude with respect to an increase in the value of the tissues parameters. No overinflations appear along the iliac branches, in all the simulated cases. However, even in the stiffest case, we observe some severe overinflations at all the three bifurcations. This non-physiological behavior is due to the lack of collagen fibers in the arterial wall model, which consequently becomes weaker at the branching points.

5.4. Numerical comparison and calibration of geometrical multiscale models

Table 5.13: Empirical external tissues coefficients at the bifurcations of the 3-D iliac (green and magenta wall regions in Figure 5.16c). From the reference case E_4^I (see Table 5.12), we define three additional configurations.

Artery	k_S [dyn/cm ³]				c_S [dyn·s/cm ³]
	E_4^I	E_{4a}^I	E_{4b}^I	E_{4c}^I	
Abdominal aorta E (bifurcation)	100000	200000	300000	400000	$k_S/10$
Left / right common iliac (bifurcations)	140000	280000	420000	560000	$k_S/10$

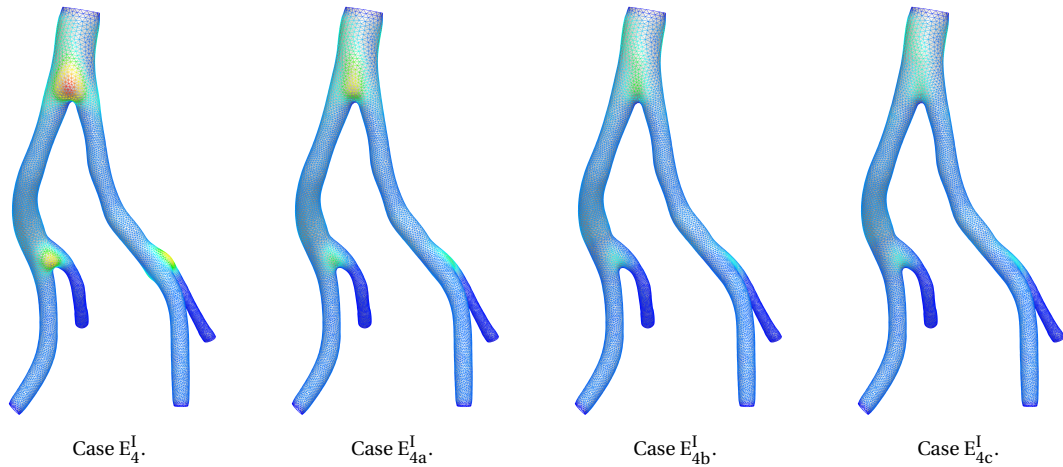


Figure 5.21: Wall displacement magnitude comparison, at the end-systole of the third heart beat ($t = 2.0$ s), for the sets of values given in Table 5.13 (stiffening of the bifurcations), of the 3-D iliac (see Figure 5.16c) coupled with the 1-D network (not shown). The color bar ranges from blue (0.0 cm) to red (0.5 cm).

To solve this issue without introducing a more complex model for the 3-D vessel wall, we use a second configuration of the iliac geometry, where two additional regions are introduced at the bifurcations (see Figure 5.16c). Then we choose case E_4^I as the reference one, and we introduce three additional sets of values for the tissues parameters at the iliac bifurcations, as detailed in Table 5.13. As before, the values of the different cases are chosen as multiples of the reference one.

In Figure 5.21 we compare the magnitude of the displacement field of the 3-D iliac arterial wall for the different cases. The images show that at each increase in the values of the tissues parameters, the overinflations at the branches diminish. This phenomenon is more visible in Figure 5.22, where an enlarged lateral view of the top and low left bifurcations is shown. In addition, a further analysis of the flow rate and pressure waveform at the coupling interfaces (which for brevity is not presented here) shows no significant changes compared to the results in Figure 5.20. In view of these results we conclude that, despite their simple formulation, Robin boundary data provide a reliable way to account for the effect of external tissues over the arterial wall. Moreover, they can be used to somehow compensate for the lack of collagen fibers in 3-D FSI models, at least in healthy arteries.

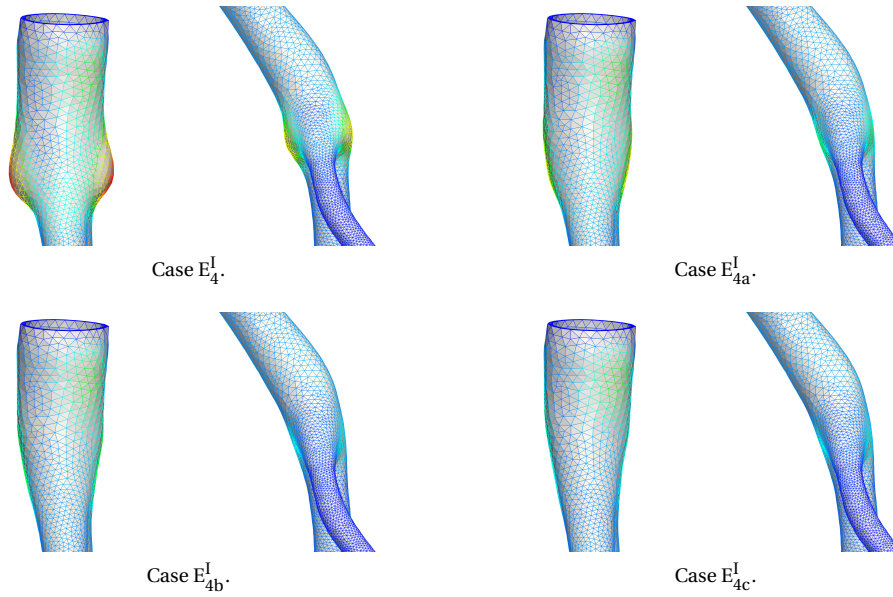


Figure 5.22: Lateral view of the top and low left bifurcations for the four cases in Figure 5.21.

5.4.2.3 Solid ring boundary condition comparisons

In this section we compare the solution of geometrical multiscale models in which the boundary solid rings of the 3-D geometries are fixed, as opposed to the case where the same 3-D boundary interfaces are scaled to enforce the continuity of the vessels size with the surrounding 1-D arteries. For these comparisons we use the same geometrical multiscale models introduced in Sections 5.4.2.1 and 5.4.2.2. For the values of the elastic parameter of the external tissues, we select cases E_4^A and E_{4b}^I for the aorta and iliac, respectively, while the viscoelastic parameter is given by the relation: $c_S = k_S/10$.

In Figures 5.23 and 5.24 several views of the magnitude difference of the two 3-D geometries displacement fields are shown. In particular, we observe that a significant difference between the two cases exists only near the coupling interfaces, where the boundary conditions change. In the other parts of the wall the result is almost the same. In addition, a further analysis of the flow rate and pressure waveform at the coupling interfaces (see Figure 5.25) shows no significant differences between the two configurations. We conclude that the continuity of the vessel area between 3-D and 1-D models is not essential for cardiovascular applications, unless the focus of the analysis is on the study of the dynamics and stresses of the wall near the boundary interfaces. However, it might still be relevant to avoid (or at least reduce) the generation of spurious interface wave reflections in other flow regimes, as shown in Chapter 4.

5.4.2.4 Geometrical multiscale models comparisons

In this section we present several comparisons among different geometrical multiscale models. More precisely we compare the results of the full 1-D arterial tree described in Section 5.3, which represents an average healthy patient, with the two dimensionally-heterogeneous models introduced in Sections 5.4.2.1 and 5.4.2.2, and a third model where the 3-D aorta and iliac geometries are coupled together within the same 1-D network. For all the configurations, we impose the continuity of the vessel area at the interfaces between the 3-D geometries and the 1-D arteries through (2.8). Regarding

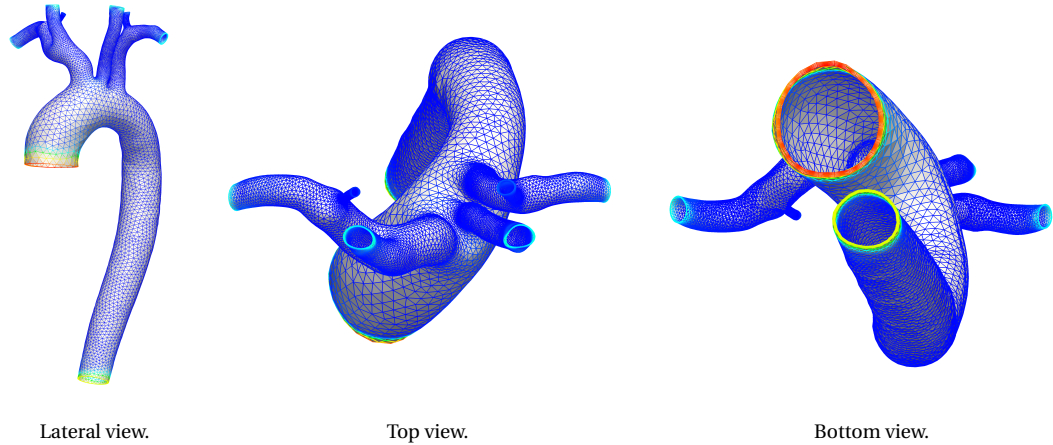


Figure 5.23: 3-D aorta wall displacement magnitude difference, at the end-systole of the sixth heart beat ($t = 4.4$ s), between the scaled area and the fixed area cases. The color bar ranges from blue (0.0 cm) to red (0.2 cm).

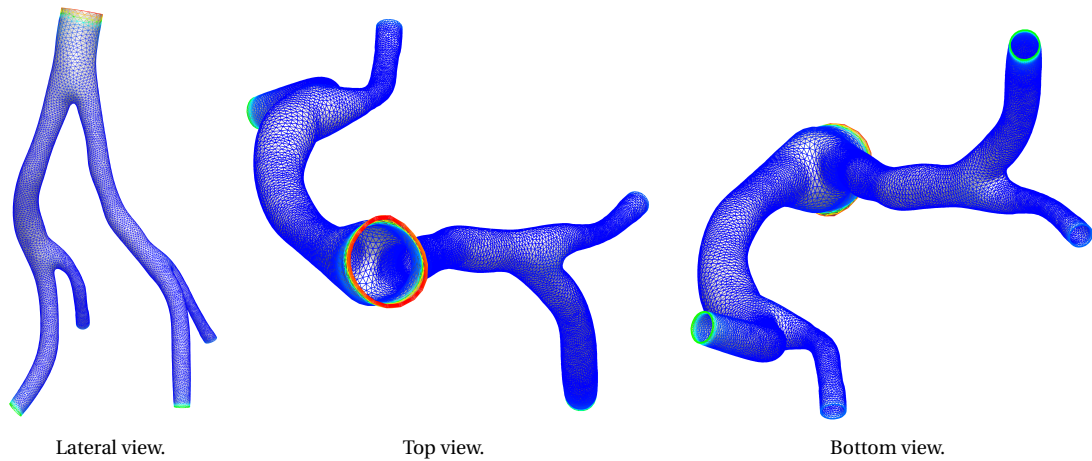


Figure 5.24: 3-D iliac wall displacement magnitude difference, at the end-systole of the sixth heart beat ($t = 4.4$ s), between the scaled area and the fixed area cases. The color bar ranges from blue (0.0 cm) to red (0.1 cm).

the values of the elastic parameter of the external tissues, we select cases E_4^A and E_{4b}^I for the aorta and iliac, respectively, while the viscoelastic parameter is given by the relation: $c_S = k_S/10$.

The results of the flow rate waveform comparison at all the coupling interfaces between the 1-D network and the 3-D aorta and iliac are summarized in Figures 5.26 and 5.27, respectively. First of all, we observe that the presence of the 3-D iliac geometry has almost no effect on the upstream solution (apart in the thoracic aorta B interface, which is quite close to the iliac artery), while the 3-D aorta produces a visible, even if small, difference in the downstream flow (see, e.g., the external iliac interfaces). In addition, the presence of the 3-D geometries, which are not symmetric and whose branches have different left and right vessel sizes, changes the splitting of the flow in the network compared to the solution of the full 1-D arterial tree (see, e.g., the vertebral arteries).

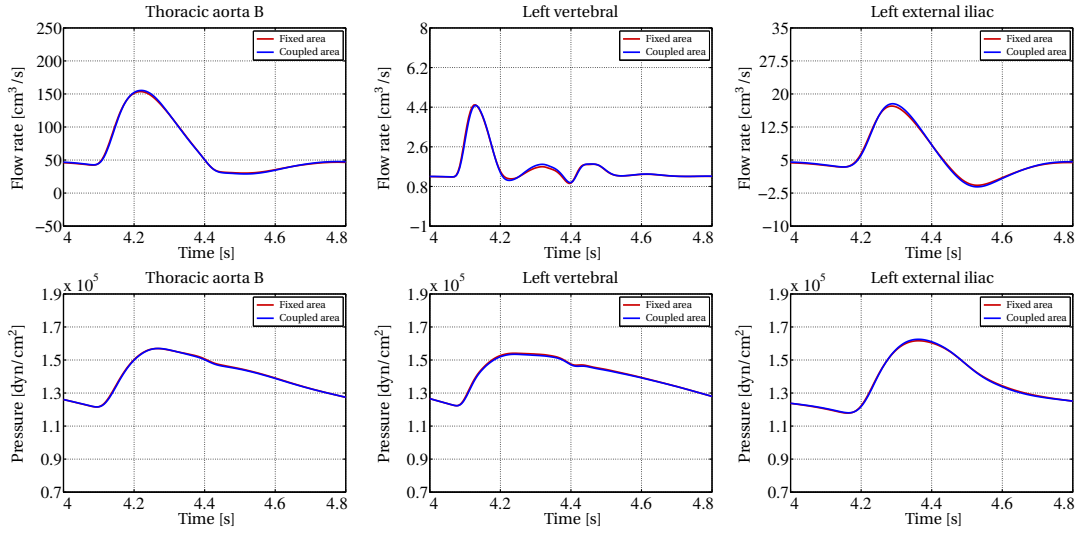


Figure 5.25: Flow rate and pressure comparisons, at the sixth heart beat, between the scaled area and the fixed area cases, at few significant coupling interfaces of the 3-D aorta and iliac.

Regarding the behavior of the pressure and the radial scale factor, which are shown in Figure 5.28, similar comments hold. In view of these results, we conclude that 3-D patient-specific geometries might have a significant effect on the arterial flow, even in the case of healthy arteries. The presence of geometrical singularities and pathologies, such as aneurysms and stenoses, would probably increase this effect and will make the subject of future works.

5.4.2.5 Interface equations comparison

In this section we make use of the previously introduced geometrical multiscale model, in which both the 3-D aorta and iliac geometries are coupled together within the same 1-D network, to set up a comparison between the imposition of the continuity of the mean normal stress and that of the mean total normal stress at the coupling nodes. In both configurations we impose the continuity of the vessel area at the interfaces between the 3-D geometries and the 1-D arteries through (2.8), while continuity of the mean normal stress is imposed at the 47 coupling nodes between the distal 1-D segments and the corresponding windkessel terminal models.

The results of this comparison are summarized in Table 5.14, where the flow rate and pressure errors have been defined as in Section 5.3.5, while the radial scale factor errors are given by

$$\mathcal{E}_{\Psi}^{\text{mean}} = \text{mean}(\mathcal{E}_{\Psi}), \quad \mathcal{E}_{\Psi}^{\text{max}} = \max(\mathcal{E}_{\Psi}), \quad (5.5)$$

being

$$\mathcal{E}_{\Psi}^n = \left| \frac{\Psi_{\mathcal{S}}^n - \Psi_{\mathcal{T}}^n}{\max(\Psi_{\mathcal{T}}^n)} \right|,$$

where, as in Section 5.3.5, the subscripts \mathcal{S} and \mathcal{T} refer to the imposed set of interface equations.

5.4. Numerical comparison and calibration of geometrical multiscale models

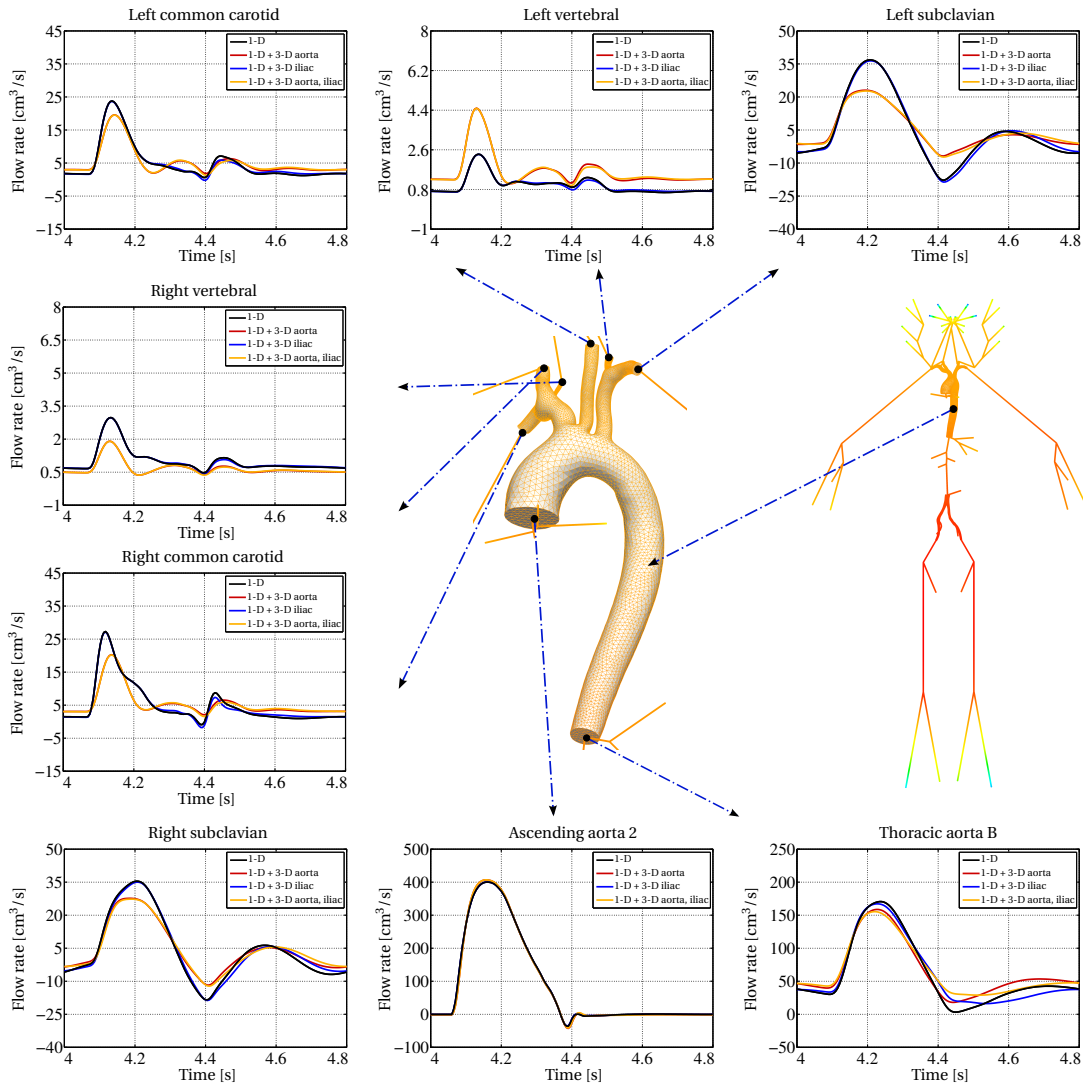


Figure 5.26: Flow rate comparison, at the sixth heart beat, for different configurations of the global arterial network, at the eight interfaces of the 3-D aorta. The color of the 3-D images represents the pressure field at the end-systole of the sixth heart beat ($t = 4.4$ s), where the color bar ranges from blue (80000 dyn/cm^2) to red (165000 dyn/cm^2). Positioning of 1-D network elements is purely visual.

From the analysis of the values in the table we can draw similar conclusions to the ones discussed in Section 5.3.5 for a network of 1-D FSI models. More precisely, the mean errors are so small that there is no significant difference between the results obtained with the two approaches. Indeed, in a graphical comparison (which for brevity is not presented here) the flow rate, pressure, and radial scale factor periodic curves of the two cases overlap almost perfectly. This behavior can be justified by the fact that the kinetic contribution to the mean total normal stress is negligible compared to the one given by the pressure; in particular, in a cardiovascular regime, the ratio between the pressure and the kinetic term is around one hundred.

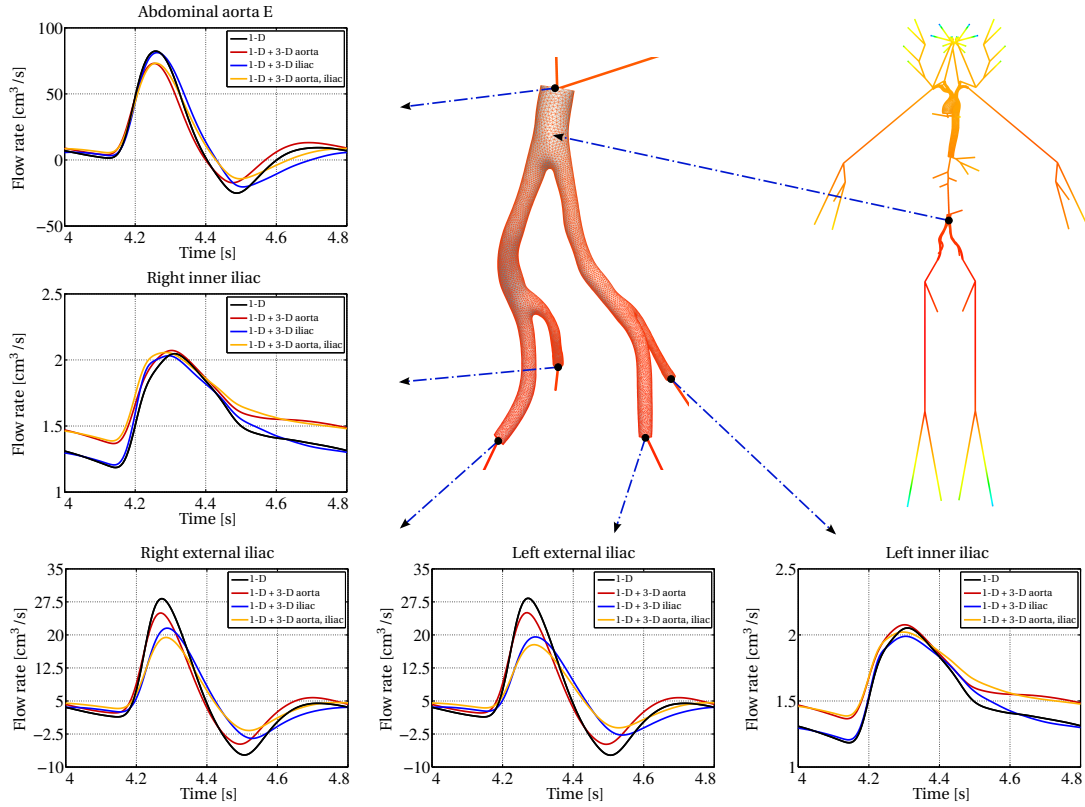


Figure 5.27: Flow rate comparison, at the sixth heart beat, for different configurations of the global arterial network, at the five interfaces of the 3-D iliac. The color of the 3-D images represents the pressure field at the end-systole of the sixth heart beat ($t = 4.4$ s), where the color bar ranges from blue (80000 dyn/cm^2) to red (165000 dyn/cm^2). Positioning of 1-D network elements is purely visual.

Table 5.14: Relative percentage errors (see equations (5.4) and (5.5)) between the results obtained by imposing the continuity of the mean normal stress at all the coupling nodes, with respect to those given by enforcing the continuity of the mean total normal stress. The errors are computed at all the interfaces of the 3-D FSI models (eight for the aorta and five for the iliac).

Interface	$\mathcal{E}_Q^{\text{mean}}$ [%]	$\mathcal{E}_Q^{\text{max}}$ [%]	$\mathcal{E}_P^{\text{mean}}$ [%]	$\mathcal{E}_P^{\text{max}}$ [%]	$\mathcal{E}_\Psi^{\text{mean}}$ [%]	$\mathcal{E}_\Psi^{\text{max}}$ [%]
Ascending aorta 2	0.0	0.2	0.1	0.3	0.2	0.7
Thoracic aorta B	0.8	2.6	0.1	0.4	0.2	1.0
Left common carotid	0.4	1.6	0.1	0.4	0.2	0.8
Right common carotid	0.3	1.5	0.1	0.3	0.2	0.8
Left vertebral	0.8	3.1	0.1	0.3	0.2	0.8
Right vertebral	1.5	3.8	0.1	0.3	0.2	0.8
Left subclavian	1.1	3.2	0.1	0.4	0.2	0.8
Right subclavian	1.1	2.9	0.1	0.4	0.3	0.9
Abdominal aorta E	0.9	2.4	0.2	0.6	0.4	1.3
Left external iliac	0.9	2.4	0.3	1.1	0.7	2.2
Right external iliac	0.7	2.0	0.3	0.9	0.6	1.9
Left inner iliac	0.3	0.8	0.3	0.8	0.5	1.7
Right inner iliac	0.3	0.7	0.2	0.7	0.5	1.5

5.4. Numerical comparison and calibration of geometrical multiscale models

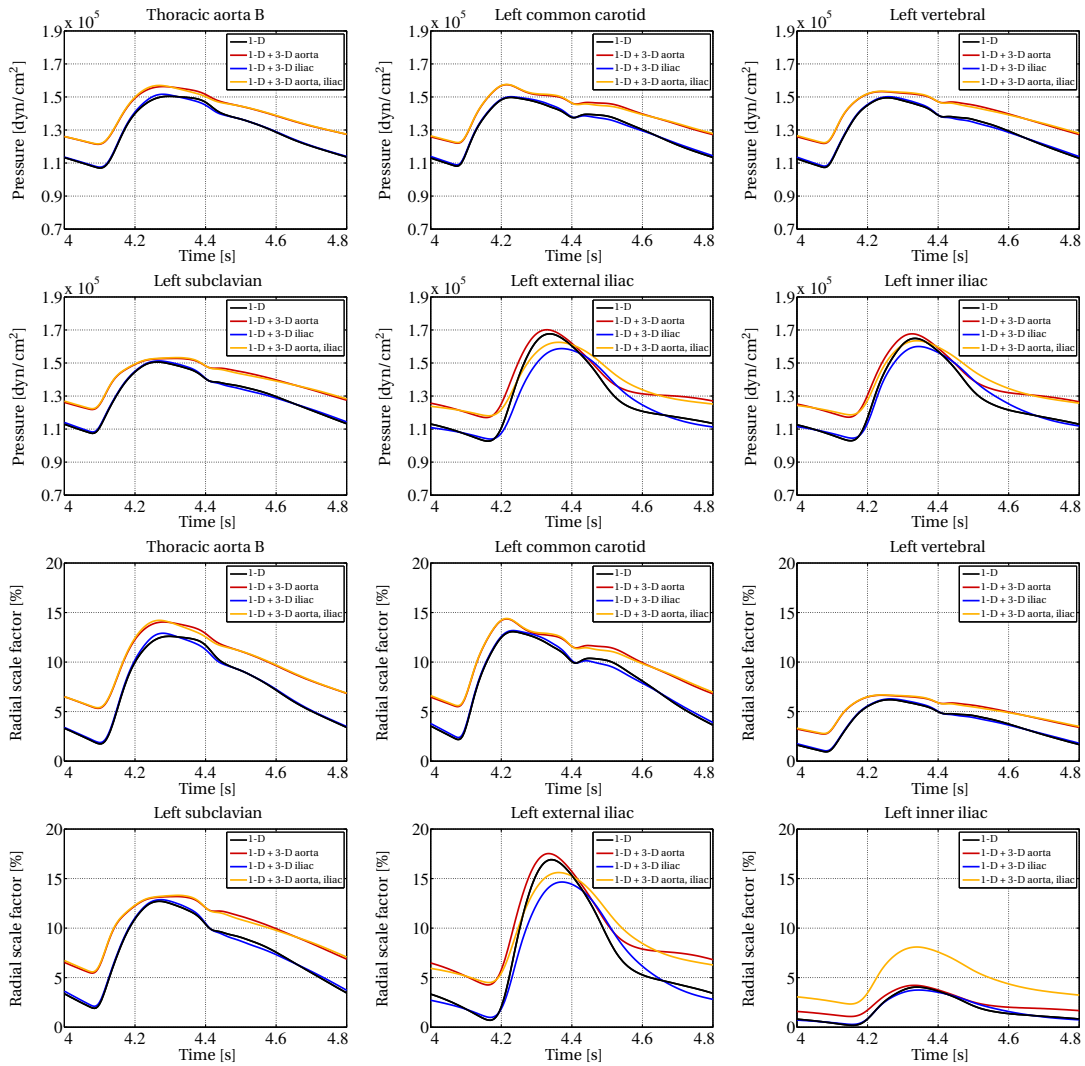


Figure 5.28: Pressure and radial scale factor comparisons, at the sixth heart beat, for different configurations of the global arterial network, at the most significant coupling interfaces of the 3-D aorta and iliac (see Figure 5.26 and 5.27).

5.4.2.6 Wall inertia comparison

In this section we make use of the previously introduced geometrical multiscale model, in which both the 3-D aorta and iliac geometries are coupled together within the same 1-D network, to study the effect of the inertia of the 3-D solid wall on the results of the global problem. In particular, we compare the results obtained by using a solid wall density of 1.2 g/cm^3 (see Table 5.9), which has been used, e.g., in Crosetto et al. (2011a) and Moireau et al. (2012), with those computed by using either $\rho_S = 1.0 \text{ g/cm}^3$ (see, e.g. Vignon-Clementel et al. (2006) and Tezduyar and Sathe (2006)) or $\rho_S = 0.0 \text{ g/cm}^3$ (purely elastic wall without inertia). As in the previous sections, we impose the continuity of the vessel area at the interfaces between the 3-D geometries and the 1-D arteries through (2.8), while the continuity of the mean normal stress is imposed at all the other coupling nodes in the network.

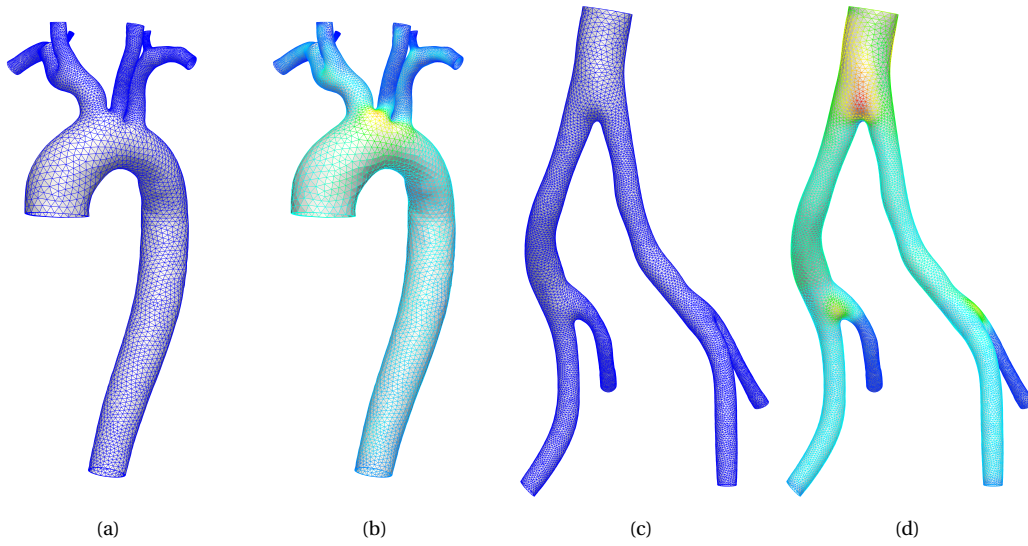


Figure 5.29: 3-D aorta and iliac wall displacement magnitude difference, at the end-systole of the sixth heart beat, between the reference solution computed with $\rho_S = 1.2 \text{ g/cm}^3$ and that obtained with either $\rho_S = 1.0 \text{ g/cm}^3$ (see images (a) and (b)) or $\rho_S = 0.0 \text{ g/cm}^3$ (see images (c) and (d)). (a,b) The color bar ranges from blue (0.0 cm) to red (0.03 cm). (c,d) The color bar ranges from blue (0.0 cm) to red (0.005 cm).

First of all, in Figure 5.29 we show the magnitude difference between the reference case, $\rho_S = 1.2 \text{ g/cm}^3$, and the other two selected values, i.e., $\rho_S = 1.0 \text{ g/cm}^3$ and $\rho_S = 0.0 \text{ g/cm}^3$. The wall displacement of the aorta in the cases $\rho_S = 1.2 \text{ g/cm}^3$ and $\rho_S = 1.0 \text{ g/cm}^3$ is indistinguishable, while comparing the reference case with the purely elastic one ($\rho_S = 0.0 \text{ g/cm}^3$) we observe a maximum difference of approximately 0.03 cm, which is still negligible with respect to the actual displacement of the wall. The same considerations hold for the 3-D iliac geometry, where the maximum wall displacement difference is approximately 0.005 cm.

Regarding the interface quantities between the 3-D and the 1-D FSI models, we compare the results in terms of flow rate, pressure, and radial scale factor, observing a perfect overlap between the curves plotted for the three cases. This behavior (which for brevity is not presented here), together with the results in Figure 5.29 can be explained by the fact that in a cardiovascular regime the inertia of the arterial wall has a relatively small effect on the main quantities of the problem; indeed, it is generally neglected in the reduced order models, as done for example in the 1-D FSI equations introduced in Chapter 1. Moreover, being the size of the area of the boundary interfaces driven by the interface equations with the surrounding models, the effect on the interface quantities is further reduced.

5.4.3 Stand-alone 3-D FSI modeling

In this section we set up a comparison between the results of the geometrical multiscale models presented in Sections 5.4.2.1 and 5.4.2.2, and their stand-alone 3-D FSI simulations counterparts. The stand-alone 3-D problems are set up by considering the same 3-D geometries and data used in the two reference geometrical multiscale models (cases E_4^A and E_{4b}^I , respectively, with $c_S = k_S/10$). However, at the boundary interfaces, instead of imposing the set of conservation equations with the surrounding

5.4. Numerical comparison and calibration of geometrical multiscale models

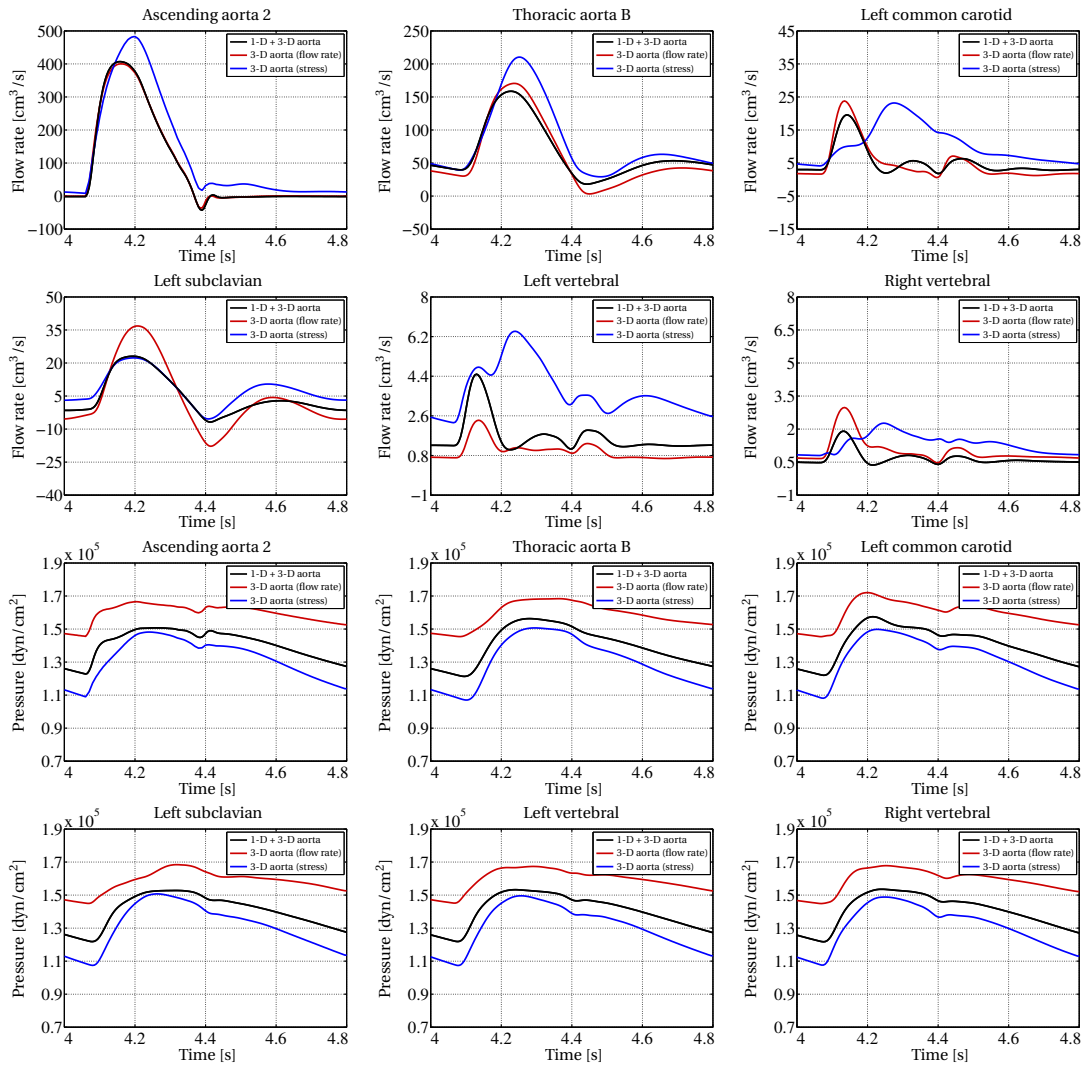
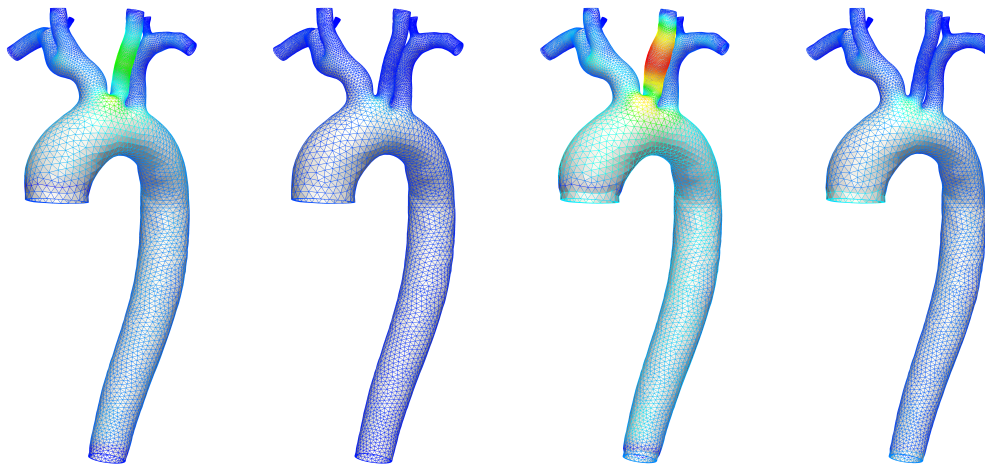


Figure 5.30: Flow rate and pressure comparisons, at the sixth heart beat, between the solution of the geometrical multiscale problem and the one of the stand-alone 3-D aorta with flow rate or stress boundary data from the full 1-D network, at the most significant coupling interfaces of the 3-D aorta.

models, as described in Chapter 2, we prescribe either flow rate or stress time profiles, taken from a precomputed solution of a full 1-D arterial tree. The advantage of this approach is the lack of interface iterations for the solution of the problem, leading to a sensible reduction of the computational cost (this is further discussed in the forthcoming Section 5.5). Following the same approach, we also impose the radial scale factor time profile on the solid ring boundary interfaces through (1.9), such that they are not fixed.

The flow rate and pressure waveform comparisons, at the most significant coupling interfaces between the 3-D aorta and the 1-D network, are summarized in Figure 5.30. The results show significant differences between the reference configuration, i.e., the geometrical multiscale model, and the solution computed by solving the stand-alone 3-D aorta model. For instance, let us consider the flow rate waveform. The red lines coincide with the precomputed (and imposed) solution of the full 1-D arterial



Flow rate imposed ($t = 4.4$ s). Stress imposed ($t = 4.4$ s). Flow rate imposed ($t = 4.8$ s). Stress imposed ($t = 4.8$ s).

Figure 5.31: 3-D aorta wall displacement magnitude difference, at the end-systole and end-diastole of the sixth heart beat, between the solution of the geometrical multiscale problem and the one of the stand-alone 3-D aorta with flow rate or stress boundary data from the full 1-D network. The color bar ranges from blue (0.0 cm) to red (0.5 cm).

tree, which is obviously different from the one of the geometrical multiscale model, as already discussed in Section 5.4.2.4. On the contrary, the blue lines are computed by imposing a stress boundary data. However, even in this case, the resulting flow rate is significantly different from the reference one. In particular, the flow rate prediction in the left common carotid and vertebral arteries are clearly incorrect. Regarding the pressure waveform, where the precomputed solution of the full 1-D arterial network coincides with the blue lines, a visible mismatch between the reference solution and the stand-alone cases is always present. In particular, the average pressure level is overestimated when the flow rate is imposed, and underestimated when the stress is prescribed. As a consequence of the different flow rate and pressure waveform, also the displacement field changes, as shown in Figure 5.31. The differences with respect to the reference case are more evident when imposing the flow rate, where we also observe a non-physiological overinflation of the left common carotid artery, even if we use the same values for the tissues parameters in both simulations.

Regarding the stand-alone 3-D iliac model, similar considerations hold, as shown in Figures 5.32 and 5.33. Among other things, we highlight the totally incorrect flow rate prediction in the left inner iliac artery when imposing a stress boundary data.

The results of these comparisons prove the importance of the geometrical multiscale approach in the modeling of cardiovascular flows. The different behavior of the stand-alone 3-D FSI simulations with respect to the geometrical multiscale model reference cases is mainly due to the lack of dynamic interplay between the dimensionally-heterogeneous models. Indeed, on the one hand, the sets of interface equations described in Chapter 2 provide a reliable and automatic way to determine the boundary data of each coupled model. On the other hand, they also provide bilateral information on both flow rate and pressure, independently from the imposed boundary condition type.

5.4. Numerical comparison and calibration of geometrical multiscale models

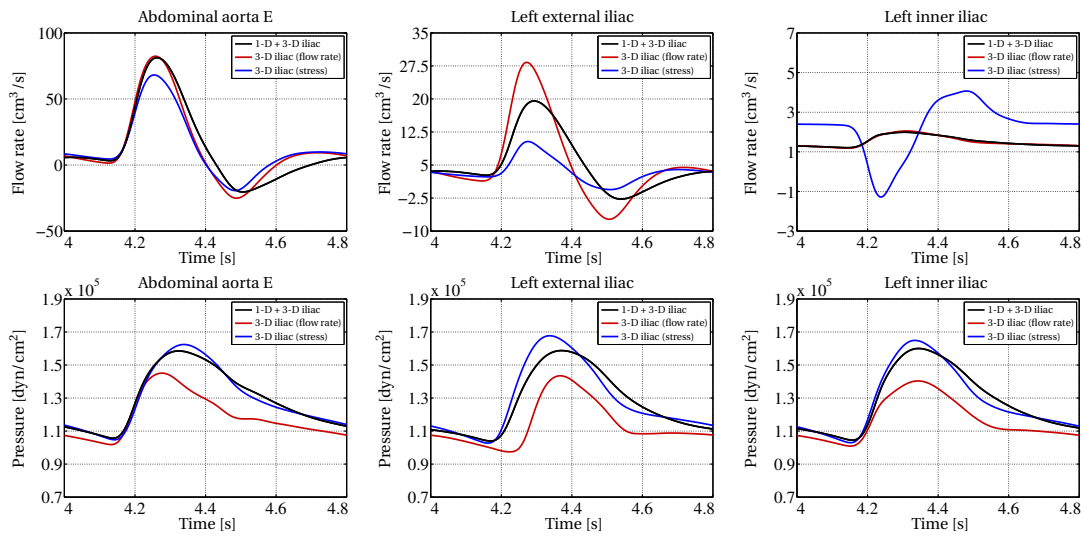
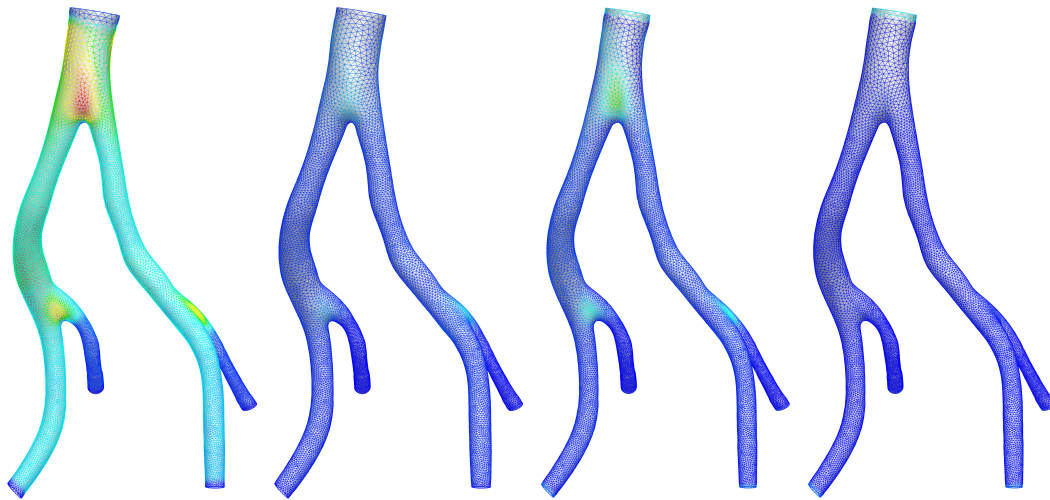


Figure 5.32: Flow rate and pressure comparisons, at the sixth heart beat, between the solution of the geometrical multiscale problem and the one of the stand-alone 3-D iliac with flow rate or stress boundary data from the full 1-D network, at the most significant coupling interfaces of the 3-D iliac.



Flow rate imposed ($t = 4.4$ s). Stress imposed ($t = 4.4$ s). Flow rate imposed ($t = 4.8$ s). Stress imposed ($t = 4.8$ s).

Figure 5.33: 3-D iliac wall displacement magnitude difference, at the end-systole and end-diastole of the sixth heart beat, between the solution of the geometrical multiscale problem and the one of the stand-alone 3-D iliac with flow rate or stress boundary data from the full 1-D network. The color bar ranges from blue (0.0 cm) to red (0.5 cm).

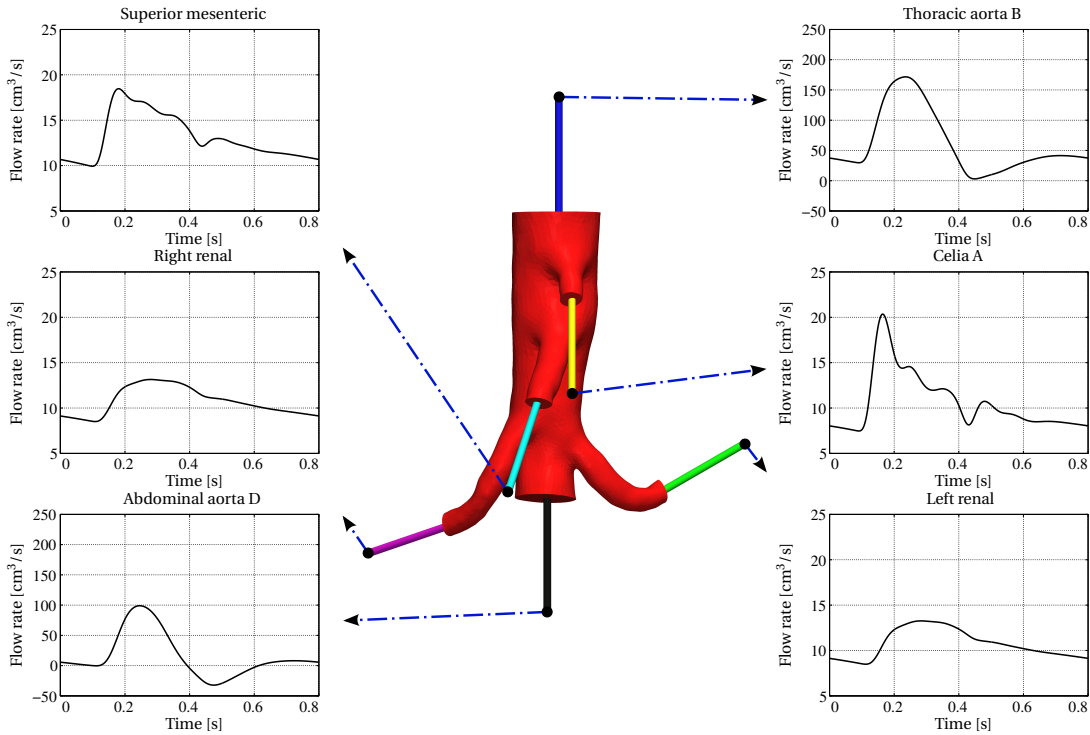


Figure 5.34: View of the 3-D FSI abdominal aorta (red color) coupled with six 1-D FSI arterial segments (other colors). On the two sides of the image, the periodic inflow/outflow volumetric flow rate profiles imposed on the six 1-D pipes are shown. More precisely, the flow imposed at the top of the 1-D thoracic aorta segment (top-right figure) is incoming, while the other five flows are outgoing.

5.5 Computational cost analysis in a heterogeneous FSI abdominal aorta simulation

In this section we aim to assess the computational efficiency of the methodology devised in Part I when applied to a realistic cardiovascular problem that includes heterogeneous FSI interaction models. More precisely, we compare the number of iterations and the CPU time required to solve a realistic flow simulation as a function of several parameters, i.e., the 3-D FSI time discretization scheme, the number of coupling interfaces, and the algorithm to solve the interface problem. To perform this analysis we select a 3-D geometry of an arterial abdominal aorta, equipped with six coupling interfaces. At each boundary interface we connect a 1-D pipe featuring a length of 1.5 cm and a uniform reference area equal to the one of the nearby fluid interface of the 3-D FSI abdominal aorta. The interface problem is defined by imposing the set of equations (2.2) at the six nodes of the network through coupling flow boundary data (i.e., $n_c^Q = 2$ with $c \in \mathcal{L}^S$, $c = 1, \dots, 6$), while all the boundary rings of the 3-D solid problem are fixed. The problem is finally closed by imposing six periodic volumetric flow rate profiles on the other sides of the 1-D pipes, as shown in Figure 5.34. These data have been taken from the periodic solution of the full 1-D arterial tree described in Section 5.3.

The wall parameters of the 3-D FSI abdominal aorta are summarized in Table 5.15, while those of the 1-D pipes are the same of the full 1-D arterial network (see Table 5.4). We remark that on the solid external wall $\Gamma_{S,ext}^0$ we apply an appropriate Robin boundary condition, whose parameters have been calibrated following the procedure described in Sections 5.4.2.1 and 5.4.2.2.

5.5. Computational cost analysis in a heterogeneous FSI abdominal aorta simulation

Table 5.15: Wall parameters of the 3-D FSI abdominal aorta.

ρ_S	Wall density	1.2 g/cm ³
h_S/D_F	Wall thickness / lumen diameter	0.05
E_S	Young's modulus	$3 \cdot 10^6$ dyn/cm ²
ν_S	Poisson's ratio	0.48
k_S	Elastic tissue (abdominal aorta)	$1.0 - 1.2 \cdot 10^5$ dyn/cm ³
	Elastic tissue (superior mesenteric)	$1.75 \cdot 10^5$ dyn/cm ³
	Elastic tissue (celiac)	$2.00 \cdot 10^5$ dyn/cm ³
	Elastic tissue (left and right renals)	$2.25 \cdot 10^5$ dyn/cm ³
c_S	Viscoelastic tissue	$k_S/10$ dyn·s/cm ³

The imposed tolerance for the interface problem is 10^{-6} , while the one for the 3-D FSI problem is 10^{-7} . The reconstruction of the 3-D geometry of the abdominal aorta and the subsequent mesh generation have been carried out following a procedure similar to the one described in Section 5.4.1 for the aorta and iliac arteries. In particular, the fluid part of the problem consists of 361969 tetrahedral elements with 62741 vertices, while the solid part is made of 236004 tetrahedral elements with 49675 vertices. The corresponding average space discretizations for the fluid and solid problems are 0.026 cm and 0.044 cm, respectively. Regarding the 1-D FSI segments, we use a uniform space discretization of 0.1 cm, corresponding to 16 vertices. The global time step is set equal to 10^{-3} s. All the simulations were performed on five cluster nodes with two Intel[®] Xeon[®] processors X5550 (quad core, 8 MB cache, 2.66 GHz CPU) each, for a total of 40 CPUs interconnected by a 20 Gb/s InfiniBand[®] architecture.

To set up the comparison we firstly run three heart beats of the problem described in Figure 5.34, to reach a quasi-periodic solution in the entire network. Then, starting from this initial condition, we run twenty time steps (corresponding to 0.020 s) for several configurations. Each of these configurations is set by removing one by one the 1-D segments from the initial problem. More precisely, from the initial configuration in Figure 5.34, the 1-D pipes are removed in the following order: left renal (green), right renal (magenta), superior mesenteric (cyan), celiac A (yellow), abdominal aorta D (black), and, finally, thoracic aorta B (blue). Note that, to preserve the same physics of the problem, each removed 1-D pipe has been replaced with the corresponding boundary volumetric flow rate profile of the fully coupled problem. Finally, we compute the average number of iterations per time step required for the solution of the interface problem and the CPU time of the entire simulation normalized over the CPU time needed by the reference case, i.e., the 3-D FSI abdominal aorta discretized by a GCE scheme and without any coupled 1-D segment. The results of this comparison are summarized in Tables 5.16 and 5.17.

From the analysis of these results, we draw that increasing the number of coupling nodes, which yields an increase of the size of the interface problem, produces a slight variation of the average number of iterations required to solve the coupled problem. A similar consideration holds comparing the results for the two solution algorithms. More precisely, the Newton method behaves as the Broyden one in the case of a GCE time discretization, and slightly better than Broyden method in the FI approach. However, there is a visible increase in the average number of iterations between the GCE and the FI time discretizations schemes. This is due to the strong nonlinearities of the FI approach.

Table 5.16: Average number of coupling iterations required for the simulation of the 3-D FSI abdominal aorta coupled with a progressively decreasing number of 1-D segments. The average number of Newton iterations for the convergence of the interaction between the fluid and the solid in the FI 3-D FSI problem is 3.88.

1-D pipes	GCE		FI	
	Newton	Broyden	Newton	Broyden
6	2.00	2.00	7.95	9.15
5	2.00	2.00	7.20	9.05
4	2.00	2.00	6.05	8.00
3	2.00	2.00	6.00	7.75
2	1.75	2.00	6.00	7.90
1	1.25	1.95	5.95	7.70

Table 5.17: Relative CPU time required for the simulation of the 3-D FSI abdominal aorta coupled with a progressively decreasing number of 1-D segments. In the last two columns, the values in the parentheses correspond to the same CPU times normalized over the CPU time needed by the FI reference case, which is 5.13 times slower than the GCE one.

1-D pipes	GCE		FI	
	Newton	Broyden	Newton	Broyden
6	9.91	2.33	120.20 [23.42]	45.46 [8.86]
5	8.58	2.30	94.09 [18.34]	44.93 [8.76]
4	7.20	2.26	67.77 [13.21]	40.22 [7.84]
3	6.00	2.23	57.08 [11.13]	39.04 [7.61]
2	4.29	2.20	47.99 [9.35]	39.64 [7.73]
1	2.27	2.15	36.33 [7.08]	38.65 [7.53]

Regarding the CPU time, we observe a quite different behavior. In particular, the Newton method shows a strong dependence from the number of coupling nodes of the problem. This is justified by the fact that, in this example, each coupling node requires the computation of two additional Jacobian entries which, in turn, requires the additional solution of a 3-D FSI tangent problem and of a 1-D FSI model (to perform the finite difference approximation), at each nonlinear Richardson iteration. On the contrary, the CPU time required to solve the interface problem with the Broyden method is almost the same. More precisely, by using the Broyden method the CPU time required to solve the coupled problem is about 2.3 and 5 times the one required to solve the uncoupled 3-D FSI model discretized with the GCE and FI time discretization approaches, respectively. Last but not least, it is interesting to notice that there is an increase of more than one order of magnitude in the CPU time required for the solution of the coupled problem when using the FI approach with respect to the GCE case.

In view of these considerations, it is clear that from the computational viewpoint the Broyden method performs much better than the Newton method. In addition, the use of a GCE time discretization is recommended, unless other needs would support the use of the more expensive FI approach. Further comparisons between these two approaches, with a focus on the main physical quantities, are addressed in Crosetto (2011). The analysis of the iterations number and the CPU time in case of continuity of mean total normal stress at the coupling nodes will be carried out in Blanco, Deparis, and Malossi (2012).

5.5. Computational cost analysis in a heterogeneous FSI abdominal aorta simulation

Main references of the chapter:

- ☆ A. C. I. Malossi, P. J. Blanco, and S. Deparis. A two-level time step technique for the partitioned solution of one-dimensional arterial networks. *Comp. Meth. Appl. Mech. Engrg.*, 237–240:212–226, 2012.
- ☆ A. C. I. Malossi, P. J. Blanco, P. Crosetto, S. Deparis, and A. Quarteroni. Implicit coupling of one-dimensional and three-dimensional blood flow models with compliant vessels. Submitted, 2012.
- ☆ A. C. I. Malossi and J. Bonnemain. Numerical comparison and calibration of geometrical multi-scale models for the simulation of arterial flows. Submitted, 2012.

Clinical problems Part III

6 Data acquisition and simulation of pathological left ventricle dynamics

Recent advancements in hardware and software performance have made computational modeling and simulation an effective tool for studying cardiac functions and relative alterations due to pathological disorders, as well as the effects of medical and surgical treatments. In this chapter we describe a procedure for the data acquisition and simulation of a patient-specific left ventricle dynamics, extending the preliminary results in Lassila et al. (2011). In this regard, the geometrical multiscale method is used to couple the pathological 3-D ventricle with a network of 1-D elements modeling the systemic arterial circulation. This allows not only to obtain a more realistic outflow boundary condition for the ventricle, but also to simulate the effects of ventricular pathologies on the global systemic circulation.

The layout of the chapter is the following: Section 6.1 provides a brief overview of the most recent research advancements in the modeling of heart dynamics. Then, in Section 6.2 we select a patient for our analysis and we describe the data acquisition process, which mainly consists in a MRI acquisition step followed by the image segmentation phase. The resulting data are used in Section 6.3 to set up a patient-specific model for the left ventricle, which is based on an ideal geometry. The preliminary results of our model are summarized in Section 6.4, with a focus on the calibration and sensitivity analysis of the main parameters. Finally, in Section 6.5 we summarize the main conclusions of this preliminary study and we briefly discuss possible future extensions of the current model.

6.1 State of the art

Simulating the function of the human heart using computational models is a vast research topic encompassing several specific applications and methodologies: some targets of study include the cardiac output (see, e.g., Ursino (1998), Segers et al. (2003), and Korakianitis and Shi (2006)), fluidic phenomena inside the heart (see, e.g., Kovács et al. (2001), Long et al. (2008), Nordsletten et al. (2011), Schenkel et al. (2009), and Watanabe et al. (2008)), biomechanics of heart valves (see, e.g., Stevanella et al. (2009, 2011), Conti et al. (2010), Wenk et al. (2010), Skallerud et al. (2011), and Marom et al. (2012)), the mechanical properties of the myocardium (see, e.g., Arts et al. (2001), Humphrey (2002), Redaelli et al. (2004), Holzapfel and Ogden (2009), and Wang et al. (2009)), and the electromechanical activity of the heart (see, e.g., Nash and Hunter (2000), Sainte-Marie et al. (2006), Sermesant et al. (2006, 2011), and Nobile et al. (2012)). In Figure 6.1 a diagram representing the hierarchy among these modeling approaches is shown.

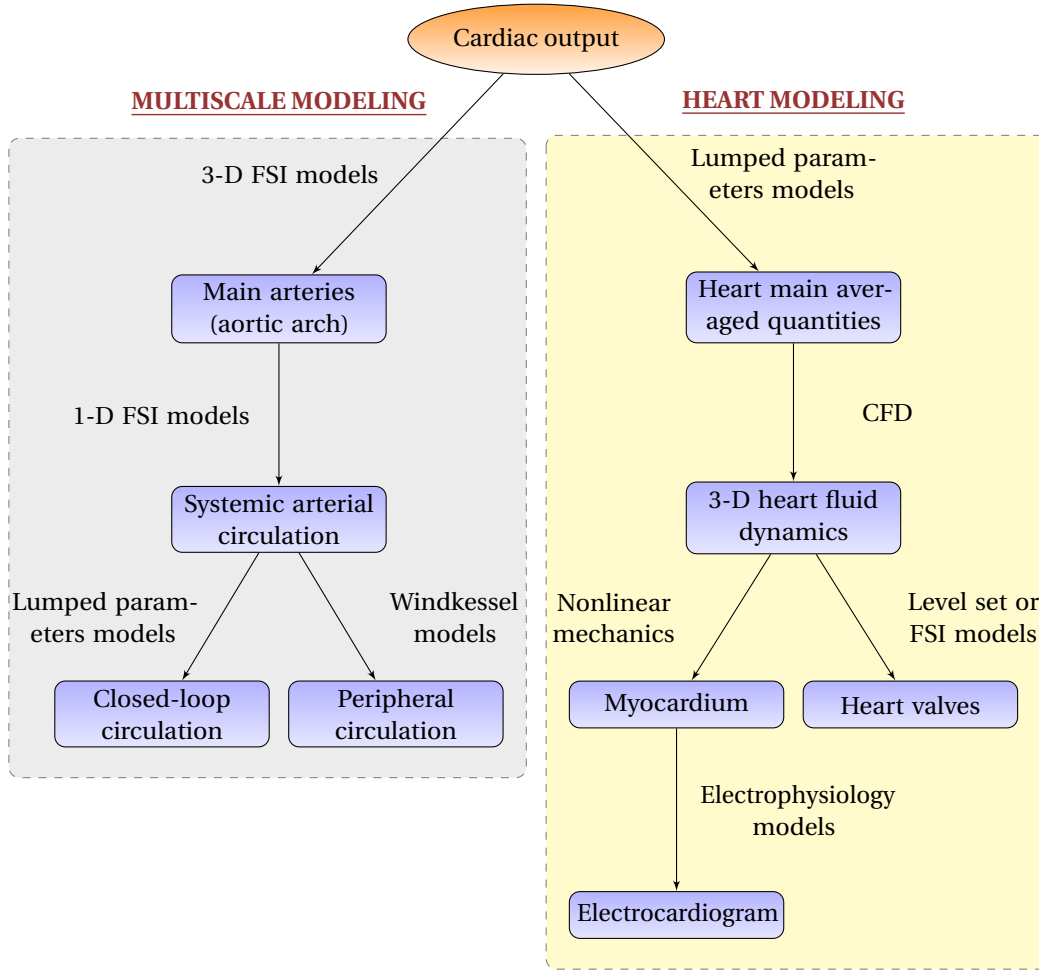


Figure 6.1: Hierarchical model tree for the simulation of the human heart. The nodes of the tree correspond to specific phenomena we might be interested in modeling. Each edge corresponds to a specific model, constitutive law, or computational paradigm needed to model the phenomena to which it leads. The blocks on the left (gray rectangle) belong to the field of geometrical multiscale modeling. In contrast, the blocks on the right (yellow rectangle) belong to the field of heart modeling.

Most of these models involve the assimilation of *in vivo* data gathered through imaging techniques, either from humans or animals. Typically the problem of patient-specific simulation of the fluid dynamics inside the heart is approached by building a high-fidelity computational geometry and then performing a 3-D FSI simulation either using the immersed interface approach advocated in Kovács et al. (2001) and McQueen and Peskin (2002), or based on the ALE method, as in Tang et al. (2010). The largest difficulty in modeling the entire function of the ventricle, including the nonlinear mechanics of the myocardial tissue, is that the direction of the fibers, needed to accurately simulate the active mechanics of the systolic phase, are usually not identifiable from patient-specific data. A less complex approach is to only simulate the fluid by prescribing the displacement of the endocardium based on medical image reconstruction to recover the flow velocity inside the ventricle, as done in Long et al. (2008).

In the following we present an approach for the simulation of pathological left ventricle dynamics extending the preliminary results shown in Lassila et al. (2011). We first reconstruct the time-dependent position of the endocardium from a series of short-axis MRI slices. Then, we use radial basis functions (in space) and trigonometric polynomials (in time) to generate a smooth extrapolation function of the wall displacement field. This is prescribed as boundary condition on a thin 3-D fictitious linear elastic structure, which surrounds an idealized left ventricle geometry. The linear elastic structure acts to regularize the dynamics of the ventricle, such that both a realistic motion of the fluid and a physiological/pathological pressure level are recovered. The geometrical multiscale method is used to couple the 3-D FSI left ventricle with a network of 1-D FSI elements modeling the systemic arterial circulation. To account for the presence of the aortic and mitral valves, we include a simple lumped description of these elements in the model. The resulting global network can be used to simulate the effects of ventricular pathologies on the arterial systemic circulation. Moreover, it solves the problem of prescribing a boundary condition at the aortic valve even if, in the case of pathological ventricles, a calibration of the terminals is required to achieve the correct pressure level.

In summary, the main novelties featuring the devised approach are (i) the use of radial basis functions and trigonometric polynomials for the smooth reconstruction of the prescribed wall displacement field, (ii) the inclusion of a thin 3-D fictitious linear elastic structure with the aim of regularizing the wall displacement field obtained from the MRI data, and (iii) the possibility to account for the dynamic interplay between the 3-D left ventricular dynamics and the global systemic arterial circulation.

6.2 Data acquisition

In this section we summarize the procedure for the acquisition and integration of the data into the numerical model, which has been carried out by the group of A. Redaelli at the BRG¹ (see Conti et al. (2011)). First, a suitable patient for the analysis is selected and his clinical history is reported. Then, the MRI is acquired and image segmentation leads to the detection of the left ventricle endocardium time-dependent position.

6.2.1 Subject enrollment

In the present study we apply our methodology to a diabetic patient, with moderate kidney dysfunction, and a history of anteroseptal acute myocardial infarction (AMI), resulting from a severe occlusion of the left anterior descending coronary artery. The consequent severe chronic ischemia (restriction in blood supply) and oxygen shortage to the myocardium has damaged the heart, causing a severe akinesia (loss of motor function) of the left ventricle. This pathological scenario is of particular interest given its high prevalence (see Hertz et al. (2008)).

The patient underwent a coronary stent implantation to restore blood circulation. Tests for residual ischemia were negative, however exams evidenced a cardiac dyssynchrony, which has been treated with the implantation of a pacemaker. In addition, a severe pump dysfunction and markedly reduced exercise tolerance were documented. The main clinical data of the patient are summarized in Table 6.1.

¹Biomechanics Research Group, Politecnico di Milano: <http://www.biomech.polimi.it>.

Table 6.1: Main clinical data of the selected patient.

Personal details		Cardiac history	
Age	67	Atrial fibrillation	no
Body mass index [kg/cm ²]	27.44	Heart failure symptoms	yes
Gender	male	Previous AMI	yes
Risk factors		Site of AMI	anterolateral
Diabetes	yes	Type of AMI	STEMI
Dyslipidemia	yes	Remodeling after AMI	yes
Hypertension	yes	New York Heart Association class	III
Comorbidities		Coronary angiography	
Cerebrovascular disease	stroke	Coronary atherosclerosis	yes
Chronic kidney dysfunction	yes	Percutaneous coronary intervention	yes (stent)
Chronic obstructive pulmonary disease	no	Left anterior descending coronary occlusion (before stent implant)	80% – 90%
Peripheral vessel disease	no		

6.2.2 MRI acquisition

Cardiac magnetic resonance studies have been performed using a 1.5 Tesla whole-body Siemens Avanto² MRI scanner, equipped with a commercial cardiac coil. Electrocardiogram-gated breath-hold cine images of the left ventricle have been acquired in multiple short axes using steady state free precession sequences (20 time frames/cardiac cycle, reconstruction matrix 256 × 256 pixels, spatial resolution 1.719 × 1.719 mm²). The ventricular coverage has been achieved with 8-mm thick slices separated by a gap of 1.6 mm, obtaining a stack of 7 cine short-axis slices; due to the poor visibility in the MRI, the apex and the valves have been excluded from the acquisition process.

6.2.3 Image processing and endocardium reconstruction

Left ventricle endocardial surface segmentation has been performed using a semi-automated detection algorithm based on region-based image noise distribution, as described in Conti et al. (2011). The endocardial contour has been detected through the approach proposed by Chan and Vese (2001), integrated with the a priori knowledge of the statistical distribution of gray levels in medical images (see Bovik (1988)). In particular, the video intensity of the MRI image pixels has been modeled as a Gaussian distributed random variable and the evolution of the surface has been drawn to achieve a maximum-likelihood segmentation of the target, with respect to the statistical distribution law of image pixels.

The boundary regularization has been achieved using a curvature-based motion designed to not allow curvature above the mean Euclidean value of the detected contour and to automatically include the papillary muscles in the left ventricular cavity. This region-based approach has been applied from basal to apical slices for each frame following this procedure: first the algorithm parameters (radius of

²Siemens Medical Solutions: <http://www.medical.siemens.com>.

the initial circle and percent of radius decrement from one slice to the following one) are initialized. Then, the operator selects one point in the basal slice of the left ventricular cavity; automatically, the algorithm expands the initial circle according to the video intensity probability distribution, which is followed by the regularizing expansion to include the papillary muscles (when present). Subsequently, the other slices are processed in a similar way; the contour detected on the current slice, reduced by the percent of radius decrement set by the operator, is used as initial guess for the following one.

At each time frame the smooth endocardial surface has been obtained by biplanar cubic spline approximation of previously detected contours. Then, the surface has been discretized into three-node triangular elements. In the end-diastolic frame, the endocardial surface has been divided into six longitudinal sections and three circumferential sections, thus obtaining a 18-segment model which resembles the one recommended by the American Heart Association (see Cerqueira et al. (2002)). For each sector, nine points forming a 3×3 mapped grid have been identified and the corresponding local principal curvatures calculated as in Vieira and Shimada (2005). Then, each point of each sector have been tracked throughout the subsequent time-points by means of a nearest neighbor search; this approach is based on the minimization of the frame-by-frame variations in spatial position and local curvature (see Conti et al. (2011)).

The results of this procedure is the time-dependent position of a set of points for the entire endocardial surface, which we define as

$$\mathbf{x}_{\text{MRI}}^{g,f} \quad g = 1, \dots, \mathcal{G}, \quad f = 1, \dots, \mathcal{F},$$

being \mathcal{G} the number of registered points and \mathcal{F} the number of time frames per heart beat; for the ventricle of the patient described in Table 6.1 these quantities are $\mathcal{G} = 84$ and $\mathcal{F} = 20$. Note that there are no points near the apex nor near the valves because these regions were not included in the slices during the acquisition of the MRI. The first acquired time frame (i.e., $f = 1$) refers to the configuration of the ventricle at the end of the diastole.

6.3 Left ventricle model

In this section we devise a model for simulating the blood flow in a pathological left ventricle, which is initially described as an ideal truncated ellipsoid geometry and modeled by the 3-D FSI equations introduced in Chapter 1. The dynamics of the ventricle are driven by the extrapolated displacement field prescribed on the external wall of the fictitious solid domain; this field is obtained through radial basis functions and trigonometric polynomial interpolations of the time-dependent position of the endocardium, which has been reconstructed in data acquisition process (see Section 6.2). Finally, the valves are accounted through simple lumped parameters models.

The methodology described in Sections 6.3.1 through 6.3.4 has been mainly developed by T. Lassila at the CMCS³, with also the support of M. Astorino and S. Deparis.

6.3.1 Definition of the ideal reference domain

To obtain an optimal trade-off between the patient-specific morphological details and standardization of the meshing procedure, the discretized geometry of the left ventricle intracavitary volume and that of the corresponding myocardial wall is obtained as following: an ideal, reference computational domain

³Chair of Modeling and Scientific Computing, EPFL: <http://cmcs.epfl.ch>.

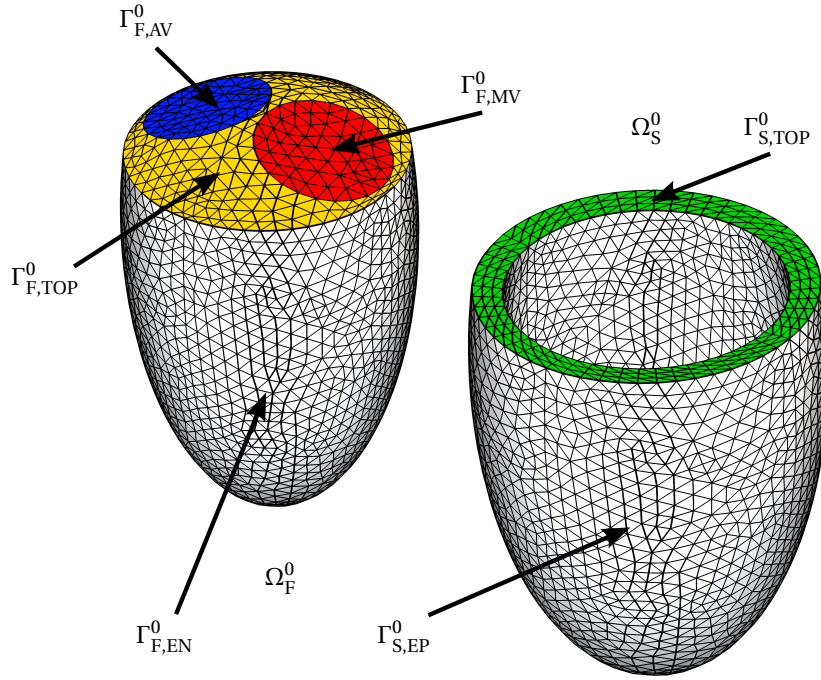


Figure 6.2: Coarse finite element meshes for the reference fluid domain Ω_F^0 and the elastic fictitious structure domain Ω_S^0 . The mitral and aortic valves are indicated in red and blue colors, respectively. The top boundaries of the fluid and solid domains are indicated in yellow and green colors, respectively.

representing the left ventricle is defined using a truncated ellipsoid, comprising the fluid domain Ω_F^0 and the surrounding thin fictitious structure Ω_S^0 , obtained by an extrusion procedure (see Figure 6.2). The mitral and aortic valves are added to the top of the reference fluid domain as flat circular surfaces, denoted $\Gamma_{F, \text{MV}}^0$ and $\Gamma_{F, \text{AV}}^0$. In the reference configuration the endocardium and the epicardium of the fictitious structure are denoted $\Gamma_{F, \text{EN}}^0$ and $\Gamma_{S, \text{EP}}^0$, respectively, while the top boundaries of the fluid and solid domains are denoted $\Gamma_{F, \text{TOP}}^0$ and $\Gamma_{S, \text{TOP}}^0$, respectively.

Remark 6.1. Compared to the notation introduced in Figure 1.1 the following relations hold: $\Gamma_{F, \text{EN}}^0 \equiv \Gamma_I^0$ and $\Gamma_{S, \text{EP}}^0 \equiv \Gamma_{S, \text{ext}}^0$. In contrast with the 3-D geometries employed in the previous chapters, the solid domain Ω_S^0 does not have inlet/outlet solid rings in correspondence of the two inflow/outflow boundaries $\Gamma_{F, \text{MV}}^0$ and $\Gamma_{F, \text{AV}}^0$ of the fluid domain Ω_F^0 .

6.3.2 Alignment and sizing

The reference computational domain is aligned and sized to match the moving geometry of the patient-specific left ventricle reconstructed from MRI, as detailed in Section 6.2. On the surface of the reference fluid domain $\Gamma_{F, \text{EN}}^0$, which corresponds to the ideal endocardial surface, we can identify the set of \mathcal{D} boundary mesh nodal points, i.e.,

$$\mathbf{x}_{\text{MESH}}^d \in \Gamma_{F, \text{EN}}^0, \quad d = 1, \dots, \mathcal{D}.$$

The spatial normalization of the reference domain to the MRI-derived points is done by minimizing a least-squares defect functional in the end-diastolic configuration, at $f = 1$. First, we apply a rigid transformation to both the reference fluid and solid domains, to align the set of points $\{\mathbf{x}_{\text{MESH}}^d\}$ with

the MRI-derived points $\{\mathbf{x}_{\text{MRI}}^{g,1}\}$. In more detail, we place the centerline of the long axis of the ventricle along the line $x = y = 0$ and the top of the ventricle on the plane $z = 0$. Then, we define the least-squares defect functional measuring the discrepancy between the two sets of points as

$$J(\boldsymbol{\eta}) = \sum_{g=1}^{\mathcal{G}} \min_{d=1,\dots,\mathcal{D}} \left\{ \sum_{\ell=1}^3 \left([\mathbf{x}_{\text{MRI}}^{g,1}]_{\ell} - \eta_{\ell} [\mathbf{x}_{\text{MESH}}^d]_{\ell} \right)^2 \right\},$$

where $\boldsymbol{\eta} = (\eta_1, \eta_2, \eta_3)^{\top}$ is the scaling vector and $[\mathbf{x}]_{\ell}$ denotes the ℓ -th component of the vector \mathbf{x} . We constrain the volume and the base-to-apex length of the ideal left ventricle to be equal to those measured by MRI. This is necessary to remove the possible indeterminacy of the solution and to obtain more accurate reconstruction of left ventricle size and volume. Thus, to find the best fit sizing, the following constrained least-squares problem is solved

$$\min_{\boldsymbol{\eta} \in \mathbb{R}_+^3} J(\boldsymbol{\eta}) \text{ s.t. } \begin{cases} \eta_1 \eta_2 \eta_3 V_{\text{F}}^0 = V_{\text{MRI}}^{\text{EDV}}, \\ \eta_3 L_{\text{F}}^0 = L_{\text{MRI}}^{\text{EDV}}, \end{cases}$$

where V_{F}^0 and L_{F}^0 are the volume and the base-to-apex length of the reference fluid domain, respectively, while $V_{\text{MRI}}^{\text{EDV}}$ and $L_{\text{MRI}}^{\text{EDV}}$ are the corresponding patient-specific end-diastolic measurements from MRI. The goodness-of-fit is measured using the root mean square error as an indicator:

$$\mathcal{E}_J = \sqrt{\frac{J(\boldsymbol{\eta})}{\mathcal{G}}}. \quad (6.1)$$

6.3.3 Ideal reference domain deformation

After alignment and sizing, the ideal fluid and solid domains are deformed through a map built on the MRI-derived points. First, for each g -th MRI-derived point at the first frame $\mathbf{x}_{\text{MRI}}^{g,1}$, we identify the closest boundary mesh nodal point $\mathbf{x}_{\text{MESH}}^g$ on the endocardial wall of the rescaled geometry. Then we build a smooth mesh displacement function with radial basis functions (see Buhmann (2003)) as

$$[\mathbf{f}_d^0(\mathbf{x})]_{\ell} = \sum_{g=1}^{\mathcal{G}} [\boldsymbol{\omega}^g]_{\ell} \varphi_{\text{RBF}}(\|\mathbf{x} - \mathbf{x}_{\text{MESH}}^g\|), \quad \ell = 1, 2, 3, \quad (6.2)$$

where $\varphi_{\text{RBF}}(r)$ is the radial basis function (being r the radial distance) and $\boldsymbol{\omega}^g$ the vector of interpolation weights associated to the g -th boundary mesh nodal point. All the interpolation weights are obtained by solving the radial basis function interpolation system

$$\begin{bmatrix} \varphi_{\text{RBF}}(r_{1,1}) & \dots & \varphi_{\text{RBF}}(r_{1,\mathcal{G}}) \\ \vdots & \ddots & \vdots \\ \varphi_{\text{RBF}}(r_{\mathcal{G},1}) & \dots & \varphi_{\text{RBF}}(r_{\mathcal{G},\mathcal{G}}) \end{bmatrix} \begin{pmatrix} [\boldsymbol{\omega}^1]_{\ell} \\ \vdots \\ [\boldsymbol{\omega}^{\mathcal{G}}]_{\ell} \end{pmatrix} = \begin{pmatrix} [\mathbf{x}_{\text{MRI}}^1 - \mathbf{x}_{\text{MESH}}^1]_{\ell} \\ \vdots \\ [\mathbf{x}_{\text{MRI}}^{\mathcal{G}} - \mathbf{x}_{\text{MESH}}^{\mathcal{G}}]_{\ell} \end{pmatrix}, \quad \ell = 1, 2, 3,$$

where

$$r_{g,g'} = \|\mathbf{x}_{\text{MESH}}^g - \mathbf{x}_{\text{MESH}}^{g'}\|, \quad g, g' = 1, \dots, \mathcal{G}.$$

It is worth recalling that, when radial basis functions are used for mesh motion, to avoid large unwanted deformations far away from the interpolation sites, either the interpolation sites need to be approximately uniformly distributed throughout the deformed domain, or the shape function must

be chosen to vanish at infinity (see, e.g., Rendall and Allen (2009)). For this reason, we use the inverse multiquadrics base function, i.e., $\varphi_{\text{RBF}}(r) = (r^2 + r_c^2)^{-1/2}$, being r_c a fixed support parameter, here set equal to one.

Once the interpolated mesh displacement field (6.2) is computed, all the fluid and solid mesh nodes are moved from the ideal truncated ellipsoid configuration to the new deformed state:

$$\mathbf{x}_{\text{MESH}} \mapsto \mathbf{x}_{\text{MESH}} + \mathbf{f}_d^0(\mathbf{x}_{\text{MESH}}).$$

In particular, we remark that

$$\mathbf{x}_{\text{MESH}}^g \mapsto \mathbf{x}_{\text{MESH}}^g + \mathbf{f}_d^0(\mathbf{x}_{\text{MESH}}^g) = \mathbf{x}_{\text{MRI}}^{g,1}, \quad g = 1, \dots, \mathcal{G}.$$

Therefore, we can define the displacement $\mathbf{d}_{\text{MRI}}^g$ of the g -th MRI-derived point as

$$\left\{ \begin{array}{l} \mathbf{d}_{\text{MRI}}^{g,1} = \mathbf{0}, \\ \mathbf{d}_{\text{MRI}}^{g,f} = \mathbf{x}_{\text{MRI}}^{g,f} - \mathbf{x}_{\text{MRI}}^{g,1}, \quad f = 2, \dots, \mathcal{F}. \end{array} \right.$$

In the following we consider the new deformed state as the reference domain configuration.

6.3.4 Epicardial displacement extrapolation

From the time-dependent displacement field of the MRI-derived points we extrapolate the displacement of the fictitious myocardial wall $\Gamma_{\text{S,EP}}^0$. This is done by interpolating the endocardial displacement with radial basis functions in space and trigonometric polynomials in time. In this regard, it is important to point out that the solid domain of the 3-D FSI left ventricle model is not aimed to the biomechanical analysis of the left ventricular wall, but to impose a proper displacement boundary condition to account for the motion of the endocardium, which in turn influences pressure, extent, and shape of the simulated left ventricular intracavitary volume during the cardiac cycle. In particular, we impose the reconstructed displacement field on a fictitious epicardium to obtain the desired endocardial motion as a consequence of the propagation of the boundary conditions through the modeled left ventricular wall; in this way it is possible to avoid the artifacts and numerical instabilities that would have occurred if time-dependent displacement boundary conditions would have been applied directly at the interface between the fluid and solid domains.

The interpolated displacement field of the MRI-derived points is computed by extending (6.2) to account for the time-dependence

$$[\mathbf{f}_d(\mathbf{x}, t)]_\ell = \sum_{g=1}^{\mathcal{G}} [\boldsymbol{\omega}^g(t)]_\ell \varphi_{\text{RBF}}(\|\mathbf{x} - \mathbf{x}_{\text{MRI}}^{g,1}\|), \quad \ell = 1, 2, 3,$$

where now the vector of interpolation weights $\boldsymbol{\omega}^g(t)$ depends on time. The corresponding radial basis function interpolation system is

$$\begin{bmatrix} \varphi_{\text{RBF}}(r_{1,1}) & \dots & \varphi_{\text{RBF}}(r_{1,\mathcal{G}}) \\ \vdots & \ddots & \vdots \\ \varphi_{\text{RBF}}(r_{\mathcal{G},1}) & \dots & \varphi_{\text{RBF}}(r_{\mathcal{G},\mathcal{G}}) \end{bmatrix} \begin{pmatrix} [\boldsymbol{\omega}^1(t)]_\ell \\ \vdots \\ [\boldsymbol{\omega}^{\mathcal{G}}(t)]_\ell \end{pmatrix} = \begin{pmatrix} [\mathbf{p}^1(t)]_\ell \\ \vdots \\ [\mathbf{p}^{\mathcal{G}}(t)]_\ell \end{pmatrix}, \quad \ell = 1, 2, 3, \quad (6.3)$$

where

$$r_{g,g'} = \left\| \mathbf{x}_{\text{MRI}}^{g,1} - \mathbf{x}_{\text{MRI}}^{g',1} \right\|, \quad g, g' = 1, \dots, \mathcal{G}.$$

The right-hand side of system (6.3) is given by a discrete Fourier series in time, such that

$$[\mathbf{p}^g(t)]_\ell = \sum_{k=-\mathcal{F}/2}^{\mathcal{F}/2} \left[a_\ell^k \sin\left(\frac{2\pi kt}{T_{\text{HB}}}\right) + b_\ell^k \cos\left(\frac{2\pi kt}{T_{\text{HB}}}\right) \right], \quad \ell = 1, 2, 3,$$

where T_{HB} is the period of the registered heart beats, while the coefficients a_ℓ^k , and b_ℓ^k are chosen in order to satisfy the interpolation condition

$$[\mathbf{p}^g(t^f)]_\ell = [\mathbf{d}_{\text{MRI}}^{g,f}]_\ell, \quad \ell = 1, 2, 3, \quad f = 1, \dots, \mathcal{F},$$

being t^f the time corresponding to the f -th frame. The use of trigonometric polynomials also allows for filtering of the noisy measurements by dropping some of the more oscillating terms from the discrete Fourier series. In that vein, we define the regularized interpolant as

$$[\mathbf{p}^g(t)]_\ell = \sum_{k=-(\mathcal{F}/2-R)}^{\mathcal{F}/2-R} \left[a_\ell^k \sin\left(\frac{2\pi kt}{T_{\text{HB}}}\right) + b_\ell^k \cos\left(\frac{2\pi kt}{T_{\text{HB}}}\right) \right], \quad (6.4)$$

where R is the number of discarded modes, with $0 \leq R \leq \mathcal{F}/2 - 1$. The resulting deformation of the endocardial surface is smooth both in space and time, as well as that of the fluid domain Ω_{F}^0 ; the propagation of the displacement boundary conditions imposed at the epicardial surface through the left ventricular wall acts as a regularization of the measured data. Since such propagation might also depend on the mechanical properties of the left ventricular wall, in the result section we perform a sensitivity analysis with respect to the parameters of the wall constitutive law.

6.3.5 Set up of the problem: boundary conditions

The dynamics of the ventricle are simulated by the 3-D FSI model described in Chapter 1. In contrast with the 3-D FSI simulations presented in the previous chapters, the displacement of the external wall $\Gamma_{\text{S,EP}}^0$ is driven by the extrapolated epicardial displacement field; in particular,

$$\mathbf{d}_{\text{S}} = \mathbf{f}_{\text{d}} \quad \text{on } \Gamma_{\text{S,EP}}^0 \times (0, T],$$

where we recall that \mathbf{d}_{S} is the displacement of the solid domain. Therefore, apart from the nearly null compressibility of the solid wall, the volume of the ventricle at each time step is determined by the extrapolated epicardial displacement field. The solid problem is closed by imposing a homogeneous Neumann boundary condition on the top boundary, i.e.,

$$\sigma_{\text{S}} \cdot \mathbf{n}_{\text{S}} = \mathbf{0} \quad \text{on } \Gamma_{\text{S, TOP}}^0 \times (0, T].$$

The fluid dynamics are mainly driven by the displacement of the endocardium and by the interface conditions at the aortic and mitral valves, whose description is postponed to the next section. On the fluid top boundary $\Gamma_{\text{F, TOP}}^0$ we impose a no-slip boundary condition (in the fluid problem), i.e.,

$$\mathbf{u}_{\text{F}} = \mathbf{w}_{\text{F}} \quad \text{on } \Gamma_{\text{F, TOP}}^t \times (0, T],$$

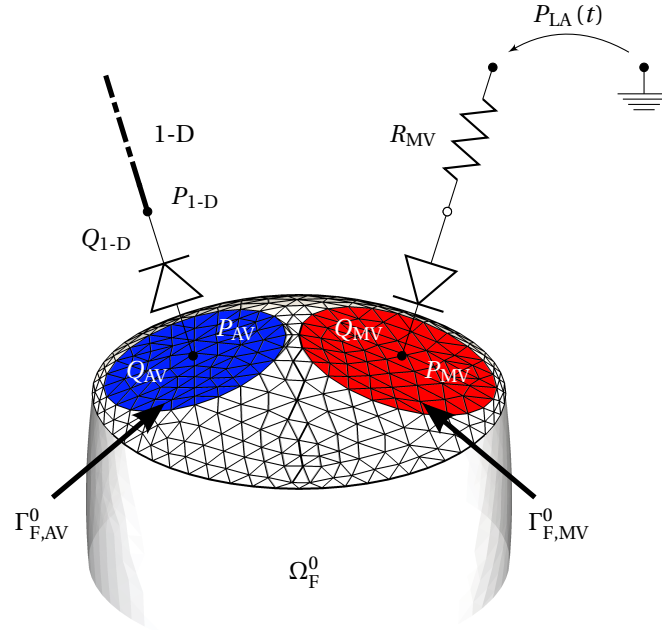


Figure 6.3: Schematic view of the lumped valves configuration. On each side of both the mitral and the aortic valves, the volumetric flow rate and pressure quantities are defined. The subscripts LA, MV, and AV stand for left atrium, mitral valve, and aortic valve, respectively. Note that, on the proximal side, the mitral valve is connected to a resistance model, while on the distal side the aortic valve is connected to the first 1-D element of the systemic arterial circulation.

and a homogeneous Neumann boundary condition (in the geometric problem), i.e.,

$$\nabla \mathbf{d}_F \cdot \mathbf{n}_F = \mathbf{0} \quad \text{on } \Gamma_{F, \text{TOP}}^0 \times (0, T].$$

The interface problem (1.11) coupling the fluid and the solid is imposed on the endocardium $\Gamma_{F, \text{EN}}$.

6.3.6 Ideal lumped model for heart valves

Following the approach proposed in Formaggia et al. (2006) we model the valve dynamics by using a simple lumped parameters model, which consist in an ideal diode, as shown in Figure 6.3. This model allows for a unidirectional blood flow when the pressure difference between the upstream and downstream location is positive, thus preventing the backflow when this condition is not satisfied. More precisely, the valve opens when the pressure difference between the proximal and distal location is positive and it closes when the flow rate becomes negative.

When a valve is closed, the pressure in the ventricle is related neither to the valve, nor to the state of the model connected to the other side; in particular, the value of the pressure on the two sides of a closed valve is generally different. Thus, the only information available as boundary data is the value of the flow rate (or the velocity field), which is null. For this reason, this data is used as boundary condition on $\Gamma_{F, \text{AV}}^0$ and $\Gamma_{F, \text{MV}}^0$.

When the aortic valve is open, the transvalvular flow is driven by the interaction between the 3-D left ventricle and the coupled 1-D arterial network described in Section 5.3 (see Table 5.4 for the main parameters). The coupling between this two dimensionally-heterogeneous models is address by imposing the set of equations (2.2) (conservation of flow rate and continuity of the mean normal stress) through coupling flow boundary data on the two interfaces.

When the mitral valve is open, the dependence of the blood flow on the pressure difference is treated in a different way. In particular, we assume a time-dependent law for the pressure in the left atrium and we prescribe the diastolic transvalvular volumetric flow rate Q_{MV} into the left ventricle as

$$Q_{MV} = \frac{P_{LA}(t) - P_{MV}}{R_{MV}},$$

where $P_{LA}(t)$ is the imposed left atrial pressure, P_{MV} the left ventricle pressure at the mitral inlet, and R_{MV} the hydraulic resistance of the mitral valve, which has been set equal to $10 \text{ dyn}\cdot\text{s}/\text{cm}^5$ to fit our model parameters.

For both valves, the transvalvular flow can be treated either without any assumption regarding the velocity profile across the valve section (flow rate defective boundary condition, see Formaggia et al. (2002) and Veneziani and Vergara (2005)) or relying on the assumption of a flat profile consistent with the target flow rate value (pointwise Dirichlet boundary condition). In the result section we perform a sensitivity analysis to assess the effects of choosing each of the two approaches on the internal dynamics of the ventricle.

Remark 6.2. In case of valvular pathologies, such as mitral regurgitation, a more refined model that takes into account the dynamic of the valves is needed to accurately capture the reversal of the flow and the resulting regurgitant volume loss (see, e.g., Mynard et al. (2011)). However, the patient selected in Section 6.2.1 does not suffer from any valve pathology, thus the diode model can be considered a reasonable approximation.

6.4 Results

In this section we present preliminary results of the pathological left ventricle coupled with a network of 1-D arteries, whose details are given in Section 5.3 (see Table 5.4 for the main parameters). The focus of our study is on the calibration and sensitivity analysis of the main parameters of the model; the study of the clinical aspects and of the associated pathology will be subject of future works.

The ideal truncated ellipsoid geometry and mesh of the ventricle has been obtained using the Gmsh⁴ mesh generator (see Geuzaine and Remacle (2009)). In particular, the fluid part of the problem consists of 41550 tetrahedral elements with 7913 vertices, while the solid part is made of 28080 tetrahedral elements with 6356 vertices. The corresponding average space discretizations for the fluid and solid problems is approximately 0.35 cm.

For all the simulations presented here we run six heart beats to achieve a nearly periodic solution of the global problem. The interface problem is defined by imposing the set of equations (2.2), i.e., conservation of flow rate and continuity of the mean normal stress, at all the nodes of the network; more precisely we set $n_c^Q = 0$, for $c = 1, \dots, 99$, and $n_c^Q = 2$, for $c = 100, 101$, where the first 99 nodes are those introduced in Section 5.3.1, while nodes 100 and 101 couple the left ventricle with the surrounding models through the valves described in Section 6.3.6. The imposed tolerance for the interface problem is 10^{-6} and the time step of the global network is set equal to 10^{-3} s. Unless otherwise specified, the main parameters of the 3-D left ventricle are those reported in Table 6.2. The interaction between the fluid and the solid in the 3-D left ventricle is approximated by using the GCE time discretization scheme (see Chapter 1).

⁴<http://www.geuz.org/gmsh>.

Table 6.2: Left ventricular wall and mitral valve parameters.

ρ_S	Wall density	1.2 g/cm ³
h_S/D_S	Wall thickness / ventricle diameter	0.1
E_S	Young's modulus	$7 \cdot 10^6$ dyn/cm ²
ν_S	Poisson's ratio	0.40
P_{LA}	Left atrial pressure	$1 - 2 \cdot 10^4$ dyn/cm ²
R_{MV}	Mitral valve resistance	10 dyn·s/cm ⁵

In the following, first we calibrate the parameters for the reconstruction of the ventricle. Then we perform a sensitivity analysis of the pressure-volume diagram with respect to the Young's modulus of the fictitious elastic structure. In addition, we also compare the fluid dynamics inside the ventricle for three different sets of boundary conditions at the two valves. Finally, we present the pressure and flow rate waveforms in several selected 1-D arterial segments; there we also provide a calibration procedure of the terminal resistances to recover the pathological value of the pressure.

All the simulations were performed on three cluster nodes with two Intel® Xeon® processors X5550 (quad core, 8 MB cache, 2.66 GHz CPU) each, for a total of 24 CPUs interconnected by a 20 Gb/s InfiniBand® architecture.

6.4.1 Regularization of the assimilated data

As discussed at the end of Section 6.3.4, in some cases it may be necessary to drop some of the most oscillating terms from the discrete Fourier series to avoid spurious oscillations in the volume-time diagram and, consequently, in the pressure-volume diagram. This might also help to recover a more accurate estimate of the end-diastolic and end-systolic volumes; more precisely, the regularization level for the trigonometric interpolation, i.e., a suitable value for the number R of discarded modes, can be chosen by computing estimates of these two reference volumes for different levels of regularization. The left ventricle measurements at end-diastole have been identified from the MRI as $V_{MRI}^{EDV} \approx 179$ cm³ and $L_{MRI}^{EDV} \approx 7.13$ cm. Being the measured end-systolic volume equal to 140 cm³, the ejection fraction of the pathological ventricle is approximately 22%. The corresponding quantities observed in the reconstructed ventricle are listed in Table 6.3. Note that from equation (6.1) the least-squares normalization of the reference computational domain to the tracking points results in $\mathcal{E}_J = 0.2065$.

The analysis of the values in the table shows that the sensitivity of the volumes with respect to the regularization level is very small. Nevertheless, some discrepancies between the reconstructed and estimated volumes can be observed. In particular, the end-systolic volume is below the respective measurement obtained from the MRI by approximately 9%. This discrepancy is likely due to the fact that the implemented computational domain includes also the left ventricle apex and the left ventricle upper end immediately adjacent, whereas the acquired stack of MRI short-axis images used to estimate left ventricle volumes did not include these two portions of the intracavitary volume.

A possible criteria to select a regularization level is to observe the relative variation of the volumes with respect to the non-regularized case, i.e., $R = 0$. In particular, $R = 5$ represents the highest level for which the end-systolic volume variation is below 1%, thus might represent a good choice. This is confirmed in Figure 6.4 where we compare the reconstructed left ventricular volumes for $R = 0$ and $R = 5$. With $R = 5$ the spurious oscillations of the volume during diastole are eliminated and the volume increases monotonically, while the end-diastolic and end-systolic volumes do not change with respect to the non-regularized case.

Table 6.3: Sensitivity analysis of the left ventricle volumetric quantities^a with respect to different regularization levels; the last row reports the reference estimates based on MRI measurements. We remark that for the patient under consideration $\mathcal{F} = 20$.

	EDV [cm ³]	ESV [cm ³]	SV [cm ³]	EF [%]
$R = 0$	175.6	129.0	46.6	26.6
$R = 1$	175.9	128.6	47.3	26.7
$R = 2$	176.3	126.8	49.5	28.1
$R = 3$	176.1	128.7	47.4	26.9
$R = 4$	176.5	129.0	47.5	26.9
$R = 5$	176.5	130.2	46.3	26.2
$R = 6$	176.8	130.3	46.5	26.3
MRI	179.0	140.0	39.0	22.0

^a ESV, end-systolic volume; EDV, end-diastolic volume; SV, stroke volume; EF, ejection factor.

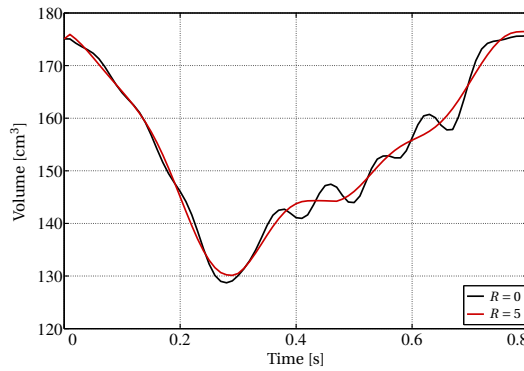


Figure 6.4: Left ventricle volume comparison with and without regularization during one heart beat (see equation (6.4) for definition).

6.4.2 Sensitivity analysis with respect to the main parameters of the fictitious structure

The calibration of the parameters of the fictitious elastic wall represents an important preliminary step to correctly simulate the dynamics of the ventricle. As pointed out in Section 6.3.4, the function of the fictitious wall is to impose a proper displacement field on the endocardium to avoid artifacts and numerical instabilities that might be induced by the noise in the measured data. The main parameters of the elastic wall are the Young's modulus, the Poisson's ratio, the thickness, and the density. Among them, the Young's modulus is the most critical (as observed, e.g., in Section 4.4 in a different context). In view of this, we perform here a sensitivity analysis of the pressure-volume diagram with respect to a variation of the Young's modulus of the left ventricular wall.

The results of this analysis are depicted in Figure 6.9a. The overall pressure-volume behavior of the left ventricle is not affected by changes in the Young's modulus of the left ventricular wall; indeed, the only differences between the three depicted diagrams is observed during the mitral valve opening (see Figure 6.9b), when a slight pressure overshooting (approximately 10^4 dyn/cm²) is observed for $E_S = 3.5 \cdot 10^6$ dyn/cm² and $E_S = 14.0 \cdot 10^6$ dyn/cm². Based on this result, the strategy adopted to impose

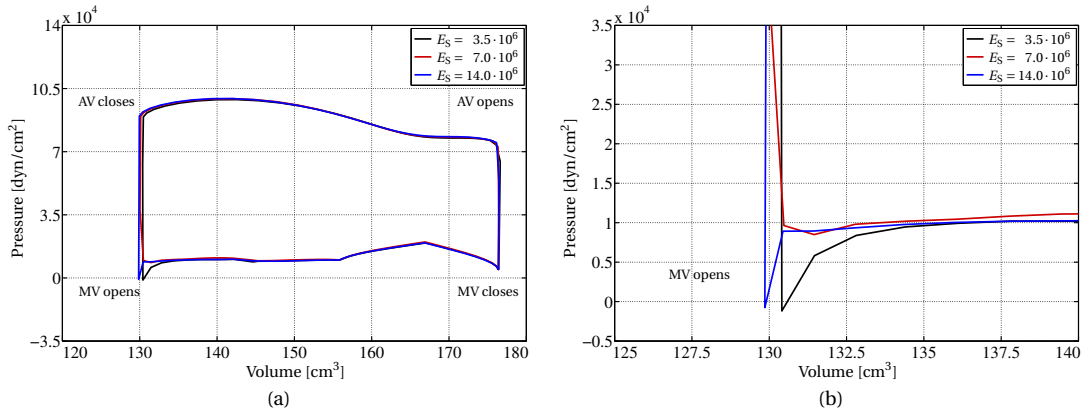


Figure 6.5: (a) Average ventricular pressure versus left ventricle volume for different values of the Young's modulus of the fictitious elastic structure. (b) Enlarged view of the left image.

left ventricular wall boundary displacements, i.e., imposing a smooth displacement field over the fictitious epicardial surface and obtaining the endocardial regional motion through the propagation of the imposed boundary conditions, can be considered robust and repeatable. Further analysis with respect to, e.g., variations of the wall thickness will be subject of future works.

6.4.3 Influence of boundary conditions at the heart valves

At the end of Section 6.3.6 we discussed two possible strategies for treating the transvalvular flow. The first one consists in imposing a flow rate defective boundary condition at the valves, without any assumption on the inflow/outflow velocity profile. The second one assumes a flat velocity profile at the valves, which is imposed through a pointwise Dirichlet boundary condition.

Now we perform a comparison between the velocity field results of these two strategies. In particular, we set up three different cases: (i) flow rate defective boundary condition at both valves, (ii) flow rate defective boundary conditions at the aortic valve and pointwise Dirichlet boundary condition at the mitral valve, and (iii) pointwise Dirichlet boundary conditions at both valves. In all cases the total flow rate through the orifice of the valve is given by the interface equations with the surrounding models.

The results of this comparison, for three different states of the ventricle, are depicted in Figure 6.6. We can observe that when a defective boundary condition is applied to both valves (see Figure 6.6a) a strong artifact appears at the mitral valve during both systole and diastole. In systole, a significant backward flow towards the atrium is observed; thus, the continence of the mitral valve during systole is not captured. This artifact is due to the proximity of the two valves and to the fact that imposing a flow rate equal to zero does not imply a pointwise null velocity field at the closed mitral valve. At mid-diastole, the inflow jet is highly non-symmetric, with a marked high velocity region next to the aorto-mitral junction, whereas the transmitral inflow should be characterized by an almost flat velocity profile. Again, this is an artifact induced by the presence of the aortic valve when imposing the flow rate. Finally, at end-diastole, a transmitral backflow into the atrium is visible.

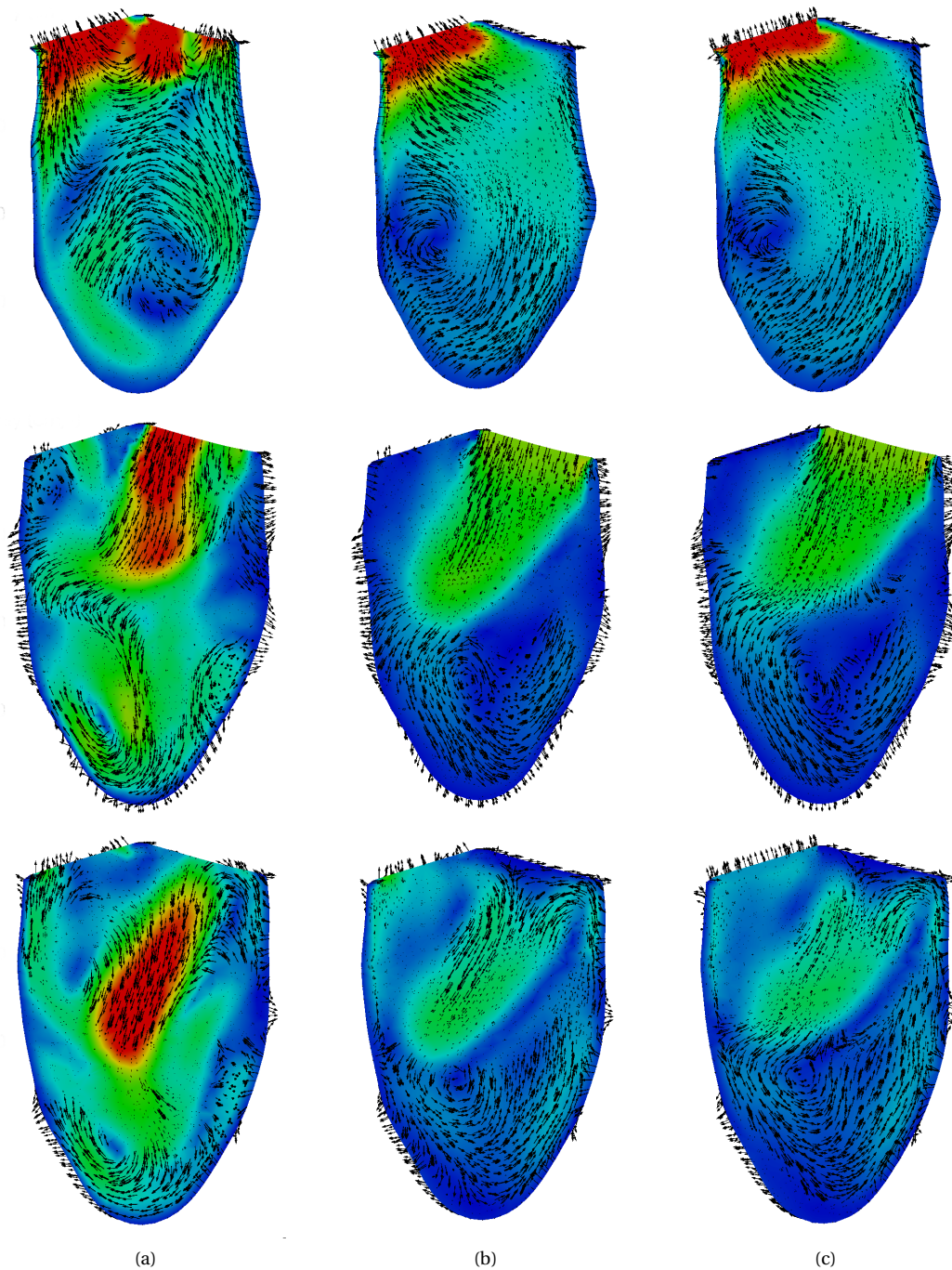


Figure 6.6: Velocity field comparison along the plane transversal to the valves, with respect to the chosen set of boundary conditions imposed at the two valves. The images refer to mid-systole (top), mid-diastole (middle), and end-diastole (bottom) of the sixth heart beat. The color bar ranges from blue (0 cm/s) to red (40 cm/s). (a) Flow rate defective boundary conditions at both valves. (b) Flow rate defective boundary condition at the aortic valve (left side) and pointwise Dirichlet boundary condition at the mitral (right side) valve. (c) Pointwise Dirichlet boundary conditions at both valves.

In contrast, the above discussed artifacts do not occur when a pointwise Dirichlet boundary condition is applied at the mitral valve (see Figure 6.6b). Moreover, the dependency on the boundary condition at the aortic valve is more subtle, such that switching from the defective strategy (see Figure 6.6b) to the pointwise one (see Figure 6.6c) does not lead to major changes in the simulated left ventricle fluid dynamics.

The results obtained in the analysis of the valve boundary condition effects are consistent with the findings by Long et al. (2003), who also studied the effects of imposing different types of boundary conditions on the mitral valve, mainly during the diastolic phase. In particular, the authors observed that if a weaker (in their case Neumann) boundary condition is used, the resulting inflow jet is highly skewed towards either the anterior or the superior wall, depending on the inflow area used to impose the boundary condition. In their experience, imposing a flat profile provides a more reliable and consistent flow field inside the ventricle.

The final conclusion on which type of boundary condition produces the closest flow with respect to real observations requires further study and comparison with experiments, e.g., using techniques of phase-contrast MRI, which were not available to us at the time of this study. It should be mentioned that our model also neglects the effect of the transient opening of the valve leaflets, which was found in Baccani et al. (2003) to have possibly larger effect on the ventricular flow velocity during diastole than the particular ventricle geometry.

6.4.4 Patient-specific calibration of the systemic arterial circulation

The reduced order arterial models available in the literature are usually tuned to represent young, healthy patients. However, the subject selected for this study is a 67-year-old patient suffering from severe ventricular dysfunction (see Table 6.1). Therefore, his arterial systemic circulation cannot be modeled by the same data given in Reymond et al. (2009), which have been previously used in Chapter 5 for simulating the arterial flow of an average healthy patient.

As an example, we report in Figures 6.7 and 6.8 the pressure and flow rate waveforms, respectively, in some selected arteries; the values obtained by using the data in Reymond et al. (2009), meant to represent the arterial properties of healthy subjects, are colored in black. From the images it is evident that the low cardiac output of the pathological heart drives the pressure level far below the pathophysiological regime. In the actual patient, the systemic autoregulation tunes the radius and stiffness of the small arteries to recover a higher pressure level. Thus, to obtain proper predictions on possible adverse effects of systolic dysfunction, a patient-specific calibration study should be performed in the way proposed, e.g., by Reymond et al. (2011).

As part of this work we did not have available patient-specific pressure and flow rate measurements. However, a typical feature of systolic left ventricle dysfunction is a moderate to severe hypertension as reported in Hedberg et al. (2001); mean and variance over one-hundred 75-year-old patients suffering from left ventricle systolic dysfunction are 220000 ± 35000 dyn/cm² in systole and 110000 ± 15000 dyn/cm² in diastole. In this pathological scenario the main altered hemodynamic features are the peripheral resistances. Therefore, we calibrate the model by tuning two parameters: the reference external pressure of the arterial vessels and the hydraulic resistances of the three-element windkessel terminals.

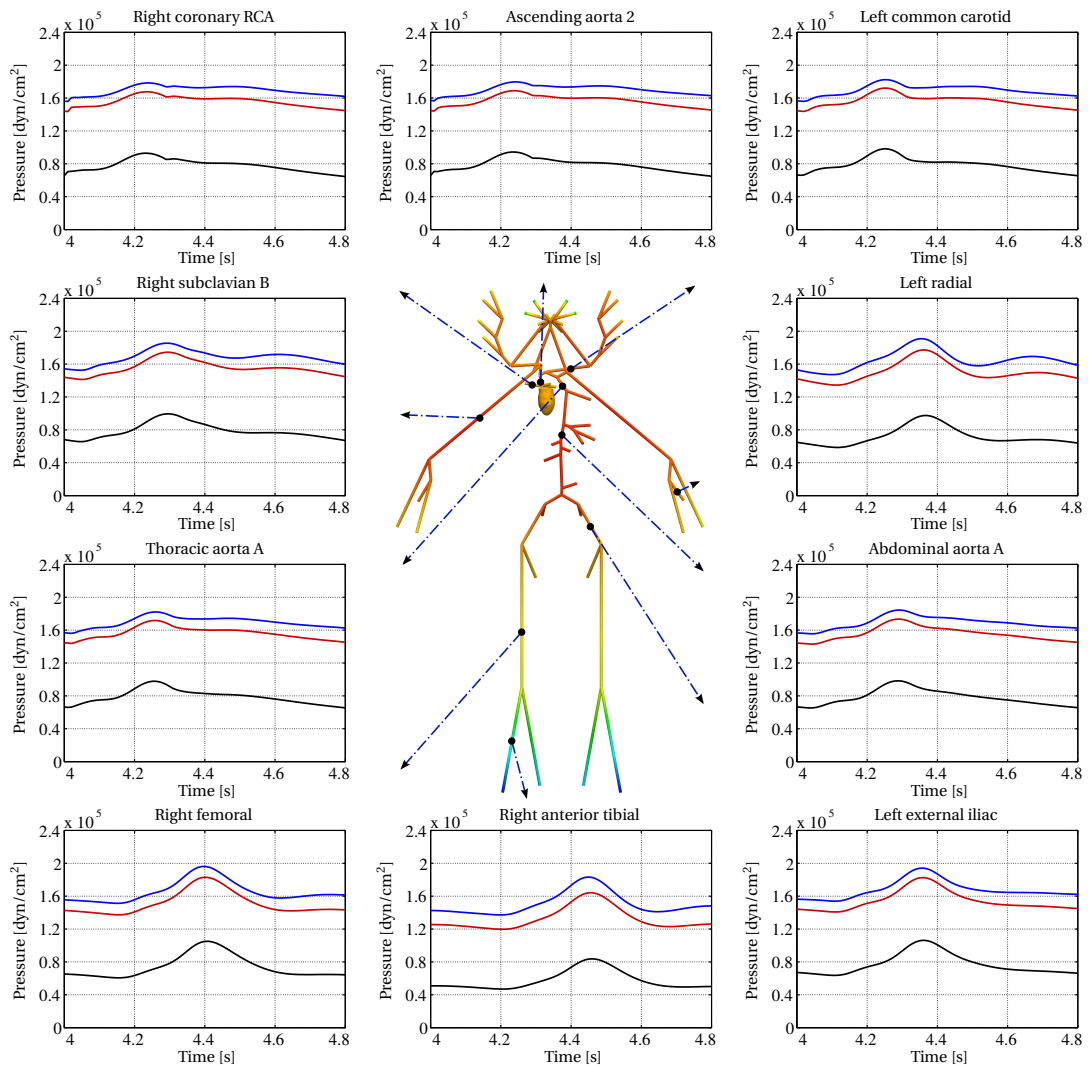


Figure 6.7: Pressure results in ten selected arterial segments. Black curves refer to the uncalibrated network. Red lines refer to a calibrated network where the terminal hydraulic resistances have been increased by a factor 2.3 and the external pressure have been raised to 135000 dyn/cm². Blue lines refer to a calibrated network where the terminal hydraulic resistances have been increased by a factor 3.0. The color of the central image represents the pressure field of the uncalibrated model at the end-systole of the sixth heart beat ($t = 4.3$ s), where the color bar ranges from blue (40000 dyn/cm²) to red (100000 dyn/cm²). Positioning of 1-D network elements and of the 3-D heart is purely visual.

A rough estimate of the resistance scale factor can be computed as the ratio between the expected pathological value and the uncalibrated systolic pressure, i.e., approximately 2.3. Nevertheless, this value is not sufficient to reach the aimed pressure level. Therefore we also raised the external pressure from 100000 dyn/cm² to 135000 dyn/cm². The results of this calibration are reported in Figures 6.7 and 6.8 colored in red. With respect to the uncalibrated black curves there is a visible increment in the pressure level (approximately 75000 dyn/cm²). Regarding the flow rate curves, we do not see significant differences between the two cases. In addition, compared to the results for a healthy patient (see, e.g., Figure 5.10), it is evident that the pathological state of the left ventricle induces some strong irregularities in various arteries. We note especially the flow reversal in the left common carotid; indeed,

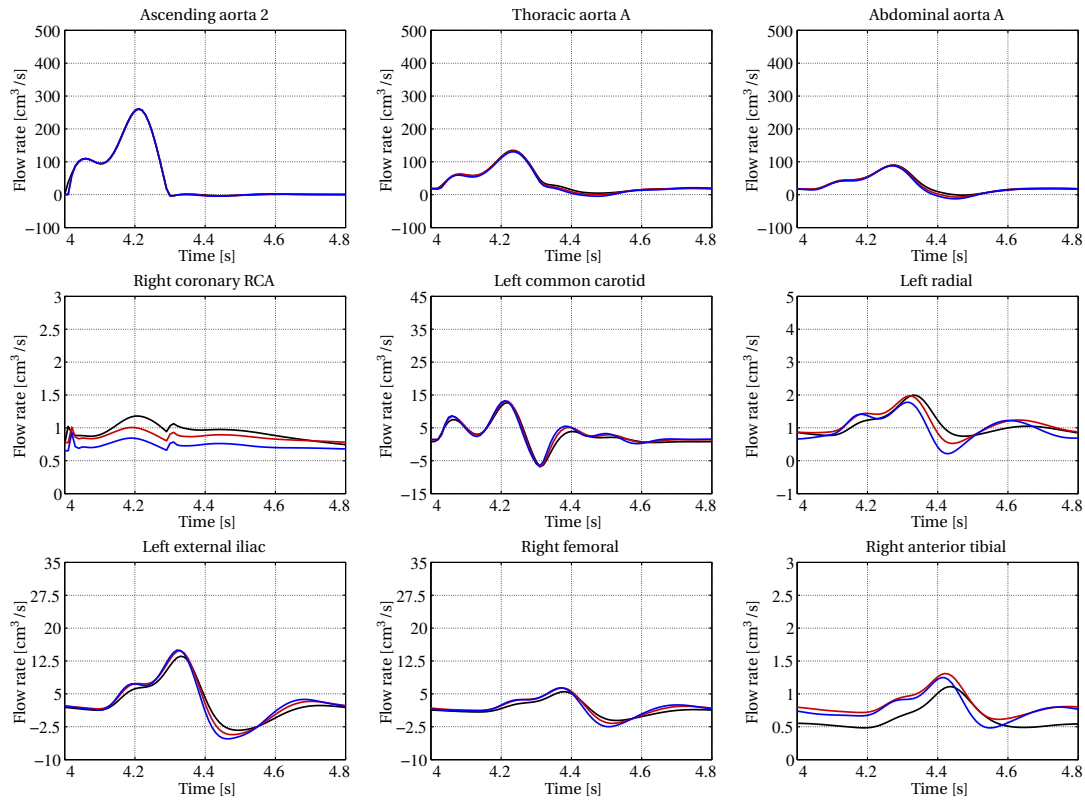


Figure 6.8: Flow rate results in six selected arterial segments. The colors refer to the same configurations described in Figure 6.7.

it is known that especially isolated systolic hypertension is a strong indicator of risk for carotid stenosis (see, e.g., Sutton-Tyrrell et al. (1993)).

A slightly different strategy for the calibration consists in applying a higher scale factor to the terminal resistances, without raising the external pressure. Indeed, increasing the resistances by a factor 3.0 we obtain a similar result compared to the previous calibration (see blue curves in Figures 6.7 and 6.8).

Finally, in Figure 6.9 we compare the left ventricular pressure between the uncalibrated and the two calibrated networks. From the images we observe that the only difference between the three cases is in the systolic pressure level. In particular, the hypertension of the pathological systemic arterial circulation results in a higher pressure at the distal side of the aortic valve, such that the ventricular pressure needs to reach that level to let the valve open.

6.5 Discussions

In this chapter we have presented a new approach for the simulation of pathological left ventricle dynamics. The main features of our technique are (i) the ideal ellipsoid geometry for the preliminary description of the left ventricle, (ii) the combined radial basis and trigonometric polynomial interpolation functions for the reconstruction of the displacement field of the epicardium from MRI data, (iii) the fictitious linear elastic structure to transfer the interpolated displacement field on the epicardium, and (iv) the geometrical multiscale method for the implicit coupling of the ventricle with the arterial systemic circulation.

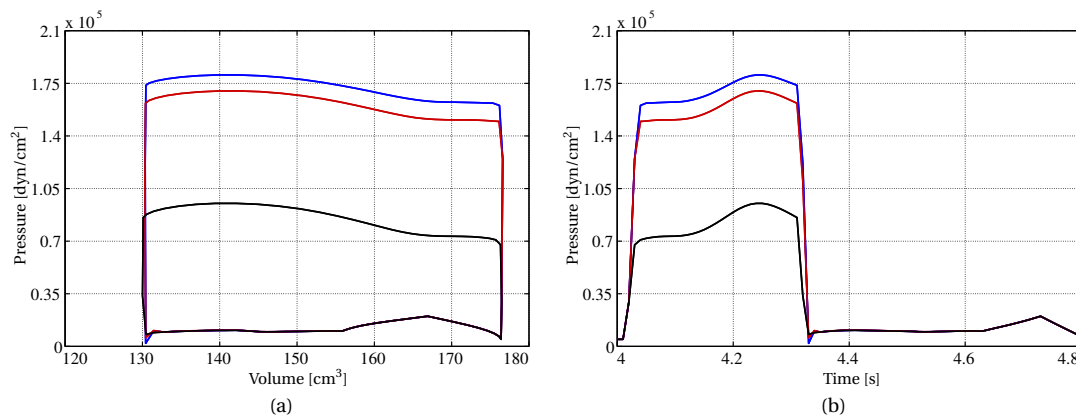


Figure 6.9: Comparison of the left ventricular pressure between the uncalibrated and calibrated configurations at the sixth heart beat. The colors refer to the same configurations described in Figure 6.7. (a) Pressure-volume diagrams. (b) Pressure-time curves.

The first two ingredients provides a quick and systematic way to set up patient-specific simulations based on the same geometry and mesh. The third aspect allows to overcome the limitations of the MRI acquisition process, representing an automatic way to smooth and filter the noise and the possible abnormalities in the measured data. The last ingredient provides a reliable way to account for the boundary conditions at the ventricle valves and to study the interaction between the ventricular pathologies and the arterial systemic circulation.

Regarding the numerical simulations, our study has mainly focused on the calibration and sensitivity analysis of the main parameters. More precisely, we have evidenced a low influence of the Young's modulus of the fictitious elastic wall on the dynamics of the ventricle, and in particular on the pressure-volume diagram. Nevertheless, further analysis should be performed at least on the calibration of the wall thickness, which might be adjusted to improve the filtering level of the MRI data noise.

Another important aspect concerns the modeling of the valve and in particular the correct choice of boundary conditions at the 3-D interfaces. The imposition of defective flow rate boundary data at the mitral valve caused strong artifacts and transmitral backflows. In contrast, more regular ventricular fluid dynamics have been observed when a flat velocity profile has been imposed. Further studies should be performed to assess which boundary data produces the flow nearest to real observations. Moreover, our model does not account for the leaflets dynamics, which might have a strong impact on the velocity field. A first possible improvement may consist in using a more sophisticated lumped parameters model to account, at least, for the transient phase between the opening and closure of the valves. Moreover, regarding the aortic valve, a further extension may consist in accounting for a short cylindrical segment between the valve and the left ventricular cavity, thus modeling the initial segment of the aortic arch.

The results of the interaction between the 3-D left ventricle and the 1-D systemic arterial circulation have evidenced the need for a calibration process to account for the pathological hypertension of the selected patient. This is important not only to recover the pathophysiological pressure level in the arteries, but also to obtain more precise estimates of the flow rate waveforms and to highlight the presence of possible backflows. The calibration of the network can be achieved acting on several parameters at the same time, such as the resistances and compliances of the terminals or the elastic and viscoelastic

Chapter 6. Data acquisition and simulation of pathological left ventricle dynamics

properties of the vessels. However, we have shown that tuning the terminal hydraulic resistances and the reference external pressure of the vessels is enough to recover preliminary reasonable pressure levels.

In summary, the model presented in this chapter can be regarded as a concrete example of how the methodology devised throughout the thesis can be effectively used to simulate complex cardiovascular pathologies of clinical interest. At the same time, we also recognize that the results and analyses presented here are not enough to assess all the benefits and drawbacks of the proposed model. For instance, among the other aspects, a true assessment of the model should include at least comparisons with (i) images data of the ventricular flow, (ii) flow rate and pressure waveforms measures in the main arteries, and (iii) numerical results obtained with simpler models, e.g., lumped parameter heart models coupled with networks of 1-D arteries. Moreover, the presented methodology can be improved in several ways as briefly discussed in the previous paragraphs.

Main reference of the chapter:

- ☆ T. Lassila, A. C. I. Malossi, M. Stevanella, E. Votta, A. Redaelli, and S. Deperis. Multiscale fluid-structure interaction simulation of patient-specific left ventricle fluid dynamics with fictitious elastic structure regularization. Submitted, 2012.

7 Numerical simulation of left ventricular assist device implantation

Mechanical circulatory supports, in particular ventricular assist devices (VADs), represent an alternative to transplantation in the treatment of terminal heart failure. The lack of donors and the resulting increasing number of patients on the waiting lists motivate the concurrent development of different devices, with the common aim of increasing the life expectations of the patients. In this regard, numerical simulations may represent an effective tool to compare and analyze the behavior of the different devices in a systematic and non-invasive way, thus helping the clinicians in the decision making process. Indeed, the complication rate of these devices is still very high and experience shows that many of them are related to haemodynamic modifications due to VAD implantation.

In this chapter we focus our analysis on the comparison of two techniques for the implantation of left ventricular assist devices (LVADs), which mainly differ in the anastomosis site of the device outflow cannula. More precisely, in Section 7.1, after a brief overview of the clinical problem, we describe the two different cannulation techniques, each one associated to a different device. Then in Section 7.2 we set up and validate a lumped parameters model for the simulation of the global circulation for different stages of heart failure and rotational speeds of the LVAD. The results of the lumped model are used in Section 7.3 as inflow boundary data for a network of 1-D elements modeling the systemic arterial circulation; the spatial description of the 1-D network allows to compare the flow rate waveforms as a function of the anastomosis site of the device outflow cannula. Finally, in Section 7.4 we summarize the main conclusions of this preliminary study and we briefly discuss possible future extensions of the current model.

7.1 Clinical problem and state of the art

Heart failure is a clinical syndrome that expresses the inability of the heart to provide enough blood to the organs to satisfy their metabolic needs. It has numerous causes (e.g., valvular disease, cardiomyopathy, myocarditis, coronary artery disease and subsequent myocardial infarction) and symptoms (e.g., dyspnea, fatigue, peripheral edema), as documented, e.g., in Jessup and Brozena (2003). Within the population studied by the European Society of Cardiology (more than 900 millions of people in 51 countries, see Dickstein et al. (2008)), heart failure prevalence is between 2% and 3%, affecting at least 15 millions of patients. In the U.S.A., 2.5% of the adult population (5.7 millions of people) suffers from heart failure and 670000 new cases occur every year. Among the deaths reported in 2004, 292000 were caused directly or indirectly by heart failure. The estimated overall cost of heart failure in the U.S.A. in 2009 was 37.2 billion of dollars (see Lloyd-Jones et al. (2009)).

The first line of treatment of heart failure includes sodium and fluid restriction, weight loss and lifestyle modifications, such as smoking cessation. These are necessary but usually not sufficient. The second line of treatment is the use of drugs, like angiotensin-converting enzyme inhibitors, angiotensin-receptor blockers, diuretics, and beta-blockers. Finally, invasive treatment includes cardiac resynchronisation therapy, which consists in the implantation of a pacemaker (biventricular pacing, with or without an implantable cardioverter-defibrillator) and transplantation (see McMurray and Pfeffer (2005)). However, heart donors are scarce (2210 transplantations in 2007 in the U.S.A.) and, in June 2008, 2607 patients were still on the waiting list (see Lloyd-Jones et al. (2009)).

Nowadays, the implant of a VAD has become a common therapeutic approach for treating heart failure, especially in relation to the lack of donors and to the raising number of patients presenting terminal heart failure (see, e.g., Thunberg et al. (2010) and Roger et al. (2011)). At the beginning the use of a VAD was indicated for patients on the transplantation waiting list (*bridge to transplantation*, see Miller et al. (2007)) and for patients with a temporary need of circulatory support (*bridge to recovery*, see Birks et al. (2006)). With the development of more effective devices and the improvement of the clinical experience, the indication for the procedure has widen and it is now proposed to patients who are ineligible for transplantation (*destination therapy*, see Rose et al. (2001)) and also in situations of extreme emergency (*bridge to decision*, see Ziemba and John (2010)).

When using a continuous flow LVADs, such as the HeartMate II[®] (Thoratec Corporation¹, see Figure 7.1a), the outflow cannula is usually anastomosed to the ascending aorta (AA). However, some devices allow to perform the anastomosis to the descending aorta (DA), such as the Jarvik 2000 FlowMaker[®] (Jarvik Heart Inc.², see Figure 7.1b). The latter procedure is less invasive for the patient as it consists in a left thoracotomy (see Westaby et al. (2002)) and avoids the adverse effects of a cardiopulmonary bypass and of a sternotomy, especially in the case of patients who are critically ill and already had multiple median sternotomy (see Frazier et al. (2006)).

Nevertheless the beneficial effect of this procedure is still controversial. For instance, Litwak et al. (2004) performed *in vivo* experiments showing that a DA anastomosis induces a significant lower flow rate in the aortic arch and an abnormal flow pattern, including turbulent regions. This has been further confirmed in Litwak et al. (2005) through *in vitro* experiments where the combined ejection of the DA anastomosed cannula and the ventricle induced regions of stagnation and turbulence which could potentially have clinical consequences (see also DiGiorgi et al. (2004)). Moreover Nawata et al. (2010) reported adverse clinical effects in patients with a DA anastomosis, especially thromboembolic events. In addition, the numerical results in Bazilevs et al. (2009) indicate deficiencies associated with the implantation of a LVAD in the descending branch of the thoracic aorta, specifically, blood flow stagnation, abnormally high mean wall shear stress in the vicinity of the implant, and abnormally low and highly oscillatory wall shear stress in the aortic arch.

On the other side, the reliability of the DA anastomosis with the Jarvik 2000 FlowMaker[®] device has been demonstrated clinically by Frazier et al. (2002). Furthermore, Tuzun et al. (2011) showed that myocardial blood flow is not adversely affected by the outflow-graft anastomosis and Ghodsizad et al. (2011) reported the advantages of the DA anastomosis without cardiopulmonary bypass; both studies were conducted on animals.

¹<http://www.thoratec.com>.

²<http://www.jarvikheart.com>.

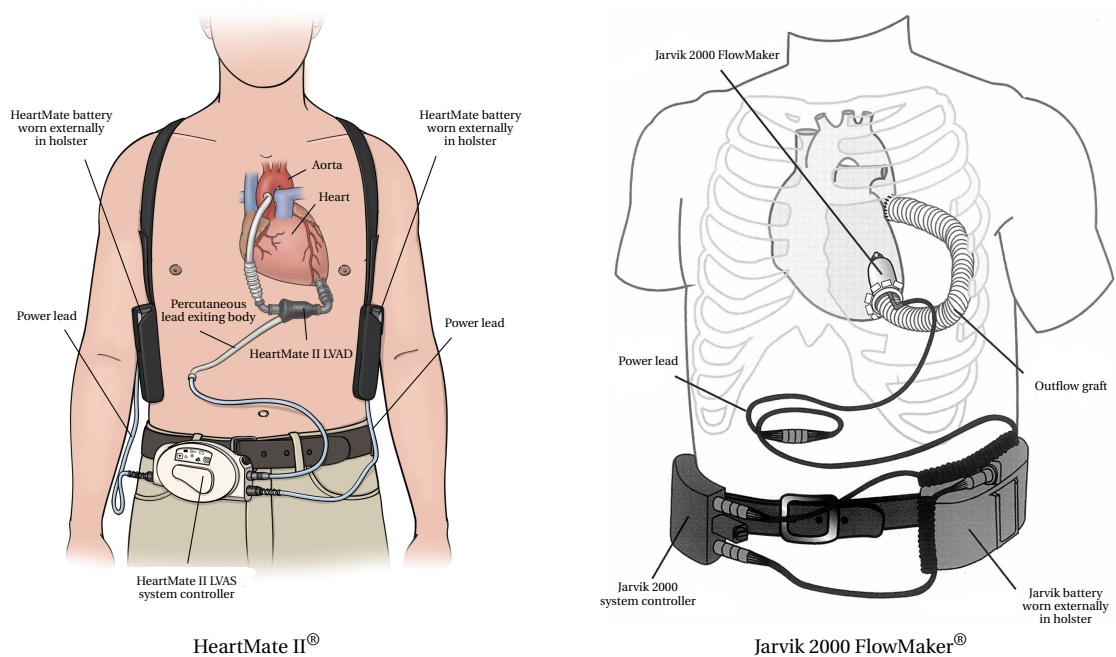


Figure 7.1: Scheme of the two LVADs: the inflow cannula is inserted in the apex of the deficient ventricle and the outflow cannula is anastomosed to either the ascending or the descending aorta. The blood flow taken from the left ventricle is actively pumped by the device and goes through the outflow cannula to the aorta. A percutaneous drive line carries the electrical cable to the battery packs and electronic controls. (a) The HeartMate II[®] pumps the blood in the ascending aorta³. (b) The Jarvik 2000 FlowMaker[®] pumps the blood in the descending aorta⁴.

Few studies were performed by mathematical and numerical models to compare the different sites of outflow cannula anastomosis (see, e.g., May-Newman et al. (2006) and Yang et al. (2009, 2010)). Moreover, at the best of our knowledge, only Kar et al. (2005) compared the AA and the DA anastomoses, highlighting the presence of stagnation zones in the aortic arch, especially with the DA anastomosis. A critical point of the numerical models is the choice of a suitable set of boundary conditions to correctly simulate the arterial systemic circulation supported by the LVAD. Up to now, experimental flow rates (either from humans or animals) have been applied as boundary data at the root of the aortic arch, while experimental or extrapolated data have been used as inflow conditions for the anastomosed cannula of the LVAD. Although these methods allow a rough estimation of the flows, they do not take into account the fact that the flow rate prescribed by the LVAD depends on the pressure difference across the device and, therefore, on the left ventricle pressure, which is determined by the cardiac function.

To overcome these limitations, in the following we first extend the global circulation lumped parameters model by Ursino (1998) to account for the presence of the LVAD. Then, we use the resulting flows as inflow boundary data for a network of 1-D FSI arteries which models the systemic circulation. The spatial description of the 1-D network allows to compare the flow rate waveforms as a function of the anastomosis site of the device outflow cannula and of other parameters of interest, such as the heart failure stage and the rotational speed of the device.

³Image reprinted from Thoratec Corporation with permission.

⁴Image reprinted from Frazier et al. (2001) with permission.

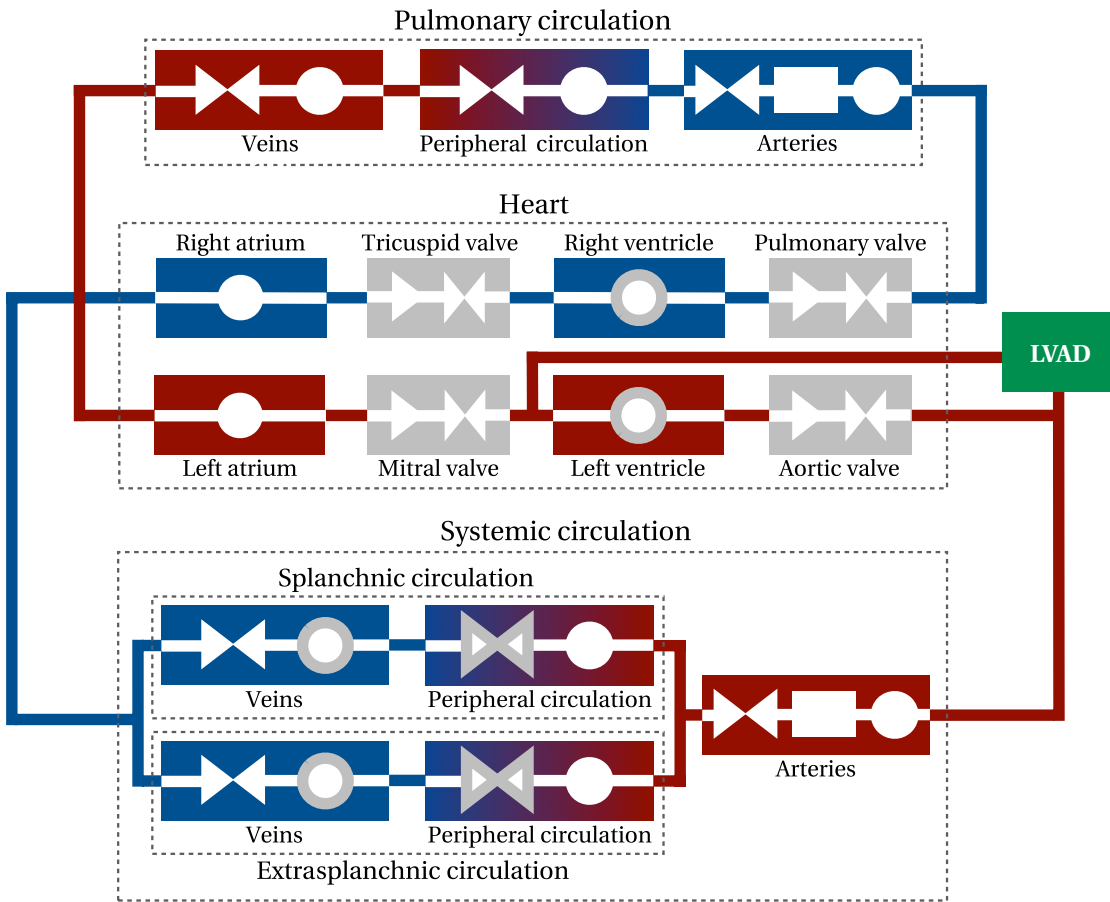


Figure 7.2: Diagram of the lumped parameters model. Four main compartments can be identified: heart, systemic circulation, and pulmonary circulation. Red and blue elements denote subcompartments containing oxygenated and deoxygenated blood, respectively. White circles represent compliances, white rectangles inertances, and white facing triangles resistances. Single triangles denote proper valves. Elements with a thick gray contour are subject to autoregulation as a function of the arterial pressure at the inlet of the systemic circulation arteries. The LVAD device pump blood from within the left ventricle to the systemic arteries.

7.2 Lumped parameters model of the global circulation

The lumped description of the cardiovascular network is obtained extending the model of Ursino (1998), which was originally developed to simulate the interaction among the carotid baroreflex, the pulsating heart, and the effector responses in different experiments. The model includes an elastance variable description of the left and right heart, the splanchnic and extrasplanchnic systemic circulation, the pulmonary circulations, the afferent carotid baroreceptor pathway, the sympathetic and vagal efferent activities, and the action of several effector mechanisms. To account for the presence of the LVAD we add a compartment representing the device pump in parallel with respect to the left ventricle. A sketch of the resulting model is depicted in Figure 7.2.

7.2. Lumped parameters model of the global circulation

The vascular compartments are modeled by using the classical electrical analogy, leading to a system of differential algebraic equations relating the volume V_C , the inlet and outlet volumetric flow rate $Q_{C,in}$ and $Q_{C,out}$, and the inlet and outlet pressure $P_{C,in}$ and $P_{C,out}$. The mass conservation reads

$$\frac{dV_C(t)}{dt} = Q_{C,in}(t) - Q_{C,out}(t), \quad t \in (0, T], \quad (7.1)$$

while the momentum conservation is given by

$$P_{C,in}(t) - \frac{dP_{C,out}(t)}{dt} = R_C Q_{C,out}(t) + L_C \frac{dQ_{C,out}(t)}{dt}, \quad t \in (0, T], \quad (7.2)$$

where R_C denotes the hydraulic resistance of the compartment and L_C the inertance of the flow. Equations (7.1) and (7.2) are complemented by a pressure-volume relation by mean of a compliance C_C , namely

$$\frac{dV_C(t)}{dt} = C_C \frac{dP_{C,in}(t)}{dt}, \quad t \in (0, T].$$

The conservation of mass and momentum is imposed at each node of the lumped parameters network through equations analogous to (2.2), where the mean normal stress coincides with the opposite of the pressure (as for the 1-D model). Inertance of the flow is considered only for arterial compartments since in the other elements that term is small compared to the resistive hydraulic pressure loss and can be neglected. Cardiac valves are considered open if the pressure in the upper chamber is greater than the one in the lower chamber and closed viceversa. In the former case, a nonlinear resistance models the hydraulic pressure loss through the valve. Autoregulation is modeled by a set of differential algebraic equations changing the elastance of the heart ventricles, the resistances, and the unstressed reference volumes of splanchnic and extrasplanchnic circulation. Both sympathetic and vagal autoregulation pathways are taken into account. For more details on equations modeling the phenomena see Ursino (1998).

The LVAD is modeled by a pressure-controlled flow generator. In particular, for each pressure difference across the device, the corresponding flow is prescribed according to interpolated experimental pressure-flow curves at different rotational speeds⁵. Note that to have comparable results for the two cannulation techniques, we decided to use the parameters of only one device, the Thoratec HeartMate II[®], although this device is not designed nor approved for a DA anastomosis.

The model can simulate different heart states. In particular, we consider the case of healthy heart (HH), mid heart failure (MHF), and severe heart failure (SHF); the last two are both in the context of dilated cardiopathy. To set up the different cases we have changed some of the parameters given in Ursino (1998); these are summarized in Table 7.1. More precisely, $E_{\max,lv}$ represents the reference value of the ventricle elastance at the instant of maximum contraction for the patient, while $E_{\max,lv,0}$ the value in absence of autoregulation, and $G_{E_{\max,lv}}$ the maximum baroreceptor gain (autoregulation effect). By lowering these parameters the contractility properties of the heart are decreased, hence modeling heart failure of different intensity. We also varied $k_{E,lv}$, the steepness of the pressure-volume curve for the ventricle (supposed to be monoexponential), to be able to correctly represent pressure-volume diagrams in patients presenting heart failure of different intensity. All the other parameters are set as in Ursino (1998).

⁵For the data we referred to the HeartMate II[®] operating manual available at: <http://www.thoratec.com>.

Table 7.1: List of the four parameters calibrated to account for the two heart failure levels (MHF and SHF). The values of the parameters for the HH are the same as those given in Ursino (1998).

Parameter ^a	HH	MHF	SHF
$E_{\max,lv}$	2.950	0.800	0.200
$E_{\max_{lv,0}}$	2.392	0.800	0.200
$G_{E_{\max,lv}}$	0.475	0.200	0.200
$k_{E,lv}$	0.140	0.130	0.110

^a $E_{\max,lv}$ [mmHg/ml], reference value of the ventricle elastance; $E_{\max_{lv,0}}$ [mmHg/ml], reference value of the ventricle elastance in absence of autoregulation; $G_{E_{\max,lv}}$ [mmHg/ml/(spikes/s)], maximum baroreceptor gain; $k_{E,lv}$ [1/ml], steepness of the pressure-volume curve.

The model has been implemented in Modelica[®] (a non-proprietary, object-oriented, equation based language aimed at conveniently model complex physical systems⁶) by J. Bonnemain and M. Lesinigo at the CMCS⁷ and solved for different device rotational speeds and ventricular elastance corresponding to the aforementioned three heart states.

7.2.1 Validation and results

An extensive overview of the results provided by the model is reported in Table 7.2 both pre- and post-LVAD implantation. Simulations performed without the LVAD aim at comparing the predictive and explanatory ability of the model for the HH, MHF, and SHF heart states (see Table 7.1). To validate our results, we compare them with the clinical data given by Cox et al. (2009), which, for the reader's convenience, are reported in Table 7.2 under the "Ref." column.

The values predicted by the model for the case of a healthy heart match the reference data (see Ref. HH column) except for the end-systolic volume, which is higher than the upper bound of the clinical range. In the case of middle and severe heart failure the model provides results that are in good agreement with the limits of the clinical ranges for the heart failure (see Ref. HF column), thus representing the case of MHF and SHF. However, in these cases, predicted pulmonary pressures are lower than expected.

Configurations including the LVAD were tested both for MHF and SHF and for different pump rotational speeds corresponding to the usual values used in the clinical practice (8k, 9k, and 10k RPM). The numerical results (see right side of Table 7.2) show that the model is able, at least qualitatively, to reproduce the main features of the continuous flow assist devices. In particular we observe (i) a flow rate increase when increasing the pump rotational speed, (ii) a flow rate increase when decreasing the pressure jump across the pump, (iii) a pulsatility decrease when increasing the pump rotational speed (measured by the pulsatile index), and (iv) a venous pulmonary pressure decrease when increasing the pump rotational speed; this is a well known behavior of LVAD, since it improves pulmonary circulation in patients.

The pressure-volume diagrams for the physiological and the two pathological situations are depicted in Figure 7.3a. The curves for stages of dilated heart failure match both qualitatively and quantitatively the typical curves observed in clinical practice (see Westerhof et al. (2010)). Note that the pathological conditions, compared to the physiological one, exhibit the presence of systolic dysfunction with increased end-systolic and end-diastolic volumes, decreased stroke volume, and increased end-diastolic pressure.

⁶<http://www.modelica.org>.

⁷Chair of Modeling and Scientific Computing, EPFL: <http://cmcs.epfl.ch>.

7.2. Lumped parameters model of the global circulation

Table 7.2: Lumped parameter model results with and without LVAD. In the latter case, both model and reference results are provided, where the reference values are clinical data given by Cox et al. (2009).

Parameter ^b	No VAD					LVAD					
	Ref.		Mod.			8k RPM		9k RPM		10k RPM	
	HH	HF	HH	MHF	SHF	MHF	SHF	MHF	SHF	MHF	SHF
EF	55-65	15-33	57	32	17	35	17	34	17	33	23
HR	60-100	76-103	71	78	85	75	81	72	77	69	71
EDV	90-162	20-522	133	180	238	169	224	156	208	140	174
ESV	27-45	140-249	56	122	197	110	185	104	172	94	134
LVADPI	-	-	-	-	-	25	15	15	10	10	9
CI	2.8-4.2	1.9-2.4	3.0	2.5	1.9	1.3	0.4	0.7	0.0	0.1	0.0
AQ	-	-	5.4	4.4	3.5	2.2	0.7	1.2	0.0	0.1	0.0
LVADQ	-	-	-	-	-	2.4	3.2	3.7	4.3	5.0	4.9
TOTQ	-	-	5.4	4.4	3.5	4.6	3.9	4.9	4.3	5.1	4.9
SAP	90-140	107-115	131	112	94	109	91	105	89	98	95
DAP	60-90	68-76	88	79	69	83	78	87	84	90	89
MAP	70-105	78-95	102	90	78	92	83	93	85	93	91
SPAP	15-28	54-62	27	30	32	29	30	28	29	27	27
DPAP	5-16	28-29	13	18	23	16	20	15	18	13	14
MPAP	10-22	27-40	18	23	26	21	24	20	22	18	19
PCWP	5-12	17-29	8	14	19	12	17	11	14	8	9

^b EF [%], ejection factor; HR [1/s], heart rate; EDV [ml], end-diastolic volume; ESV [ml], end-systolic volume; LVADPI, LVAD pulsatile index; CI [L/min/m²], cardiac index; AQ [L/min], aortic flow rate; LVADQ [L/min], LVAD flow rate; TOTQ [L/min], total flow rate; SAP [mmHg], systolic arterial pressure; DAP [mmHg], diastolic arterial pressure; MAP [mmHg], mean arterial pressure; SPAP [mmHg], systolic pulmonary arterial pressure; DPAP [mmHg], diastolic pulmonary arterial pressure; MPAP [mmHg], mean pulmonary arterial pressure; PCWP [mmHg], pulmonary capillary wedge pressure.

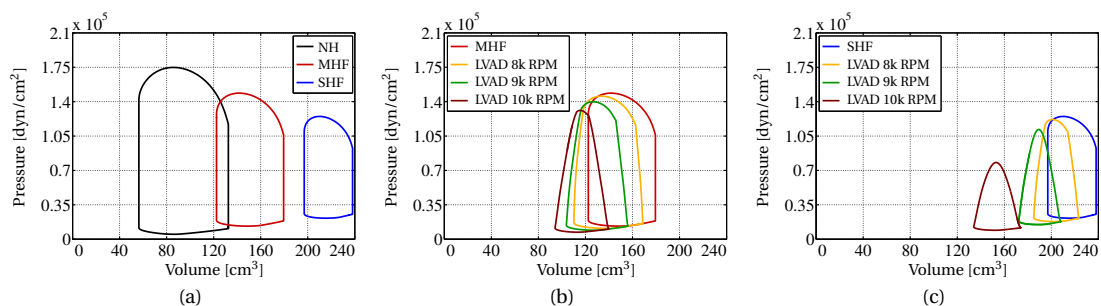


Figure 7.3: Pressure-volume diagrams for several heart conditions and LVAD speeds. (a) Physiological and pathological cases without LVAD. (b) MHF with and without LVAD. (c) SHF with and without LVAD.

The same curves for the middle and severe heart failure states are reported in Figures 7.3b and 7.3c, respectively, for different rotational speeds. In all the cases the device helps in unloading the ventricle from its pumping workload and the effect becomes more evident when the rotational speeds and, hence, the LVAD flow rate are increased. The model reproduces the typical triangular pressure volume curves observed in clinical practice for patients under ventricular assistance (see Koenig et al. (2004)).

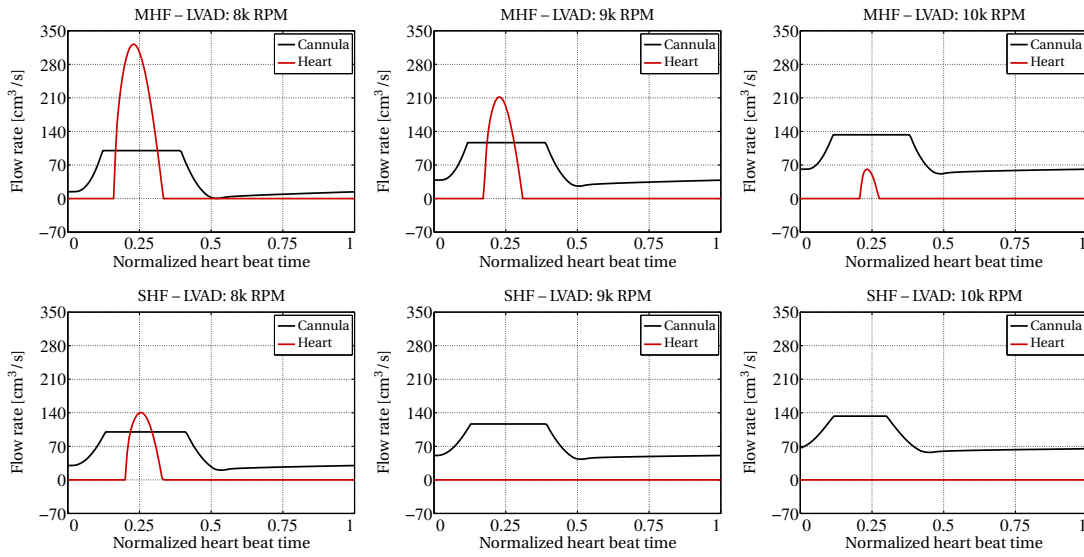


Figure 7.4: Time-dependent periodic flow rate boundary conditions for the 1-D arterial network computed with the lumped parameters model with respect to different LVAD rotational speeds and heart failure levels.

7.2.2 Inflow boundary data for the 1-D network

As shown in the previous section, the lumped parameters model provides a reliable description of the behavior of the device in different relevant physiological and pathological conditions, since it accounts for the interaction among the ventricle, the assist device, the aorta, and the other compartments of the circulatory system. Consequently, it can be used to estimate a proper set of inflow boundary conditions for the network of 1-D arteries. In particular, we generate six sets of boundary data given by the combination of the two stages of heart failure and the three considered rotational speeds of the device, as shown in Figure 7.4. There, for the reader's convenience, the timescale in the images has been normalized to one heart beat; the real timescale can be deduced by the heart rate values reported in Table 7.2.

The curves exhibit a good qualitative agreement with the experimental data reported, for example, by Khalil et al. (2008). In particular, the lumped parameters model allows to take into account the dynamic interaction between the device and the cardiovascular system itself, predicting, for instance, the blood stealing effect that the device has on the ventricle chamber, especially at high rotational speeds. In effect, the device empties the ventricle chamber continuously, reducing the amount of blood available to be ejected by the aortic valve during heart contraction. Coherently, the aortic valve flow rate provided by the lumped parameters model is present only at the systolic phase peak and it is reduced by increasing the device RPM, being effectively null in the case of 9k and 10k RPM with SHF. By using the lumped parameters model results as boundary data for the networks of 1-D arteries we take into account these effects.

7.3 Numerical comparisons of LVAD implantations

We now use the network of 1-D arteries described in Section 5.3 to set up several numerical comparisons between different LVAD implantations. The driving motivation of this numerical study is the assessment of modeling evidences that the site of the anastomosis of the outflow cannula is clinically relevant. Indeed, the network of 1-D arteries allows to perform this analysis by comparing the blood pressures and flow rate waveforms at different locations for the selected clinical scenarios.

The main parameters of the 1-D network are the same as in Table 5.4, apart from the heart rate, which depends on both the stage of heart failure and the chosen rotational speed of the device (see Table 7.2). To account for the presence of the LVAD, the global network of 103 arteries has been extended by including an additional segment representing the outflow cannula. In case of the AA anastomosis the cannula is connected to the middle of segment 95 (ascending aorta 2), while in case of the DA anastomosis it is attached at the junction between segments 18 (thoracic aorta A) and 27 (thoracic aorta B); see Reymond et al. (2009, Figure 2 and Table 2) for the connectivity of the original network. In both configurations, the outflow cannula of the LVAD is modeled as a stiffer 1-D element (Young's modulus $E_S = 4 \cdot 10^7$ dyn/cm²; Poisson's ratio $\nu_S = 0.5$) and in agreement with the device manufacturer, with a diameter of 1.6 cm. At the coupling nodes of the network the set of equations (2.2) is imposed through mean normal stress boundary data on all the coupling interfaces (i.e., $n_c^Q = 0$, $c = 1, 2, \dots$).

The aortic and the LVAD periodic flow rates computed by the lumped parameters model (see Figure 7.4) are used as inflow boundary data for the network of 1-D arteries, as described in Section 7.2.2. Note that these data are supposed to be valid for both the AA and the DA anastomoses, since the lumped parameters model is not able to take into account the exact site of the cannula. This might introduce a small bias in our comparisons by attenuating the differences between the AA and the DA anastomoses. The total number of analyzed clinical scenarios is twelve, given by the combination of the two possible sites for the anastomosis of cannula, the two stages of heart failure, and the three considered rotational speeds of the device. We remark that these scenarios are not only frequent among different patients presenting heart failure, but may also regard a single patient at different stage of the disease, for example in the case of the idiopathic dilated cardiomyopathy in which the device, implanted as a *bridge to recovery*, weans to the progressive full recovery of the heart (see, e.g., Birks et al. (2006)).

In Table 7.3 we select nine arteries from the global 1-D network and we compare the predicted mean flow rates for the two cannulation techniques. The results show that, regardless of the heart failure stage (MHF or SHF) and of the device rotational speed (8k, 9k, and 10k RPM), the mean flow rate in the case of the AA and the DA anastomoses is similar. More precisely, the flow rates in the coronaries and in the cerebral arteries for the two approaches can be considered clinically equivalent. This is relevant due to the importance of the heart and cerebral perfusions. Moreover, for all the other arterial segments, the differences between the two techniques have been quantified in less than 1%, thus negligible.

In a second analysis we want to assess whether there is any significant difference in the flow rates and pressures waveforms between the two different cannulation techniques. In this respect, we compare the flow rates and pressures waveforms for two limit configurations: the MHF state with LVAD at 8k RPM and the SHF state with LVAD at 10k RPM. In the first case both the cannula and the aortic valve inflows are non-null, such that the systemic circulation is fed from two different sites and with flows characterized by different shape and amplitude. In the second case the device is the only flow source since it sucks too much blood from the ventricle for the aortic valve flow rate to be present; thus, the heart does not contribute to the systemic circulation. The results of these comparisons are shown in Figures 7.5 and 7.6, respectively. In both configurations, the flow rate and pressure waveforms resulting from the two different approaches are very similar in all the vessels.

Chapter 7. Numerical simulation of left ventricular assist device implantation

Table 7.3: Mean flow rate comparison, at several location of the 1-D arterial network, between the AA and the DA anastomoses, for different heart failure stages and device rotational speeds. The flow rates are expressed in $[\text{cm}^3/\text{s}]$.

Location	HF	8k RPM		9k RPM		10k RPM	
		AA	DA	AA	DA	AA	DA
Abdominal aorta	MHF	40.822	40.880	42.715	42.783	44.798	44.849
	SHF	34.596	34.665	37.719	37.776	43.160	43.208
Left main coronary	MHF	3.215	3.210	3.356	3.349	3.507	3.500
	SHF	2.751	2.746	2.979	2.973	3.382	3.376
Left anterior descending coronary	MHF	1.532	1.530	1.599	1.596	1.673	1.669
	SHF	1.309	1.307	1.418	1.415	1.612	1.609
Right coronary RCA	MHF	1.346	1.344	1.407	1.404	1.472	1.469
	SHF	1.146	1.143	1.244	1.242	1.418	1.416
Right common carotid	MHF	4.123	4.101	4.322	4.297	4.528	4.508
	SHF	3.483	3.460	3.798	3.779	4.356	4.341
Right vertebral	MHF	0.891	0.886	0.920	0.913	0.949	0.941
	SHF	0.815	0.808	0.856	0.849	0.927	0.919
Right renal	MHF	8.821	8.825	9.219	9.225	9.651	9.656
	SHF	7.509	7.515	8.157	8.162	9.298	9.303
Right common iliac	MHF	5.521	5.520	5.771	5.772	6.059	6.061
	SHF	4.629	4.629	5.062	5.064	5.826	5.831
Right anterior tibial	MHF	0.940	0.939	0.977	0.977	1.022	1.022
	SHF	0.778	0.778	0.848	0.848	0.980	0.980

Finally, we compare the flow rate at different rotational speeds for the MHF (see Figure 7.7) and SHF (see Figure 7.8) cases. Since the AA and the DA anastomoses lead to very similar waveforms, in the images we show only the results associated to the AA anastomosis. Similar curves are obtained for the case of the DA anastomosis. The results show that, regardless of the stage of heart failure, an increase of the rotational speed of the device reduce the pulsatility of the flow, which becomes more flat. This effect is particularly pronounced in the MHF case, in which wave profile alterations are observed in the right common carotid, in the right vertebral artery, and in the left anterior descending coronary. We remark that loss or reduction of pulsatility and, more generally, flow rate wave profile alterations may have adverse effects on human physiology. For this reason, even if numerical simulations have proven that the AA and the DA anastomoses techniques are similar, particular care should be taken in setting the correct device rotational speed.

7.4 Discussions

In this chapter we have presented a preliminary study of LVAD implantations. In particular, we studied several clinical scenarios, given by the combination of two possible sites for the anastomosis of cannula of the LVAD (AA and DA), three rotational speeds of the device (8k, 9k, and 10k RPM), and two stages of heart failure (MHF and SHF). The analysis of the results presented in Section 7.3 showed that, for all the considered clinical cases, the AA and the DA anastomoses lead to similar waveforms and mean flow rates in the systemic arteries. Therefore, in view of the fact that anastomosis of the cannula at the ascending aorta is considered by clinicians more invasive, the DA anastomosis appears to be a reliable approach.

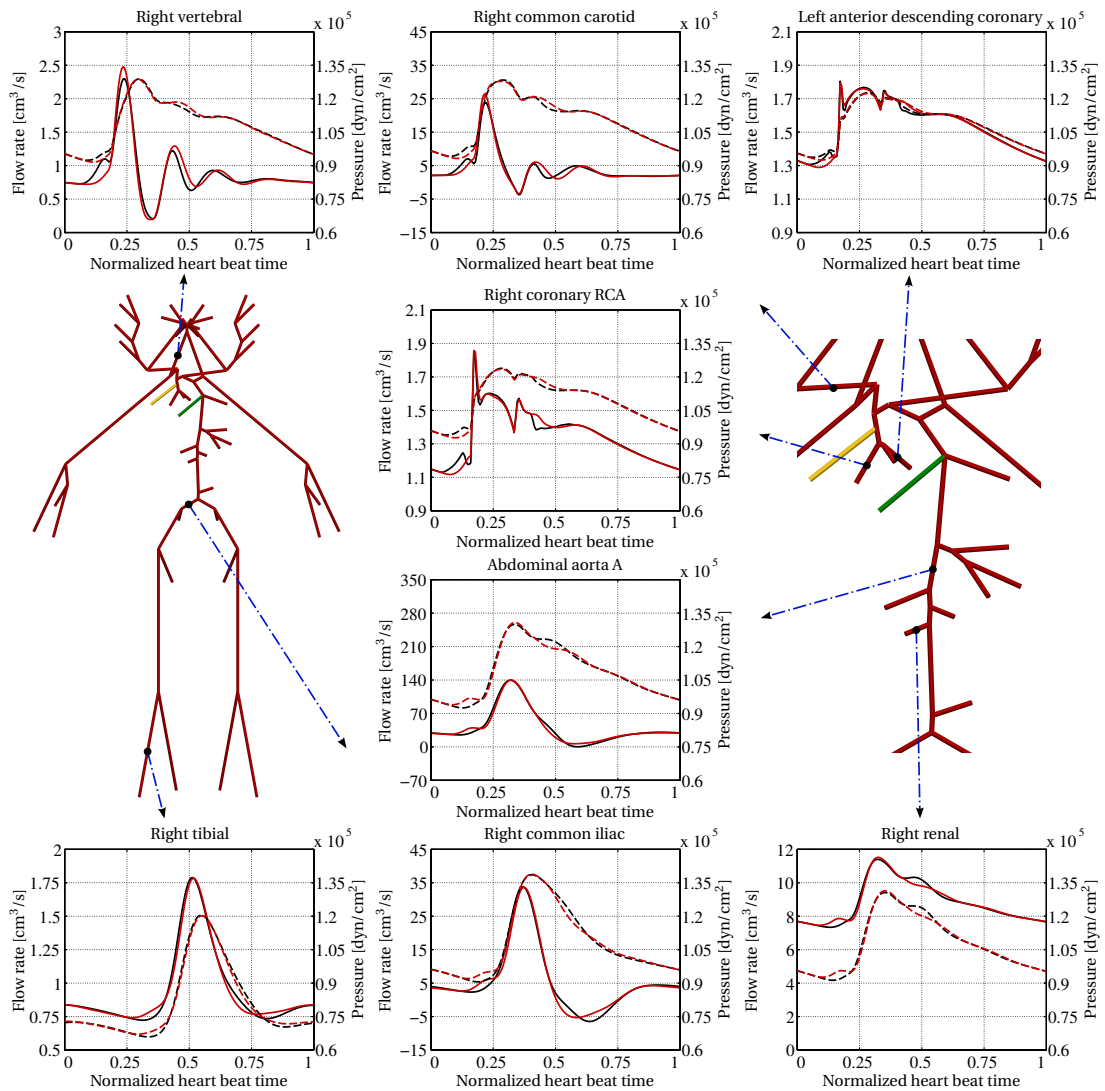


Figure 7.5: Flow rate (solid lines) and pressure (dashed lines) comparison, in eight different arterial vessels, between the AA (black lines) and the DA (red lines) anastomoses, for a MHF with LVAD at 8k RPM. The left image represents a global view of the 1-D network elements, while the right one is an enlarged view of the aortic region. The yellow and green segments represent the two configurations for the cannula (AA and DA anastomoses, respectively). Positioning of the elements is purely visual.

Nevertheless, we remark that our analysis is based on reduced models, which provide only spatial averages of the quantities of interest. In particular, these models do not take into account the 3-D effects of the anastomosis, e.g., turbulent regions, zones of stagnation, energy losses, and wall shear stress abnormal distributions. For this reasons, further studies should be performed to confirm these results also in a 3-D setting. In this regard, similarly to what has been done in Section 5.4.2 for the 3-D patient-specific aorta and iliac geometries, we can replace the 1-D description of the cannula anastomosed to the aorta with a global 3-D geometry, thus considering the 3-D dynamics of the flow in that regions. Some preliminary studies in this direction have been performed in Bazilevs et al. (2009), with stand-alone 3-D FSI simulations, and also in Bonnemain et al. (2012a) and Faggiano et al. (2012), coupling the 3-D aorta and its anastomosed cannula with a 1-D network modeling the peripheral

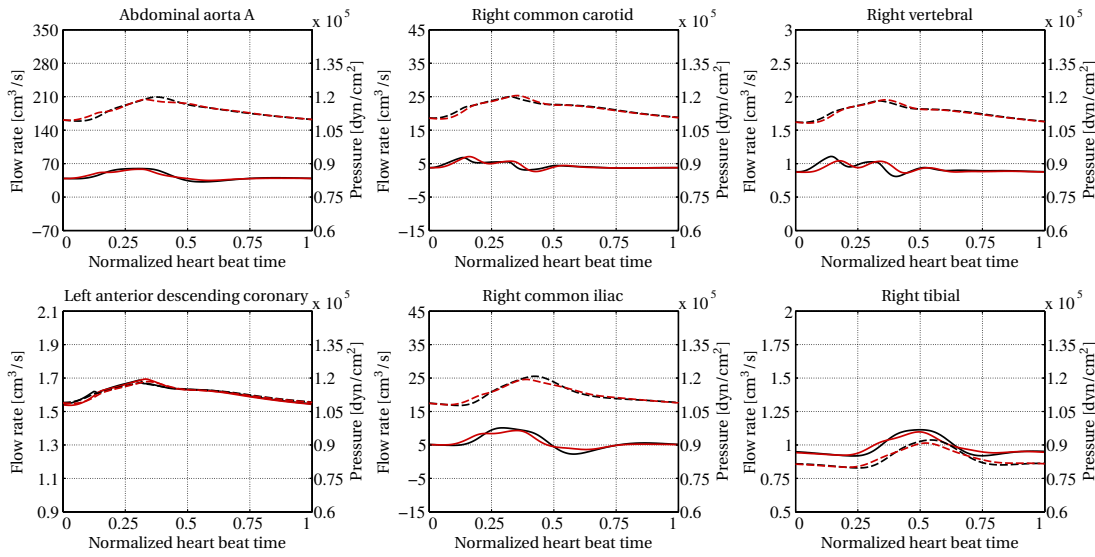


Figure 7.6: Flow rate (solid lines) and pressure (dashed lines) comparison, in six different arterial vessels, between the AA (black lines) and the DA (red lines) anastomoses, for a SHF with LVAD at 10k RPM.

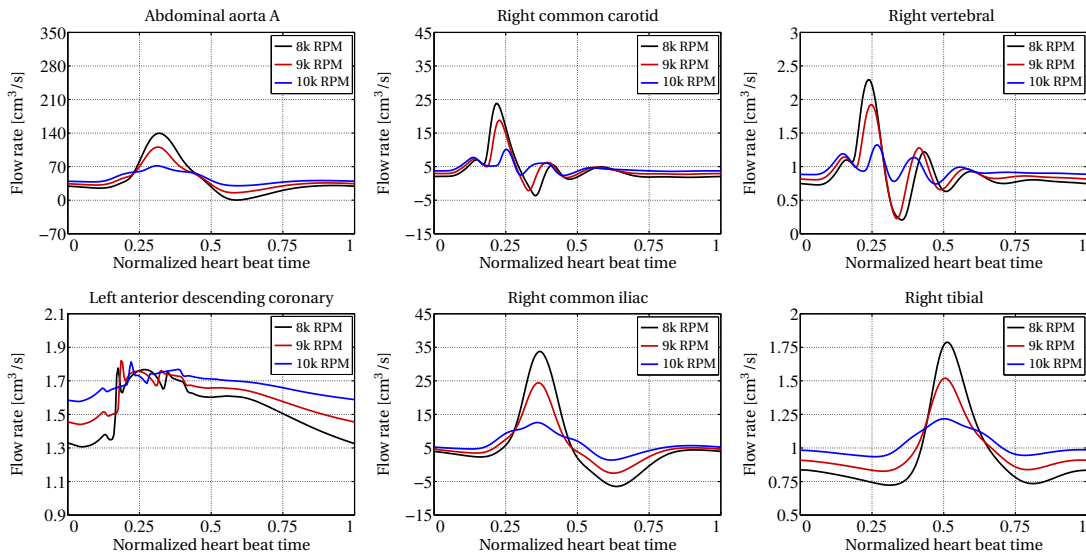


Figure 7.7: Flow rate comparison for the three considered rotational speeds of the device, in six different arterial vessels, for a patient with MHF with the cannula anastomosed to the AA.

systemic arterial circulation. The use of 3-D geometries allows not only to study the effect of the site of the anastomosis of the cannula, but also to compare the results for a range of different angles between the cannula and the aortic wall.

Another limitation of the present work is that the lumped parameters model used to generate the inflow boundary condition is decoupled from the geometrical multiscale model. The development of a closed-loop model which accounts for the interaction between the detailed (1-D and 3-D) systemic circulation and the lumped (0-D) description of the peripheral and venous compartments as well as of the LVAD pump, may provide different results and will be subject of future works.

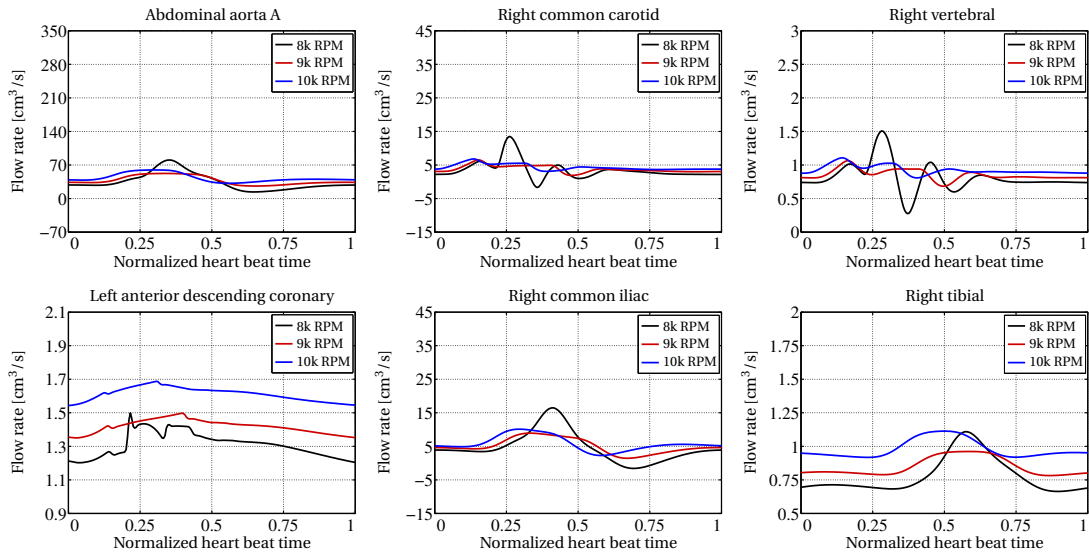


Figure 7.8: Flow rate comparison for the three considered rotational speeds of the device, in six different arterial vessels, for a patient with SHF with the cannula anastomosed to the AA.

In practice, the geometrical multiscale method devised in this thesis allows to progressively extend the current model, replacing some of the reduced order elements with a more detailed description or including more components in the network, depending on the specific needs of the analysis of interest.

Main reference of the chapter:

- ☆ J. Bonnemain, A. C. I. Malossi, M. Lesinigo, S. Deparis, A. Quarteroni, and L. K. von Segesser. Numerical simulation of left ventricular assist device implantations: comparing the ascending and the descending aorta cannulations. Submitted, 2012.

Conclusions

In this thesis we have developed a geometrical multiscale framework for the simulation of the human cardiovascular system under physiological and pathological conditions. The framework has been designed in an abstract setting to ease the development of numerical algorithms for the implicit coupling of heterogeneous compartments. With this aim, the local specific mathematical equations (partial differential equations, differential algebraic equations, etc.) and the numerical approximation (finite elements, finite differences, etc.) of the heterogeneous compartments have been hidden behind generic operators, such that the resulting global interface problem has been formulated and solved in a completely transparent way.

To set up the coupling among the heterogeneous compartments we have devised three sets of interface equations based on the continuity/conservation of averaged/integrated quantities, i.e., the mean normal stress, the mean total normal stress, the area, and the flow rate. These quantities are particularly effective in connecting models of different scale (three-dimensional, one-dimensional, etc.) and type (Navier–Stokes, fluid-structure interaction, etc.) thanks to their dimensionless nature. The flexibility of the devised framework has allowed to choose the set of interface equations and the type of boundary data to be applied at each network node and on each model interface independently from the geometrical and mathematical features of the connected compartments.

The resulting global interface problem has been written in an abstract residual form and solved using a nonlinear Richardson strategy. More precisely, we have compared three different iterative methods: Aitken/fixed-point, Newton/inexact-Newton, and Broyden. The first one has shown strong limitations and poor convergence properties even in very simple configurations, such as serial networks of homogeneous elements. In contrast, the Newton and the Broyden methods behave quite successfully even on large networks made of more than one-hundred components and characterized by complex topologies including bifurcations and closed loop circulations. Moreover, exploiting the fact that the interaction between the connected compartments is just at the level of the boundary conditions, we have devised an effective two-level parallelization of the algorithms, which is another appealing feature of the proposed methodology.

One of the main contribution of this work has been the development of a strategy for the assembling and computation of the exact Jacobian matrix of the interface problem required by the Newton method. Indeed, being the interface equations written in terms of averaged/integrated quantities, the size of the Jacobian matrix is very small and its storage is not an issue. To assemble the exact Jacobian matrix we have took advantage of its block structure. The corresponding entries have been computed by solving the tangent problems associated with the specific connected models. The computation of the exact Jacobian matrix has served not only to set up the Newton method, but also to properly initialize the Broyden matrix.

Conclusions

The methodology presented throughout the thesis has been mainly developed for cardiovascular problems, however its generality goes much beyond, e.g., it can be applied to the study of fluid/gas flows in industrial pipe networks. To model the systemic arterial circulation we have taken from the literature two different dimensionally-heterogeneous fluid-structure interaction models. For both of them we have devised some valuable extensions accounting for the missing relevant modeling features.

An important part of the work has been devoted to the analysis and validation of the proposed methods. In particular, we have set up several benchmark tests to study (i) the entity of the numerical spurious reflections at the interfaces between the connected heterogeneous compartments, (ii) the number of nonlinear Richardson iterations required to achieve the convergence of the global problem with respect to the employed iterative methods, and (iii) the computational efficiency of our algorithms as a function of the number of interfaces in the global problem. In addition, we have also simulated blood flows in large networks of arteries modeled through dimensionally-heterogeneous fluid-structure interaction models; in this regard, we have performed several numerical comparisons to study the dynamic of the flow with respect to both published data and simplified models, where the simplifications take place at either the level of the specific model or that of the global network of elements; in both cases, the analysis of the results has proven the benefits of the geometrical multiscale method.

Last but not least, we have addressed a couple of real clinical problems as an example of possible concrete fields of application of our framework. The preliminary results of these studies have evidenced the potentialities of the geometrical multiscale method, which can be considered a valuable tool to study pathological scenarios and to help the clinicians in the decision making process.

Perspectives and future works

The methodology devised here can be further extended in several directions. In the following we briefly mention some of those that we consider to be the most relevant.

Monolithic coupling. The partitioned strategy for the solution of the global network of dimensionally-heterogeneous models has proven to be robust and effective. Nevertheless, the time consumed by the nonlinear Richardson iterations on the interface problem is still relevant. A further extension might consist in the development of a monolithic assembler to build a single global system of equations representing all the elements in the network. Nevertheless, the heterogeneity of the models equations represents a huge obstacle towards this aim. A possible intermediate solution is to partition the network in macro components made up of homogeneous compartments, thus significantly reducing the size of the original interface problem.

Preconditioning strategies based on weak coupling. By exploiting the partitioned solution of the weakly coupled geometrical multiscale network we can develop a coarse preconditioner for a global strongly coupled problem. For instance, a strongly coupled network composed by several three-dimensional fluid-structure interaction domains may be preconditioned by the solution of the same network weakly coupled through averaged/integrated quantities; in turn, the weakly coupled network may be preconditioned by the solution of a reduced order one-dimensional network, leading to a two-level multigrid preconditioner approach.

Closed loop models and autoregulation. In the simulated networks, the cumulative effects of the distal vessels (small arteries, arterioles, and capillaries) have been taken into account through simple three-element windkessel terminals, while the venous circulation has been modeled as a constant distal pressure. By integrating a lumped parameters solver in the geometrical multiscale framework we may replace these simple elements with a more accurate description of the peripheral circulation. This allows to simulate not only the closed loop blood circulation, but also the effects of the systemic autoregulation, thus significantly extending the possible fields of application of the methodology devised here.

Numerical suitability analysis. The broad range of benchmark and cardiovascular examples discussed throughout the work have already demonstrated the accuracy and robustness of the proposed methodology. As an example we recall the good results obtained during the assessment of a network of 1-D FSI models against *in vitro* and *in silico* published data. Nevertheless, further analyses can be carried out to confirm this behavior in more demanding conditions, such as in presence of in-plane velocity fields near the boundary interfaces. In addition, direct comparisons with medical images data might help in evaluating the accuracy of the computed solution. On the basis of the results of these additional studies, the interface equations might be further extended, e.g., including a model to account for the effect of energy losses at the nodes of the network.

Bibliography

- A. Abdulle, E. Weinan, B. Engquist, and E. Vanden-Eijnden. The heterogeneous multiscale method. *Acta Numerica*, 21:1–87, 2012.
- J. Alastruey, K. H. Parker, J. Peiró, S. M. Byrd, and S. J. Sherwin. Modelling the circle of Willis to assess the effects of anatomical variations and occlusions on cerebral flows. *J. Biomech.*, 40(8):1794–1805, 2007.
- J. Alastruey, S. M. Moore, K. H. Parker, T. David, J. Peiró, and S. J. Sherwin. Reduced modelling of blood flow in the cerebral circulation: Coupling 1-D, 0-D and cerebral auto-regulation models. *Int. J. Num. Meth. Fluids*, 56(8):1061–1067, 2008.
- J. Alastruey, A. W. Khir, K. S. Matthys, P. Segers, S. J. Sherwin, P. R. Verdonck, K. H. Parker, and J. Peiró. Pulse wave propagation in a model human arterial network: Assessment of 1-D visco-elastic simulations against in vitro measurements. *J. Biomech.*, 44(12):2250–2258, 2011.
- T. Arts, K. D. Costa, J. W. Covell, and A. D. McCulloch. Relating myocardial laminar architecture to shear strain and muscle fiber orientation. *Am. J. Physiol. Heart Circ. Physiol.*, 280(5):H2222–H2229, 2001.
- A. P. Avolio. Multi-branched model of the human arterial system. *Med. Biol. Engrg. Comp.*, 18(6):709–718, 1980.
- B. Baccani, F. Domenichini, and G. Pedrizzetti. Model and influence of mitral valve opening during the left ventricular filling. *J. Biomech.*, 36(3):355–361, 2003.
- S. Badia, F. Nobile, and C. Vergara. Fluid-structure partitioned procedures based on Robin transmission conditions. *J. Comput. Phys.*, 227(14):7027–7051, 2008.
- Y. Bazilevs, V. M. Calo, Y. Zhang, and T. J. R. Hughes. Isogeometric fluid–structure interaction analysis with applications to arterial blood flow. *Comput. Mech.*, 38:310–322, 2006.
- Y. Bazilevs, V. M. Calo, T. J. R. Hughes, and Y. Zhang. Isogeometric fluid-structure interaction: theory, algorithms, and computations. *Comput. Mech.*, 43(1):3–37, 2008.
- Y. Bazilevs, J. R. Gohean, T. J. R. Hughes, R. D. Moser, and Y. Zhang. Patient-specific isogeometric fluid-structure interaction analysis of thoracic aortic blood flow due to implantation of the Jarvik 2000 left ventricular assist device. *Comp. Meth. Appl. Mech. Engrg.*, 198(45–46):3534–3550, 2009.
- E. J. Birks, P. D. Tansley, J. Hardy, R. S. George, C. T. Bowles, M. Burke, N. R. Banner, A. Khaghani, and M. H. Yacoub. Left ventricular assist device and drug therapy for the reversal of heart failure. *N. Engl. J. Med.*, 355(18):1873–1884, 2006.

Bibliography

- P. J. Blanco, R. A. Feijóo, and S. A. Urquiza. A unified variational approach for coupling 3D–1D models and its blood flow applications. *Comp. Meth. Appl. Mech. Engrg.*, 196(41–44):4391–4410, 2007.
- P. J. Blanco, R. A. Feijóo, and S. A. Urquiza. A variational approach for coupling kinematically incompatible structural models. *Comp. Meth. Appl. Mech. Engrg.*, 197(17–18):1577–1602, 2008.
- P. J. Blanco, M. R. Pivello, S. A. Urquiza, and R. A. Feijóo. On the potentialities of 3D–1D coupled models in hemodynamics simulations. *J. Biomech.*, 42(7):919–930, 2009.
- P. J. Blanco, S. A. Urquiza, and R. A. Feijóo. Assessing the influence of heart rate in local hemodynamics through coupled 3D-1D-0D models. *Int. J. Num. Meth. Biomed. Engrg.*, 26(7):890–903, 2010.
- P. J. Blanco, J. S. Leiva, R. A. Feijóo, and G. C. Buscaglia. Black-box decomposition approach for computational hemodynamics: One-dimensional models. *Comp. Meth. Appl. Mech. Engrg.*, 200(13–16):1389–1405, 2011.
- P. J. Blanco, S. Deparis, and A. C. I. Malossi. On the continuity of mean total normal stress in geometrical multiscale cardiovascular problems. In preparation, 2012.
- J. Bonnemain, S. Deparis, and A. Quarteroni. Connecting ventricular assist devices to the aorta: a numerical model. In *Imagine Math. Between Culture and Mathematics*, pages 211–224. Springer-Verlag, 2012a.
- J. Bonnemain, A. C. I. Malossi, M. Lesinigo, S. Deparis, A. Quarteroni, and L. K. von Segesser. Numerical simulation of left ventricular assist device implantations: comparing the ascending and the descending aorta cannulations. Submitted, 2012b.
- A. C. Bovik. On detecting edges in speckle imagery. *IEEE T. Acoust. Speech Signal Process.*, 36(10):1618–1627, 1988.
- M. D. Buhmann. *Radial Basis Functions: Theory and Implementations*, volume 12 of *Cambridge Monographs on Applied and Computational Mathematics*. Cambridge University Press, Cambridge, 2003.
- E. Burman, M. A. Fernández, and P. Hansbo. Continuous interior penalty finite element method for Oseen’s equations. *SIAM J. Numer. Anal.*, 44(3):1248–1274, 2006.
- S. Čanić, K. Ravi-Chandar, Z. Krajcer, D. Mirković, and S. Lapin. Mathematical model analysis of Wallstent® and AneuRx®: Dynamic responses of bare-metal endoprosthesis compared with those of stent-graft. *Tex. Heart Inst. J.*, 34(4):502–506, 2005.
- P. Causin, J.-F. Gerbeau, and F. Nobile. Added-mass effect in the design of partitioned algorithms for fluid-structure problems. *Comp. Meth. Appl. Mech. Engrg.*, 194(42–44):4506–4527, 2005.
- M. D. Cerqueira, N. J. Weissman, V. Dilsizian, A. K. Jacobs, S. Kaul, W. K. Laskey, D. J. Pennell, J. A. Rumberger, T. Ryan, M. S. Verani, et al. Standardized myocardial segmentation and nomenclature for tomographic imaging of the heart. *Circulation*, 105(4):539–542, 2002.
- T. F. Chan and L. A. Vese. Active contours without edges. *IEEE T. Image Process.*, 10:266–277, 2001.
- M. Cinthio, A. R. Ahlgren, J. Bergkvist, T. Jansson, H. W. Persson, and K. Lindström. Longitudinal movements and resulting shear strain of the arterial wall. *Am. J. Physiol. Heart Circ. Physiol.*, 291(1):H394–H402, 2006.

- C. A. Conti, E. Votta, A. Della Corte, L. Del Viscovo, C. Bancone, M. Cotrufo, and A. Redaelli. Dynamic finite element analysis of the aortic root from MRI-derived parameters. *Med. Eng. Phys.*, 32(2): 212–221, 2010.
- C. A. Conti, E. Votta, C. Corsi, D. De Marchi, G. Tarroni, M. Stevanella, M. Lombardi, O. Parodi, E. G. Caiani, and A. Redaelli. Left ventricular modelling: a quantitative functional assessment tool based on cardiac magnetic resonance imaging. *J. R. Soc. Interface*, 1(3):384–395, 2011.
- L. G. E. Cox, S. Loerakker, M. C. M. Rutten, B. A. J. M. de Mol, and F. N. van de Vosse. A mathematical model to evaluate control strategies for mechanical circulatory support. *Artif. Organs*, 33(8):593–603, 2009.
- P. Crosetto. *Fluid-Structure Interaction Problems in Hemodynamics: Parallel Solvers, Preconditioners, and Applications*. PhD thesis, École Polytechnique Fédérale de Lausanne, 2011.
- P. Crosetto, S. Deparis, G. Fourestey, and A. Quarteroni. Parallel algorithms for fluid-structure interaction problems in haemodynamics. *SIAM J. Sci. Comput.*, 33(4):1598–1622, 2011a.
- P. Crosetto, P. Reymond, S. Deparis, D. Kontaxakis, N. Stergiopoulos, and A. Quarteroni. Fluid-structure interaction simulation of aortic blood flow. *Comput. Fluids*, 43(1):46–57, 2011b.
- P. Crosetto, S. Deparis, L. Formaggia, G. Mengaldo, F. Nobile, and P. Tricerri. A comparative study of different nonlinear hyperelastic isotropic arterial wall models in patient-specific vascular flow simulations in the aortic arch. Submitted, 2012.
- S. Deparis. *Numerical Analysis of Axisymmetric Flows and Methods for Fluid-Structure Interaction Arising in Blood Flow Simulation*. PhD thesis, École Polytechnique Fédérale de Lausanne, 2004.
- S. Deparis, M. Discacciati, G. Fourestey, and A. Quarteroni. Fluid-structure algorithm based on Steklov–Poincaré operators. *Comp. Meth. Appl. Mech. Engrg.*, 195(41–43):5797–5812, 2006a.
- S. Deparis, M. Discacciati, and A. Quarteroni. A domain decomposition framework for fluid-structure interaction problems. In *Proceedings of the Third International Conference on Computational Fluid Dynamics (ICCFD3)*, pages 41–58. Springer Berlin Heidelberg, 2006b.
- K. Dickstein, A. Cohen-Solal, G. Filippatos, J. J. V. McMurray, P. Ponikowski, P. A. Poole-Wilson, A. Strömberg, D. J. van Veldhuisen, D. Atar, A. W. Hoes, et al. ESC guidelines for the diagnosis and treatment of acute and chronic heart failure 2008. *Eur. Heart J.*, 29(19):2388–442, 2008.
- P. L. DiGiorgi, D. L. Smith, Y. Naka, and M. C. Oz. In vitro characterization of aortic retrograde and antegrade flow from pulsatile and non-pulsatile ventricular assist devices. *J. Heart Lung Transplant.*, 23(2):186–192, 2004.
- L. Euler. *Principia pro motu sanguinis per arterias determinando* (1775). *Opera posthuma mathematica et physica*, 2:814–823, 1844.
- E. Faggiano, J. Bonnemain, A. Quarteroni, and S. Deparis. A patient-specific framework for the analysis of the haemodynamics in patients with ventricular assist device. Submitted, 2012.
- M. A. Fernández and M. Moubachir. A Newton method using exact Jacobian for solving fluid-structure coupling. *Comput. Struct.*, 83(2–3):127–142, 2005.
- C. A. Figueroa, I. E. Vignon-Clementel, K. E. Jansen, T. J. R. Hughes, and C. A. Taylor. A coupled momentum method for modeling blood flow in three-dimensional deformable arteries. *Comp. Meth. Appl. Mech. Engrg.*, 195(41–43):5685–5706, 2006.

Bibliography

- C. A. Figueroa, S. Baek, C. A. Taylor, and J. D. Humphrey. A computational framework for fluid-solid-growth modeling in cardiovascular simulations. *Comp. Meth. Appl. Mech. Engrg.*, 198(45–463): 3583–3601, 2009.
- F. Fontan and E. Baudet. Surgical repair of tricuspid atresia. *Thorax*, 26(3):240–248, 1971.
- L. Formaggia and F. Nobile. A stability analysis for the arbitrary Lagrangian Eulerian formulation with finite elements. *East-West J. Numer. Math.*, 7(2):105–131, 1999.
- L. Formaggia, F. Nobile, A. Quarteroni, and A. Veneziani. Multiscale modelling of the circulatory system: a preliminary analysis. *Comput. Visual. Sci.*, 2(2–3):75–83, 1999.
- L. Formaggia, J.-F. Gerbeau, F. Nobile, and A. Quarteroni. On the coupling of 3D and 1D Navier–Stokes equations for flow problems in compliant vessels. *Comp. Meth. Appl. Mech. Engrg.*, 191(6–7):561–582, 2001.
- L. Formaggia, J.-F. Gerbeau, F. Nobile, and A. Quarteroni. Numerical treatment of defective boundary conditions for the Navier–Stokes equations. *SIAM J. Numer. Anal.*, 40(1):376–401, 2002.
- L. Formaggia, D. Lamponi, and A. Quarteroni. One-dimensional models for blood flow in arteries. *J. Eng. Math.*, 47(3–4):251–276, 2003.
- L. Formaggia, D. Lamponi, M. Tuveri, and A. Veneziani. Numerical modeling of 1D arterial networks coupled with a lumped parameters description of the heart. *Comput. Methods Biomech. Biomed. Engin.*, 9(5):273–288, 2006.
- L. Formaggia, A. Moura, and F. Nobile. On the stability of the coupling of 3D and 1D fluid-structure interaction models for blood flow simulations. *ESAIM: Mathematical Modelling and Numerical Analysis*, 41(4):743–769, 2007.
- L. Formaggia, A. Quarteroni, and A. Veneziani. *Cardiovascular Mathematics*, volume 1 of *Modeling, Simulation & Applications*. Springer-Verlag, Milan, 2009.
- L. Formaggia, A. Quarteroni, and C. Vergara. On the physical consistency between three-dimensional and one-dimensional models in haemodynamics. Submitted, 2012.
- O. Frank. Die Grundform des Arteriellen Pulses. *Zeitschrift für Biologie*, 37:483–526, 1899.
- O. H. Frazier, T. J. Myers, R. K. Jarvik, S. Westaby, D. W. Pigott, I. D. Gregoric, T. Khan, D. W. Tamez, J. L. Conger, and M. P. Macris. Research and development of an implantable, axial-flow left ventricular assist device: the Jarvik 2000 heart. *Ann. Thorac. Surg.*, 71(3 Suppl):S125–S132, 2001.
- O. H. Frazier, T. J. Myers, I. D. Gregoric, T. Khan, R. Delgado, M. Croitoru, K. Miller, R. Jarvik, and S. Westaby. Initial clinical experience with the Jarvik 2000 implantable axial-flow left ventricular assist system. *Circulation*, 105(24):2855–2860, 2002.
- O. H. Frazier, I. D. Gregoric, and W. E. Cohn. Initial experience with non-thoracic, extraperitoneal, off-pump insertion of the Jarvik 2000 heart in patients with previous median sternotomy. *J. Heart Lung Transplant.*, 25(5):499–503, 2006.
- Y. C. Fung. *Biomechanics: Mechanical Properties of Living Tissues*. Springer-Verlag, New York, 2nd edition, 1993.
- A. Gardel. Les pertes de charge dans les écoulements au travers de branchements en té. Technical Report 10, Bulletin Technique de la Suisse Romande, 1957.

- L. Gerardo-Giorda, F. Nobile, and C. Vergara. Analysis and optimization of Robin–Robin partitioned procedures in fluid–structure interaction problems. *SIAM J. Sci. Comput.*, 48(6):2091–2116, 2010.
- J.-F. Gerbeau, M. Vidrascu, and P. Frey. Fluid–structure interaction in blood flows on geometries based on medical imaging. *Comput. Struct.*, 83(2–3):155–165, 2005.
- C. Geuzaine and J. F. Remacle. Gmsh: A 3-D finite element mesh generator with built-in pre-and post-processing facilities. *Int. J. Num. Meth. Engng.*, 79(11):1309–1331, 2009.
- A. Ghodsizad, B. J. Kar, P. Layolka, A. Okur, J. Gonzales, C. Bara, M. N. Ungerer, M. Karck, I. D. Gregoric, and A. Ruhparwar. Less invasive off-pump implantation of axial flow pumps in chronic ischemic heart failure: Survival effects. *J. Heart Lung Transplant.*, 30(7):834–837, 2011.
- V. Gravemeier, A. Comerford, L. Yoshihara, M. Ismail, and W. A. Wall. A novel formulation for Neumann inflow boundary conditions in biomechanics. *Int. J. Num. Meth. Biomed. Engng.*, 28(5):560–573, 2012.
- L. Grinberg and G. E. Karniadakis. Outflow boundary conditions for arterial networks with multiple outlets. *Ann. Biomed. Eng.*, 36(9):1496–1514, 2008.
- P. Hedberg, I. Lönnberg, T. Jonason, G. Nilsson, K. Pehrsson, and I. Ringqvist. Left ventricular systolic dysfunction in 75-year-old men and women. A population-based study. *Eur. Heart J.*, 22(8):676–683, 2001.
- M. I. Hertz, P. Aurora, J. D. Christie, F. Dobbels, L. B. Edwards, R. Kirk, A. Y. Kucheryavaya, A. O. Rahmel, A. W. Rowe, and D. O. Taylor. Registry of the international society for heart and lung transplantation: a quarter century of thoracic transplantation. *J. Heart Lung Transplant.*, 27(9):937–942, 2008.
- J. G. Heywood, R. Rannacher, and S. Turek. Artificial boundaries and flux and pressure conditions for the incompressible Navier–Stokes equations. *Int. J. Num. Meth. Fluids*, 22(5):325–352, 1996.
- G. A. Holzapfel and R. W. Ogden. *Mechanics of Biological Tissue*. Springer-Verlag, Berlin Heidelberg, 2006.
- G. A. Holzapfel and R. W. Ogden. Constitutive modelling of passive myocardium: a structurally based framework for material characterization. *Phil. Trans. R. Soc. Lond. A*, 367(1902):3445–3475, 2009.
- G. A. Holzapfel, T. C. Gasser, and R. W. Ogden. A new constitutive framework for arterial wall mechanics and a comparative study of material models. *J. Elasticity*, 61(1–3):1–48, 2000.
- T. J. R. Hughes and J. Lubliner. On the one-dimensional theory of blood flow in the larger vessels. *Math. Biosci.*, 18(1-2):161–170, 1973.
- J. D. Humphrey. *Cardiovascular Solid Mechanics*. Springer-Verlag, Berlin, 2002.
- Y. Huo and G. S. Kassab. A hybrid one-dimensional/Womersley model of pulsatile blood flow in the entire coronary arterial tree. *Am. J. Physiol. Heart Circ. Physiol.*, 292(6):H2623–H2633, 2007.
- K. P. Ivanova and E. G. Bournaski. Combined distributed and lumped parameters model for transient flow analysis in complex pipe networks. *Comp. Meth. Appl. Mech. Engrg.*, 130(1–2):47–56, 1996.
- M. Jessup and S. Brozena. Heart failure. *N. Engl. J. Med.*, 348(20):2007–2018, 2003.
- V. Kanyanta, A. Ivankovic, and A. Karac. Validation of a fluid–structure interaction numerical model for predicting flow transients in arteries. *J. Biomech.*, 42(11):1705–1712, 2009.

Bibliography

- B. Kar, R. M. Delgado, O. H. Frazier, I. D. Gregoric, M. T. Harting, Y. Wadia, T. J. Myers, R. D. Moser, and J. Freund. The effect of LVAD aortic outflow-graft placement on hemodynamics and flow: Implantation technique and computer flow modeling. *Tex. Heart Inst. J.*, 32(3):294–298, 2005.
- M. Karamanoglu, D. E. Gallagher, A. P. Avolio, and M. F. O’Rourke. Functional origin of reflected pressure waves in a multibranched model of the human arterial system. *Am. J. Physiol.*, 267(5):H1681–1688, 1994.
- G. E. Karniadakis and S. J. Sherwin. *Spectral/hp Element Methods for Computational Fluid Dynamics*. Numerical Mathematics and Scientific Computation. Oxford University Press, Oxford, 2005.
- C. T. Kelley. *Iterative Methods for Linear and Nonlinear Equations*. Frontiers in applied mathematics, SIAM, 1995.
- H. A. Khalil, W. E. Cohn, R. W. Metcalfe, and O. H. Frazier. Preload sensitivity of the Jarvik 2000 and HeartMate II left ventricular assist devices. *ASAIO J.*, 54(3):245–248, 2008.
- H. J. Kim, C. A. Figueroa, T. J. R. Hughes, K. E. Jansen, and C. A. Taylor. Augmented Lagrangian method for constraining the shape of velocity profiles at outlet boundaries for three-dimensional finite element simulations of blood flow. *Comp. Meth. Appl. Mech. Engrg.*, 198(45–46):3551–3566, 2009a.
- H. J. Kim, I. E. Vignon-Clementel, C. A. Figueroa, J. F. LaDisa, K. E. Jansen, J. A. Feinstein, and C. A. Taylor. On coupling a lumped parameter heart model and a three-dimensional finite element aorta model. *Ann. Biomed. Eng.*, 37(11):2153–2169, 2009b.
- T. Kiuchi. An implicit method for transient gas flows in pipe networks. *Int. J. Heat Fluid Fl.*, 15(5): 378–383, 1994.
- Y. Kivity and R. Collins. Nonlinear wave propagation in viscoelastic tubes: application to aortic rupture. *J. Biomech.*, 7(1):67–76, 1974.
- S. C. Koenig, G. M. Pantalos, K. J. Gillars, D. L. Ewert, K. N. Litwak, and S. W. Etoch. Hemodynamic and pressure-volume responses to continuous and pulsatile ventricular assist in an adult mock circulation. *ASAIO J.*, 50(1):15–24, 2004.
- T. Korakianitis and Y. Shi. A concentrated parameter model for the human cardiovascular system including heart valve dynamics and atrioventricular interaction. *Med. Eng. Phys.*, 28(7):613–628, 2006.
- S. J. Kovács, D. M. McQueen, and C. S. Peskin. Modelling cardiac fluid dynamics and diastolic function. *Phil. Trans. R. Soc. Lond. A*, 359(1783):1299–1314, 2001.
- U. Küttler, M. Gee, C. Förster, A. Comerford, and W. A. Wall. Coupling strategies for biomedical fluid-structure interaction problems. *Int. J. Num. Meth. Biomed. Engrg.*, 26(3–4):305–321, 2010.
- G. J. Langewouters. *Visco-elasticity of the human aorta in vitro in relation to pressure and age*. PhD thesis, Free University, Amsterdam, 1982.
- E. Lanzarone, P. Liani, G. Baselli, and M. L. Constantino. Model of arterial tree and peripheral control for the study of physiological and assisted circulation. *Med. Eng. Phys.*, 29(5):542–555, 2007.
- T. Lassila, A. C. I. Malossi, M. Astorino, and S. Deparis. Geometrical multiscale model of an idealized left ventricle with fluid-structure interaction effects coupled to a one-dimensional viscoelastic arterial network. In *Proceedings of the ECCOMAS Thematic International Conference on Simulation and Modeling of Biological Flows (SIMBIO)*, Brussels, Belgium, September 2011.

- T. Lassila, A. C. I. Malossi, M. Stevanella, E. Votta, A. Redaelli, and S. Deparis. Multiscale fluid-structure interaction simulation of patient-specific left ventricle fluid dynamics with fictitious elastic structure regularization. Submitted, 2012.
- J. S. Leiva, P. J. Blanco, and G. C. Buscaglia. Iterative strong coupling of dimensionally-heterogeneous models. *Int. J. Num. Meth. Engng.*, 81(12):1558–1580, 2010.
- J. S. Leiva, P. J. Blanco, and G. C. Buscaglia. Partitioned analysis for dimensionally-heterogeneous hydraulic networks. *SIAM J. Multiscale Model. Simul.*, 9(2):872–903, 2011.
- D. Li and A. M. Robertson. A structural multi-mechanism damage model for cerebral arterial tissue. *J. Biomech. Eng.*, 131(10):101013 (8 pages), 2009.
- F. Liang and H. Liu. A closed-loop lumped parameter computational model for human cardiovascular system. *JSME International Journal*, 48(4):484–493, 2005.
- K. N. Litwak, S. C. Koenig, H. Tsukui, S. I. Kihara, Z. Wu, and G. M. Pantalos. Effects of left ventricular assist device support and outflow graft location upon aortic blood flow. *ASAIO J.*, 50(5):432–437, 2004.
- K. N. Litwak, S. C. Koenig, R. C. Cheng, G. A. Giridharan, K. J. Gillars, and G. M. Pantalos. Ascending aorta outflow graft location and pulsatile ventricular assist provide optimal hemodynamic support in an adult mock circulation. *Artif. Organs*, 29(8):629–635, 2005.
- Y. Liu, C. Dang, M. Garcia, H. Gregersen, and G. S. Kassab. Surrounding tissues affect the passive mechanics of the vessel wall: theory and experiment. *Am. J. Physiol. Heart Circ. Physiol.*, 293(6):H3290–H3300, 2007.
- D. Lloyd-Jones, R. Adams, M. Carnethon, G. De Simone, T. B. Ferguson, K. Flegal, E. Ford, K. Furie, A. Go, K. Greenlund, et al. Heart disease and stroke statistics–2009 update: A report from the american heart association statistics committee and stroke statistics subcommittee. *Circulation*, 119(3):e21–e181, 2009.
- Q. Long, R. Merrifield, G. Z. Yang, X. Y. Xu, P. J. Kilner, and D. N. Firmin. The influence of inflow boundary conditions on intra left ventricle flow predictions. *J. Biomech. Eng.*, 125(6):922–927, 2003.
- Q. Long, R. Merrifield, X. Y. Xu, P. Kilner, D. N. Firmin, and G. Z. Yang. Subject-specific computational simulation of left ventricular flow based on magnetic resonance imaging. *P. I. Mech. Eng. H*, 222(4):475, 2008.
- A. C. I. Malossi and J. Bonnemain. Numerical comparison and calibration of geometrical multiscale models for the simulation of arterial flows. Submitted, 2012.
- A. C. I. Malossi, P. J. Blanco, and S. Deparis. Algorithms for the coupling of one-dimensional arterial networks with three-dimensional fluid-structure interaction problems. In *Proceedings of the ECCO-MAS Thematic International Conference on Simulation and Modeling of Biological Flows (SIMBIO)*, Brussels, Belgium, September 2011a.
- A. C. I. Malossi, P. J. Blanco, S. Deparis, and A. Quarteroni. Algorithms for the partitioned solution of weakly coupled fluid models for cardiovascular flows. *Int. J. Num. Meth. Biomed. Engng.*, 27(12):2035–2057, 2011b.
- A. C. I. Malossi, P. J. Blanco, P. Crosetto, S. Deparis, and A. Quarteroni. Implicit coupling of one-dimensional and three-dimensional blood flow models with compliant vessels. Submitted, 2012a.

Bibliography

- A. C. I. Malossi, P. J. Blanco, and S. Deparis. A two-level time step technique for the partitioned solution of one-dimensional arterial networks. *Comp. Meth. Appl. Mech. Engrg.*, 237–240:212–226, 2012b.
- C. C. Marin-Artieda and G. F. Dargush. Approximate limit load evaluation of structural frames using linear elastic analysis. *Eng. Struct.*, 29(3):296–304, 2007.
- G. Marom, R. Haj-Ali, E. Raanani, H. J. Schäfers, and M. Rosenfeld. A fluid-structure interaction model of the aortic valve with coaptation and compliant aortic root. *Med. Biol. Engrg. Comp.*, 50(2):173–182, 2012.
- H. G. Matthies and J. Steindorf. Partitioned strong coupling algorithms for fluid-structure interaction. *Comput. Struct.*, 81(8–11):805–812, 2003. K.J Bathe 60th Anniversary Issue.
- K. S. Matthys, J. Alastruey, J. Peiró, A. W. Khir, P. Segers, P. R. Verdonck, K. H. Parker, and S. J. Sherwin. Pulse wave propagation in a model human arterial network: Assessment of 1-D numerical simulations against in vitro measurements. *J. Biomech.*, 40(15):3476–3486, 2007.
- K. May-Newman, B. Hillen, and W. Dembitsky. Effect of left ventricular assist device outflow conduit anastomosis location on flow patterns in the native aorta. *ASAIO J.*, 52(2):132–139, 2006.
- J. J. V. McMurray and M. A. Pfeffer. Heart failure. *The Lancet*, 365(9474):1877–1889, 2005.
- D. M. McQueen and C. S. Peskin. Heart simulation by an immersed boundary method with formal second-order accuracy and reduced numerical viscosity. In *Proceedings of the International Conference on Theoretical and Applied Mechanics (ICTAM)*, pages 429–444. Mechanics for a New Millennium, 2002.
- F. Migliavacca, R. Balossino, G. Pennati, G. Dubini, T. Y. Hsia, M. R. de Leval, and E. L. Bove. Multiscale modelling in biofluidynamics: Application to reconstructive paediatric cardiac surgery. *J. Biomech.*, 39(6):1010–1020, 2006.
- V. Milišić and A. Quarteroni. Analysis of lumped parameter models for blood flow simulations and their relation with 1D models. *ESAIM: Mathematical Modelling and Numerical Analysis*, 38(4):613–632, 2004.
- L. W. Miller, F. D. Pagani, S. D Russell, R. John, A. J. Boyle, K. D. Aaronson, J. V. Conte, Y. Naka, D. Mancini, R. M. Delgado, et al. Use of a continuous-flow device in patients awaiting heart transplantation. *N. Engl. J. Med.*, 357(9):885–896, 2007.
- M. E. Moghadam, Y. Bazilevs, T.-Y. Hsia, I. E Vignon-Clementel, and A. L. Marsden. A comparison of outlet boundary treatments for prevention of backflow divergence with relevance to blood flow simulations. *Comput. Mech.*, 48(3):277–291, 2011.
- P. Moireau, N. Xiao, M. Astorino, C. A. Figueroa, D. Chapelle, C.-A. Taylor, and J.-F. Gerbeau. External tissue support and fluid-structure simulation in blood flows. *Biomech. Model. Mechanobiol.*, 11(1–2): 1–18, 2012.
- D. P. Mok and W. A. Wall. Partitioned analysis schemes for the transient interaction of incompressible flows and nonlinear flexible structures. *Trends in Computational Structural Mechanics (K. Schweizerhof and W. Wall, eds.)*, K.U. Bletzingler, CIMNE, Barcelona, pages 689–698, 2001.
- J. P. Mynard and P. Nithiarasu. A 1D arterial blood flow model incorporating ventricular pressure, aortic valve and regional coronary flow using the locally conservative Galerkin (LCG) method. *Commun. Numer. Meth. Engrg.*, 24(5):367–417, 2008.

- J. P. Mynard, M. R. Davidson, D. J. Penny, and J. J. Smolich. A simple, versatile valve model for use in lumped parameter and one-dimensional cardiovascular models. *Int. J. Num. Meth. Biomed. Engng.*, 28(6–7):626–641, 2011.
- M. P. Nash and P. J. Hunter. Computational mechanics of the heart. *J. Elasticity*, 61(1–3):113–141, 2000.
- K. Nawata, T. Nishimura, S. Kyo, M. Hisagi, O. Kinoshita, A. Saito, N. Motomura, S. Takamoto, and M. Ono. Outcomes of midterm circulatory support by left ventricular assist device implantation with descending aortic anastomosis. *J. Artif. Organs*, 13(4):197–201, 2010.
- F. H. Netter. *Atlas of Human Anatomy*. Icon Learning Systems, Los Angeles, 2nd edition, 1997.
- W. W. Nichols, M. F. O’Rourke, and C. Vlachopoulos. *McDonald’s Blood Flow in Arteries: Theoretical, Experimental and Clinical Principles*. Hodder Arnold, London, 6th edition, 2011.
- F. Nobile. *Numerical approximation of fluid-structure interaction problems with application to haemodynamics*. PhD thesis, École Polytechnique Fédérale de Lausanne, 2001.
- F. Nobile. Coupling strategies for the numerical simulation of blood flow in deformable arteries by 3D and 1D models. *Math. Comput. Model.*, 49(11–12):2152–2160, 2009.
- F. Nobile and C. Vergara. An effective fluid-structure interaction formulation for vascular dynamics by generalized Robin conditions. *SIAM J. Sci. Comput.*, 30(2):731–763, 2008.
- F. Nobile, A. Quarteroni, and R. Ruiz-Baier. An active strain electromechanical model for cardiac tissue. *Int. J. Num. Meth. Biomed. Engng.*, 28(1):52–71, 2012.
- D. Nordsletten, M. McCormick, P. J. Kilner, P. Hunter, D. Kay, and N. P. Smith. Fluid–solid coupling for the investigation of diastolic and systolic human left ventricular function. *Int. J. Numer. Methods Biomed. Engr.*, 27(7):1017–1039, 2011.
- M. S. Olufsen. *Modeling the arterial system with reference to an anesthesia simulator*. PhD thesis, Roskilde University, May 1998.
- M. S. Olufsen, C. S. Peskin, W. Y. Kim, E. M. Pedersen, A. Nadim, and J. Larsen. Numerical simulation and experimental validation of blood flow in arteries with structured-tree outflow conditions. *Ann. Biomed. Eng.*, 28:1281–1299, 2000.
- J. T. Ottesen, M. S. Olufsen, and J. K. Larsen. *Applied Mathematical Models in Human Physiology*, volume MM09 of *Monographs on Mathematical Modeling and Computation*. SIAM, 2004.
- G. Papadakis. Coupling 3D and 1D fluid-structure-interaction models for wave propagation in flexible vessels using a finite volume pressure-correction scheme. *Commun. Numer. Meth. Engng.*, 25(5): 533–551, 2009.
- T. Passerini, M. de Luca, L. Formaggia, A. Quarteroni, and A. Veneziani. A 3D/1D geometrical multiscale model of cerebral vasculature. *J. Eng. Math.*, 64(4):319–330, 2009.
- A. J. Pullan, N. P. Smith, and P. J. Hunter. An anatomically based model of transient coronary blood flow in the heart. *SIAM J. Appl. Math.*, 62(3):990–1018, 2002.
- L. Quartapelle. *Numerical Solution of the Incompressible Navier–Stokes Equations*, volume 113 of *International Series of Numerical Mathematics*. Birkhäuser Verlag, Basel, 1993.

Bibliography

- A. Quarteroni and L. Formaggia. *Modelling of Living Systems*, chapter Mathematical Modelling and Numerical Simulation of the Cardiovascular System. Handbook of Numerical Analysis Series. Elsevier, 2003.
- A. Quarteroni and A. Veneziani. Analysis of a geometrical multiscale model based on the coupling of ODEs and PDEs for blood flow simulations. *SIAM J. Multiscale Model. Simul.*, 1(2):173–195, 2003.
- A. Quarteroni, R. Sacco, and F. Saleri. *Numerical Mathematics*, volume 37. Springer-Verlag, New York, 2000.
- M. Rahman, J. Smietana, E. Hauck, B. Hoh, N. Hopkins, A. Siddiqui, E. I. Levy, H. Meng, and J. Mocco. Size ratio correlates with intracranial aneurysm rupture status: a prospective study. *Stroke*, 41(5): 916–920, 2010.
- A. Redaelli, F. Maisano, M. Soncini, O. Alfieri, and F. M. Montecchi. Haemodynamics and mechanics following partial left ventriculectomy: a computer modeling analysis. *Med. Eng. Phys.*, 26(1):31–42, 2004.
- J. Reichold, M. Stampanoni, A. L. Keller, A. Buck, P. Jenny, and B. Weber. Vascular graph model to simulate the cerebral blood flow in realistic vascular networks. *J. Cereb. Blood Flow Metab.*, 29(8): 1429–1443, 2009.
- T. C. S. Rendall and C. B. Allen. Efficient mesh motion using radial basis functions with data reduction algorithms. *J. Comput. Phys.*, 228(17):6231–6249, 2009.
- P. Reymond, F. Merenda, F. Perren, D. Rüfenacht, and N. Stergiopulos. Validation of a one-dimensional model of the systemic arterial tree. *Am. J. Physiol. Heart Circ. Physiol.*, 297(1):H208–H222, 2009.
- P. Reymond, Y. Bohraus, F. Perren, F. Lazeyras, and N. Stergiopulos. Validation of a patient-specific one-dimensional model of the systemic arterial tree. *Am. J. Physiol. Heart Circ. Physiol.*, 301(3): H1173–H1182, 2011.
- A. M. Robertson, M. R. Hill, and D. Li. Structurally motivated damage models for arterial walls. Theory and application. In *Modeling of Physiological Flows*, volume 5 of *Modeling, Simulation & Applications*, pages 143–185, Springer-Verlag, Milan, 2011.
- V. L. Roger, A. S. Go, D. M. Lloyd-Jones, R. J. Adams, J. D. Berry, T. M. Brown, M. R. Carnethon, S. Dai, G. de Simone, E. S. Ford, et al. Heart disease and stroke statistics – 2011 update: A report from the American Heart Association. *Circulation*, 123(4):e18–e209, 2011.
- E. A. Rose, A. C. Gelijns, A. J. Moskowitz, D. F. Heitjan, L. W. Stevenson, W. Dembitsky, J. W. Long, D. D. Ascheim, A. R. Tierney, R. G. Levitan, et al. Long-term mechanical left ventricular assistance for end-stage heart failure. *N. Engl. J. Med.*, 345(20):1435–1443, 2001.
- J. Sainte-Marie, D. Chapelle, R. Cimrman, and M. Sorine. Modeling and estimation of the cardiac electromechanical activity. *Comput. Struct.*, 84(28):1743–1759, 2006.
- T. Schenkel, M. Malve, M. Reik, M. Markl, B. Jung, and H. Oertel. MRI-based CFD analysis of flow in a human left ventricle: methodology and application to a healthy heart. *Ann. Biomed. Eng.*, 37(3): 503–515, 2009.
- P. Segers and P. Verdonck. Role of tapering in aortic wave reflection: hydraulic and mathematical model study. *J. Biomech.*, 33(3):299–306, 2000.

- P. Segers, N. Stergiopoulos, N. Westerhof, P. Wouters, P. Kolh, and P. Verdonck. Systemic and pulmonary hemodynamics assessed with a lumped-parameter heart-arterial interaction model. *J. Eng. Math.*, 47(3):185–199, 2003.
- M. Sermesant, P. Moireau, O. Camara, Sainte-Marie J., R. Andriantsimiavona, R. Cimrman, D. L. G. Hill, D. Chapelle, and R. Razavi. Cardiac function estimation from MRI using a heart model and data assimilation: Advances and difficulties. *Medical Image Anal.*, 10(4):642–656, 2006.
- M. Sermesant, R. Chabiniok, P. Chinchapatnam, T. Mansi, F. Billet, P. Moireau, J. M. Peyrat, K. Wong, J. Relan, K. Rhode, et al. Patient-specific electromechanical models of the heart for the prediction of pacing acute effects in CRT: A preliminary clinical validation. *Medical Image Anal.*, 16(1):201–215, 2011.
- S. J. Sherwin, V. Franke, J. Peiró, and K. Parker. One-dimensional modelling of a vascular network in space-time variables. *J. Eng. Math.*, 47(3):217–250, 2003.
- Y. Shi, P. Lawford, and R. Hose. Review of Zero-D and 1-D models of blood flow in the cardiovascular system. *BioMedical Engineering OnLine*, 10(33):1–38, 2011.
- B. Skallerud, V. Prot, and I. S. Nordrum. Modeling active muscle contraction in mitral valve leaflets during systole: a first approach. *Biomech. Model. Mechanobiol.*, 10(1):11–26, 2011.
- J. Sokołowski and J.-P. Zolésio. *Introduction to shape optimization*, volume 16 of *Series in computational mathematics*. Springer-Verlag, Berlin–Heidelberg, 1992.
- N. Stergiopoulos, D. F. Young, and T. R. Rogge. Computer simulation of arterial flow with applications to arterial and aortic stenoses. *J. Biomech.*, 25(12):1477–1488, 1992.
- N. Stergiopoulos, B. Westerhof, and N. Westerhof. Total arterial inertance as the fourth element of the windkessel model. *Am. J. Physiol.*, 276(1):H81–H88, 1999.
- J. C. Stettler, P. Niederer, and M. Anliker. Theoretical analysis of arterial hemodynamics including the influence of bifurcations, Part I: mathematical model and prediction of normal pulse patterns. *Ann. Biomed. Eng.*, 9(2):145–164, 1981.
- M. Stevanella, E. Votta, and A. Redaelli. Mitral valve finite element modeling: Implications of tissues' nonlinear response and annular motion. *J. Biomech. Eng.*, 131(12):121010 (pages 9), 2009.
- M. Stevanella, F. Maffessanti, C. A. Conti, E. Votta, A. Arnoldi, M. Lombardi, O. Parodi, E. G. Caiani, and A. Redaelli. Mitral valve patient-specific finite element modeling from cardiac MRI: Application to an annuloplasty procedure. *Cardiovasc. Engr. Tech.*, 2(2):66–76, 2011.
- K. Sutton-Tyrrell, H. G. Alcorn, S. K. Wolfson, S. F. Kelsey, and L. H. Kuller. Predictors of carotid stenosis in older adults with and without isolated systolic hypertension. *Stroke*, 24(3):355–361, 1993.
- D. Tang, C. Yang, T. Geva, and P. J. del Nido. Image-based patient-specific ventricle models with fluid-structure interaction for cardiac function assessment and surgical design optimization. *Progr. Pediatr. Cardiol.*, 30(1–2):51–62, 2010.
- C. A. Taylor and C. A. Figueroa. Patient-specific modeling of cardiovascular mechanics. *Annu. Rev. Biomed. Eng.*, 11:109–134, 2009.
- T. E. Tezduyar and S. Sathe. Modeling of fluid-structure interactions with the space-time finite elements: Solution techniques. *Int. J. Num. Meth. Fluids*, 54(6–8):855–900, 2006.

Bibliography

- T. E. Tezduyar, S. Sathe, and K. Stein. Solution techniques for the fully discretized equations in computation of fluid-structure interactions with the space-time formulations. *Comp. Meth. Appl. Mech. Engrg.*, 195(41–43):5743–5753, 2006.
- C. A. Thunberg, B. D. Gaitan, F. A. Arabia, D. J. Cole, and A. M. Grigore. Ventricular assist devices today and tomorrow. *J. Cardiothorac. Vasc. Anesth.*, 24(4):656–680, 2010.
- R. Torii, M. Oshima, T. Kobayashi, K. Takagi, and T. Tezduyar. Fluid-structure interaction modeling of a patient-specific cerebral aneurysm: influence of structural modeling. *Comput. Mech.*, 43(1):151–159, 2008.
- E. Tuzun, C. Narin, I. D. Gregoric, W. E. Cohn, and O. H. Frazier. Ventricular assist device outflow-graft site: effect on myocardial blood flow. *J. Sur. Res.*, 171(1):71–75, 2011.
- S. A. Urquiza, P. J. Blanco, M. J. Vénere, and R. A. Feijóo. Multidimensional modelling for the carotid artery blood flow. *Comp. Meth. Appl. Mech. Engrg.*, 195(33–36):4002–4017, 2006.
- M. Ursino. Interaction between carotid baroregulation and the pulsating heart: a mathematical model. *Am. J. Physiol. Heart Circ. Physiol.*, 275(5):H1733–H1747, 1998.
- A. Veneziani and C. Vergara. Flow rate defective boundary conditions in haemodynamics simulations. *Int. J. Num. Meth. Fluids*, 47(8–9):803–816, 2005.
- M. Vieira and K. Shimada. Surface mesh segmentation and smooth surface extraction through region growing. *Comput. Aided Geom. D.*, 22(8):771–792, 2005.
- I. E. Vignon-Clementel, C. A. Figueroa, K. E. Jansen, and C. A. Taylor. Outflow boundary conditions for three-dimensional finite element modeling of blood flow and pressure in arteries. *Comp. Meth. Appl. Mech. Engrg.*, 195(29–32):3776–3796, 2006.
- J. J. Wang and K. H. Parker. Wave propagation in a model of the arterial circulation. *J. Biomech.*, 37(4):457–470, 2004.
- V. Y. Wang, H. I. Lam, D. B. Ennis, B. R. Cowan, A. A. Young, and M. P. Nash. Modelling passive diastolic mechanics with quantitative MRI of cardiac structure and function. *Medical Image Anal.*, 13(5):773–784, 2009.
- H. Watanabe, S. Sugiura, and T. Hisada. The looped heart does not save energy by maintaining the momentum of blood flowing in the ventricle. *Am. J. Physiol. Heart Circ. Physiol.*, 294(5):H2191–H2196, 2008.
- R. R. Wemple and L. F. Mockros. Pressure and flow in the systemic arterial. *J. Biomech.*, 5(6):629–641, 1972.
- J. F. Wenk, Z. Zhang, G. Cheng, D. Malhotra, G. Acevedo-Bolton, M. Burger, T. Suzuki, D. A. Saloner, A. W. Wallace, J. M. Guccione, and M. B. Ratcliffe. First finite element model of the left ventricle with mitral valve: insights into ischemic mitral regurgitation. *Ann. Thorac. Surg.*, 89(5):1546–1553, 2010.
- S. Westaby, O. H. Frazier, D. W. Pigott, S. Saito, and R. K. Jarvik. Implant technique for the Jarvik 2000 heart. *Ann. Thorac. Surg.*, 73(4):1337–1340, 2002.
- N. Westerhof, N. Stergiopoulos, and M. I. M. Noble. *Snapshots Of Hemodynamics: An Aid For Clinical Research And Graduate Education*. Basic Science for the Cardiologist. Springer-Verlag, 2nd edition, 2010.

- J. R. Womersley. An elastic tube theory of pulse transmission and oscillatory flow in mammalian arteries. Technical Report WADC-TR-56-614, Wright Air Dev. Center, Dayton, Ohio, 1957.
- N. Yang, S. Deutsch, E. G. Paterson, and K. B. Manning. Numerical study of blood flow at the end-to-side anastomosis of a left ventricular assist device for adult patients. *J. Biomech. Eng.*, 131(11):111005 (9 pages), 2009.
- N. Yang, S. Deutsch, E. G. Paterson, and K. B. Manning. Hemodynamics of an end-to-side anastomotic graft for a pulsatile pediatric ventricular assist device. *J. Biomech. Eng.*, 132(3):031009 (13 pages), 2010.
- Y. B. Yang, S. R. Kuob, and Y. S. Wu. Incrementally small-deformation theory for nonlinear analysis of structural frames. *Eng. Struct.*, 24(6):783–798, 2002.
- E. A. Ziemba and R. John. Mechanical circulatory support for bridge to decision: Which device and when to decide. *J. Card. Surg.*, 25(4):425–433, 2010.

Curriculum vitae

Adelmo Cristiano Innocenza MALOSSI

Personal details

Date of birth September 14th, 1982
Place of birth Milan, Italy

Academic education

- 2009-2012 **Ph.D. Student at the École Polytechnique Fédérale de Lausanne (EPFL)**
Laboratory CMCS - Chair of Modeling and Scientific Computing,
MATHICSE, SMA, SB
Advisors Prof. Alfio Quarteroni and Dr. Simone Deparis
- 2007-2008 **Fellowship Researcher at the Politecnico di Milano**
Laboratory MOX - Modeling and Scientific Computing,
Department of Mathematics
Project *Numerical simulation of the evolution of sedimentary basins*
- 2004-2007 **Master's Degree in Aeronautical Engineering: Aerodynamics**
Graduated on October 22nd, 2007 from the Politecnico di Milano
Grade 110/110 summa cum laude
Thesis *A Galerkin–Lagrange approach for numerical approximation of incompressible stratified fluids*
Advisors Dr. Stefano Micheletti and Prof. Lorenzo Valdetaro
- 2001-2004 **Bachelor's of Science in Aerospace Engineering**
Graduated on October 4th, 2004 from the Politecnico di Milano
Grade 110/110 summa cum laude
Thesis *Aerodynamic project of the ducted fans of a VTOL aircraft*
Advisors Prof. Pierangelo Masarati

Scientific publications

- P. J. Blanco, S. Deparis, and A. C. I. Malossi. On the continuity of mean total normal stress in geometrical multiscale cardiovascular problems. *In preparation*, 2012.
- J. Bonnemain, A. C. I. Malossi, M. Lesinigo S. Deparis, A. Quarteroni, and L. K. von Segesser. Numerical simulation of left ventricular assist device implantations: comparing the ascending and the descending aorta cannulations. *Submitted*, 2012.
- T. Lassila, A. C. I. Malossi, M. Stevanella, E. Votta, A. Redaelli, and S. Deparis. Multiscale fluid-structure interaction simulation of patient-specific left ventricle fluid dynamics with fictitious elastic structure regularization. *Submitted*, 2012.
- A. C. I. Malossi and J. Bonnemain. Numerical comparison and calibration of geometrical multi-scale models for the simulation of arterial flows. *Submitted*, 2012.
- A. C. I. Malossi, P. J. Blanco, P. Crosetto, S. Deparis, and A. Quarteroni. Implicit coupling of one-dimensional and three-dimensional blood-flow models with compliant vessels. *Submitted*, 2012.
- A. C. I. Malossi, P. J. Blanco, and S. Deparis. A two-level time step technique for the partitioned solution of one-dimensional arterial networks. *Comp. Meth. Appl. Mech. Engrg.*, 237–240:212–226, 2012.
- A. C. I. Malossi, P. J. Blanco, S. Deparis, and A. Quarteroni. Algorithms for the partitioned solution of weakly coupled fluid models for cardiovascular flows. *Int. J. Num. Meth. Biomed. Engrg.*, 27(12):2035–2057, 2011.
- M. Longoni, A. C. I. Malossi, A. Quarteroni, A. Villa, and P. Ruffo. An ALE-based numerical technique for modeling sedimentary basin evolution featuring layer deformations and faults. *J. Comput. Phys.*, 230(8):3230–3248, 2011.
- M. Longoni, A. C. I. Malossi, and A. Villa. A robust and efficient conservative technique for simulating three-dimensional sedimentary basins dynamics. *Comput. Fluids*, 39(10):1964–1976, 2010.

Technical reports

- A. C. I. Malossi and S. Deparis. LifeV development guidelines. EPFL, Lausanne (Switzerland), 2010.

Conference papers and proceedings

- T. Lassila, A. C. I. Malossi, M. Astorino, and S. Deparis. Geometrical multiscale model of an idealized left ventricle with fluid-structure interaction effects coupled to a one-dimensional viscoelastic arterial network. In *Proceedings of the ECCOMAS Thematic International Conference on Simulation and Modeling of Biological Flows (SIMBIO)*, Brussels, Belgium, September 21-23, 2011.
- A. C. I. Malossi, P. J. Blanco, and S. Deparis. Algorithms for the coupling of one-dimensional arterial networks with three-dimensional fluid-structure interaction problems. In *Proceedings of the ECCOMAS Thematic International Conference on Simulation and Modeling of Biological Flows (SIMBIO)*, Brussels, Belgium, September 21-23, 2011.

Presentations, conferences, and seminars

- SIMBIO 2011, ECCOMAS Thematic International Conference on Simulation and Modeling of Biological Flows. Contributed talk in plenary session: *Algorithms for the coupling of one-dimensional arterial networks with three-dimensional fluid-structure interaction problems*. Brussels, Belgium, September 22nd, 2011.
- RMMM 2011, Reliable Methods of Mathematical Modeling. Contributed talk in plenary session: *Geometrical mutiscale algorithms for the coupling of dimensionally heterogeneous cardiovascular problems*. EPFL, Lausanne (Switzerland), July 3rd, 2011.
- EPFL, Seminar for the course “Mathematical modeling and Numerical Simulation II”: *Geometrical multiscale modeling of the cardiovascular system. Focus on 1-D modeling of the human arterial tree*. Lausanne (Switzerland), December 2nd, 2010.
- MPF 2010, IV International Symposium on Modeling of Physiological Flows. Contributed talk in plenary session: *Algorithms for the Coupling of Geometrical Multiscale Models*. Chia Laguna (Italy), June 4th, 2010.
- EPFL, Seminar for the course “Mathematical modeling and Numerical Simulation I”: *Algorithms for the Coupling of Geometrical Multiscale Fluid Models*. Lausanne (Switzerland), December 17th, 2009.